Fundamental properties of M-dwarfs in eclipsing binary star systems

Samuel Gill

Doctor of Philosophy

Department of Physics, Keele University

March 2019

Abstract

The absolute parameters of M-dwarfs in eclipsing binary systems provide important tests for evolutionary models. Those that have been measured reveal significant discrepancies with evolutionary models. There are two problems with M-dwarfs: 1. M-dwarfs generally appear bigger and cooler than models predict (such that their luminosity agrees with models) and 2. some M-dwarfs in eclipsing binaries are measured to be hotter than expected for their mass. The exact cause of this is unclear and a variety of conjectures have been put forward including enhanced magnetic activity and spotted surfaces. There is a lack of M-dwarfs with absolute parameters and so the exact causes of these disparities are unclear. As the interest in low-mass stars rises from the ever increasing number of exoplanets found around them, it is important that a considerable effort is made to understand why this is so.

A solution to the problem lies with low-mass eclipsing binary systems discovered by the WASP (Wide Angle Search for Planets) project. A large sample of these systems have been followed up with spectroscopic orbits that ultimately exclude them from the planet-hunting process. In this work I obtained follow-up photometry for 9 of these systems and used these data to measure the absolute parameters of each star. These will eventually be used to create empirical calibrations for low mass stars when the number of EBLMs (eclipsing binary, low-mass) measured within this framework increases.

Breaking the mass degeneracy required supplementary information from evolutionary models and the primary stars atmospheric parameters. I successfully created, tested and deployed a spectral analysis routine which used wavelet decomposition to analyse the spectra of FGK stars in exoplanet/eclipsing binary systems. Careful selection of wavelet coefficients filter out large systematic trends and noise typically observed in spectra. I used this principle to reliably measure $T_{\rm eff}$, $V \sin i$ and [Fe/H] from CORALIE spectra. My method had a systematic offset in [Fe/H] of -0.18 dex relative to equivalent-width measurements of higher-quality spectra. There is also a correlation between $T_{\rm eff}$ and $\log g$.

The sample of eclipsing binary systems in this work highlight that only a fraction are suitable for empirical calibrations. I found that three of systems have primary stars which

have evolved into the “blue-hook” part of their main-sequence evolution. They have two distinct solutions for mass and age which require supplementary information before they can be used in empirical calibrations. A further two systems have large impact parameters which increase the uncertainty in radius above the required precision of a few percent. I advocate the need for a volume-limited sample to avoid spending time observing and measuring such systems.

The method used to measure low-mass eclipsing binaries is well-established, yet there is a dearth of well-studied F+M binaries. The EBLM project has provided spectroscopic orbits for 118 F+M binaries and I expect the absolute parameters for these systems to follow timely. However, there is a requirement for a *hare-and-hounds* style experiment to assess how absolute parameters differ between different research groups and methods of analysis. Using a subset of systems, I show that subtle choices in helium-enhancement and mixing-length parameters can introduce a 2-4% uncertainty in mass and age. A similar effect is seen for different limb-darkening laws and so an in-depth review into how this will affect empirical mass-radius calibrations is required.

Acknowledgements

> "*Results based on 12 mental health symptoms (GHQ-12) showed that 32% of PhD students are at risk of having or developing a common psychiatric disorder, especially depression.*"
>
> – Levecque et al. (2017)

I would like to thank my primary supervisor, Pierre Maxted, for always encouraging me do science better. No Journey through research is straightforward. The journey which produced this work involved scaling many mountains, crossing many riverines and navigating the thickest fog. You patiently nudged me in the right direction to ensure I never ventured too far from the beaten track, and for that I am exceptionally grateful. I would also like to thank my second supervisor, Barry Smalley, who always had an open ear to discuss all things spectroscopy. I thank Jessica Evans, Daniel Evans, John Southworth, David Anderson, Leslie Hebb, Bruce Gary, Uffe Jørgensen, Martin Dominik, Colin Snodgrass, Penélope Longa-Peña and Amaury Triaud for assisting in observations which feature in this work.

Students in research degrees, and academia in general, face higher mental health risks than other professions. Stress and lone-working often leads to depression, guilt, isolation and negative thoughts. This often degrades ones self-confidence and the relationships with those closest to us. I would be fooling myself if I didn't acknowledge that I have experienced some, if not all of the symptoms mentioned above whilst studying for my doctorate. I would never have been able to survive my Ph.D without the endless love and support of my fiance, Katie. Thank you for always bringing a smile to my face and helping me weather the harshest of storms. I thank my parents, Jean and Simon Gill. You provided me with emotional and financial support during my research, as well as invaluable guidance. For this I am eternally grateful.

I would also like to honourably mention our beagle, Bruce McGill. You kept me company day and night, taxed all my crunchy goods and pestered me for walks. Those walks provided crucial down time which helped me relax and preserved my sanity. Thank you for needing so little and doing so much.

Contents

List of Figures

List of Tables

1 Introduction

When you observe the night sky with only your eyes none of the stars you see will be M-dwarfs, yet they are the most common stars in the galaxy making up over 75% of all stars[1] (Henry et al. 2006). Some stars you will see are of the spectral type M, but these are giant stars which have evolved and swelled to the point in which their outer-layers have cooled. These are called M-giants and can be easily seen with a reddish twinkle in the night-sky; an example is Betelgeuse which is North-East of Orion's belt in the northern hemisphere. One property the M-dwarfs/giants share is outer layers cool enough to permit opacities from diatomic molecules ($T_{\rm eff} \approx 3000\,{\rm K}$). If you were to split the visible light from an M-dwarf with a prism you would see large absorption bands corresponding to titanium-oxide (TiO), carbon-monoxide (CO) and water (H_2O). These signatures denote an M-type star by the classical Harvard spectral classification scheme.

Despite the observational similarities, M-dwarfs and M-giants differ when you peer below the outer layers. Betelgeuse probably started its life as a 20-$M_\odot$ O-type main-sequence star, the exact mass depending on an assumed initial rotation, parallax measurement and which stellar models you employ (van Loon 2013). Internally, Betelgeuse's hydrogen core has collapsed and brought in more hydrogen resulting in shell burning around the core. This results in a swelling of the outer layers lowering the surface temperature (giving Betelgeuse it's reddish glint and spectral type) but increasing it's overall luminosity. During this phase Betelgeuse underwent short periods of heavy mass-loss and developed an extended atmosphere (Mackey et al. 2014). M-dwarfs lead much less flamboyant lives, but are anything but boring.

[1] Updated counts provided at www.reons.org

1.1 Properties of M-dwarfs

M-dwarfs form like any other star; a cloud of gas and dust clumps together by means of gravity and begins rotating. A potential source of energy comes from the gravitational potential released when such contraction occurs in the pre-main sequence (PMS). The virial theorem informs us that only half of the change in gravitational energy is available to be radiated away upon contraction; the rest heats the internal gas. It is possible to calculate[2] the energy released assuming a radial density distribution,

$$\Delta E_g = \frac{3}{10}\frac{GM_\star^2}{R_\star}, \tag{1.1}$$

where $M_\star$ is the mass of the star, $R_\star$ is the radius and G is the gravitational constant. For the Sun, $\Delta E_g \approx 1.2 \times 10^{48}$ erg (1 erg = 10^{-7} J). If a star radiates at a luminosity $L_\star$, the *Kelvin-Helmholtz* timescale can be calculated,

$$\tau_{\rm KH} = \frac{\Delta E_g}{L_\star}. \tag{1.2}$$

This is essentially the time taken for a protostar to reach the zero-age main-sequence (ZAMS). Contraction is slowest when both $R_\star$ and $L_\star$ are small ($\tau_{\rm KH} = \Delta E_g / L_\star$ and $\Delta E_g \propto 1/R_\star$) and thus the PMS lifetime of an M-dwarf is largely spent in the final stages of contraction. For example, a 0.3 $M_\odot$ M-dwarf remains in the PMS phase for approximately 0.18 Gyr.[3] In the Solar case $\tau_{\rm KH} \sim 10^7$ yr, which is two orders of magnitude smaller than the age of the solar system measured measured from radioactive dating (e.g. Baker et al. 2005).

Kelvin-Helmholtz contraction and late-stage accretion increase the young M-dwarf's angular momentum. However, interactions with the protostellar disk counteract this (Matt & Pudritz 2005). Eventually, the protostellar disk is cleared and the M-dwarf enters the main sequence (MS) where few drastic changes will occur. During this phase subsequent spin-down is caused by magnetised winds carrying away angular momentum (Barnes 2003). For FGK dwarfs older than 500 Myr, the loss of angular momentum is predictable ($\propto t^{-0.5}$)

[2] https://www.ast.cam.ac.uk/~pettini/STARS/Lecture07.pdf

[3] Estimated using MESA evolutionary tracks (Dotter 2016; Choi et al. 2016) for a M-dwarf with $M = 0.3\,M_\odot$ at solar metalicity.

leading to the field of *gyrochronolgy*: predicting a stars age from its rotation rate (Mamajek & Hillenbrand 2008). Using gyrochronology for M-dwarfs is not so straightforward. Below the convective limit (the mass at which an M-dwarf becomes fully convective) there appears to be two distinct populations of faster and slower rotators ($P_{\rm rot} < 10$ d and $P_{\rm rot} > 70$ d; Irwin et al. 2011a; Newton et al. 2016) making it difficult to determine the age of M-dwarfs from rotation alone. This gap likely originates from a short and rapid loss of angular momentum (Irwin et al. 2011a). M-dwarfs ultimately reach a rotational period of > 100 d at a typical age of 5 Gyr (Newton et al. 2016). A further indicator of age comes from Hα emission with coincidental X-ray emission in M-dwarfs (Covey et al. 2007). These indicators mark the presence and strength of magnetic fields which are intertwined with age and rotation (West et al. 2006, West et al. 2008).

A scaling argument used by Shields, Ballard & Johnson (2016) states that a star's main-sequence lifetime scales as $M_\star/L_\star$, where $L_\star \sim M_\star^3$ for low-mass stars (Prialnik 2009). A 0.1-$M_\odot$ star is therefore expected to stay on the main sequence 100 times longer compared to the Sun. In reality however, this factor is more like 1000 due to additional sources of longevity unique to M-dwarfs. The first is slower rate of fusion as a consequence of a cooler core temperature. The second stems from the (almost) fully-convective nature of M-dwarfs. This replenishes hydrogen in the core which is being fused via the P-P chain whilst simultaneously preventing He ash building up. M-dwarfs therefore have access to almost all of their hydrogen to burn (Adams, Graves & Laughlin 2004) compared to Solar type stars which are restricted to hydrogen in the core (about 10% of the total amount of hydrogen; Shields, Ballard & Johnson 2016). The combined effect extends the MS lifetime of late M-dwarfs well in excess of the age of the universe (~ 200 Gyr; Baraffe et al. 1998).

The spectral type of an M-dwarf is generally estimated by comparing its spectrum to a set of benchmark spectra (e.g. Covey et al. 2007). The spectral type M is defined by strong moleculer absorption from titanium oxide (TiO) blueward of the optical (~450-570 nm; Morgan 1943). Molecular opacity from diatomic hydrogen (H_2), water (H_2O) and vanadium oxide (VO) obscure the continuum making the task of determining atmospheric parameters a subtle endeavour (see Fig. 1.1). The classification of M-dwarf boundaries is subject to the quirks of astronomical history. For example, strong TiO lines can be measured

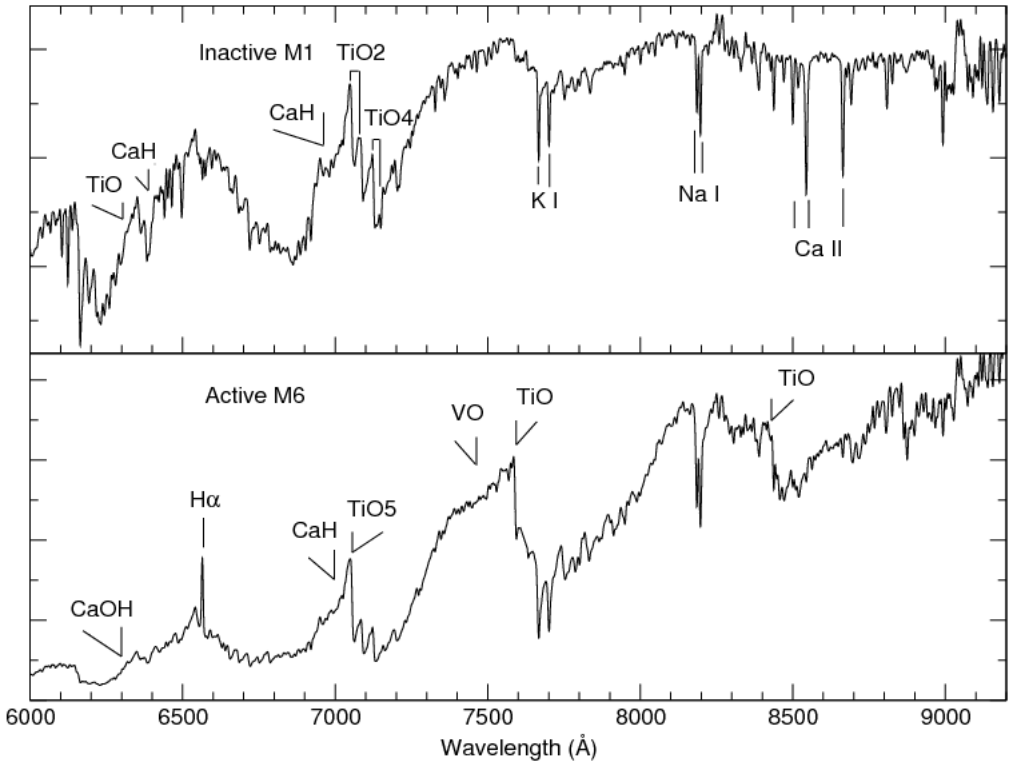

Figure 1.1: Illustrative example of spectra for an inactive M1 star and an active M6 star with strong molecular and atomic feautures labelled. Figure reproduced from Bochanski et al. (2007).

at redder wavelengths for stars hotter than M0 but required the development of red-sensitive detectors at the end of 20^{th} century (Kirkpatrick, Henry & McCarthy 1991, Bessell 1991).

The lower limit of the M spectral type is M7/M8 (the hydrogen burning limit; Baraffe et al. 1998). Determining spectral types for stars in this regime is challenging as small mass and metallicity variations result in physical changes which move objects from one category to another (Dieterich et al. 2014). Young brown dwarfs look almost identical to late M-dwarfs and requires diligent analysis of the atmosphere to discern the two. For example, molecules like ammonia or methane can only survive at colder temperatures ($\sim$ 1000 K; Cuby et al. 1999) pointing towards a brown-dwarf. Brown dwarfs are also distinguished by their inability to fuse hydrogen, but they can fuse less abundant isotopes like deuterium and lithium. A further complication arises from spectral types as late as L2 occasionally possessing the minimum mass required for hydrogen fusion to occur (Dieterich et al. 2014).

1.2 Absolute parameters of low-mass stars

1.2.1 Interferometry

M-dwarfs may be monitored simultaneously through two or more telescopes. The light from these instruments can be combined to produce an interference pattern of alternating light and dark bands. The most common measurement in optical and infrared interferometry is a measurement of the amplitude of the fringes. This fringe contrast is often called the "*visibility*" of the fringes. The normalised visibility amplitude (V) is computed from the maximum and minimum intensity (P) of the fringes, given by

$$V = \frac{P_{max} - P_{min}}{P_{max} + P_{min}}. \tag{1.3}$$

An unresolved point source will have a normalised visibility amplitude of 1. For a spatially resolved star, light from across the stellar surface combines incoherently causing the visibility amplitude to be less than 1. The bigger the star, the smaller the fringes and lower the fringe amplitude. By measuring this drop in the fringe amplitude it is possible to measure

the size (angular diameter), shape, and surface features of stars. Accurate parallax measurements also permit a measurement of the effective temperature. A binary star will produce two fringe packets, one for each star in the system. If the separation between the stars is small enough, the fringe packets from each star will overlap, producing a periodic signal in the visibility amplitudes. The separation between the peaks in the visibility curve provides a measurement of the binary separation while the minimum visibility reflects the flux ratio between the components.

There have been many successful attempts to measure the radius and temperature of single M-dwarfs (e.g. Leinert et al. 1997, Berger et al. 2006; Nelan et al. 2001; Ségransan et al. 2003b; Demory et al. 2009; Boyajian et al. 2012; von Braun et al. 2015). The fraction of M-dwarfs which have companions within 1000 AU is estimated to be ~40% (Fischer & Marcy 1992; Lada 2006; Raghavan et al. 2010). If the system is close and bright enough, interferometry can monitor the relative positions of each component $\Delta\alpha$, $\Delta\delta$) relative to the centre of mass. An example is given by Benedict et al. (2016) who used white-light interferometric observations from the Hubble Space Telescope with radial velocity data from the McDonald Observatory to obtain astrometric solutions of M-dwarfs in binary systems. They achieved mass uncertainties as low as 0.4% in some cases (median error of 1.8%). However the radius of each component was determined from photometric relations which have substantially larger uncertainties.

1.2.2 Eclipsing binaries

Eclipsing binaries can be used to measure absolute parameters of M-dwarfs. The drop in light as one companion occults another sets the scale of radii for each component. Binary companions of equal luminosity have spectral features that can be attributed to individual components. This may permit a measurement of temperature and radial velocity for each star from a single spectrum. Radial velocity measurements at numerous points in an orbit characterise the *spectroscopic orbit* which sets the mass scale of the system. Eclipsing binaries where both spectra are discernible are called double-lined eclipsing binaries (SB2s). These systems allow a measurement of the absolute parameters of each star. In John South-

worth's catalogue of well-studied detached eclipsing binaries (Southworth 2015) there are 11 systems[4] in which both systems have the M-spectral type (Windmiller, Orosz & Etzel 2010, Torres & Ribas 2002, Kraus et al. 2011, Hartman et al. 2018, Ribas 2003, Kraus et al. 2017, Irwin et al. 2011b, David et al. 2016, David et al. 2016). Systems where only one spectral component can be measured are called single-lined eclipsing binaries (SB1s) and require supplementary information to determine some absolute parameters (e.g. masses and radii). A more in-depth theory of eclipsing binaries is given in Sect. 2.

A different approach is to measure the absolute parameters of eclipsing binary systems where only one of the stars is an M-dwarf. One such example is M-dwarf + white-dwarf systems. The small size of the white-dwarf ($R \sim 1\,R_{\oplus}$) results in very sharp, total eclipses which can be used to measure radii to a precision of a few percent (Parsons et al. 2010). Consequently, it is possible to obtain a clean M-dwarf spectrum free from contamination of the white dwarf. The cooling of white dwarfs is well understood (e.g. Salaris et al. 1997, Salaris, Althaus & García-Berro 2013, Valyavin et al. 2014) making them ideal systems to determine the age of an M-dwarf. These systems have experienced a brief common envelope phase when the progenitor star to the white dwarf evolved off the main sequence. This has a negligible effect on the M-dwarf as the common envelope phase is short (0.001-0.01 Myr) compared to the thermal timescale of the M-dwarf (0.1-1 Gyr). Additionally, the common envelope has a much higher specific entropy than the surface of an M-dwarf so very little accretion will take place (Hjellming & Taam 1991).

1.3 Tension with stellar models

There is an emerging tension between measurements of mass, radius and temperature compared to what is predicted from evolutionary models. M-dwarfs across the spectral type are reported to have a radius ~5% higher than expected (Chabrier et al. 2000; Torres & Ribas 2002; Ribas 2003; López-Morales & Ribas 2005; Ribas et al. 2008; Torres et al.

[4] Accessed 25th Oct 2018.

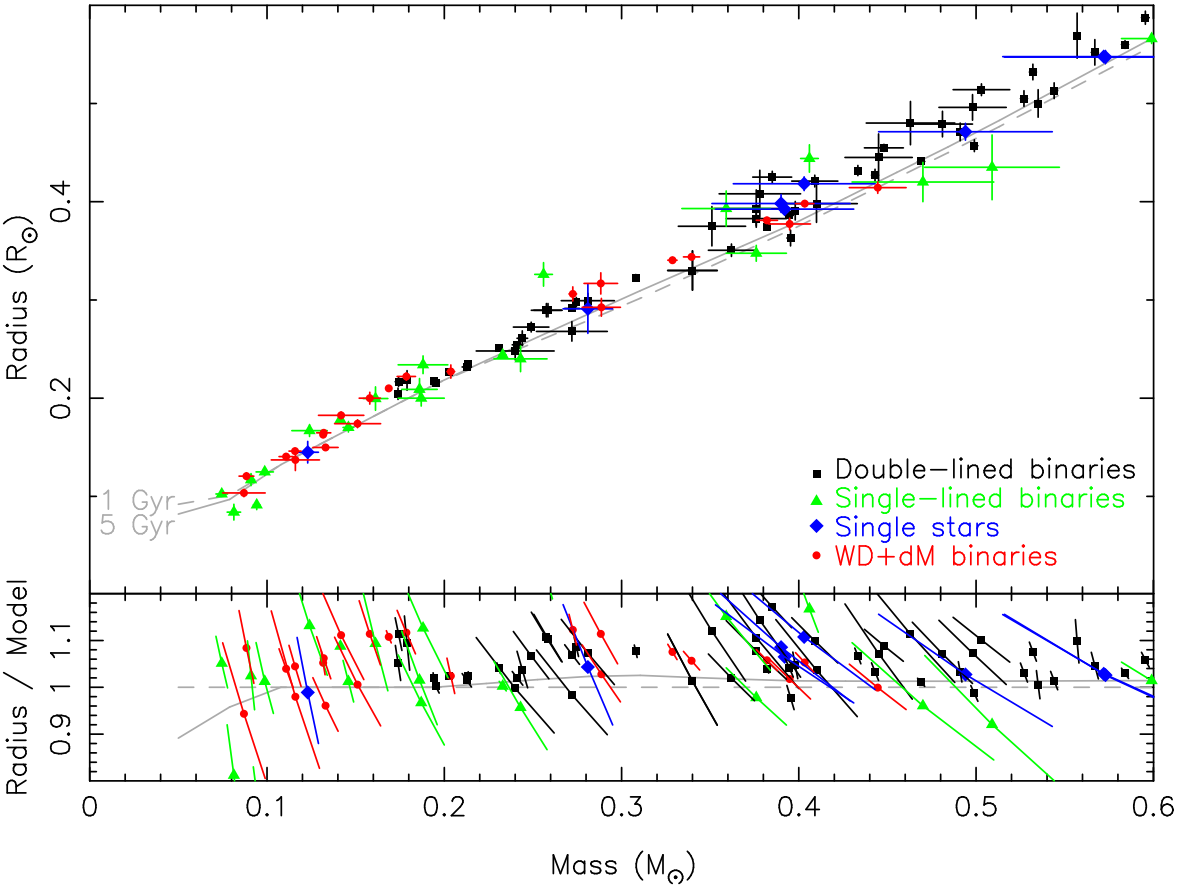

Figure 1.2: Mass-radius plot for low-mass stars (with mass and radius uncertainties of less than 10 per cent). The type of system that the measurement came from is indicated by the different colours and symbols and all are detailed in either Table 2 (red points) or the Appendix (all other points) of Parsons et al. (2018). Also shown are the theoretical mass-radius tracks from Baraffe et al. (2003); Baraffe et al. (2015). Figure reproduced from Parsons et al. (2018)

.

2014; Baraffe et al. 2015; Lubin et al. 2017). Some also have temperatures hotter than predicted (Ofir et al. 2012, Gómez Maqueo Chew et al. 2014). The most glaring discrepancies are measured for low-mass stars near the convective transition ($\sim 0.35 M_{\odot}$; López-Morales 2007). The disparity also seems to be equally evident in single M-dwarfs and those in eclipsing binaries (Fig. 1.2; Spada et al. 2013). A recent discovery of an over-luminous late-type M-dwarf around a solar-like star, CWW 89Ab ($\sim 0.035 M_{\odot}$; Beatty et al. 2018) suggests that this problem could extend into the brown-dwarf region. There are a few competitive theories circulated in the literature to explain the origins of this phenomena.

1.3.1 Magnetic activity

The presence of magnetic fields is often invoked to explain the systematic inflation of M-dwarfs. Enhanced magnetic fields generated by the dynamo affect the convectional stability criteria leading to larger radii for the same temperature (or vice versa; Spada et al. 2013). For low-mass stars, strong surface magnetic fields (0.01-1 kG; see Reiners 2012) are generated in the convective zone via dynamo mechanisms (Charbonneau 2013; Mullan & MacDonald 2001). In eclipsing binary systems, low-mass stars can be coerced into a regime of fast rotation which enhances dynamo mechanisms leading to increased magnetic activity. Stabilisation of convection in stellar models can reproduce the observed radius inflation of fully-convective M-dwarfs with reasonable surface magnetic fields, but require super-MG magnetic fields in the interior (Feiden & Chaboyer 2014). As noted by Feiden & Chaboyer (2014), the presence of such a strong internal magnetic fields is unlikely for a number of reasons: turbulent dynamos in convective regimes cannot generate magnetic fields in excess of 50 kG (Dobler, Stix & Brandenburg 2006, Browning 2008) and there is no mechanism describing how MG magnetic fields would accumulate in the interior of convective stars.

López-Morales & Ribas (2005) conjectured that spots may explain the enhanced radius measured for GU Bootis. Star spots are manifestations of suppressed surface convection brought upon by magnetic fields. They have the effect of creating regions of different temperatures on the stellar surface; they can shift stars bluer or redder depending on their density, location, temperature differences and the photometric colours used (Feiden & Chaboyer 2013).

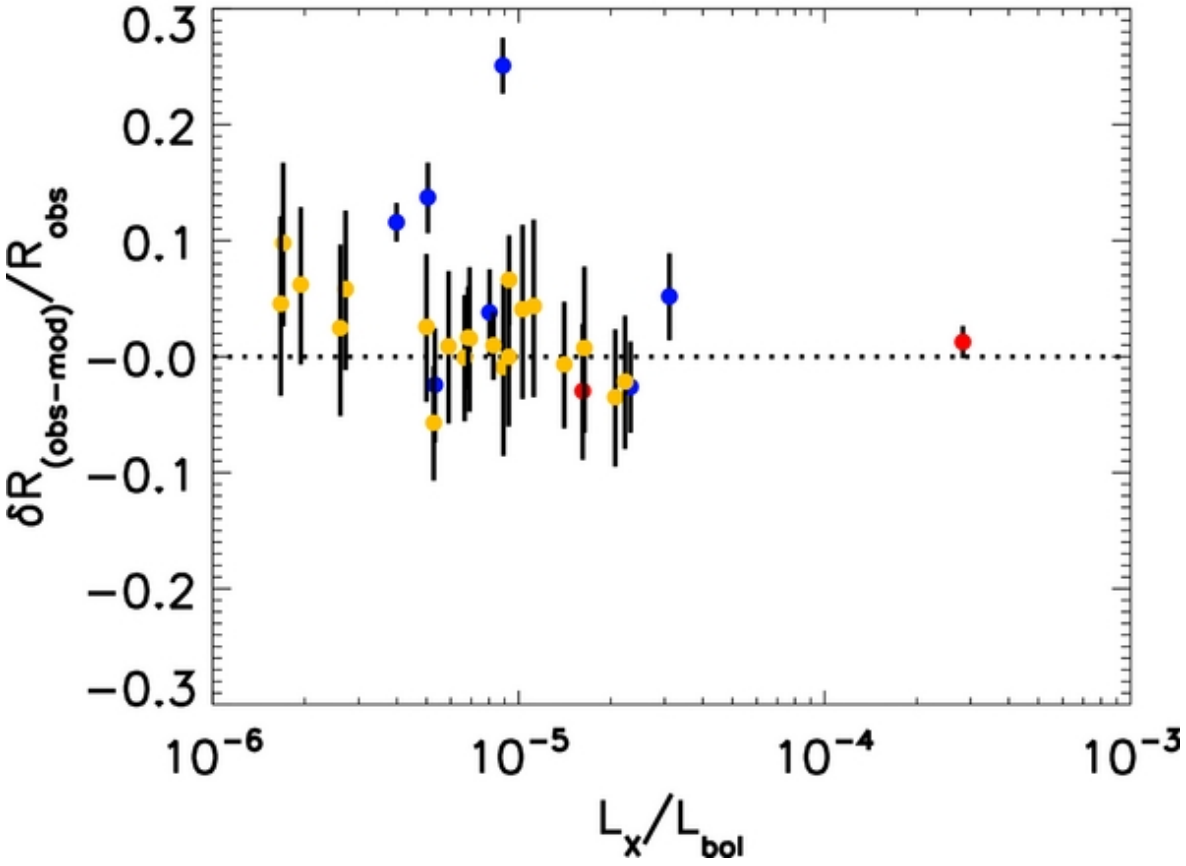

Figure 1.3: The fractional radius residual between interfferometric radii and expected radius interpolate by mass (from the photometric relations of Henry & McCarthy 1993) as a function of the activity indicator, $L_X/L_{\rm bol}$. The color of the symbols encodes the metallicity of the star: metal-poor ([Fe/H] < -0.25): blue; solar ($-0.25 \leq$ [Fe/H] $\leq +0.15$): yellow; metal-rich ([Fe/H] $> +0.15$): red. Figure reproduced from Spada et al. (2013).

Significant spot coverage has the effect of lowering the overall photospheric temperature. To maintain radiative equilibrium, a star must increase its radius to conserve total flux output. If this were to be the case, we would see a clear trend of inflation with magnetic indicators (e.g. Hα emission, X-ray emission), rotation and age. Work by Spada et al. (2013) found activity indicators were independent of inflation for single and binary M-dwarfs (see Fig. 1.3). Significant inflation has been observed for both short period (e.g., KOI-126, $P_{\rm orb}$ = 1.77 d; Carter et al. 2011) and long period systems (e.g., Kepler-16, $P_{\rm orb}$ = 41.1 d; Doyle et al. 2011; Winn et al. 2011) making it unclear whether tidally-induced magnetic fields can be blamed.

1.3.2 Metalicity

Berger et al. (2006) used the CHARA array to measure the radius of M-dwarfs using interferometry. In their figure 5 (Fig. 1.4) there exists a clear trend between a star's metalicity and fractional radius residual, with less inflation observed for metal-poor stars. The same conclusion is found by Leggett et al. (2000) and López-Morales (2007) who used spectral fits to determine a systematic inflation in stars with higher metalicity. However, more recent results from Demory et al. (2009) which excluded measurements from Berger et al. (2006) no longer show this trend (Fig. 1.5). It is likely that metallicity plays some role in inflation due to its direct affect on stellar structure. The accuracy and uncertainty of spectroscopic techniques is often questioned in *hare-and-hounds* [5] experiments which reveals significant discrepancies in stellar atmospheric parameters from identical spectra (Jofré et al. 2017).

1.4 Empirical relations of M-dwarfs

Measurements of absolute stellar parameters for low-mass stars can be used to derive empirical relations and bypass the disagreement with stellar models. Such relations join observable

[5] Controlled experiments whereby individual scientists or research groups are given identical data sets which they must measure. The difference in measurements provides an estimate of the method-dependent scatter typical across the literature.

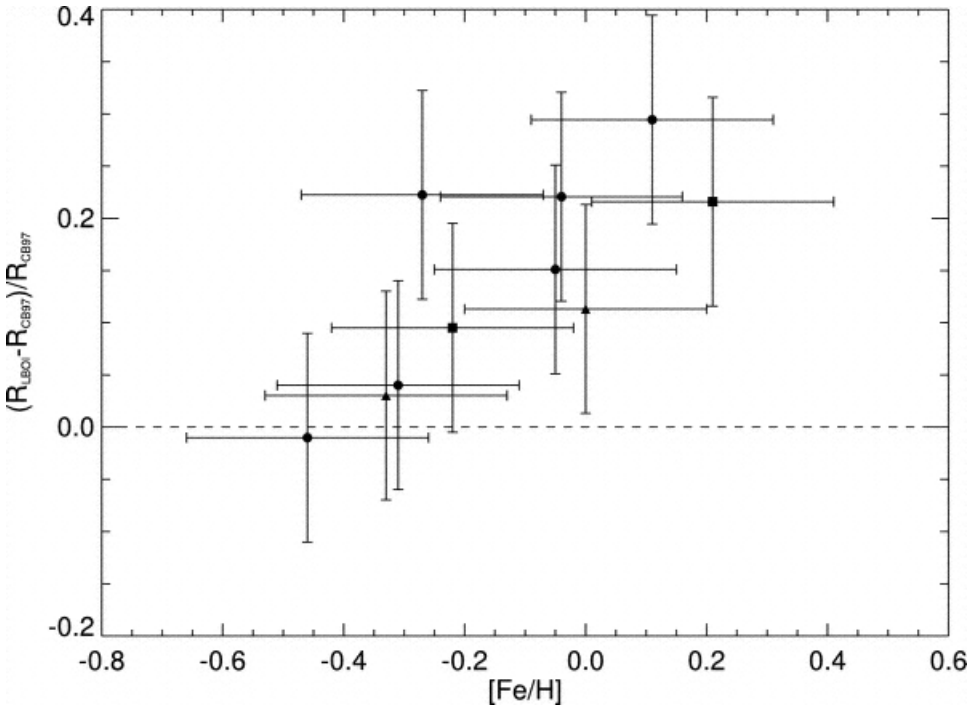

Figure 1.4: Fractional deviation between the radii measured through long baseline optical interferometry and from the model predictions for stellar radius from Chabrier & Baraffe (1997) plotted as a function of metallicity. The representative errors are ±0.2 dex in [Fe/H] and ±0.1 in fractional deviation of the radius (due to 10% errors in the mass estimates). Image reproduced from Berger et al. (2006).

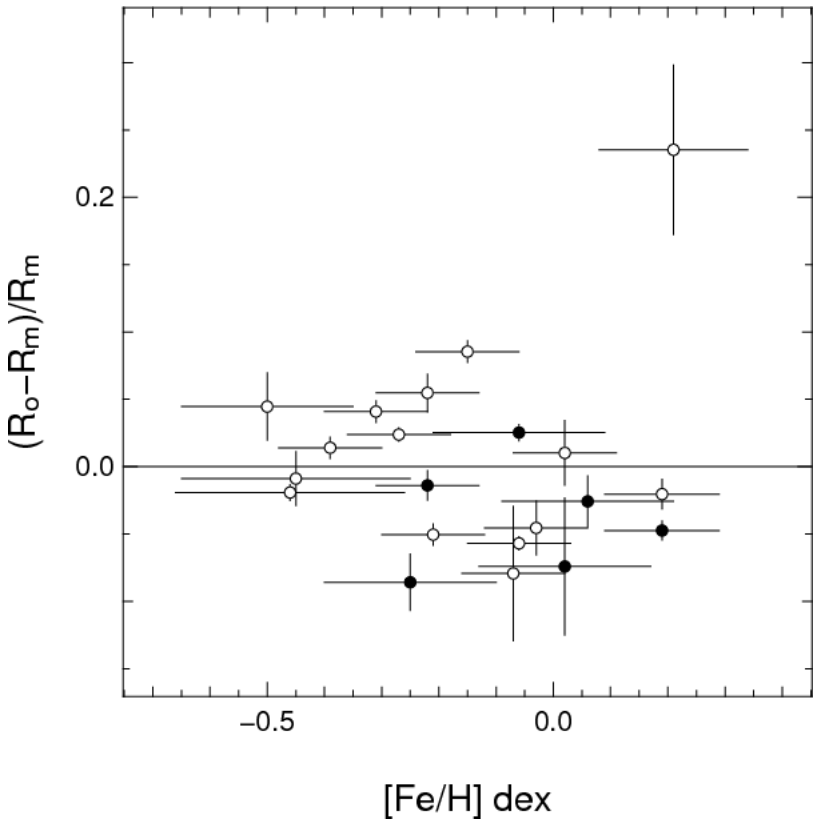

Figure 1.5: The fractional radius residual of interferometric measurements of radii compared to the 5 Gyr isochrones from (Baraffe et al. 1998). The filled circles are measuremnets from Demory et al. 2009 (filled circles) and open circles corrospond to measurements from Lane, Boden & Kulkarni (2001), Ségransan et al. (2003b), Boyajian et al. (2008), di Folco et al. (2007), Kervella et al. (2008), Berger et al. (2006). Image reproduced from Demory et al. (2009).

parameters with absolute parameters (e.g. luminosity-mass relations), or only absolute parameters (e.g. mass-radius relations). In principle, these are applicable to more distant and fainter stars (Mann et al. 2013). Assuming the sample presented by Parsons et al. (2010) in Fig. 1.2 is representative of M-dwarfs measurements across the field, there are few single stars (measured with interferometry) with mass below $\sim 0.4\,M_{\odot}$; empirical calibrations calibrated from this sub-sample will only be accurate for the early-type M-dwarfs. The situation is somewhat better for double-lined eclipsing binaries; these are abundant across the M-dwarf spectral type down to $\sim 0.2\,M_{\odot}$. The best choice is single-lined eclipsing binaries which are abundant across the entire spectral type. However, the precision in mass and radius appears inferior to double-lined eclipsing binaries and single stars. It is imperative to exercise caution when constructing empirical relations to ensure that they come from a sample of homogeneously measured systems and that the extent of such calibrations are explicitly stated.

1.4.1 Luminosity relations

The mass of an M-dwarf is a fundamental property from which most other stellar properties depend steeply on. Therefore a mass-luminosity relation is a useful astrophysical tool which can convert observable light into a stellar mass. This can then be used to derive initial mass function (IMF) from more readily obtained luminosity functions. The IMF has been subjected to numerous reviews (Bastian, Covey & Meyer 2010; Jeffries 2012; Kroupa et al. 2013; Offner et al. 2014; van Dokkum et al. 2017). One of the first attempts to measure the IMF determined a power-law function which decreases between 0.1-10 $M_{\odot}$. However, recent studies (Luhman 2000; Luhman et al. 2000; Offner et al. 2014; Chabrier 2003; Lada 2006) have found a break from the power law in the mass range 0.05-10 $M_{\odot}$. Numerous theories have been put forward to explain the deviation (e.g. Larson 1992; Bate & Bonnell 2005; Narayanan & Davé 2012; Goldsmith 2001; Omukai 2007; Vaytet et al. 2013; McKee & Krumholz 2010); each has its own degree of successes and shortcomings which are beyond the scope of this work. However, the field will be better understood with accurate empirical relationships between fundamental stellar properties.

The mass-luminosity relationship is well constrained for solar-type stars. This is in-part due to the large number of systems which have mass measurements better than 1% uncertainty (Andersen 1991). Absolute parameters typically match stellar models when both metallicity and evolution is accounted for (Bedding, Booth & Davis 1997). This work addresses empirical relations of M-dwarfs ($M \lesssim 0.6\,M_{\odot}$) where stellar models face two major hurdles:

- the onset of low temperature electron degeneracy in the stellar core (Chabrier et al. 2000);
- a complex cold and high gravity stellar atmosphere, dominated by molecular and dust opacity (Allard 1998).

There has been considerable progress in stellar models over the last few decades which has addressed shortcomings such as boundary conditions of stellar interior equations and atmospheric models (e.g. Choi et al. 2016; Chabrier, Gallardo & Baraffe 2007). However, the description of input physics still remains incomplete: some molecular opacities and line-lists remain unfinished and the validity of the mixing-length approximation for 1D models remains questionable. Therefore an independent check of absolute parameters with a mass-luminosity relationships is desirable.

Delfosse et al. (2000) used a sample of 32 M-dwarfs in eclipsing and astrometric binaries to derive empirical mass-luminosity relations. They adopted a 10% mass accuracy cutoff for the inclusion as a compromise between good statistics and quality of individual measurements. Absolute magnitudes for various colours (M) were then calibrated against mass using fourth-degree polynomials:

$$\begin{aligned} \log(M/M_{\odot}) &= 10^{-3}\times[0.3 + 1.87\times M_V + 7.6140\times {M_V}^2 \\ &- 1.6980\times {M_V}^3 + 0.060958\times {M_V}^4] \qquad \text{for } M_V \in [9, 17] \end{aligned} \tag{1.4}$$

$$\begin{aligned} \log(M/M_{\odot}) &= 10^{-3}\times[1.6 + 6.01\times M_J + 14.888\times {M_J}^2 \\ &- 5.3557\times {M_J}^3 + 2.8518.10^{-4}\times {M_J}^4] \qquad \text{for } M_J \in [5.5, 11] \end{aligned} \tag{1.5}$$

$$\begin{aligned}\log(M/M_\odot) &= 10^{-3}\times[1.4 + 4.76\times M_H + 10.641\times {M_H}^2 \\ &- 5.0320\times {M_H}^3 + 0.28396\times {M_H}^4] \qquad \text{for } M_H \in [5, 10] \end{aligned} \tag{1.6}$$

$$\begin{aligned}\log(M/M_\odot) &= 10^{-3}\times[1.8 + 6.12\times M_K + 13.205\times {M_K}^2 \\ &- 6.2315\times {M_K}^3 + 0.37529\times {M_K}^4] \qquad \text{for } M_K \in [4.5, 9.5] \end{aligned} \tag{1.7}$$

$$\begin{aligned}\log(M/M_\odot) &= 10^{-3}\times[7.4 + 17.61\times(V-K) \\ &+ 33.216\times(V-K)^2 + 34.222\times(V-K)^3 \\ &- 27.1986\times(V-K)^4 + 4.94647\times(V-K)^5 \\ &- 0.27454\times(V-K)^6] \qquad \text{for } V-K \in [4, 7] \end{aligned} \tag{1.8}$$

These relations are impressively accurate for the JHK magnitudes (1-2%) and relatively poorer for M_V (~5%) due to the increasing effect of metallicity on the M-dwarfs spectra blue of the infrared (Ségransan et al. 2003a). This sample has measurements of mass spanning the entire spectral type with most residing in the 0.1-0.4 $M_\odot$ range. In practise, the mass-luminosity relation of Delfosse et al. (2000) is typically used with conservatively larger errors (e.g. Mann et al. 2015).

Empirical radius-/temperature-luminosity calibrations have been derived from interferometric observations of single stars. Mann et al. (2015) used measurements of 183 nearby K7-M7 stars to derive a radius-luminosity relation using a third-order polynomial with a correction for metallicity (Fig. 1.6),

$$R_\star = \left(a + bX + cX^2\right)[\times(1 + f[Fe/H])], \tag{1.9}$$

where X is the relevant absolute magnitude and a, b, c and f are coefficients summarised in Table 1.1. The best fit has a remarkably tight scatter of 2.9% despite an average radius uncertainty of 3-4%. There is small, but statistically significant improvement including [Fe/H],

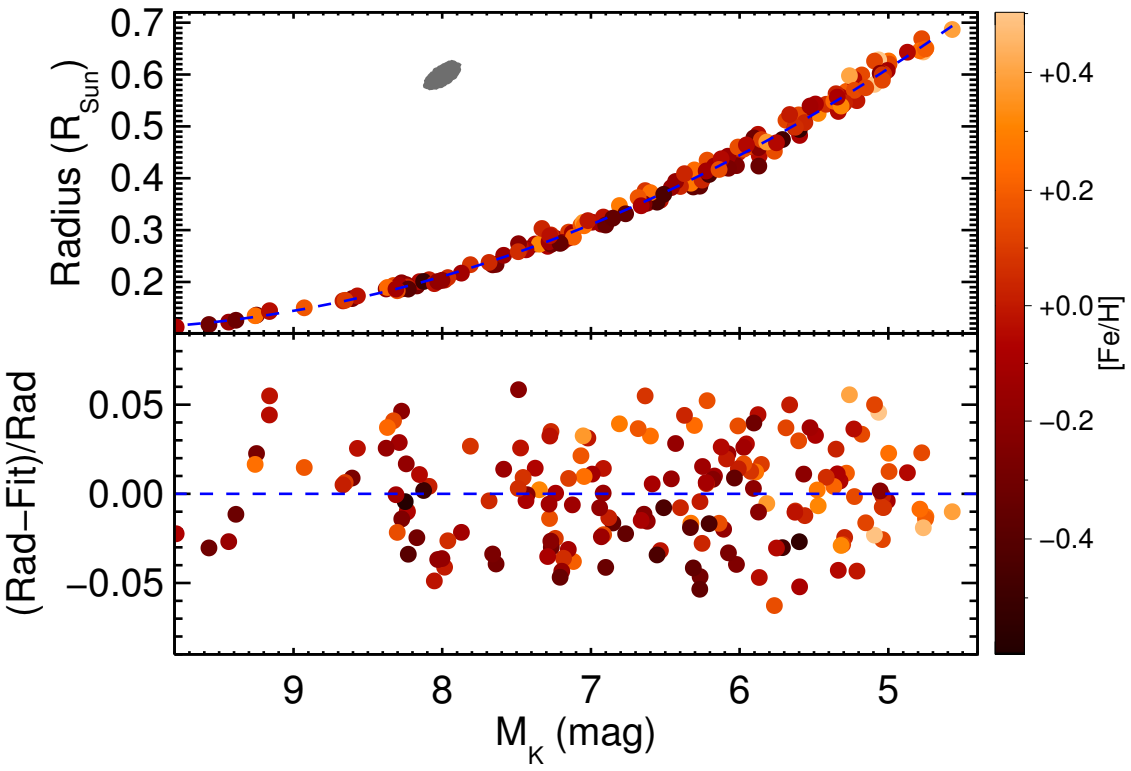

Figure 1.6: Top: Radii from interferometry (R_*) as a function of absolute K_S-band magnitude. The best-fit to the data is shown as a blue dashed line. M_K and radius both depend on the distance, so the errors are correlated. A typical error is shown a gray ellipse in the top left of the plot. Bottom: fractional radius residual to the fit. All points are colour-coded by metallicity. Image reproduced from Mann et al. (2015).

Table 1.1: Mass and radius relations of Mann et al. (2015).

Y	X	a	b	c	d	e	f	σ^a	χ_μ
R_*	M_{K_S}	1.9515	−0.3520	0.01680				2.89	0.93
R_*	M_{K_S},[Fe/H]	1.9305	−0.3466	0.01647			0.04458	2.70	0.88
R_*	$T_{\rm eff}$/3500	10.5440	−33.7546	35.1909	−11.5928	-	-	13.4	2.35
R_*	$T_{\rm eff}$/3500,[Fe/H]	16.7700	−54.3210	57.6627	−19.6994	-	0.4565	9.3	1.10
$T_{\rm eff}$/3500	$BP-RP$	3.245	−2.4309	1.043	−0.2127	0.01649		52	0.88
$T_{\rm eff}$/3500	$V-J$	2.840	−1.3453	0.3906	−0.0546	0.002913		55	0.93
$T_{\rm eff}$/3500	$V-Ic$	2.455	−1.5701	0.6891	−0.1500	0.01254		53	0.94
$T_{\rm eff}$/3500	$r-z$	1.547	−0.7053	0.3656	−0.1008	0.01046		58	1.06
$T_{\rm eff}$/3500	$r-J$	2.445	−1.2578	0.4340	−0.0720	0.004502		58	1.04
$T_{\rm eff}$/3500	$BP-RP$,[Fe/H]	2.835	−1.893	0.7860	−0.1594	0.01243	0.04417	45	0.60
$T_{\rm eff}$/3500	$V-J$,[Fe/H]	2.515	−1.054	0.2965	−0.04150	0.002245	0.05262	42	0.53
$T_{\rm eff}$/3500	$V-Ic$,[Fe/H]	1.901	−0.6564	0.1471	−0.01274		0.04697	48	0.67
$T_{\rm eff}$/3500	$r-z$,[Fe/H]	1.572	−0.7220	0.3560	−0.09221	0.009071	0.05220	50	0.71
$T_{\rm eff}$/3500	$r-J$,[Fe/H]	2.532	−1.319	0.4449	−0.07151	0.004333	0.05629	47	0.63

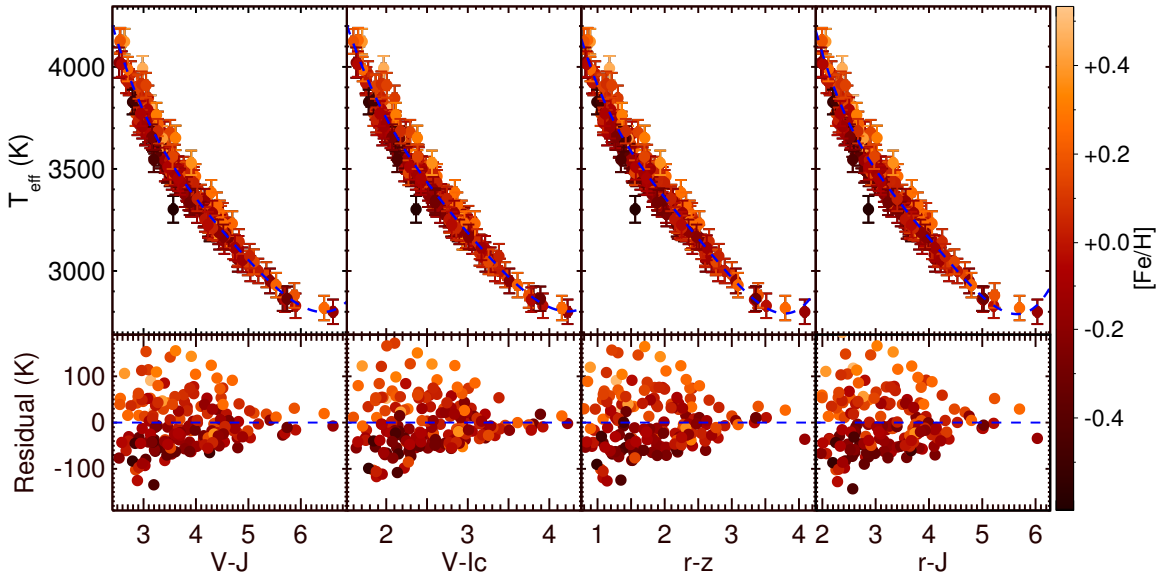

Figure 1.7: Spectroscopically derived $T_{\rm eff}$ as a function of different color combinations. The best-fit is overplotted as a blue dashed line. The bottom panels show the fit residuals. Fit coefficients are given in Table 1.1. Image reproduced from Mann et al. (2015).

with a resulting scatter of 2.7%. They tested calibrations for all SDSS and 2MASS magnitudes ($grizJHK_s$); K_s had the lowest scatter due to smaller variations of an M-dwarf's spectra at bluer wavelengths due to metallicity. Mann et al. (2015) also created a colour-temperature relationship using a fourth-order polynomial with a metallicity correction (Fig. 1.7),

$$T_{\rm eff}/3500 = a + bX + cX^2 + dX^3 + eX^4 \left[+f[Fe/H]\right], \tag{1.10}$$

where X is a metal-sensitive colour (Table 1.1). The authors caution the use of of this calibration outside the colour range of the sample where non-real slope changes are observed. The sample is well-populated between ~2800-4000 K and the calibration appears to have a scatter below 100 K which significantly decreases for redder objects.

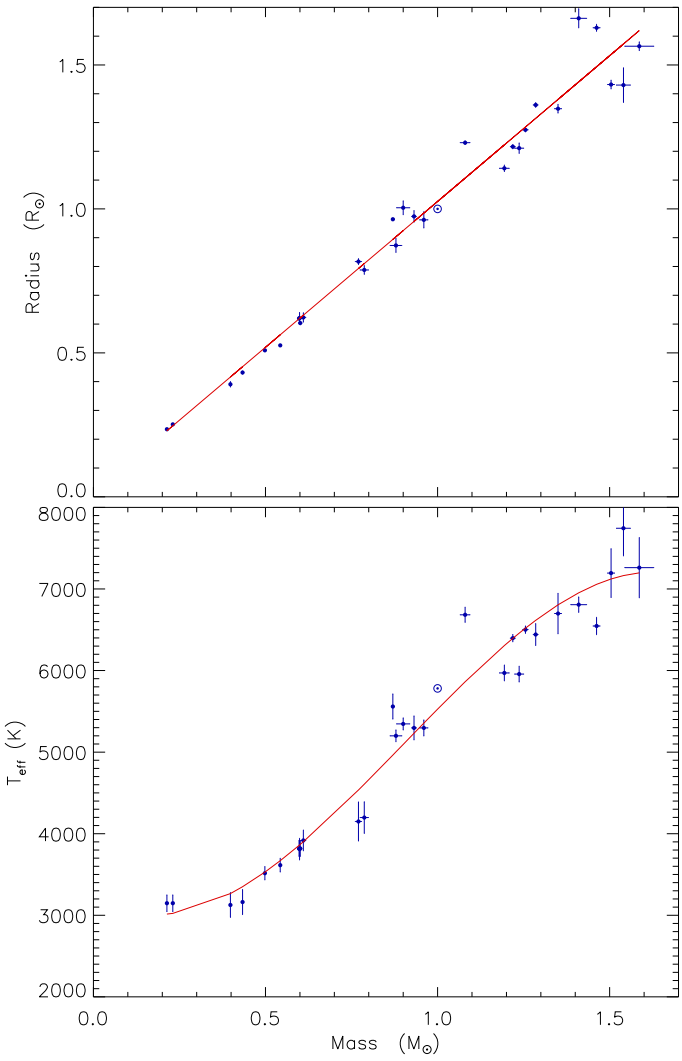

Figure 1.8: Mass–radius and mass–$T_{\rm eff}$ diagrams for exoplanet host stars. The filled circles show the properties of stars in eclipsing binary systems and the Sun is represented by a $\odot$. The solid lines represent the mass–radius and mass–$T_{\rm eff}$ relations. Image reproduced from Southworth (2009).

1.4.2 Mass-radius-temperature relations

Testing evolutionary models requires a diligent comparison of mass, radius and temperature measurements. Because there is a commonly observed discrepancy between observed and predicted fundamental parameters (Sect. 1.3), it is common-place to derive empirical relations instead. A rudimentary approach by Southworth (2009) achieved this using a sample of 29 stars in eclipsing binaries (plus the Sun) which covers the masses 0.124-1.586 $M_{\odot}$ (Fig. 1.8). They fitted a first-order polynomial to the mass-radius relation which did not account for [Fe/H] and age,

$$R_{\star} = (0.00676 \pm 0.03408) + (1.01824 \pm 0.03368) M_{\star}, \tag{1.11}$$

where $R_{\star}$ and $M_{\star}$ are in solar units. The authors quote an rms scatter of $0.073\,R_{\star}$ about the fit; the scatter is significantly smaller for low-mass stars ($\leq 0.6\,M_{\odot}$) but there are less than 10 stars with measurements with mass below $0.6\,M_{\odot}$. Southworth (2009) also present a mass-temperature relationship,

$$\begin{aligned} T_{\rm eff} &= (3217 \pm 564) - (2427 \pm 2304) \cdot M_{\star} \\ &\quad +(7509 \pm 2802) \cdot M_{\star}^2 - (2771 \pm 1030) \cdot M_{\star}^3, \end{aligned} \tag{1.12}$$

which has an rms scatter of 328 K about the best fit.

Interferometry can provide both radius and temperature to a high precision. In addition to the luminosity relations stated above, Mann et al. (2015) created an empirical radius-temperature calibration (Fig. 1.9),

$$R_{\star} = \left(a + bX + cX^2\right) \times (1 + f[Fe/H]) \tag{1.13}$$

where $X = T_{\rm eff}/3500\,{\rm K}$ (Table 1.1). This calibration has a significant scatter in radius of 13% which is reduced to 9% when metallicity is accounted for. Interformetric measurements of single M-dwarfs are excluded from empirical mass-radius relations as the mass of a single star is typically determined from its colours. Mann et al. (2015), who determined stellar mass through colour relations from Delfosse et al. (2000), attempted to create a *semi-empirical* mass-radius relation with a second order polynomial. Their fit is compared to

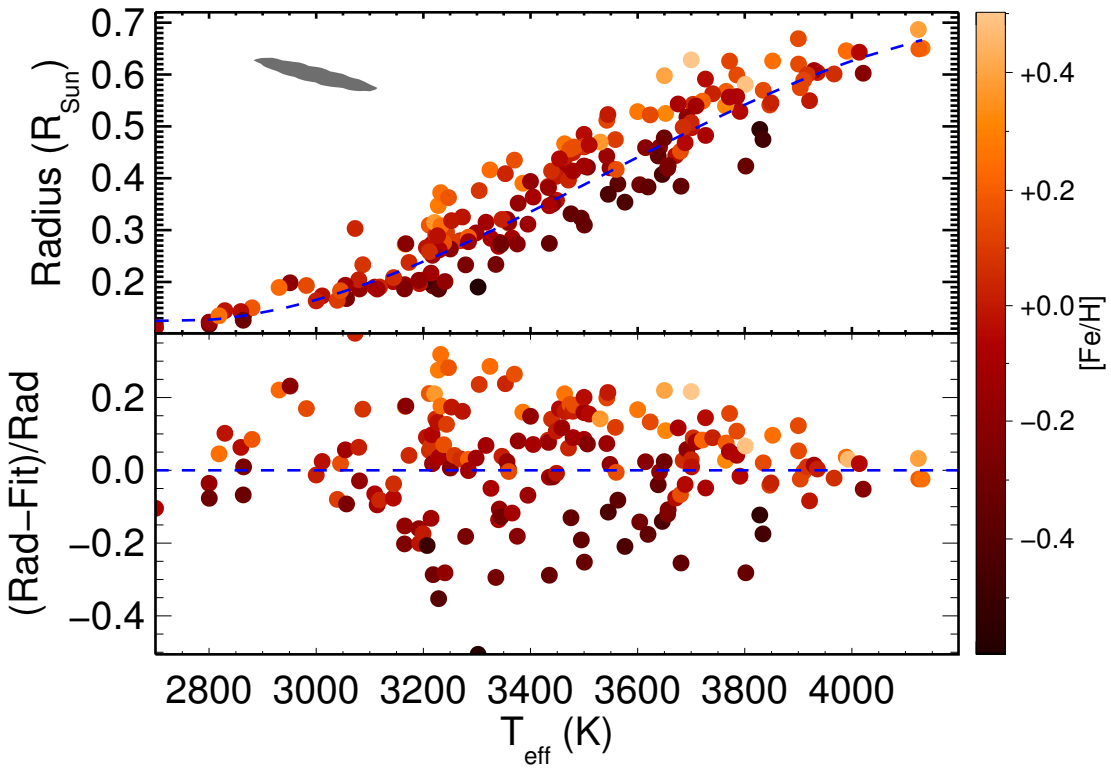

Figure 1.9: Top: R_* as a function of stellar $T_{\rm eff}$. The derived R_* depends on $T_{\rm eff}$ so the errors are strongly correlated. A typical error is shown a gray ellipse in the top left of the plot. The best-fit ignoring [Fe/H] is shown as a dashed blue line. Bottom: residual from the best-fit. Points are coloured according to their metallicity. Image reproduced from Mann et al. (2015).

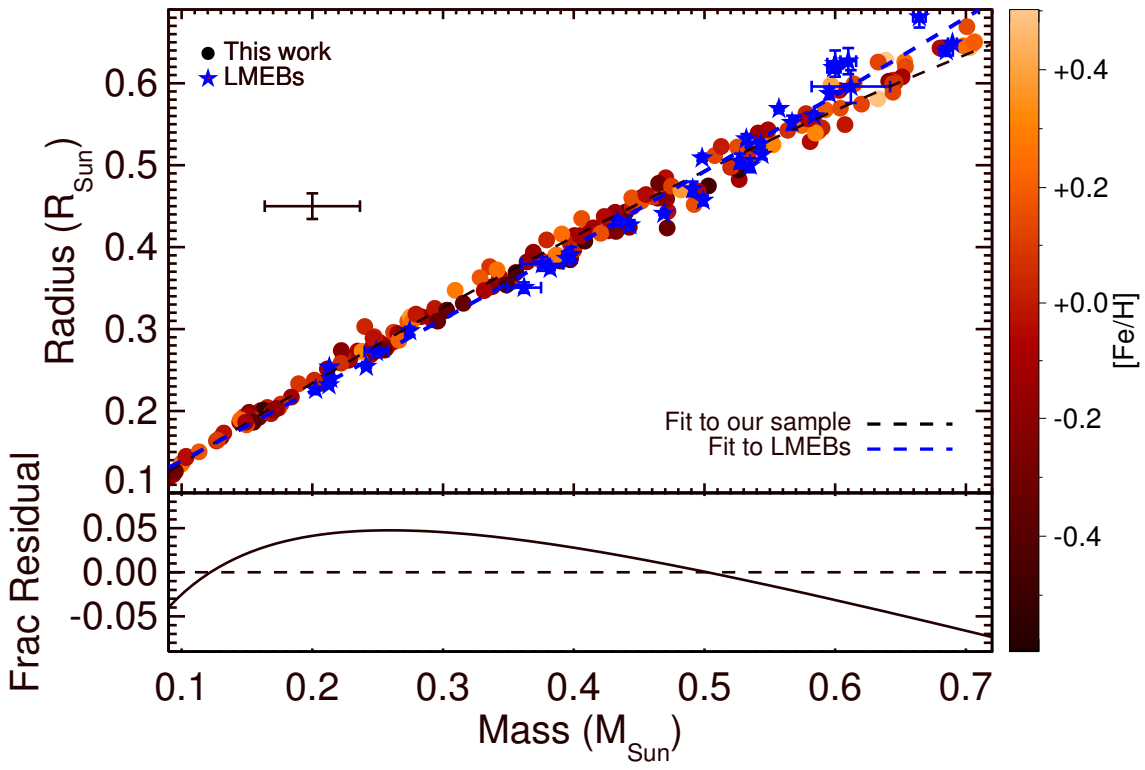

Figure 1.10: Mass–radius diagram for single stars measured with interferometry (red circles) from Mann et al. (2015) and those from low-mass eclipsing binaries compiled from the literature (LMEBs, blue stars). A typical error bar for the interferometry sample is shown to the left and are color-coded by their metallicity. The fit to both samples is shown as a dashed line. The bottom panel shows the fractional residual between these two fits. Image reproduced from Mann et al. (2015).

a sample of detached eclipsing binaries with mass and radius errors below 5% and find a notable discrepency above 0.65 $M_{\odot}$. The authors state that model-inferred masses better reproduce the mass-luminosity relation measured for low-mass eclipsing binaries and thus the disagreement in Fig. 1.10 is most likely due to errors in the luminosity relation of Delfosse et al. (2000), which was based on only 3 objects with masses in this range.

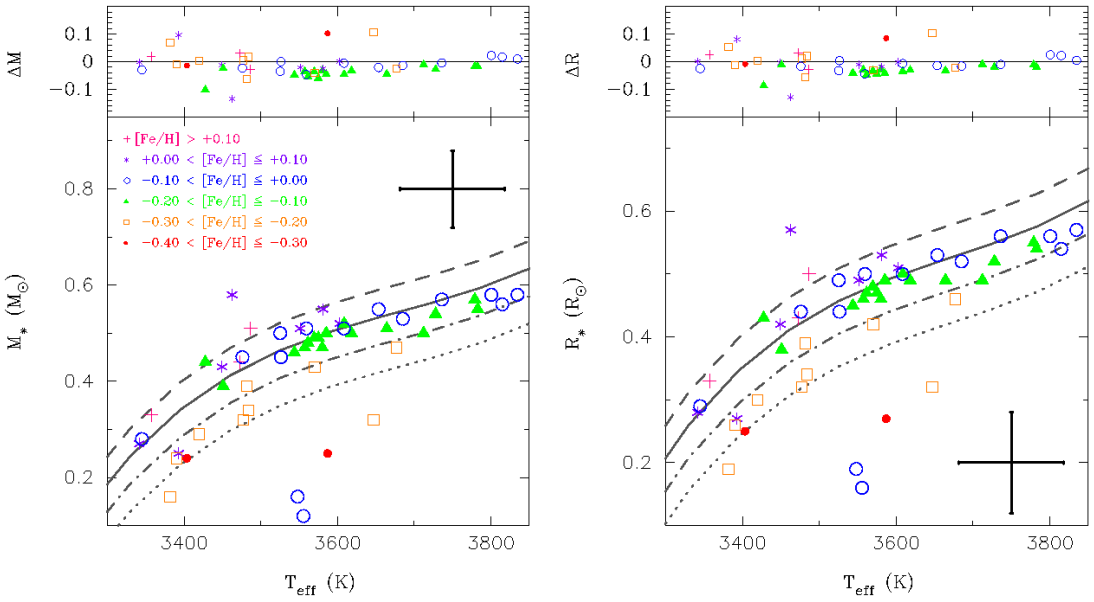

Figure 1.11: Stellar mass (left panel), and radius (right panel), as a function of the effective temperature. Stars are plotted using different colours and symbols according to their metallicity. Several fits for fixed metallicity values are plotted: +0.15 (dashed line), +0.00 (solid line), -0.15 (dash-dotted line), and -0.30 (dotted line). The upper left panel shows the differences between the mass and those derived by using Henry & McCarthy (1993) relationship. Image taken from Maldonado et al. (2015).

Similar relations were derived by Maldonado et al. (2015) using interferometric observations of M-dwarfs. They fitted radii with masses calculated from the mass-luminosity relations of Henry & McCarthy (1993) using a second-order polynomial,

$$R = 0.0753 + 0.7009M + 0.2356M^2. \tag{1.14}$$

There are significantly more calibrators in the Maldonado et al. (2015) sample than the Southworth (2009) sample and it provides a much better fit; the rms about the best fit is

$0.02\,M_{\odot}$ and $0.02\,R_{\odot}$. However, their sample consists of a combination of single stars and those in eclipsing binary systems and there is no attempt to account for age or metallicity. They do form mass-temperature and radius-temperature relations using third-order polynomials which account for metallicity,

$$\begin{aligned} M_{\star} &= -171.616 + 0.139T_{\rm eff} - 3.776 \times 10^{-5}T_{\rm eff}^{2} \\ &+ 3.419 \times 10^{-9}T_{\rm eff}^{3} + 0.382[{\rm Fe/H}]; \end{aligned} \tag{1.15}$$

$$\begin{aligned} R_{\star} &= -159.857 + 0.130T_{\rm eff} - 3.534 \times 10^{-5}T_{\rm eff}^{2} \\ &+ 3.208 \times 10^{-9}T_{\rm eff}^{3} + 0.347[{\rm Fe/H}]. \end{aligned} \tag{1.16}$$

These calibrations (Fig. 1.11) are moderately good: the scatter in mass and radius is $0.02\,M_{\odot}$ (13.1%) and $0.02\,R_{\odot}$ (11.8 %) respectively and are valid for $3340\,{\rm K} < {\rm T_{eff}} < 3840\,{\rm K}$ and $-0.4\,{\rm dex} < {\rm [Fe/H]} < +0.16\,{\rm dex}$. The authors caution that relative errors in mass tend to increase for low-mass stars, and can be up to 40% for stars with mass below $0.25\,M_{\odot}$. The same is true for uncertainty in radius and can be larger than 20% for stars with radius below $0.35\,R_{\odot}$. A possible explanation for the increase in mass error for later-type M-dwarfs is that the relative mass errors from the Henry & McCarthy (1993) relationship tend to be larger at lower masses.

1.5 Eclipsing binary, low mass

Measuring the absolute parameters of M-dwarfs typically involves stars which are measured by interfereometry or those in binary configurations such that the companions occult the light from one another. For low-mass stars ($< 0.6\,M_{\odot}$) there is a dearth of systems with absolute parameters known to the desired precision of a few percent. A recent compilation of M-dwarfs with masses and radii errors below 10% yield only 90 M-dwarfs (Chaturvedi et al. 2018). The reason is due to the intrinsic brightness of M-dwarfs and low-probability of finding eclipsing binary systems from which mass and radius can be empirically derived. While the sample presented by Chaturvedi et al. (2018) is sizeable, it is not large enough

to reliably determine empirical relations and they are not measured using consistent and homogenous techniques.

A solution to this problem is in the remit of exoplanet surveys. The Wide Angle Search for Planets (WASP; Pollacco et al. 2006a) is a survey for 0.8–2 R_{Jup} objects transiting solar-like stars. Objects in this radius range can have masses which span three orders of magnitude, from Saturn-like planets to M-dwarfs. Consequently, WASP photometry has been used to identify hundreds of FGK stars with transiting M dwarf companions as a by-product of its successful exoplanet search. These systems are termed EBLMs (eclipsing binary, low-mass). The EBLM consortium has invested considerable effort to characterise these systems, including hundreds of hours of telescope time to measure their spectroscopic orbits. The determination of absolute parameters of EBLM systems has been coordinated within the EBLM project. This first three instalments of the project measured the absolute parameters of 4 EBLMs: EBLM I (Triaud et al. 2013b), EBLM II (Gómez Maqueo Chew et al. 2014) and EBLM III (von Boetticher et al. 2017). Secondary eclipses of J0113+31 (EBLM II) resulted in an effective M-dwarf temperature that is ~ 600 K hotter than predicted with evolutionary models. The fourth instalment, EBLM IV (Triaud et al. 2017), was the product of hundreds of hours of observations of EBLMs leading to the spectroscopic orbits of 118 EBLM systems.

Almost a thousand candidate EBLM systems have been flagged as a result of the WASP project.[6] The M-dwarfs in EBLM systems are most likely to be found around F stars as opposed to G-K/stars. The reason for this has its origins in tidal evolution theory. If the rotation of the primary star is less than that of the companion star's orbital period, then the torque induced by tidal interaction will increase the rotation of the host star. This is at the expense of the semi-major axis which must decrease in order to conserve angular momentum. This causes a spiral-like orbit which may eventually lead to engulfment of the low-mass companion. This is most probable for G/K host stars whereas the rotation of F-type hosts is sufficient to avoid colliding (Poppenhaeger 2017; Bouchy et al. 2011b; Bouchy et al. 2011a).

The sample presented by Triaud et al. (2017) is ideal to measure the absolute parame-

[6] As of 10^{th} Oct 2018.

ters of M-dwarfs in EBLM systems. As they were discovered by the WASP project, they are in transiting configurations which provides information about the radii of each component. However, the light from the M-dwarf companion is significantly small such that it is only possible to measure the radial velocity and hence mass for the brighter star. Subsequently, it is not possible to measure the absolute parameters without supplementary information from stellar models. The crux of the EBLM method (and perhaps its Achilles' heel) is how the mass and radius degeneracy is broken (see Sect. 5.7 for a discussion of different methods). The EBLM method hinges on the assumption that the uncertainties in evolutionary models for the primary star are much smaller than the absolute parameters which can be derived given the quality of the data. In reality, this may not be the case (see Sect. 7.3).

1.6 Motivation

Over 200 planets have been found around M-dwarfs (Anglada-Escudé et al. 2013; Quintana et al. 2014; Rowe et al. 2014; Torres et al. 2015; Crossfield et al. 2015; Barclay et al. 2015; Schlieder et al. 2016; Anglada-Escudé et al. 2016; Gillon et al. 2017). These discoveries come from radial velocity surveys, transit surveys (both ground- and space-based) along with microlensing events. Of note are the exciting discoveries of exoplanets around Trappist-1 (Gillon et al. 2017) and Proxima Centauri (Anglada-Escudé et al. 2016) which increased the popularity of M-dwarfs for the public and scientists alike.

M-dwarfs are promising targets for exoplanet surveys. At a given distance, a, from a star of radius $R_\star$, an exoplanet (of radius R_p) is less likely to transit an M-dwarf than a K-/F-dwarf as the transit probability scales as $R_\star/a$. Conversely, exoplanets in habitable zones are more likely to transit an M-dwarf than a larger star due to a decreasing faster than $R_\star$ as we consider less massive stars. The transit depth of an eclipse scales as $(R_p/R_\star)^2$ so a similar planet will produce a deeper eclipse for a lower-mass star. An M-dwarf's low luminosity results in a habitable zone which is much closer to the star than for solar-type stars. If finding exoplanets in the M-dwarf habitable zone is the goal, then there is an increased geometric probability of observing a transit as well as number of transits observed

in a given time period (Nutzman & Charbonneau 2008). Such systems are also suitable to study the atmospheres of exoplanets. de Wit & Seager (2013) showed that for a given planet of fixed mass, radius and equilibrium temperature, the signal-to-noise ratio of an exoplanet atmospheric spectral signature scales as $\sqrt{B_\lambda(T_\star)}/R_\star$, where B_λ is the Planck function and $R_\star$ and $T_\star$ are the radius and temperature of the M-dwarf. This ratio significantly increases for stars later than M2 meaning that fewer transit observations need to be co-added to significantly detect atmospheric features of an exoplanet than those found around solar-type stars.

A promising project is the Search for habitable Planets EClipsing ULtra-cOOl Stars whos acronym was inspired by the sweet treat (SPECULOOS; Delrez et al. 2018a). Comprising of four 1-m telescope, it's mission is to detect terrestrial exoplanets around stars of spectral type M7 and later. SPECULOOS is designed to detect terrestrial exoplanets in the habitable zone of the nearest 500 red-/brown-dwarfs. This project should detect a few dozens of planets [7] which will be seminal to our understanding of other worlds. A similar project is the MEarth project (Irwin et al. 2010) which uses 16 0.4-m telescopes across two sites: 8 at Mount Hopkins, Arizona and 8 at the Cerro Tololo Inter-American Observatory, Chile. The atmospheres of exoplanets discovered from these surveys can be studied by the next generation of telescopes such as the 6.5-m James Webb Space Telescope (JWST; Gardner et al. 2006) or the 24.5-m Giant Magellan Telescope (Bernstein et al. 2014). However, a big question-mark remains for the reliability of stellar models for M-dwarfs, which ultimately govern the precision of exoplanet properties. There is a need for reliable empirical calibrations of M-dwarfs to compliment and verify stellar models.

Empirical and semi-empirical relations presented in Sect. 1.4 do a moderately good job of linking fundamental parameters of M-dwarfs. There is a significant scatter in these relations which may be a combination of the intrinsic properties of M-dwarfs and methods used to measure them. It is clear that a larger sample of M-dwarfs with precise absolute parameters is required to derive reliable empirical relations. To this end, I will measure the absolute parameters of 9 M-dwarfs in EBLM systems. Before I could achieve this, I had to

[7] www.speculoos.uliege.be/cms/c$_3$272723/*en*/*speculoos* − *exoplanets*

find a fast and robust way to measure the stellar atmospheric parameters of the brighter star from a spectrum. I decided to use wavelet decomposition to achieve this task and inspired the first research question of this work:

How well can we measure the atmospheric parameters of FGK stars using wavelet decomposition?

Exoplanet candidates discovered by the WASP survey (Pollacco et al. 2006a) were typically observed with the CORALIE échelle spectrograph (Queloz et al. 2001b). CORALIE is optimised for radial velocity measurements while raw spectra have significant systematic trends from échelle merging and poor blaze-function corrections. Atmospheric parameters are usually measured by experienced spectroscopists using measurements of equivalent widths (e.g. Santos et al. 2013; Cantat-Gaudin et al. 2014; Sousa et al. 2015), synthetic models (e.g. Masseron, Merle & Hawkins 2016; Plez 2012; Piskunov & Valenti 2017) or a combination of both (e.g. Stempels et al. 2007; Doyle 2015). This is time consuming and a fast, reliable method to measure atmospheric parameters from CORALIE spectra was required.

This problem can be solved with wavelet decomposition. A wavelet is a special function in space which can identify noise and systematic trends when convolved with a stellar spectrum (see Sect. 4.1). This was used to create a Bayesian method to measure $T_{\rm eff}$, [Fe/H], $V \sin i$ and $\log g$ for the primary star. These parameters inform limb-darkening coefficients for transit photometry and the stellar models used to determine the masses, radii and age of EBLM systems. This leads to the second research question:

To what extent can EBLM systems contribute to empirical mass-radius relationships at the bottom of the main sequence?

It is growing increasingly evident that there are systemic uncertainties in the accuracy of different analysis techniques. Measurements of individual systems by different groups have lead to absolute parameters that differ by more than 10% in some cases (e.g., Çakırlı, İbanoğlu & Sipahi 2013 vs Iglesias-Marzoa et al. 2017 vs Han et al. 2017; or Kraus et al. 2017 vs Gillen et al. 2017). Due to the dearth of M-dwarfs with reliable measurements, em-

pirical relations are typically composed of results from different analysis methods making it difficult to interpret the observed scatter as astrophysical or methodological. The exoplanet community has faced a similar issue which lead to a community-wide data challenge. For example, the eclipse depths of exoplanet XO-3b observed with post-cryogenic Spitzer was measured by 7 different groups to assess the accuracy of each technique. This helped clarify the difference between instrumental and other sources of error (Ingalls et al. 2016). In the absence of a data-challenge for EBLMs, I must assess the validity of my methods to determine possible sources of non-astrophysical scatter in future empirical relations derived from EBLMs.

2 Theory

The theory relating to this work can be split into two halfs: stellar spectroscopy and binary stars. The former relates to the atmospheric parameters which can be measured using specific absorption lines from a star's spectrum. The theory surrounding binary stars relates to Kepler's equations and how they can be solved to calculate models for transit photometry and radial velocities.

2.1 Stellar spectroscopy

The atmospheres of FGK stars are significantly hotter than M-dwarfs and so have a much lower abundance of molecules in the photosphere. Consequently, atmospheric models for FGK stars are well understood and allow for accurate measurements of mass and radius from photometry and spectroscopy alone. In the following sections I will give a basic description of the atmospheric parameters required for the EBLM analysis ($T_{\rm eff}$, $\log g$, [Fe/H] and $V \sin i$) and how they are typically measured from a spectrum.

2.1.1 Effective temperature

The effective temperature, $T_{\rm eff}$, is the apparent temperature of a star (Doyle 2015). The effective temperature is related to the stellar radius, $R_\star$, and luminosity, $L_\star$, via the Stefan-Boltzmann relationship:

$$T_{\rm eff} = \sqrt[4]{\frac{L_\star}{4\pi R_\star^2 \sigma_{\rm sb}}}, \tag{2.1}$$

where $\sigma_{\rm sb}$ is the Stefan-Boltzmann constant. Spectral lines can be fitted to give good indications of $T_{\rm eff}$. A good choice would typically include the Balmer lines, which have almost no gravity dependence for stars below 8000 K (Gray 2008). The Hα absorption line is formed just above the convection zone while Hβ forms just within it and parameters obtained from the latter are affected by convection; this causes temperature to be underestimated by around

150 K (Doyle et al. 2014). The Balmer lines can also be modelled in non-local thermodynamic equilibrium to account for formation in the hot and diffuse regions of the stellar photosphere. This has the effect of strengthening the core and weakening the core-wing transition changing the derived temperature by 100 K for Hα (Doyle 2015).

2.1.2 Broadening processes

The shape of a spectral line is influenced by processes in the stellar atmosphere. Doppler broadening is caused by random thermally-induced velocities in the photosphere; this Doppler shift creates an uncertainty of the emitted frequency which is Gaussian in nature (Gray 2008). A greater effect is atomic collisional broadening where an atom's electron energy levels are altered by a collision with a nearby atom. This changes the energy of a photon which can be absorbed by the perturbed atom leading to a broadening effect that is typically greater than its thermal counterpart. On top of all this is the rotational broadening caused by a stars rotation about an axis. Simultaneously observing the whole stellar disk averages the effect of rotation and broadens line profiles.

The presence of velocity fields within the stellar atmosphere has a substantial effect on the shape of spectral lines (Doyle 2015). Solar observations (e.g. Nordlund, Stein & Asplund 2009) and 3D models (e.g. Caffau et al. 2011) show that turbulence occurs over a broad range of length scales. For 1D models this is parameterised in terms of broadening due to motion on length scales shorter and longer than the mean photon path length.

Microturbulence, ζ_t

Basic atomic modelling fails to reproduce the expected equivalent widths of saturated lines. To circumvent this issue requires an adhoc broadening parameter: the microturbulence ζ_t. The size of a microturbulance cell is defined to be less than the mean free path of a photon. Microturbulance broadening is Gaussian in form, has magnitude around 2 km s^{-1} and is added in quadrature with thermal broadening. Introducing ζ_t can resolve the disagreement of determined abundances using strong and weak lines. To this end, one can determine ζ_t by plotting equivalent width versus abundance and vary the microturbulence until there is

negligible correlation (Doyle 2015; Magain 1984).

Macroturbulence, $\nu_{\rm mac}$

The size of a macroturbulence cell is defined to be more than the optical depth and does not alter the equivalent width of spectral lines. Macroturbulence resembles granulation and acoustic oscillations in the stellar atmosphere (Bruntt et al. 2010; Gray 1984).

2.1.3 Surface gravity

Surface gravity is a measure of acceleration due to gravity and usually takes a logarithmic form of Newtons law of gravitation:

$$\log g = \log\left(\frac{M_\star}{M_\odot}\right) - 2\left(\frac{R_\star}{R_\odot}\right) + \log g_\odot. \tag{2.2}$$

By convention this value is quoted in centimeter-gram-seconds units (c.g.s). The constant $\log g_\odot$ (≈ 4.438) can be obtained from the IAU system of astronomical constants (Prša et al. 2016). A larger surface gravity results in a higher frequency of atomic collisions which broaden the wings of strong spectral lines. This effect is absent in evolved giants with very large radii, resulting in much narrower lines in the spectra of these stars cf. dwarf stars (Smalley 2005).

By modelling the wings of pressure sensitive lines we can determine log g. A suitable line choice should be stable over a wide temperature range and not blended with other lines. The Na I D lines at 588.9 nm and 589.3 nm persist over a large temperature range along with Mg I b lines at 516.7 nm, 517.3 nm and 518.4 nm although the magnesium lines can suffer from C_2 and MgH absorption (Doyle 2015).

2.1.4 Composition

The abundance of an element in the stellar atmosphere is normally measured relative to the abundance of hydrogen, and can be given on an absolute scale or relative to the Sun. The

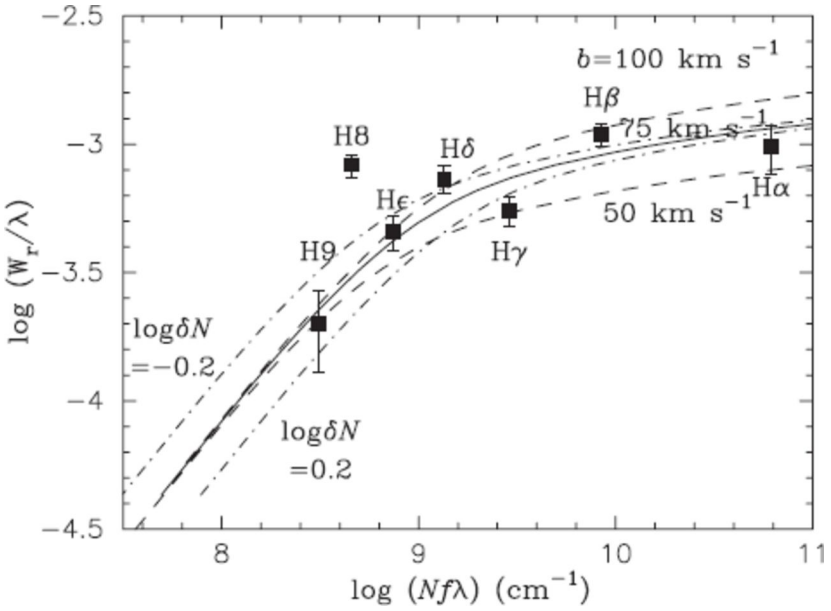

Figure 2.1: Curve of growth measurements and fit for Balmer line absorption of SDSS J1723+5553. Here the initial rise and the plateau can be seen, but not the second rise due to radiation damping and collisional broadening. Image taken from Aoki (2010)

.

former is typically quoted as $\log A+12$ where A is the number ratio of an element to hydrogen in the star, N_X/N_H. It is also convenient to express composition relative to the Sun:

$$[X/H] = \log\left(\frac{N_x}{N_H}\right)_\star - \log\left(\frac{N_x}{N_H}\right)_\odot , \tag{2.3}$$

where N_H is the number density of hydrogen and N_X is the number density for the star ($\star$) and the Sun ($\odot$). One way to measure composition is to look at the curve-of-growth of equivalent widths for lines of the same species with the following theory: if we consider only a few absorbers in a photospheric region then a line opacity is relatively weak and takes a thermal Doppler form mostly due to the line core region. Here, a plot of $\log(EW)$ V. $\log(N_{\text{absorbers}})$ increases linearly (see Fig. 1). As the number of absorbers increase the line core begins to fully absorb the continuum and adding more absorbers does not appreciably increase the EW; the plot of $\log(EW)$ V. $\log(N_{\text{absorbers}})$ plateaus. Eventually the line wings begin to add EW due to radiation damping and collisional broadening and our graph begins to rise again with

a gradient lower than the first. Measuring the equivalent widths for an element and adjusting the abundance until a theoretical curvature of growth matches the data gives a good handle on abundances in a star. This is the curve of growth method (Phillips 1995).

2.2 Binary stars

The position and velocity of each component in a binary system relative to a distant observer are imperative when calculating models of radial velocity and transit photometry. In the following sections I detail how these models are created for a given set of orbital parameters.

2.2.1 Positions of binary stars

Johannes Kepler published his first two laws about planetary motion in 1609, having found them by analysing the astronomical observations of Tycho Brahe. They are

1. All planets move about the Sun in elliptical orbits, where the Sun in one of the foci.
2. A line joining a planet to the Sun sweeps out equal areas in equal lengths of time.

Kepler's third law was published later in 1619,

3. The squares of the sidereal periods (of revolution) of the planets are directly proportional to the cubes of their mean distances from the Sun.

Any Keplerian trajectory in space can be characterised by a position vector and a velocity vector. Each of these has three components which change through an orbit. It is convenient to instead use *Keplerian elements* - six parameters which can be used to calculate the position and velocity of an orbiting body. Two define the scale and elongation of the orbit:

- e - eccentricity,
- a - semi-major axis,

three define the orientation of the orbital plane:

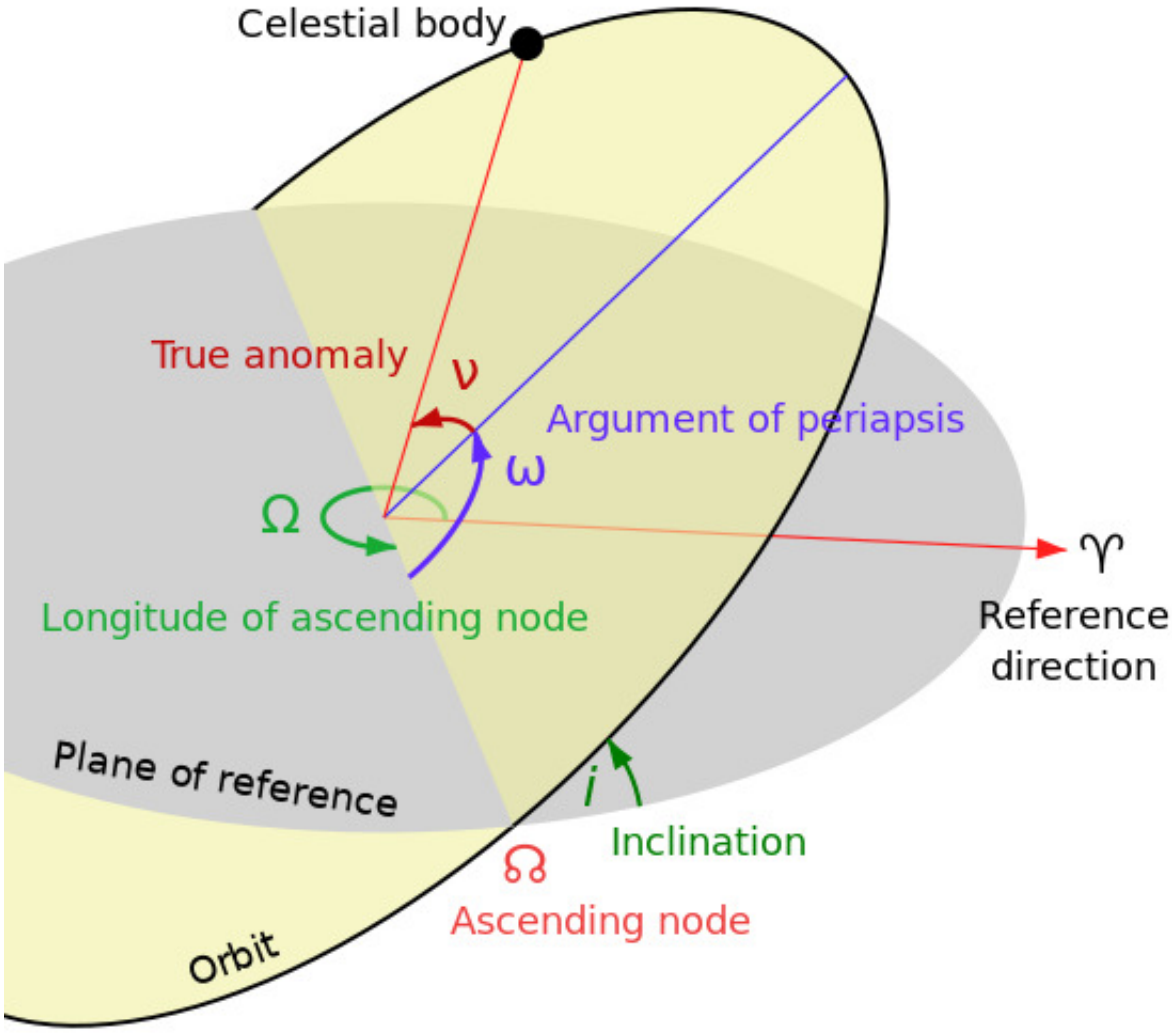

Figure 2.2: Visual representation of Keplerian elements.

- i - orbital inclination, the angle between the orbital plane and the reference frame
- Ω- longitude of the ascending node which defines the angle between the reference direction and the upward crossing of the orbit on the reference plane,
- ω-argument of periapsis which defines the angle between the ascending node and the periapsis.

The position of the star(s) at a given time is specified by

- ν - true anomaly which defines the position of the orbiting body along the trajectory, measured from periapsis.

A visual representation of Keplerian elements can be seen Fig. 2.2. The advantage of the Keplerian system over a Cartesian is that only one parameter changes through an orbit - ν.

It is convenient to measure time relative to a reference time, t_0, that corresponds to a minimum in sky-projected separation between two stars (conjunction). At time t_o star 2 is closer to the observer than star 1. The true anomaly of star 1 at this time is $\nu_{1,t_0} \approx \pi/2 - \omega_0$. At other times, t_i, the true anomaly requires calculation of the time of periastron passage immediately prior to a given time of eclipse, t_c. The mean anomaly can then be calculated,

$$M = 2\pi \frac{t_i - t_c}{P_a} \tag{2.4}$$

where P_a is the anomalistic period. Keplers law,

$$M = E - e \sin E \tag{2.5}$$

and its differential form,

$$\frac{dM}{dE} = 1 - e \cos E \tag{2.6}$$

can be used to solve for the eccentric anomaly, E, using the Newton-Raphson method. The true anomaly can then be calculated for star 1,

$$\nu_1 = 2 \tan^{-1} \left[\sqrt{\frac{1+e}{1-e}} \tan(E/2) \right] \tag{2.7}$$

and $\nu_2 = \nu_1 + \pi$ for star 2.

2.2.2 Radial velocity

The motion of each component in a binary system relative to the barycentre results in motion projected onto the line of sight. We can obtain spectroscopic orbital parameters (e, ω and the semi-amplitude, K_1) by measuring accurate radial velocities at several orbital phases and fitting a Keplerian orbit to these measurements. The wavelength shift, $\Delta\lambda$, is a function of radial velocity, $V_{\rm rad}$, and the rest wavelength of a particular spectral line, λ_0. Hence an observed spectrum appears to shift by different amounts depending on the wavelength of the line that is measured. One way to overcome this is to convert from a linear wavelength scale to a natural logarithm wavelength scale:

$$\ln\left(\frac{\lambda}{\lambda_0}\right) = \ln\lambda - \ln\lambda_0 \tag{2.8}$$

$$\approx \ln\left(1 + \tfrac{V_{\rm rad}}{c}\right). \tag{2.9}$$

Now a radial velocity shift, $V_{\rm rad}$, shifts the spectra along the $\ln\lambda$ axis, proportional to $V_{\rm rad}$ in a manner that is independent of λ_0. With this known, we can employ the cross-correlation tool to compare a spectrum to a template spectrum of known radial velocity. A cross correlation is defined:

$$c(x) = \int_{-\infty}^{\infty} f(\lambda)g(\lambda - x)d\lambda \tag{2.10}$$

where for the independent variable, x, $c(x)$ is equal to the product of the two functions f & g, which are the programme spectrum and a template spectrum respectively. The function $c(x)$ is a measure of how well matched the two functions are over the range of displacement values, x. Providing the luminosity ratio between the two stars is not too extreme and the motion of each component along the line of sight is sufficiently different, there will be two peaks in $c(x)$ corresponding to each component moving towards and away from us. In EBLM systems, the FGK star dominates the light and only one peak will be measurable (SB1s). It is beneficial to mask spectral features which may broaden/modify $c(x)$. The 8 EBLMs in this work with CORALIE spectra were cross-correlated with a numerical mask[1] around Fe lines. The other EBLM with INT spectra masked the core of the Hα line. Gaussian functions are

[1] "Spectrum" of 0s and 1s at the position of spectral lines.

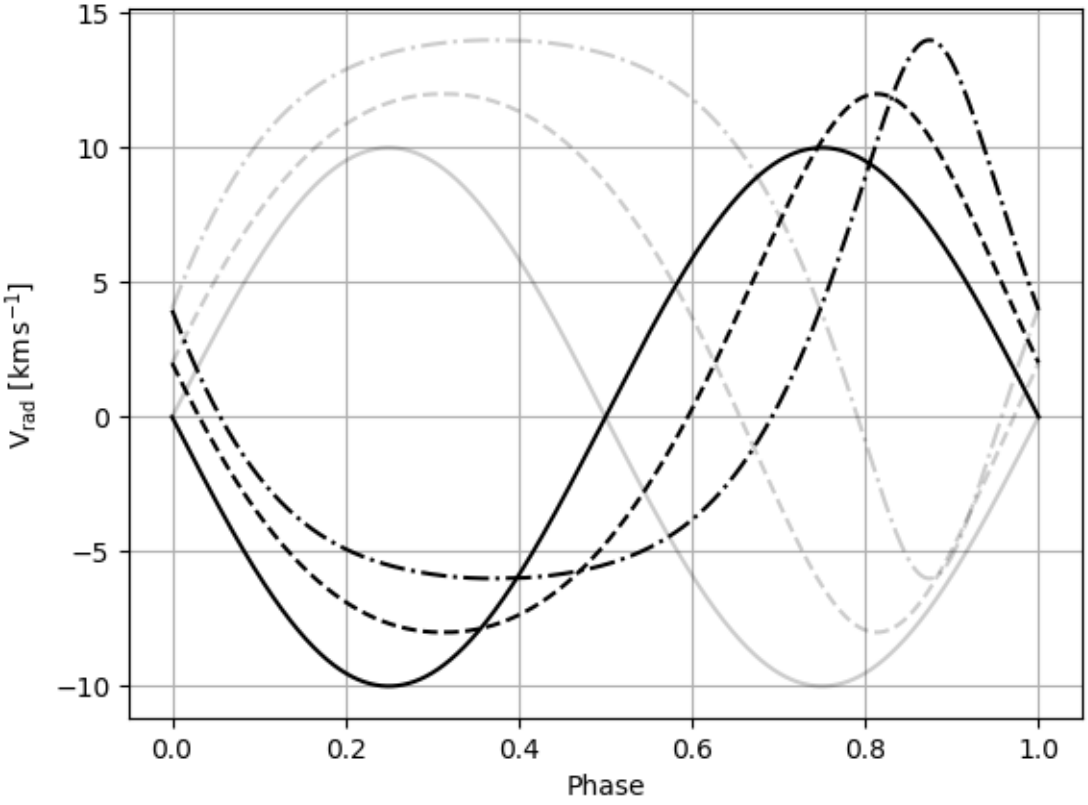

Figure 2.3: Example radial velocity models of the primary star for a circular orbit (solid), $e = 0.2$ (dashed) and $e = 0.4$ (dash-dot). The respective radial velocity models of the secondary stars are shown in light grey.

often used to fit the peaks in $c(x)$ giving the relative radial velocity motion between the star and the template spectrum.

Calculating a model for the projected radial velocity ($V_{\rm rad}$) of star 1 at time t_i is trivial once its true anomaly ($\nu_{1,i}$) is calculated,

$$V_{\rm rad} = K_1 \left(e \cos\omega + \cos\nu_{1,i} + \omega\right) + \gamma \quad \left[+d(\gamma)/dt\right], \tag{2.11}$$

where K_1 is the semi-amplitude and γ is the systematic velocity of the binary system. Example radial velocity models are shown in Fig. 2.3. Unresolved faint companions in long-period

orbits (tens of years) can introduce drifts in systematic velocity which require an extra term $d(\gamma)/dt$ to account for the inner-binary's orbit around the centre-of-mass.

The SB1 nature of EBLMs mean that masses of each component cannot be calculated directly. The binary mass function, $f(m)$, can be used to constrain the the mass of the unseen component using parameters from Eqn. 2.11,

$$f(m) = \frac{(M_2 \sin i)^3}{(M_1 + M_2)^2} = (1 - e^2)^{\frac{3}{2}} \frac{P K_1^3}{2\pi G}. \tag{2.12}$$

The orbital inclination is generally not known but can be assumed to be near 90° if the binary system is transiting. In the case of exoplanets, $M_1 + M_2 \approx M_1$ which yields M_2 assuming prior knowledge of M_1 (e.g. from empirical relations). It is important to note that $f(m) \propto K_1^3$ and any uncertainty in K_1 propagates by a factor of three into the mass function, and thus the masses of each star/planet. If the spectral lines of both stars can be measured it is possible to calculate the minimum masses of both components,

$$M_{1,2} \sin^3 i = c_m (1 - e^2)^{\frac{3}{2}} (K_1 + K_2)^2 K_{2,1} P \tag{2.13}$$

where i is the orbital inclination, P is the orbital period and $c_m = 1.0361 \times 10^{-7}\, M_\odot$ is an up-to-date constant from IAU resolution B3 (Prša et al. 2016). Similarly, the two semi-major axes of the orbits are,

$$a_{1,2} \sin i = c_a (1 - e^2)^{\frac{1}{2}} K_{1,2} P \tag{2.14}$$

where $c_a = 1.9758 \times 10^{-2}\, R_\odot$.

2.2.3 Light-curves

Knowledge of the Keplerian elements of an orbit permits the determination of the *sky-projected separation*,

$$\delta = \frac{1 - e^2}{1 + e \cos \nu} \sqrt{1 - \sin^2 i \sin^2(\nu + \omega)}, \tag{2.15}$$

where δ is normalised in terms of the semi-major axis, a. At this stage, it is convenient to introduce the radius of star 1 normalised in units of semi-major axis, $R_\star/a$, the ratio of the radii, $k = R_2/R_\star$, and assume spherical star shapes. The inclination, i, is strongly correlated

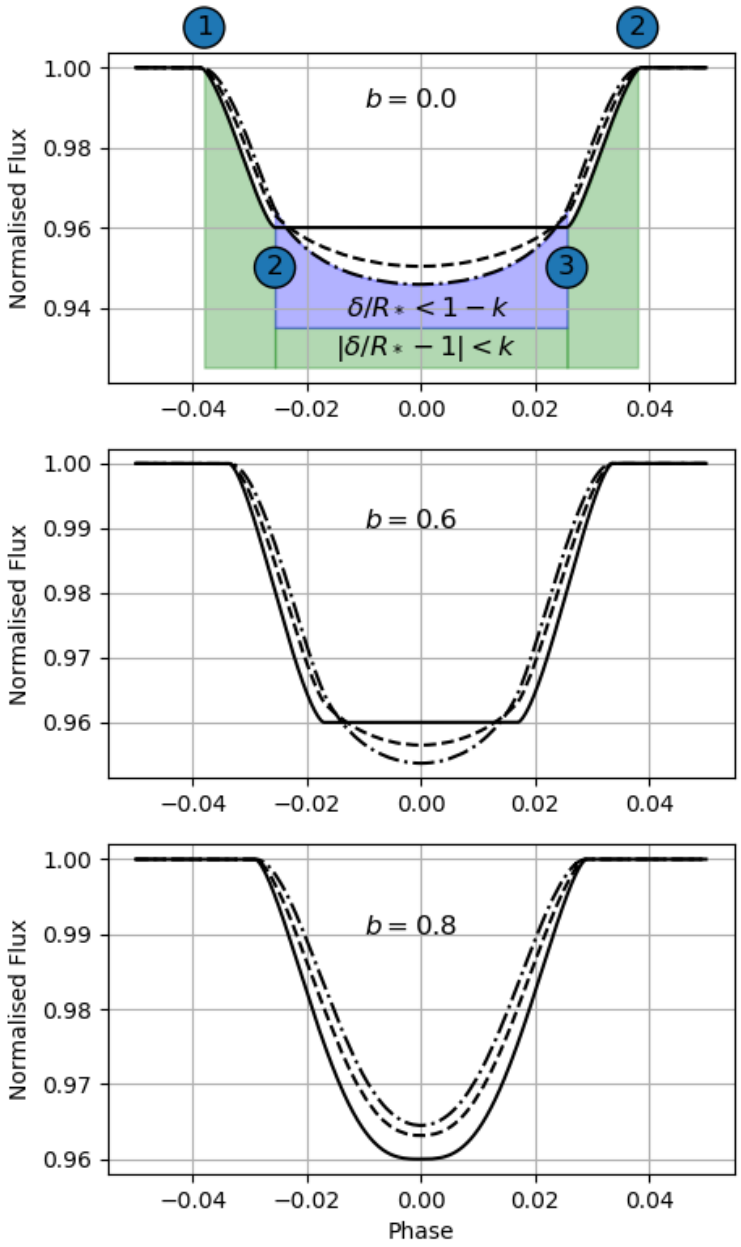

Figure 2.4: The primary eclipse for a uniformly illuminated star (solid), linear limb-darkened star ($c_1 = 0.6$; dashed) and a quadratically limb-darkened star ($c_1 = 0.6$, $c_2 = 0.4$; dash-dot) for impact parameters of $b = 0.0$ (top panel), $b = 0.6$ (middle panel) and $b = 0.8$ (lower panel). The contact points are marked in the top panel along with ingress/egress regions ($|\delta/R_\star - a| < k$; green) and when the apparent disk of star 2 is entirely encompassed by that of star 1 ($\delta/R_\star < 1 - k$; blue).

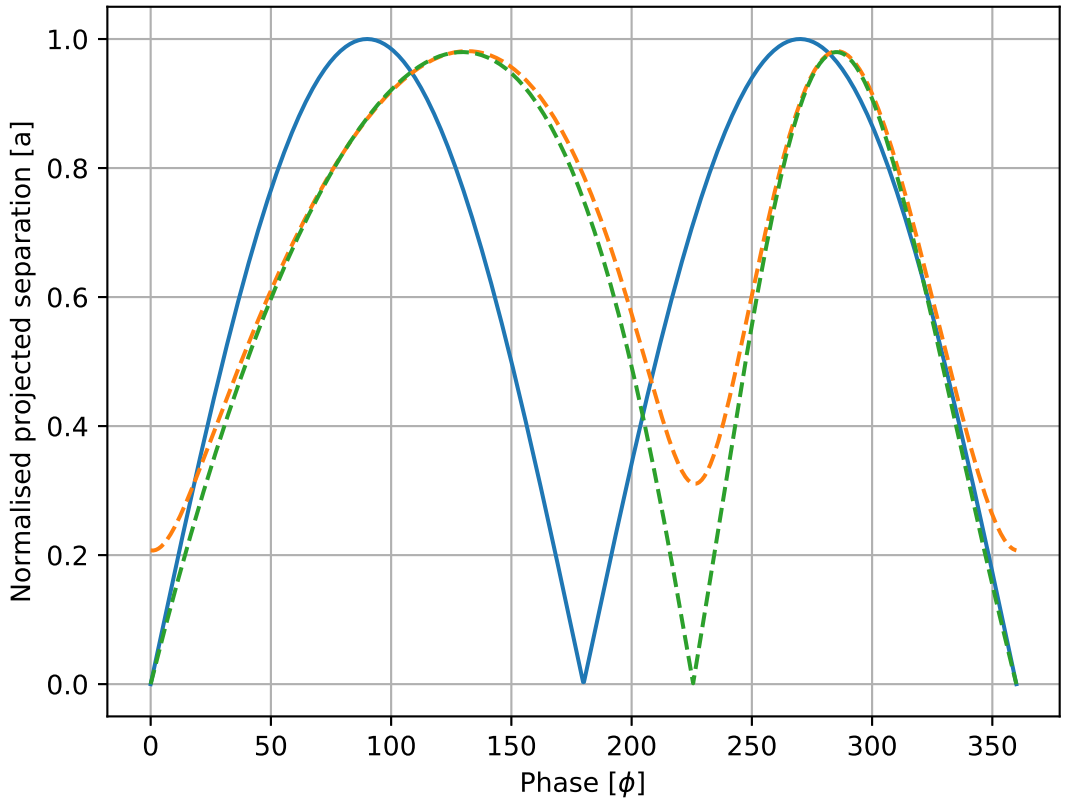

Figure 2.5: The normalised orbital separation in terms of semi-major axis for a circular orbit inclined at 90° (blue), an orbit with $e = 0.2$ at an inclination of 90° (green-dashed) and an orbit with $e = 0.2$ at an inclination of 75° (orange-dashed).

with other transit parameters and so it is convinient to introduce the *impact parameter* ($b = a\cos i/R_\star$). Dividing δ from Eqn. 2.15 by $R_\star/a$ gives the projected sky separation in units of stellar radii. When $\delta/R_\star > 1 + k$, the projected sky-separation of each components disk is such that there is no overlap, and the light from each star is visible. However, when the projected sky-separation is such that $|\delta/R_\star - 1| < k$, there is a partial overlap between the disks of each star. For a primary eclipse (where star 2 is in-front of star 1), this would be the ingress/egress parts of a transit between contact points 1-2, and 3-4 (Fig. 2.4). Between contact points 2-3 is where $\delta < 1 - k$ and the disk of star 2 sits entirely within the disk of star 1.

The calculation of δ makes no assumption about the absolute position of each star. Over a single period for a transiting binary system, there are two occasions when $|\delta/R_\star - 1| < k$ (Fig. 2.5). Determining if a transit is a primary or secondary eclipse requires the calculation of the position for star 1 along the line of sight,

$$\bar{l} = \sin\left[2\arctan\left[\sqrt{\frac{1+e}{1-e}}\tan\frac{E}{2}\right] + \omega\right]\sin i. \tag{2.16}$$

Instances where $\bar{l} > 0$ are primary eclipses (star 2 in front of star 1) and $\bar{l} < 0$ are secondary eclipses. For systems with low values of k, the entirety of the secondary star is obscured in secondary eclipses leading to a flat-bottomed eclipse. The shape of the secondary eclipse is typically parameterised by the surface brightness ratio, $S = k^2 F_{\lambda,2}/F_{\lambda,\star}$, where F_λ is the flux of each star observed in some bandpass. The normalised depth of a secondary eclipse is then given by $1 - S \times k^2$.

2.2.4 Limb darkening

Creating a model for an eclipse would be trivial if the disc of each star was uniformly illuminated. In this case, the drop in flux would be proportional to the area occulted on the furthest star by the nearest star. This would result in transits where all contact points would be easily discernible and the flux between contact points 2 and 3 would be constant. Unfortunately, lightcurves taken in filters blueward of $\sim 1\mu m$ show a slight "rounding" of the lightcurve

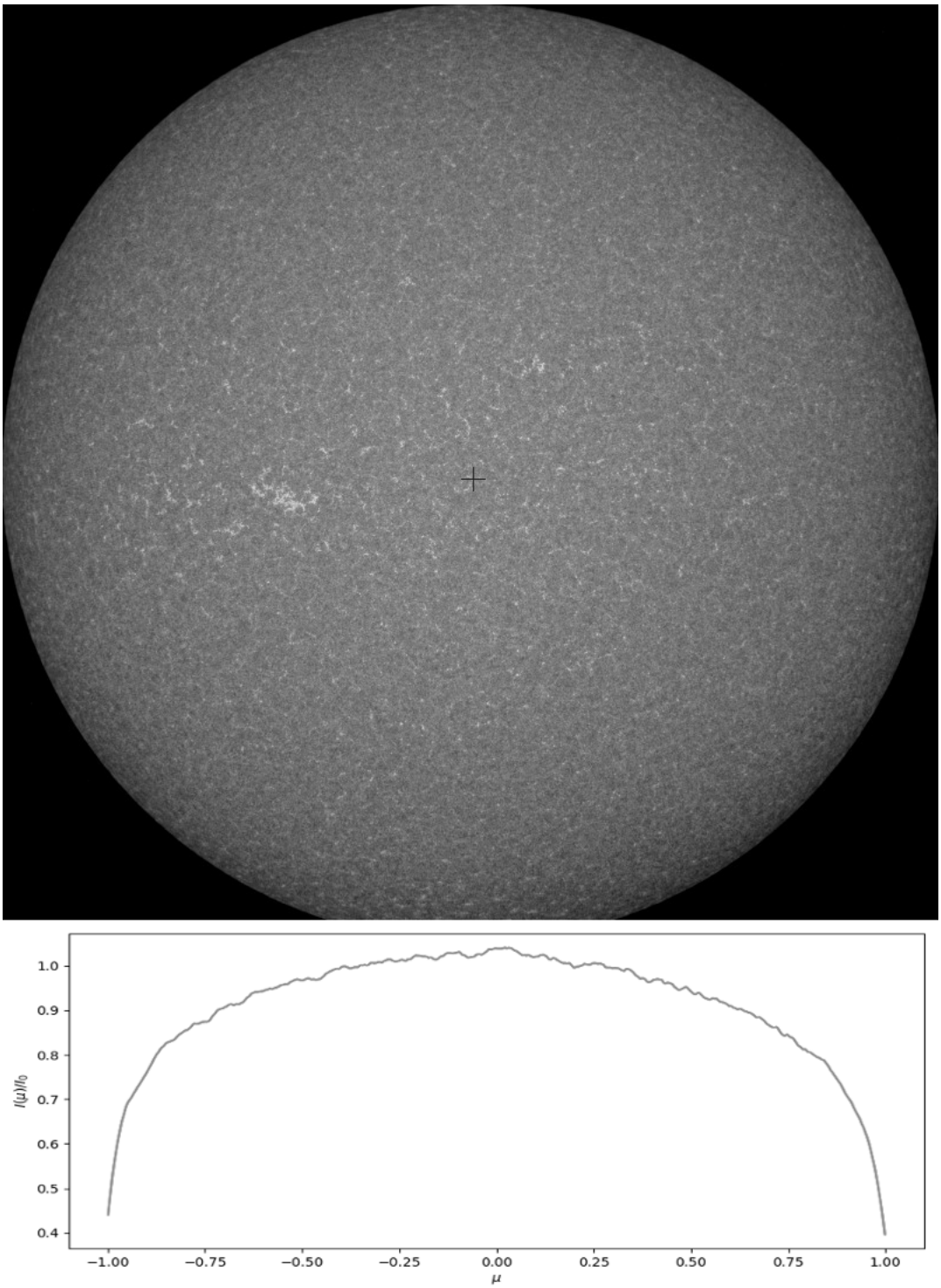

Figure 2.6: (top) An image obtained from the Solar Dynamics Observatory on March 3^{rd} 2018, 01:04:29 UT using the 1700Åfilter. (bottom) The normalised intensity profile of the Sun using the SDO 1700Åimage (top).

caused by stars emitting more light at the centre than the edge (limb); this is called limb darkening. The reason for this is that light occulted near the limbs originates from a colder column of gas which emits less light than a hotter column of gas near the centre of the disk. This can be seen in an image of the Sun from the Solar Dynamics Observatory (Fig. 2.6) which shows a clear drop in light emitted toward the edge of the solar disk. This intensity across a stellar disk is typically defined in terms of $\mu = \cos\gamma$, where γ is the angle between a line normal to the stellar surface and the line of sight. How the normalised intensity $I(\mu)/I_0$ is related to μ largely remains a task for theoreticians since very few stars are resolvable (see Altair Monnier et al. 2007; π^1 Gruis, Paladini et al. 2018; Betelgeuse, Uitenbroek, Dupree & Gilliland 1998; Antares, Ohnaka, Weigelt & Hofmann 2017 ...) and provide little or no constraints on surface intensity distributions across different spectral types.

As stated by Seager & Mallen-Ornelas (2002), the generel effect of limb darkening is to (1) change the depth of the lightcurve as a function of impact parameter, where the transit is deeper for most values of impact parameter, (2) make the flat bottom between contact points 2 and 3 rounder and (3) blur the boundary between contact points 2 and 3. These effects are show in Fig. 2.4. There are a number of limb-darkening laws used to describe how $I(\mu)/I_0$ changes with μ. These largely depend on a series of coefficients, c_i, depending on the number of parameters. Some examples are,

$$I(\mu)/I_0 = 1 - c_1(1-\mu) \quad \text{[Linear]}^2 \tag{2.17}$$

$$I(\mu)/I_0 = 1 - c_1(1-\mu) - c_2(1-\mu)^2 \quad \text{[quadratic]}^3 \tag{2.18}$$

$$I(\mu)/I_0 = 1 - c_1(1-\mu) - c_2(1-\sqrt{\mu}) \quad \text{[square-root]}^4 \tag{2.19}$$

$$I(\mu)/I_0 = 1 - c_1(1-\mu) - c_2\mu\log\mu \quad \text{[logarithmic]}^5 \tag{2.20}$$

$$I(\mu)/I_0 = 1 - c_1(1-\mu) - \tfrac{c_2}{1-\exp\mu} \quad \text{[exponential]}^6 \tag{2.21}$$

$$I(\mu)/I_0 = 1 - c_1(1-\mu) - c_2(1-\mu^{\frac{3}{2}}) - c_3(1-\mu^2) \quad \text{[sing]}^7 \tag{2.22}$$

$$I(\mu)/I_0 = 1 - c_1(1-\mu^{c_2}) \quad \text{[power-2]}^8 \tag{2.23}$$

$$I(\mu)/I_0 = 1 - c_1(1-\mu^{\frac{1}{2}}) - c_2(1-\mu) - c_3(1-\mu^{\frac{3}{2}}) - c_4(1-\mu^2) \quad \text{[claret]}^9. \tag{2.24}$$

Many of these limb-darkening laws have tables of coefficients (c_i) for a given set of stellar atmospheric parameters ($T_{\rm eff}$, [Fe/H] and $\log g$). I used the Claret 4-parameter law to fit the lightcurves of 5 EBLMs observed from ground-based instruments by interpolating coefficients for a given limb-darkneing temperature. I used the power-2 law to measure 4 EBLMs observed with K2 by fitting the coefficients, c_i, as free parameters (see Sect. 5.6). To model secondary eclipses I assumed that the M-dwarf is uniformly illuminated and use the analytical expression presented by Kreidberg (2015).

2.3 Absolute parameters

Photometric transit parameters ($R_\star/a$, k & i) set the radii scale of the system whilst radial velocity parameters (K_1 & e) set the mass scale between the components. Often, we are more interested in dimensional parameters such as the mass of each companion, or the semi-major axis in astronomical units. For those, the orbital solution (best-fitting transit and radial velocity parameters) must be combined with supplementry information such as the mass or radius of the primary star obtained by other means (e.g. stellar parallax, spectrum or angular diameter; Winn 2009). A brief description on how masses, radii and age are interpolated in this work, and across the field, is given in Sect. 5.7. However, two important parameters can be calculated from the orbital solution directly.

The surface gravity of the secondary star/planet, $\log g_2$, can be obtained by combining the mass function (Eqn. 5.20) with the mathematical expression of Keplers third law,

$$\frac{P^2}{a^3} = \frac{4\pi^2}{G(M_\star + M_2)}, \tag{2.25}$$

[2]Schwarzschild (1906)
[3]Kopal (1950)
[4]Diaz-Cordoves & Gimenez (1992)
[5]Klinglesmith & Sobieski (1970)
[6]Claret & Hauschildt (2003)
[7]Sing et al. (2009)
[8]Hestroffer (1997)
[9]Claret (2000)

which can be solved for the sum of the masses of the two components,

$$(M_\star + M_2)^2 = \frac{2\pi G M_2^3 \sin^3 i}{(1-e^2)^{3/2} K_1^3 P} = \frac{(2\pi)^4 a^6}{G^2 P^4}. \tag{2.26}$$

By substituting $R_2 = a r_2$, where $r_2 = R_2/a$, into the definition of surface gravity and replacing a using Eqn. 2.26, the surface gravity of star 2 can be calculated:

$$g_2 = \frac{2\pi}{P} \frac{\sqrt{1-e^2} K_1}{r_2^2 \sin i}. \tag{2.27}$$

The total transit duration can be calculated assuming a circular orbit,

$$t_T = \frac{P}{\pi} \arcsin\left(\frac{R_\star}{a} \sqrt{\frac{(1+k)^2 - b^2}{1-\cos^2 i}} \right), \tag{2.28}$$

where the impact parameter, b, is defined as

$$b = \frac{a \cos i}{R_\star}. \tag{2.29}$$

By combining Eqn. 2.25 with Eqn. 2.28 it is possible to calculate the stellar density,

$$\rho_\star \equiv \frac{M_\star}{\frac{4}{3}\pi R_\star^3} = \frac{3\pi}{G P^2} \left(\frac{a}{R_\star} \right)^3 - \frac{M_2}{R_\star^3}. \tag{2.30}$$

For exoplanets ($M_\star >> M_2$), the second term on the right-hand side of Eqn. 2.30 can be ignored to give a robust estimate of the stellar density. For EBLMs systems, the mass ratio $q = M_2/M_\star \approx 0.1$-$0.6$ and so Eqn. 2.30 requires further constraints on masses and radii.

3 Observations

Table 3.1: Summary of observations used to derive stellar atmospheric and orbital solutions for 5 EBLMs observed from the ground. The square brackets indicate the filter corresponding to the preceding number of observations.

	J2349−32	J2308−46	J0218−31	J1847+39	J1436−13
J2000.0					
α	$23^h49'15.23"$	$23^h08'45.66"$	$02^h18'13.24"$	$18^h47'52.34"$	$14^h36'46.42"$
δ	$-32°46'17.5"$	$-46°06'36.6"$	$-31°05'17.3"$	$+39°58'51"$	$-13°32'35.5"$
Vmag	11.53	11.36	9.96	11.73	12.48
observations					
WASP	8144	14,369	7872	9639	53,259
SAAO 1-m	345 [I]	474 [R]	-	-	136 [R]
CTIO	-	-	78 [g'] 62 [z'] 71 [r'] 70 [z']	-	-
HAO	-	-	-	605 [CBB] 311 [g'] 371 [z']	-
CORALIE	20	19	70	-	20
INT	-	-	-	10	-
Gaia					
G	11.448 ± 0.001	11.381 ± 0.001	9.775 ± 0.001	11.755 ± 0.001	12.334 ± 0.001
$G_{BP} - G_{RP}$	0.721 ± 0.002	0.728 ± 0.002	0.779 ± 0.002	0.818 ± 0.002	0.759 ± 0.002
parallax [mas]	3.881 ± 0.108	2.299 ± 0.127	3.874 ± 0.108	3.695 ± 0.109	2.175 ± 0.112
photometry					
APASS9 [B]	12.142 ± 0.039	12.072 ± 0.015	10.519 ± 0.037	12.382 ± 0.021	12.986 ± 0.009
APASS9 [V]	11.541 ± 0.010	11.517 ± 0.045	9.903 ± 0.026	11.913 ± 0.022	12.480 ± 0.014
APASS9 [g']	11.785 ± 0.013	11.749 ± 0.016	10.202 ± 0.032	12.007 ± 0.031	12.690 ± 0.018
APASS9 [r']	11.438 ± 0.033	11.382 ± 0.014	9.779 ± 0.029	11.704 ± 0.006	12.354 ± 0.021
APASS9 [i']	11.317 ± 0.013	11.286 ± 0.006	9.632 ± 0.079	11.548 ± 0.006	12.231 ± 0.064
TYCHO [B_T]	12.278 ± 0.138	11.801 ± 0.091	10.655 ± 0.039	12.146 ± 0.137	-
TYCHO [V_T]	11.593 ± 0.100	11.398 ± 0.108	9.958 ± 0.033	11.766 ± 0.150	-
2MASS [J]	10.530 ± 0.023	10.477 ± 0.022	8.783 ± 0.034	10.682 ± 0.026	11.353 ± 0.027
2MASS [H]	10.249 ± 0.022	10.270 ± 0.024	8.555 ± 0.031	10.362 ± 0.032	11.040 ± 0.021
2MASS [K_S]	10.184 ± 0.019	10.166 ± 0.020	8.493 ± 0.025	10.306 ± 0.021	10.987 ± 0.019
DENIS [I_C]	-	-	-	-	11.790 ± 0.030
DENIS [J]	-	-	-	-	11.371 ± 0.070
DENIS [K_S]	-	-	-	-	10.912 ± 0.070
E(B-V)	0.010 ± 0.034	0.007 ± 0.034	0.024 ± 0.030	0.088 ± 0.030	0.072 ± 0.034

Table 3.2: Summary of observations used to derive stellar atmospheric and orbital solutions for 5 EBLMs observed with K2. The square brackets indicate the filter corresponding to the preceding number of observations.

	J0055−00 EPIC220196587	J0457+14 EPIC246712205	J1652−19 EPIC205148699	J2217−04 EPIC206500801
J2000.0				
α	$00^h55'13.72"$	$04^h57'20.84"$	$16^h52'38.52"$	$22^h17'58.13"$
δ	$-00°07'54.00"$	$+14°43'30.40"$	$-19°09'41.70"$	$-04°51'52.60"$
Vmag	10.96	12.14	12.75	12.18
CORALIE	24	15	14	13
*K*2				
Campaign	8	13	2	3
data points	3595	3703	2601	3199
Usable transits	7	23	9	9
Gaia				
G-mag	10.912 ± 0.001	11.916 ± 0.001	12.413 ± 0.001	12.003 ± 0.001
$G_{BP} - G_{RP}$	0.834 ± 0.002	0.844 ± 0.002	1.013 ± 0.002	1.029 ± 0.002
Parallax [mas]	3.188 ± 0.118	1.449 ± 0.107	2.121 ± 0.151	2.510 ± 0.141
photometry				
APASS9 [B]	11.711 ± 0.027	12.677 ± 0.036	13.344 ± 0.026	13.047 ± 0.053
APASS9 [V]	11.043 ± 0.032	12.088 ± 0.034	12.614 ± 0.043	12.221 ± 0.030
APASS9 [g']	11.339 ± 0.021	12.374 ± 0.035	12.949 ± 0.031	12.582 ± 0.040
APASS9 [r']	10.884 ± 0.033	11.920 ± 0.021	12.391 ± 0.047	11.957 ± 0.024
APASS9 [i']	10.745 ± 0.059	11.772 ± 0.072	12.113 ± 0.065	11.922 ± 0.215
2MASS [J]	9.899 ± 0.023	10.801 ± 0.023	11.027 ± 0.023	10.749 ± 0.022
2MASS [H]	9.613 ± 0.027	10.663 ± 0.032	10.649 ± 0.025	10.404 ± 0.022
2MASS [K_S]	9.534 ± 0.021	10.529 ± 0.021	10.554 ± 0.022	10.296 ± 0.023
E(B-V)	0.023 ± 0.034	0.350 ± 0.034	0.298 ± 0.034	0.09 ± 0.034

Measuring the masses and radii of EBLM systems requires two types of data. The first type are spectroscopic observations which are taken at different phases of an EBLMs orbit. Spectra have two uses in this work: 1) they provide radial velocity measurements and 2) they can be co-added to estimate atmospheric parameters. I also use photometric colours to fit the spectral energy distribution to measure the photometric temperature and reddening. The second data type is transit photometry which sets the scale of each component. The quality of WASP photometry is not good enough to measure masses and radii to the desired precision of a few percent. To this end, I obtained higher-quality follow-up photometry which was used to determine the orbital solution. In the following sections I detail the origin and processing of data used in this work; this is summarised in Table 3.1 & 3.2.

3.1 Photometric colours used for SED fitting

Photometry for each target was extracted from the following catalogues: B_T and V_T magnitudes from the Tycho-2 catalogue (Høg et al. 2000); B, V, g′, r′ and i′ magnitudes from data release 9 of the AAVSO Photometric All Sky Survey (APASS9; Henden et al. 2016; J, H and K_s magnitudes from the Two-Micron All-Sky Survey (2MASS; Skrutskie et al. 2006; i′, J and K magnitudes from the DEep Near-Infrared Southern Sky Survey (DENIS; Epchtein et al. 1997). The reddening maps by Schlafly & Finkbeiner (2011) were used to estimate the total line-of-sight extinction in the direction of each target, $E(B-V)_{map}$. Values of $E(B-V)_{map}$ were calculated using the NASA/IPAC Extragalactic Database (NED) operated by the Jet Propulsion Laboratory, California Institute of Technology[1]. Not all EBLMs have photometry in all catalogues; those that do are reported in Tables 3.1 & 3.2.

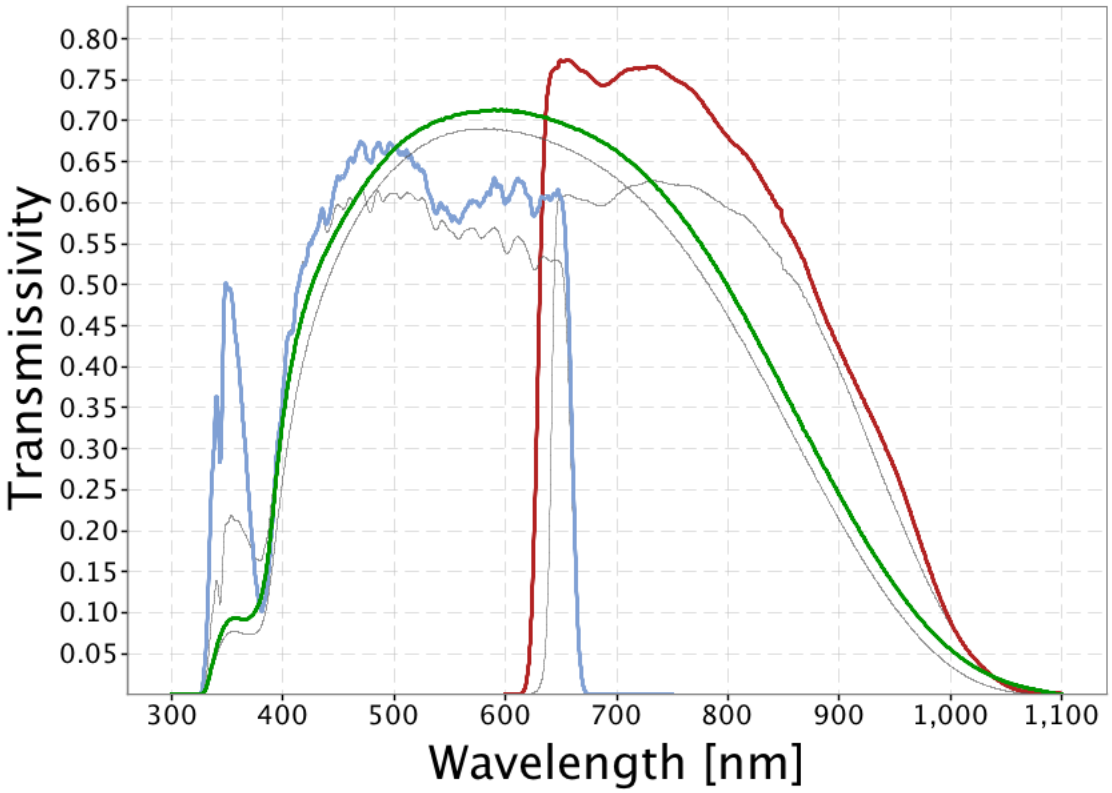

Figure 3.1: The coloured lines in the figure show the revised passbands for G, $G_{\rm BP}$ and $G_{\rm RP}$ (green: G; blue: $G_{\rm BP}$; red: $G_{\rm RP}$), defining the Gaia DR2 photometric system. The thin, grey lines show the nominal, pre-launch passbands published in Jordi et al. 2010, used for Gaia DR1. Image taken from *www.cosmos.esa.int*.

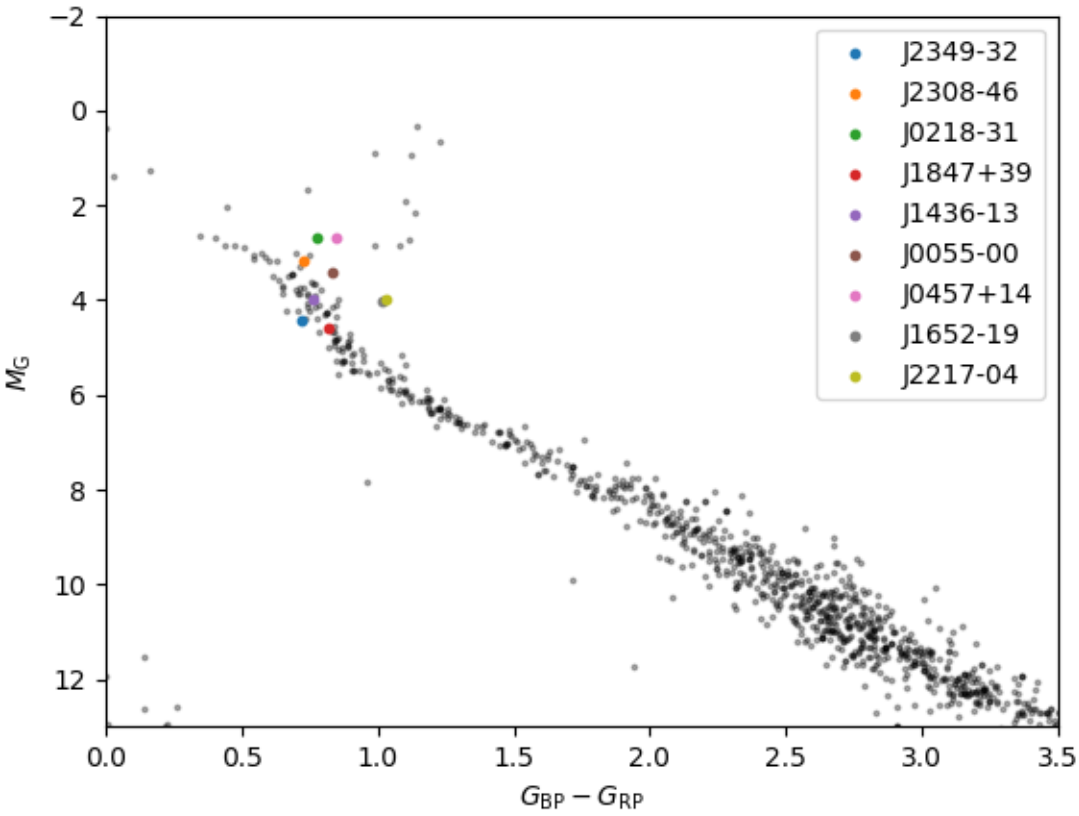

Figure 3.2: The M_G-$G_{BP} - G_{RP}$ plane for 160 randomly selected source fields (black) filtered using Eqns. 1 & 2 from Arenou et al. (2018). The EBLMs used in the work are also plotted and coloured appropriately.

3.2 Gaia colours and Interferometry used to estimate distance and evolutionary status

The second Gaia data release (Gaia DR2; Gaia Collaboration et al. 2018) provides mean flux counts in three bands – G, $G_{\rm BP}$ and $G_{\rm RP}$ (see Fig. 3.1). The G-band has a wider wavelength coverage and is optimised to determine astrometric solutions. The mean magnitudes $G_{\rm BP}$ and $G_{\rm RP}$ provide a "slice" through the spectral energy distribution of stars and reveal how red or blue a star is. I obtained the mean G, $G_{\rm BP}$ and $G_{\rm RP}$ magnitudes along with parallax measurements for all nine EBLM systems from Gaia DR2 using the Gaia archive[2] (Tables 3.1 & 3.2). There is evidence of systematic offsets in parallax measurements from Gaia DR2 (e.g. Stassun & Torres 2018) which is likely correlated with on-sky positions (α & δ), G and $G_{\rm BP}$ - $G_{\rm RP}$ (Lindegren et al. 2018). I added a systematic zero-point offset of 0.03 mas to the parallax and added an additional 0.1 mas in quadrature to the quoted parallax uncertainty (Lindegren et al. 2018). I plot the position of all EBLMs in the $M_{\rm G}$-$G_{\rm BP} - G_{\rm RP}$ plane using data from 160 randomly selected source fields (Fig. 3.2) filtered using Eqns. 1 & 2 from Arenou et al. (2018).

3.3 WASP photometry for initial transit parameters

The WASP survey (Pollacco et al. 2006b) operates two survey instruments: one at the South African Astronomical Observatory (SAAO), South Africa, and another at the Observatorio del Roque de los Muchachos, La Palma. Each instrument consists of an equatorial fork mount with eight cameras with 200-mm lenses and 2k×2k CCD detectors. Each camera coveres approximately 64 square degrees per exposure. The data are processed by a detrending algorithm which was developed from the SysRem algorithm of Tamuz, Mazeh & Zucker (2005) and that is described by Collier Cameron et al. (2007). In July 2012, lenses on the southern installation (WASP-South) were changed to 85-mm with f/1.2 to search for brighter

[1] https://ned.ipac.caltech.edu/help/extinction_law_calc.html
[2] https://gea.esac.esa.int/archive

exoplanet hosts (Smith & WASP Consortium 2014). Data from 85-mm lenses were not used in this study.

Photometry from the WASP cameras can suffer from a large amount of scatter due to clouds, instrumental artefacts, scattered light and other non-optimal observing conditions. I cleaned the data by removing points that were not detrended in the standard WASP reduction pipeline and removed points more than 0.5 mag from the median magnitude of each star. Additional cleaning of the light curve was done by comparing each night of data to a phase-folded light curve binned into 500 phase bins. Any measurement 3-σ or more from the mean in each bin was excluded. The entire night of data was excluded if more than a quarter of the night's data was excluded this way or if there are fewer than 10 observations. The binned light curve is then inspected by eye to further exclude bad data points.

3.4 SAAO 1-m follow-up transit photometry

The SAAO hosts an equatorial-mounted 1-m telescope built by Grubb and Parsons that is equipped with an STE4 CCD camera with 1024×1024 pixels. This camera was operated in 2×2 binning mode to reduce readout time. I observed a single transit for J2349−32 on 18 October 2016 and J2308−46 on 12 October 2016 using I (exposure time of $t_{\rm exp}$ = 50 s) and R ($t_{\rm exp}$ = 40 s) Bessel filters. Jess Kirkby-Kent observed J1436−13 on 23 April 2017 in the R ($t_{\rm exp}$ = 40 s) Bessel filter. Photometry was extracted using standard aperture photometry routines (Southworth et al. 2009) and uncertainties were estimated from photon counting statistics. A by-eye approach was used to clean the light curve and select the best comparison star in the $5' \times 5'$ field. A slow variation in differential magnitude with time was observed corresponding to changes in the effective airmass. To correct for this, I defined out-of-transit regions and then used the IDL/AMOEBA[3] routine to fit a polynomial which minimised the square of the magnitude residuals. I then divided this trend resulting in light curves which were normalised to zero differential magnitude.

[3]http://www.harrisgeospatial.com/docs/AMOEBA.html

3.5 HAO follow-up transit photometry

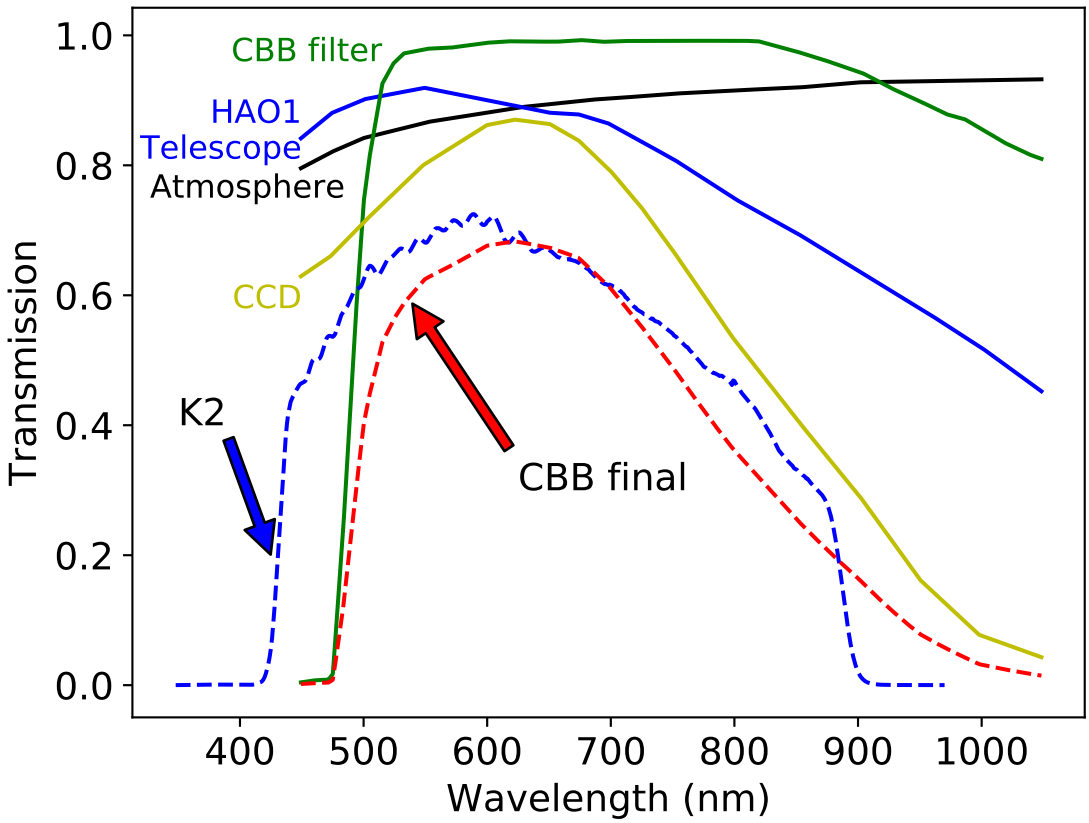

Figure 3.3: The response function of the HAO+CBB instrument. The atmospheric transmission is plotted in black, the transmission of the HAO telescope in blue-solid, the CBB filter in green and CCD response in yellow. The final response of HAO-1 with the CBB filter is plotted in red-dashed along with the K2 transmission (blue-dashed). The atmospheric transmission line originated from equations for Rayleigh, aerosol and ozone extinction vs. wavelength for Palomar Observatory (Hayes & Latham 1975). Coefficients were adjusted until they agreed with observations of extinction at HAO over a few dates.

Optical photometry for J1847+39 was provided by Bruce Gary at the Hereford Arizona Observatory (HAO). Three separate transits were observed with a Meade 14-inch LX200GPS

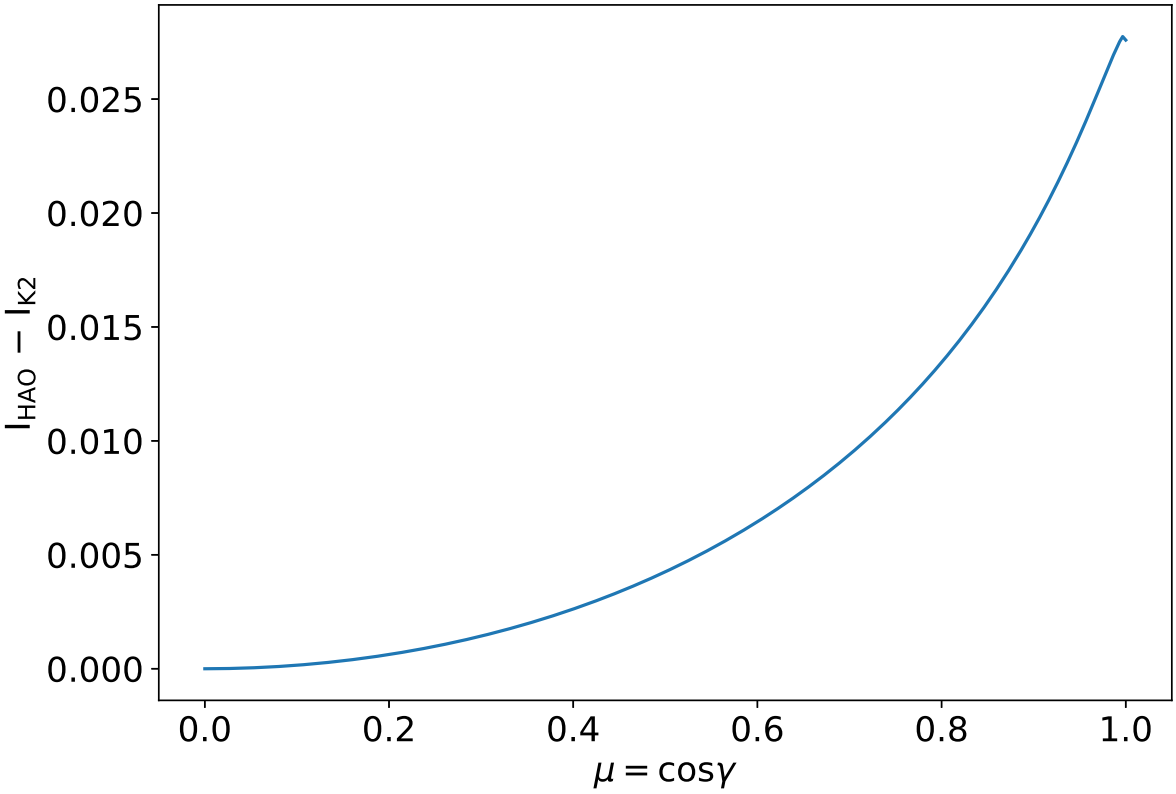

Figure 3.4: The difference in theoretical intensity acoss the stellar disk for the HAO+CBB filter and the Kepler/K2 filter as a function of the angle between a line normal to the stellar surface and the line of sight of the observer (γ) for J1847+39.

telescope. The first was obtained with the clear blue-blocking filter (CBB) on 9 October 2009 with $t_{\rm exp} = 100$ s. The second was with a g' filter on 18 May 2011 with $t_{\rm exp} = 60$ s. The last was with a z' filter on 15 June 2010 with $t_{\rm exp} = 60$ s. Aperture photometry was extracted using standard photometry routines with systematic trends removed and outliers rejected. I used transmission information of the telescope throughput, atmosphere, filter and CCD[4] to calculate the final transmission of HAO with the CBB filter (see Fig. 3.3). I used the four-

[4]http://www.brucegary.net/HAO/

parameter limb-darkening look-up table for the K2 passband instead of the CBB filter due to the similarity in final transmission since I do not have access to a four-parameter look-up table for the CBB filter. In Sect. 7.3.3 I fit light curves using the two-parameter quadratic limb-darkening instead of the Claret law. The final response function in Fig. 3.3 is used along with estimates of stellar atmospheric parameters (from Sect. 5.1 & 5.2) to calculate quadratic coefficients using LDTK (Parviainen & Aigrain 2015).

The discrepancy between the K2 and HAO+CBB pass-band differ in the blue where the limb-darkening is most significant. The validity of this assumption hinges on the fact that 1) the intensity across the stellar disc is similar in both the K2 and HAO+CBB bandpass and 2) the difference in limb-darkening coefficients for each band in negligable. The first assumption was tested using LDTK to synthesise intensity profiles for J1847+39 across the stellar disk for each pass-band and calculate the discrepancy as a function of γ (the angle between a line normal to the stellar surface and the line of sight of the observer; Fig. 3.4). The K2 pass-band emits 2.5 % less flux than what would be observed with HA0+CBB towards the limb. The second assumption was tested by calculating quadratic limb-darkening coefficients for the K2 pass-band to be $u_1 = 0.496 \pm 0.050$, $u_2 = 0.157 \pm 0.050$ and for the HAO+CBB pass-band to be $u_1 = 0.468 \pm 0.050$, $u_2 = 0.148 \pm 0.051$. These are comparable within 1-σ and so adopting the K2 pass-band for J1847+39 will have a negligible effect on the transit shape.

3.6 CTIO follow-up transit photometry

J0218-31 was observed on 14 November 2010 with the CTIO-0.9-m telescope and Tek2K CCD camera. The detector consists of a 2K×2K array of 15μm pixels placed at Cassegrain focus giving a 0.4″/pixel plate scale. Thus the entire array projects to a 13.7′ FOV. J0218-31 and the surrounding field were monitored throughout the night using the Sloan *griz* filter set alternating and continuously between all four filters. Exposure times were chosen to maximise the flux in the target star and nearby reference stars while keeping the peak pixel value in J0218−31 below 60, 000 counts (well depth). Leslie Hebb adopted an exposure time of

10 seconds for the g', r', and i'–band observations and longer exposures of 15 seconds in the z' filter where the detector is less sensitive. The light curves were created from approximately 75 images taken in each filter during the single observing night.

A set of 11 bias calibration frames and 11 dome flat fields in all four filters were obtained at the beginning of the observing night. The images were processed in a standard way using routines written by L. Hebb in the IDL programming language. All object and calibration frames were first overscan corrected (by subtracting a line-by-line median overscan value), bias subtracted and then trimmed. Stacked bias images were created by averaging all bias frames observed each night and subtracted from all science and flat-field frames. All dome flats were averaged into a single dome flat in each filter and then applied to the trimmed and bias-corrected science images.

Source detection and aperture photometry were performed on all processed science images using the Cambridge Astronomical Survey Unit catalogue extraction software (Irwin & Lewis 2001). The software has been compared with SExtractor (Bertin & Arnouts 1996) and found to be very similar in the completeness, astrometry and photometry tests.[5] This photometry software was applied to all processed images of J0218−31. Adopting conservative parameters to define the detection threshold, the target star and dozens of fainter stars in the field were detected in each image. Aperture photometry was performed on all detected stars using a 5 pixel radius circular aperture, which was selected to match the typical seeing. Five bright, non-variable reference stars were selected from the many detected stars and used to perform differential photometry on the target star. In each image, the flux from all reference stars was summed into a single *super* comparison star that was divided by the aperture flux from J0218−31 and converted to a differential magnitude.

[5]https://www.ast.cam.ac.uk/ioa/research/vdfs/docs/reports/simul/index.html

3.7 K2 follow-up transit photometry

The Kepler mission was launched in 2009 and spent over four years monitoring over 150,000 stars in the constellations of Cygnus and Lyra[6]. The spacecraft has a 0.95-m Schmidt telescope with a 110-square degree field of view imager (pixel scale of 4"/ pixel). The primary science goal of Kepler was to detect and characterise terrestrial planets ($R_p < 2.5\,R_\oplus$) which reside in the habitable zone of Sun-like stars. Observations for tens of thousands of stars with short cadence (1-min) and many more thousands with long cadence (30-min) lead to the discovery of many exoplanet (e.g. Weiss et al. 2013; Muirhead et al. 2012; Nesvorný et al. 2013) and eclipsing binary systems (e.g. Carter et al. 2011; Welsh et al. 2011; Szabó et al. 2011).

Kepler exceeded its nominal mission lifetime (3 years) by 1 year until the loss of the second of four reaction wheels in May 2013. In the following months the mission was rebranded "K2" - a name chosen to honour the two remaining reaction wheels or the second Kepler mission (Howell et al. 2014). The K2 mission consists of sequential observing *campaigns* in the ecliptic plane. This is so the torque excerpted on the spacecraft by solar wind pressure can be balanced with altitude thrusters and the two remaining reaction wheels to control pointing. The pointing is significantly worse than the original Kepler mission but the photometric quality approaches that of the original mission after decorrelation of the position-dependent instrument noise. Four EBLMs with spectroscopic orbits published by Triaud et al. (2017) have been observed with K2 (J0055+00, J0457+14, J1652−19 and J2217−04). In the following sections I describe how photometry was extracted from target pixel files and how I corrected for position-dependent instrumental noise.

[6]https://keplerscience.arc.nasa.gov/objectives.html

3.7.1 Extraction

The target pixel files for each target were acquired from the Mikulski Archive for Space Telescopes (MAST[7]). I used data from Gaia DR2 to inform how masks were created for the target pixel files. For J0055−00, J0457+14 and J2217−04 I found no significant ($\Delta G < 6$) companions within 1' so I choose masks which match the shape of the stellar profile of the 100^{th} target pixel file (Fig. 3.5). For J1652−19 I found three close companions within 20" eastwards (Fig. 3.6). The brightest ($\Delta G = 3.33$) is 14" away at a position angle (PA) of 107°. This, and the other two fainter companions at PA = 85° ($\Delta G = 4.28$) and PA = 54° ($\Delta G = 4.17$) may be visible in the target pixel files. If I used full-frame photometry I could expect up to 9% contamination. I excluded these stars by creating a box-like mask at the east and south side of J1652−19. The pointing precision (estimated from centroiding; Sect. 3.7.2) is above 1 pixel and so very little flux from the three nearby stars entered into the aperture. I used the KEPEXTRACT function (Vincius et al. 2017) to extract raw photometry using the masks created for each system.

3.7.2 De-trending

The KEPEXTRACT function fitted a 2-dimensional Gaussian to the target pixel files in each frame to measure each star's CCD position as a function of time. I used the K2SC algorithm (Aigrain, Parviainen & Pope 2016) to detrend against time, x-position and y-position using Gaussian processes. I used an exponential-squared kernel provided by the GEORGE with the DETRENDER function (Ambikasaran et al. 2014) provided with K2SC. This was used to predict variations in the out-of-transit photometry correlated with time and pixel positions. The remaining outliers between transits were detected using basic iterative sigma-clipping, where a data point was excluded if the flux value was over 5-σ from median out-of-eclipse flux level. Although I observed significant "jumps" in photometry continuum levels and evolving

[7] archive.stsci.edu

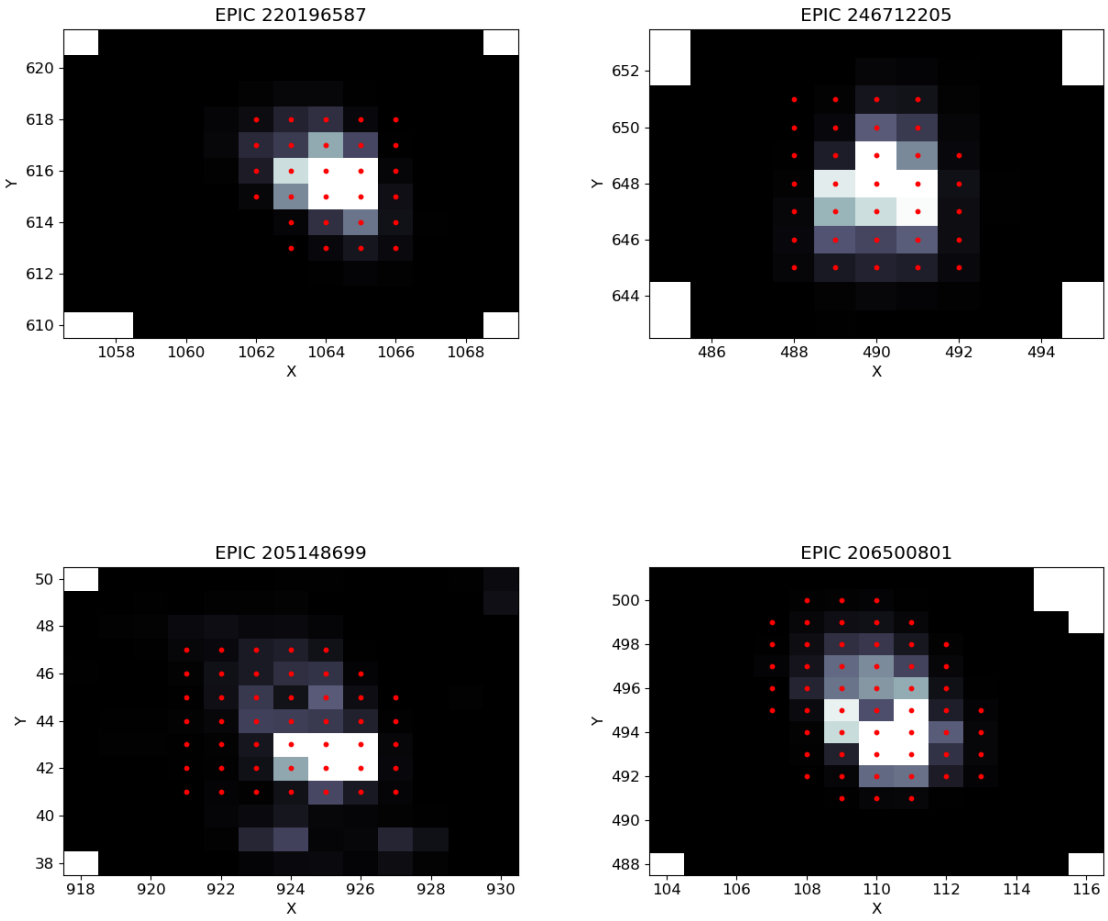

Figure 3.5: The 100^{th} target pixel frame for all EBLM systems observed with K2. Red dots indicate a pixel that was used to in the aperture photometry using PYKE.

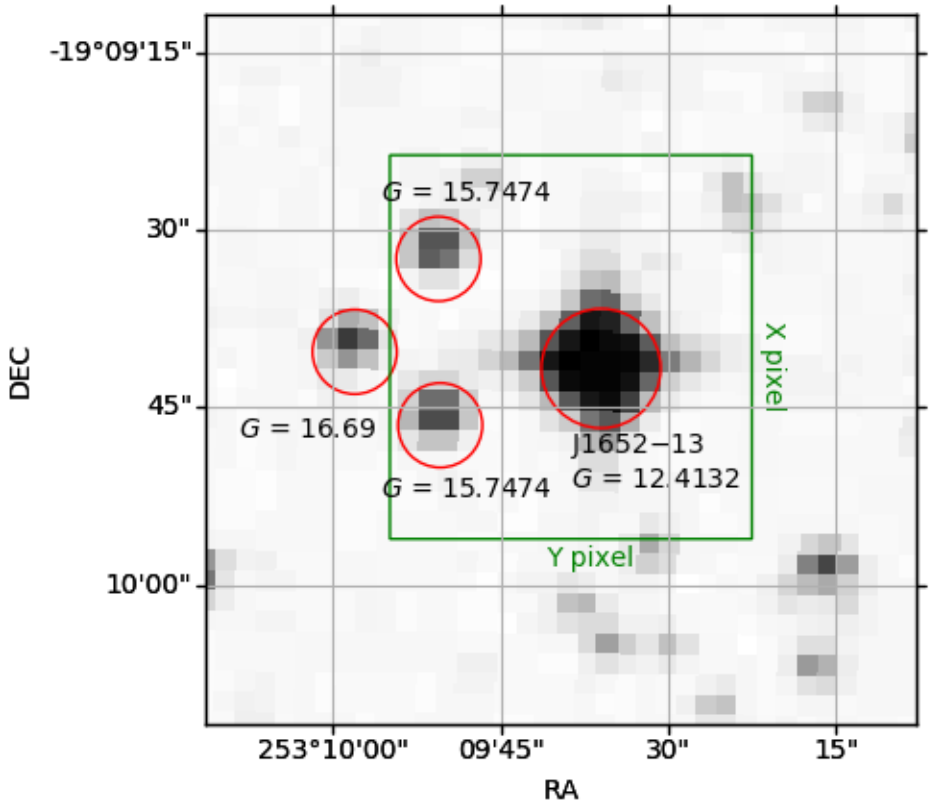

Figure 3.6: The 2MASS finder image of J1652−19. Red apertures mark significant stars in the field with Gaia magnitudes labelled. The green box approximates the extent of the K2 pixel files for J1652−19 (Fig. 3.5).

noise profiles, I assumed that the remaining variation is caused by stellar activity/binary interaction.

3.8 CORALIE spectra used for radial velocities and atmospheric parameters

CORALIE is a fiber-fed échelle spectrograph installed on the 1.2-m Leonard Euler telescope at the ESO La Silla Observatory and has a resolving power R = 50,000 – 60,000 (Queloz et al. 2001a; Wilson et al. 2008). The spectra used in this study were all obtained with an exposure time $t_{\rm exp}$ = 600 s. Observations of J0218−31 include spectra obtained through the transit that show the Rossiter-McLaughlin effect. The spectra for each star were processed with the CORALIE standard reduction pipeline (Baranne et al. 1996). Radial velocity measurements were obtained using standard cross-correlation techniques (using numerical masks) and checked for obvious outliers (Triaud et al. 2017). Each spectrum was corrected into the laboratory reference frame and co-added onto a common wavelength range. Maximum and median filters were applied to identify continuum regions which were fitted with spline functions (one every nm) to normalise the spectra (a standard function within ISPEC v20161118; Blanco-Cuaresma et al. 2017).

3.9 INT spectra used for radial velocities and atmospheric parameters

Spectra for J1847+39 were obtained using the intermediate dispersion spectrograph (IDS) mounted on the 2.5-m Isaac Newton telescope (INT) at the Roque de Los Muchachos Observatory. The 235-mm camera and EEV10 CCD detector was used with the H1800V grating to obtain spectra in a small region around the Hα line with R≈10,000[8]. A total of 10 spectra

[8]Calculated from http://www.ing.iac.es/

were obtained for J1847+39 with an exposure time $t_{\rm exp}$ = 600-900 s. Radial velocity measurements were extracted using cross-correlation routines provided within ISPEC. I used a synthetic F0 spectrum as a template with a mask applied to the core of the Hα line. A Gaussian function was fitted to the peak in each cross-correlation function to obtain the radial velocity measurement (the peak of the Gaussian function), and uncertainty (standard deviation of the Gaussian function). Each spectrum was corrected into a laboratory reference frame and co-added onto a common wavelength range. The relatively small wavelength range does not permit the use of maximum and median filters to normalise the spectra. I instead identified suitable continuum regions by-eye and normalised the spectrum using a second-order polynomial fit by least-squares.

3.10 Lucky imaging used to identify nearby companions

The lucky-imaging technique (e.g. Law, Mackay & Baldwin 2006) was used to obtain high-resolution images of J2308−46, J2349−32, J0055-00, J1652-19 and J2217-04 in July 2017, in order to search for stars contributing contaminating light, as well as potential bound companions to the eclipsing binaries. The observations were conducted using the Two Colour Instrument (TCI) on the Danish 1.54-m Telescope at La Silla Observatory. The TCI consists of two Electron Multiplying CCDs capable of imaging simultaneously in two passbands at a frame rate of 10 Hz, with a 40" × 40" field of view. The 'red' arm has a passband similar to a combined $i + z$ filter or the Cousins I filter, whilst the 'visible' arm has a mean wavelength close to that of the Johnson V filter. A detailed description of the instrument can be found in Skottfelt et al. (2015) and the lucky imaging reduction pipeline is described by Harpsøe et al. (2012).

The observations and data reduction were carried out using the method outlined in Evans et al. (2018), and is briefly described here. Both targets were observed for 170 s. The raw data were reduced automatically by the instrument pipeline, which performs bias and flat frame corrections, removes cosmic rays, and determines the quality of each frame, with the end product being ten sets of stacked frames, ordered by quality. The data were run through

a custom star-detection algorithm that is described in Evans et al. (2018), which is designed to detect close companion stars that may not be fully resolved.

4 Atmospheric parameters of FGK stars using wavelet analysis

Accurate measurements of temperature and composition are needed to estimate limb-darkening coefficients and the mass of the primary star. For EBLM systems discovered by WASP, these parameters are usually made with CORALIE spectra using measurements of equivalent widths and by fitting individual spectral lines (Gillon et al. 2009; Doyle et al. 2013; Doyle 2015). These methods need to allow for noise and systematic errors present in the CORALIE spectra. The sample of EBLM spectra presented in Gómez Maqueo Chew et al. (2014) typically have a signal-to-noise ratio per Ångstrom (S/N) between 3 and 7. The ongoing radial velocity campaign to study EBLMs typically yields between 10 and 40 spectra per star. Co-adding spectra can increase the S/N ($\propto \sqrt{N_{\rm obs}}$) to over 40 in some parts of the spectrum, but the regions of the spectrum near the ends of each échelle order suffer from both large photon noise and systematic errors due to inaccurate order-merging.

Wavelet decomposition has been used previously as part of methods developed for spectral analysis. Manteiga et al. (2010) used multi-level wavelet decomposition in connectionist systems (artificial neural networks) to derive fundamental stellar parameters in the low S/N domain (5-25) in preparation for spectra from the Gaia radial velocity spectrograph (RVS). This work was extended by Dafonte et al. (2016) by using a generative artificial neural network resulting in predicted uncertainties of 220 K, 0.32 dex and 0.20 dex for $T_{\rm eff}$, $\log g$ and [Fe/H], respectively for stars with a Gaia magnitude $G = 13$. Using neural networks to estimate atmospheric properties has well-known problems such as long training times and a strong dependence on the initial training set. Li et al. (2015) use wavelet decomposition in a regression framework to detect representative spectral features from a set of 30,000 SDSS spectra to estimate atmospheric parameters with better precision than those from neural network (83 K, 0.23 dex and 0.16 dex for $T_{\rm eff}$, $\log g$ and [Fe/H]).

The method in this work determines the best-fitting atmospheric parameters ($T_{\rm eff}$, $\log g$, [Fe/H] and Vsin i) for EBLM host stars by comparing a selected subset of coefficients from a wavelet decomposition to those from a grid of stellar models. This reduces systematic errors

in the estimated parameters due to poor continuum normalisation and low-quality regions of the spectrum. I introduce wavelet decomposition as it applies to a spectrum in Sect. 4.1 before reviewing my Bayesian approach to determine $T_{\rm eff}$, [Fe/H], $\log g$ and $V \sin i$ in Sect. 4.2. I show that my method converges and is self-consistent in Sect. 4.3 and test against a sample of independently analysed FGK stars in Sect. 4.4. This work in this chapter is published in Astronomy & Astrophysics (Gill, Maxted & Smalley 2018).

4.1 Wavelet decomposition theory

Analysis of spectral components at different scales can be done using a discrete wavelet transform (DWT). A DWT tiles the wavelength-scale plane by convolving a spectrum, $f(\lambda)$, with variable sized functions (Stumpe et al. 2012). These functions are called daughter wavelets, $\psi_{\rm a,b}(\lambda)$, which are created from a mother wavelet, $\psi(\lambda)$, using a shift-and-scale operation,

$$\psi_{a,b}(\lambda) = \frac{1}{\sqrt{a}}\psi(\frac{\lambda - b}{a}), \quad a, b \in \Re, a \neq 0, \tag{4.1}$$

where a is a member of the dyadic sequence,

$$a_i = 2^i, \quad i = 0, 1, 2, 3, ..., n \tag{4.2}$$

and $b = kb_0$, where k is an integer and b_0 is chosen to ensure the recovery of $f(\lambda)$. By employing a DWT, the appropriate values of b are selected to minimise overlap between wavelet convolutions. Following the notation in chapter 8 of Olkkonen (2011), a discrete wavelet transform can be calculated for each dyadic scale (i) and displacement (k):

$$WT_{f(\lambda)}(i,k) = \frac{1}{\sqrt{2^i}} \int f(\lambda)\overline{\psi\left(\frac{\lambda - k2^i b_0}{2^i}\right)}d\lambda = f(\lambda), \psi_{i,k}(\lambda). \tag{4.3}$$

The likeness of a wavelet, $\psi_{i,k}$, to a section of the spectrum is given by the wavelet coefficient $WT_{f(\lambda)}(i,k)$ from Eq. (4.3). Performing this calculation over the series of dyadic scales and displacements yields wavelet coefficients which represent different sized structures at different wavelengths. I split coefficients into bands with constant scales, $\{WT_{f(\lambda)}(0,b)\}_k$,

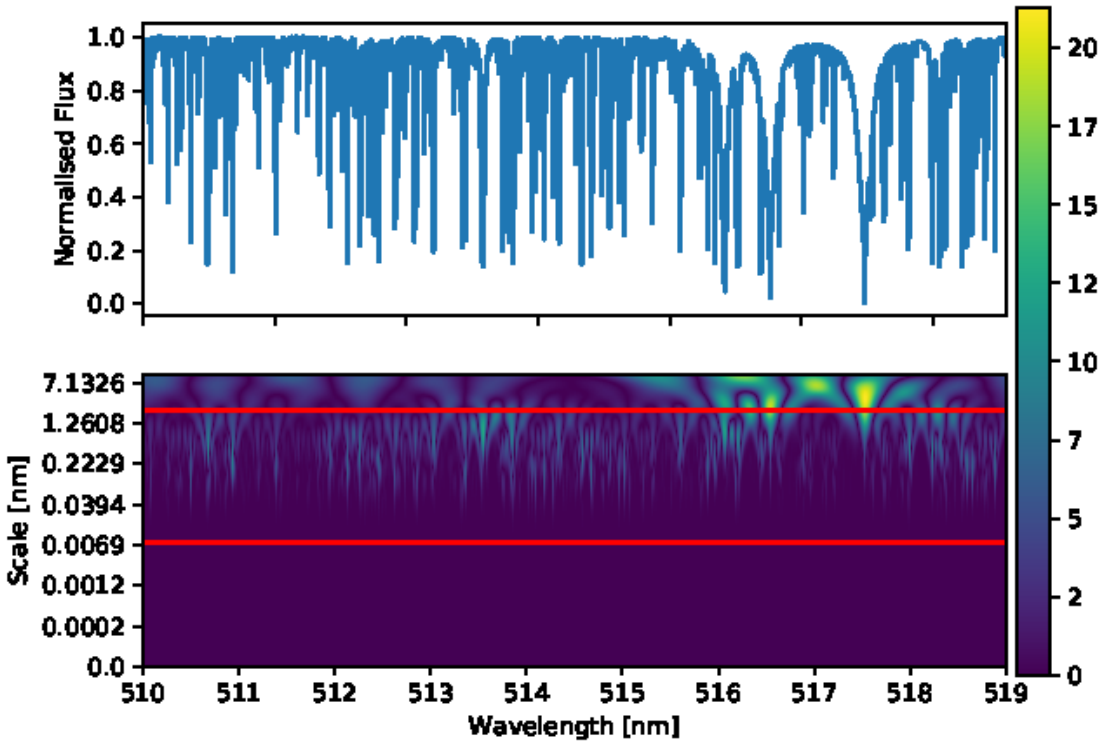

Figure 4.1: The power Hövmoller of wavelet coefficients (lower panel) for a region around the Mg triplet for WASP-19 (upper panel). There is significant power ($|WT_{i,k}|$ from Eq. 4.3) for scales ∼1 nm in the region of the Mg lines corresponding the wavelets likeness to spectral features. Horizontal red lines represent the scales 0.012 – 3.125 nm.

which represent the likeness of a single scale across the entire spectrum. The power of each scale, $\{WT_{f(\lambda)}(i,b)\}_k^2$, can be visualised in a power Hövmoller (one value of i per row) in Fig. 4.1. Bands of coefficients which correspond to noise and low-order continuum artefacts (such as merged échelle orders) can then be excluded. A filtered spectrum may be reconstructed with an inverse DWT (IDWT):

$$f(\lambda) = \sum_{i=-\infty}^{\infty} 2^{\frac{-3i}{2}} \int WT_{f(\lambda)}(i,k)\hat{\psi}\left(\frac{\lambda - b}{2^i}\right) db, \tag{4.4}$$

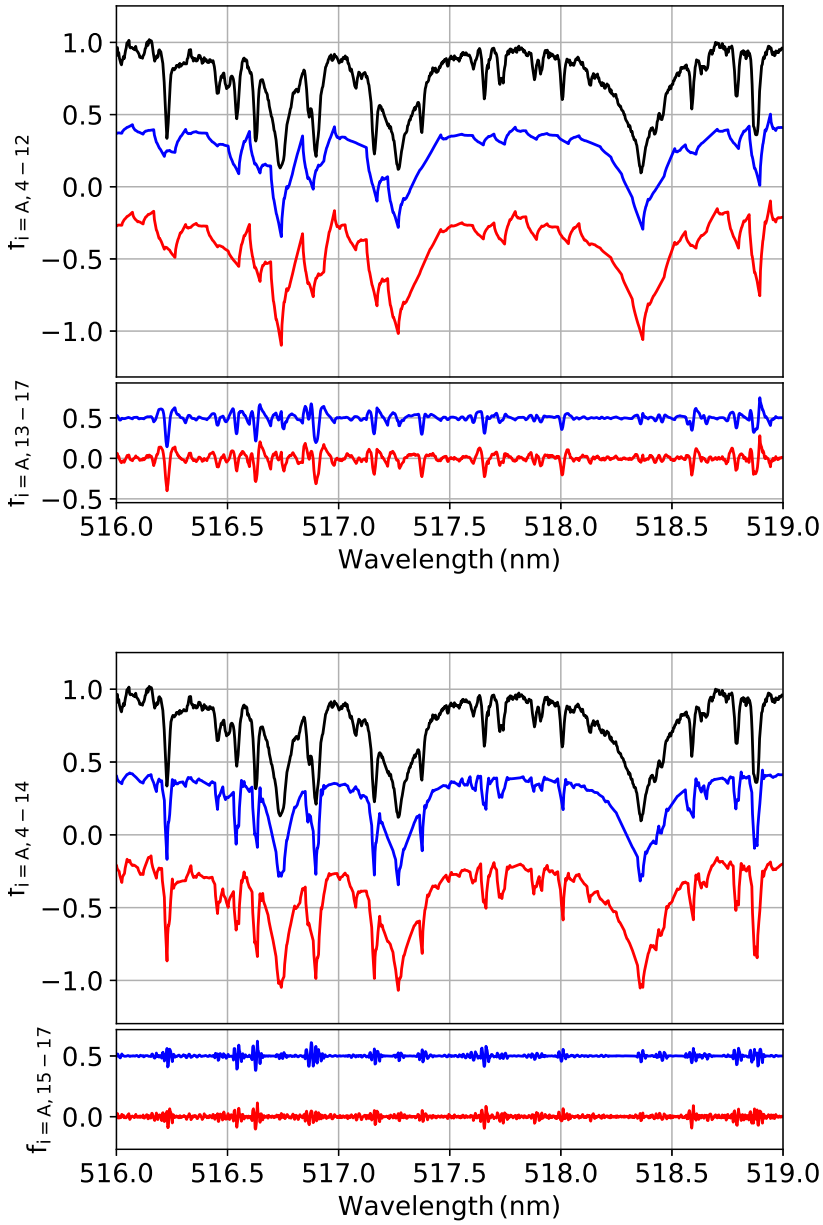

Figure 4.2: The reconstruction of spectra using Eq. (4.4) for subsets of wavelet coefficients. (Left panel - top) Raw spectra for WASP-19 (black) and the flux reconstruction using wavelet coefficients from bands i = 4-12 using the raw spectrum (blue; offset −0.6) and the best fitting model for WASP-19 (red; offset −1.2). (Left panel - bottom) The reconstruction of the best-fitting model for WASP-19 (red) and the raw spectrum (blue; offset +0.5) using coefficients i = 13-17. (Right panel) As in the left panel except with reconstructions using coefficients i = 4-14 (top) and coefficients i = 15-17 (bottom).

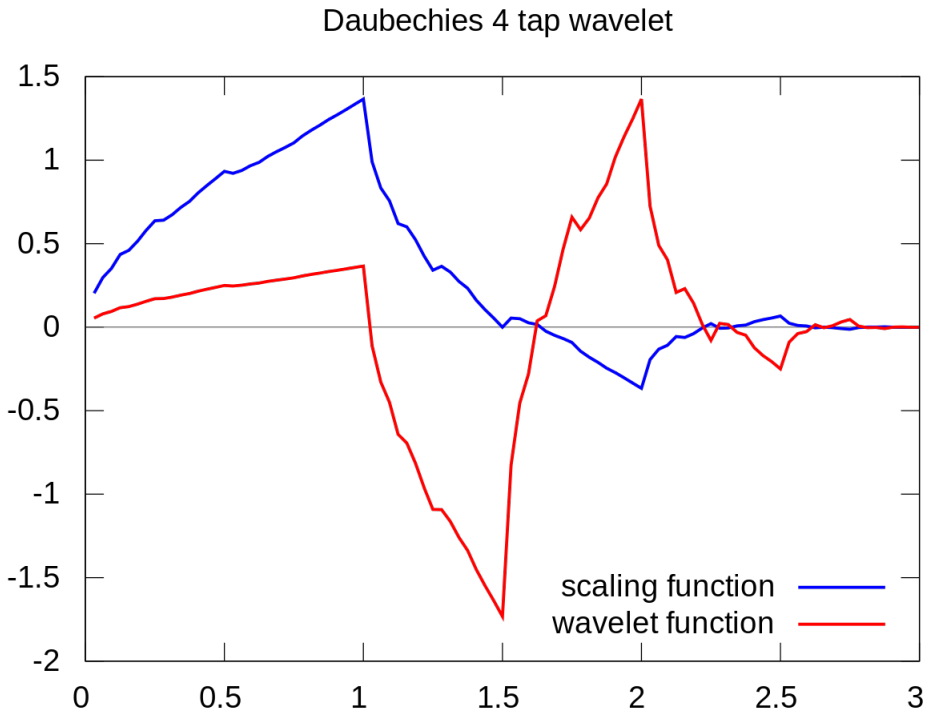

Figure 4.3: Scaling and wavelet function for a Daubechies-4 wavelet. Image take from en.wikipedia.org (accessed 7/1/2019).

where

$$\hat{\psi}\left(\frac{\lambda - b}{2^i}\right) = \frac{\psi\left(\frac{\lambda - b}{2^i}\right)}{\sum_{i=0}^{i=n} |\psi(\lambda - b)|^2}. \tag{4.5}$$

The process of reconstructing a spectrum using a subset of wavelet coefficients is called wavelet filtering and is analogous with Fourier filtering. Alternatively, the subset of coefficients may be chosen to meet a threshold criteria (i.e. $\left[WT_{f(\lambda)}(i,k)\right]^2 \geq 0.01$) which eliminates information that has little contribution to a signal; this is called wavelet compression.

I do not require Eq. (4.4) to determine atmospheric parameters as I perform a χ^2 fit using a subset of coefficients from Eq. (4.3) to those from a grid of models (see Sect. 4.2). I also do not apply any threshold criterion. The nominal resolving power of the CORALIE spectrograph is R=55 000, so at least 2^{16} values are required to sample a spectrum over the wavelength range 450-650nm. I decided to use 2^{17} values for the wavelet decomposition to

ensure no loss of information and to give us more choice in the number of wavelet bands used in my analysis. I used Eq. (4.3) to obtain wavelet coefficients which have information on scales in the range 0.003 nm–200 nm. My wavelet method only uses a subset of i values. To select these, I constructed power Hövmoller diagrams (similar to Fig. 1) for a variety of regions between 450 nm and 650 nm, for different co-added spectra in my sample. I found that power associated with line absorption lies in the range 0.04–4 nm, with larger scales typically corresponding to systematic trends and shorter scales with noise. This corresponds to values of i=4–12 (0.048–3.125 nm). The application of Eq. (4.4) to the two subsets of coefficients (4–12 and 13–17) is shown in the top panel of Fig. 4.2. I found that the subset range $i = 4 - 12$ is too restrictive to reproduce short-scale information (e.g. weak lines) and so I decide to extend this range to $i = 4 - 14$ (0.012–3.125 nm; lower panel of Fig. 4.2) which better represents the boundary between noise and weak lines. I do not show the reconstruction of subset $i = 0 - 3$ in Fig. 4.2 as using only 16 coefficients to reconstruct a spectrum leads to a large Daubechies-4 wavelet (red line in Fig. 4.3) with some sub-structure.

I demonstrate the sensitivity of wavelet coefficients to atmospheric parameters in Fig. 4.4 for wavelet coefficients in the range $i = 11 - 12$ (0.04 − 0.09 nm). I see a slow variation of some wavelet coefficients which corresponds to changes in individual spectral line geometries as each parameter changes. One thing to note is the sensitivity of each parameter; $T_{\rm eff}$ varies the most, followed by $V \sin i$ and [Fe/H]. Surface gravity is the least varying parameter in wavelet space and is dominated by a few lines sensitive to $\log g$. As $V \sin i$ increases, I see positive and negative structures form and become stronger at higher $V \sin i$ values. This is likely to be a continuum effect as weaker lines are smeared out to average a lower continuum whilst stronger lines persist.

The choice of mother wavelet depends on the objective of the work. A Daubechies-4 wavelet performs well for frequency identification and is widely used in signal processing and data compression (Belmon et al. 2002). A Haar wavelet, with a more step-like structure, is more suited to identifying discontinuity and is widely used in computer-vision projects (e.g. Essaouabi, Regragui & Ibnelhaj 2009). I investigated the effects of wavelet choice on the determined atmospheric parameters in Sect. 4.5.1, but proceeded with the Daubechies (k=4) wavelet for the rest of this work.

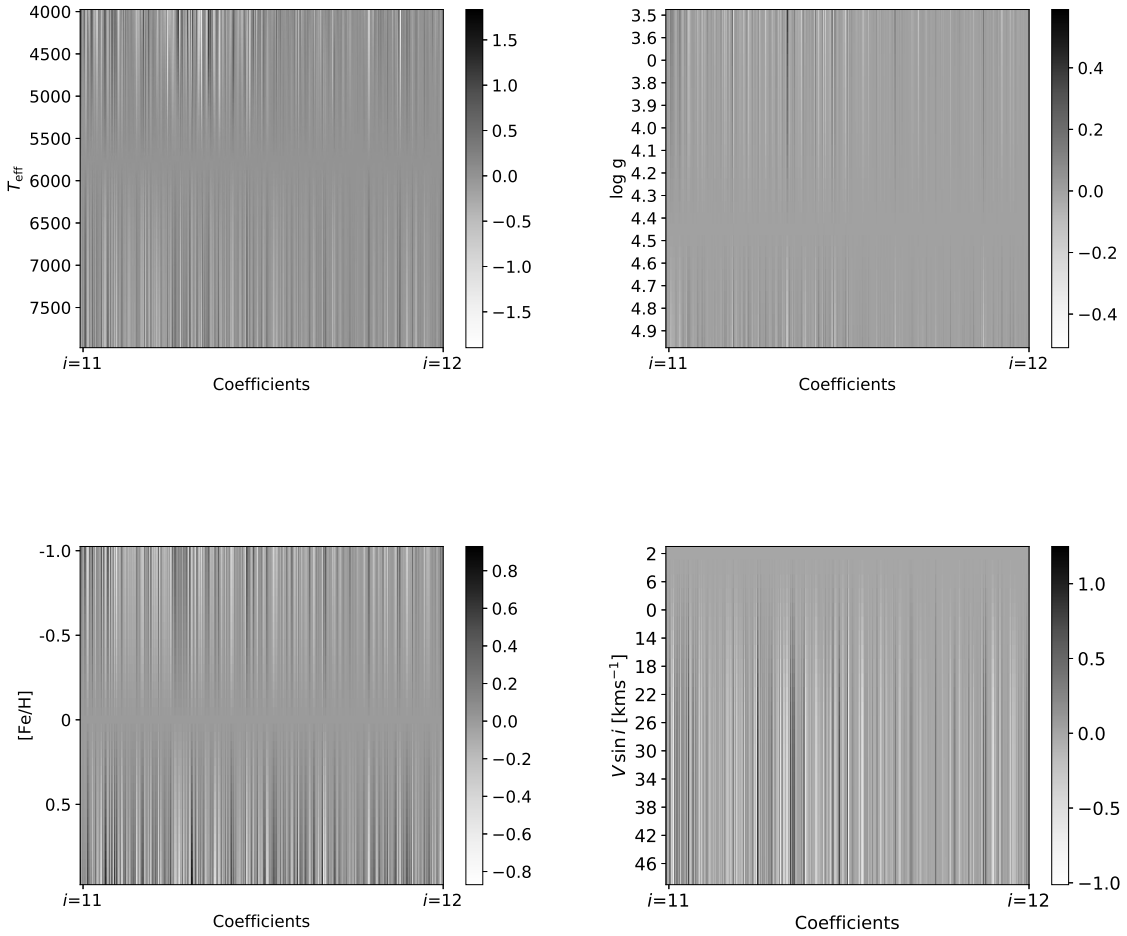

Figure 4.4: Changes in wavelet coefficients in the range $i = 11 - 12$ for model spectra as a function of atmospheric parameters. The wavelet coefficient from a solar model has been subtracted to emphasise the subtle change in wavelet coefficients for each parameter. A similar result is seen for other values of i between 4 and 14. The colour-bar indicates the magnitude of the difference of coefficients. We note that these bars are not on the same scale and highlight the wavelet response to each coefficient.

4.2 Bayesian measurements

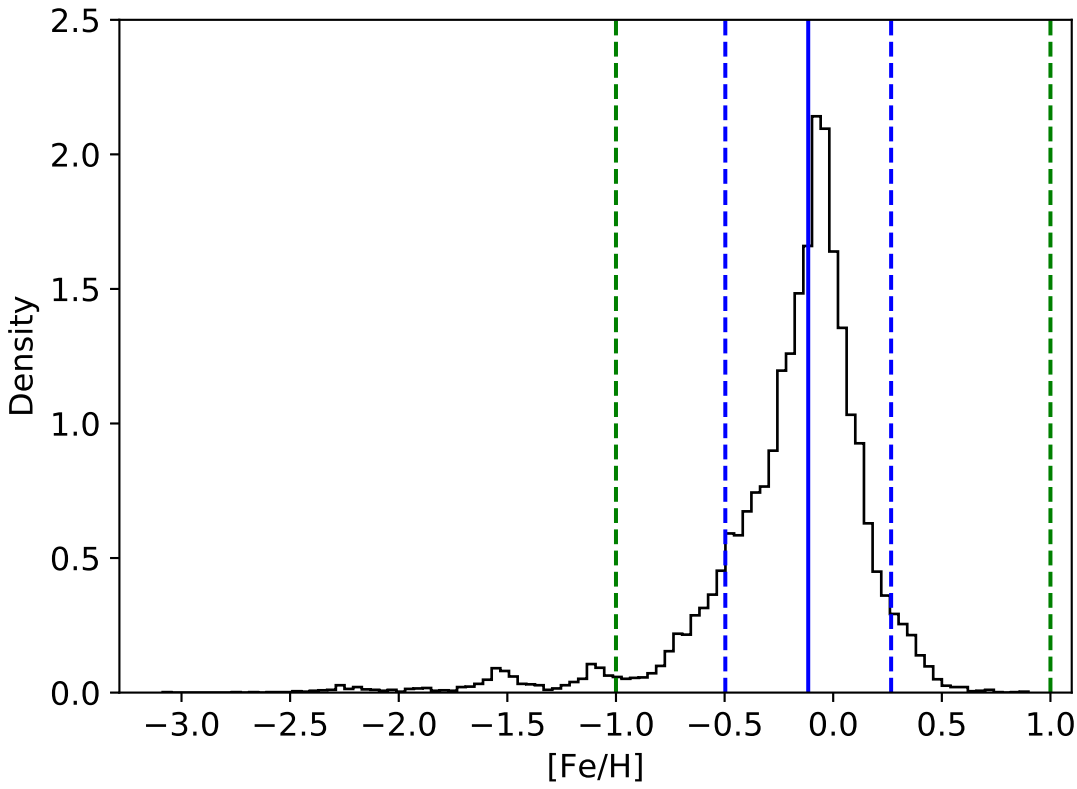

Figure 4.5: Histogram of 14,681 [Fe/H] measurements for stars from Gaia-ESO data release 3 (Smiljanic et al. 2014). Plotted is the median value of [Fe/H] (solid blue), with 1σ from the median (dashed blue). The grid range used is enclosed by the dashed green lines.

I used the Markov chain Monte Carlo method to determine the posterior probability distribution for $T_{\rm eff}$, $\log g$, $V \sin i$ and [Fe/H] given an observed spectrum. My method is a global χ^2 fitting routine which compares subsets of wavelet coefficients ($i = 4 - 14$) to those from a pre-synthesised grid of spectra. My grid was synthesised with the radiative transfer code SPECTRUM (Gray & Corbally 1994) using MARCS model atmospheres (Gustafsson

et al. 2008), and version 5 of the GES (GAIA ESO survey) atomic line list provided within ISPEC (Blanco-Cuaresma et al. 2016) with solar abundances from Asplund et al. (2009). I computed models spanning 450nm–650nm over a temperature range of 4000 to 8000 K in steps of 250K, −1 to +1 dex in steps of 0.5 dex for [Fe/H] and 3.5 to 5 dex in steps of 0.5 for $\log g$. I selected the range of [Fe/H] by looking at composition measurements of over 14,000 FGK stars from Gaia-ESO Survey data release 3 (Fig. 4.5; Smiljanic et al. 2014). I found that 96% of stars with measurements of composition had [Fe/H] in the range −1 to 1 dex. This range in [Fe/H] is also much larger than the full range in [Fe/H] for the benchmark sample described in Sect. 4.4.

Spectra in the grid are calculated with zero instrumental, rotational, or macroturbulence broadening. These are accounted for in post-processing by convolving the grid spectra with the appropriate kernels. In this work, I allow $V \sin i$ to have values in the range 0 - 50 km s^{-1}. The upper limit of 50 km s^{-1} would need to be extended for hotter stars beyond the Kraft break[1] (Kraft 1967), but is suitable for this work on late-type stars. Macroturbulence are estimated using Eq. (5.10) from Doyle (2015) and microturbulence was accounted for at the synthesis stage using Eq. (3.1) from the same source. Spectra in-between grid points are extracted by trilinear interpolation, broadened to the desired value of $V \sin i$ and macroturbulence, and then convolved with a Gaussian to account for instrumental broadening. For the self-consistency tests in Sect. 4.3 instrumental broadening was ignored, but for the CORALIE spectra in Sect. 4.4 I used an instrumental resolving power $R = 55,000$ (Queloz et al. 2001b; Doyle 2015). I then re-sample between 450 and 650 nm with 2^{17} values (the same as the observed spectrum) and apply Eq. (4.3) to obtain the wavelet coefficients $WT_{f(\lambda)}(4-14, k)$ for the model spectra.

The subset of wavelet coefficients from the interpolated model, $WT_{\mathbf{m}}$, are compared to those from the data, $WT_{\mathbf{d}}$, in the following Bayesian framework: the probability of observing a spectrum for a given model is given by $\mathrm{p}(\mathbf{m}|\mathbf{d}) \propto \mathcal{L}(\mathbf{d}|\mathbf{m})\mathrm{p}(\mathbf{m})$. The vector of model parameters is given by $\mathbf{m} = (\mathrm{T_{eff}}, [\mathrm{Fe/H}], \log \mathrm{g}, \mathrm{V} \sin \mathrm{i})$ and I assume uniform prior

[1] An abrupt reduction in a stars surface rotation for stars with effective temperatures below 6200 K due to the presence of a efficient magnetic dynamo which transfers angular momentum from the star through stellar winds.

probability for the model parameters within the grid range. I used the likelihood function $\mathcal{L}(\mathbf{d}|\mathbf{m}) = \exp(-\chi^2/2)$ where

$$\chi^2 = \frac{(WT_{\mathbf{d}} - WT_{\mathbf{m}})^2}{\sigma^2_{WT_{\mathbf{d}}}}, \tag{4.6}$$

and

$$\sigma^2_{WT_{\mathbf{d}}} = \beta\sigma^2_{MC}. \tag{4.7}$$

The term σ^2_{MC} was calculated by generating 1000 spectra from the co-added spectrum with noise generated from a standard normal distribution centred around $f(\lambda)$ and with σ equal to the standard deviation of the spectrum, $\sigma_{f(\lambda)}$ (calculated from the standard deviation in co-added spectra). The blaze function is corrected prior to co-addition of the spectra and so deviations in blaze functions will result in uncertainties propagating through to $\sigma_{f(\lambda)}$, and σ^2_{MC}, effectively down-weighting regions with poor blaze corrections. The free parameter β has been introduced to account for additional noise, incomplete atomic data, deviations from solar metallicity scaling, lines which form under non-local thermodynamic equilibrium, and other unaccounted errors. In principle, I could have used stellar models or empirical relations to set priors on these atmospheric parameters but decided not to do this for two reasons. Firstly, allowing the MCMC sampler to explore regions with a-priori low probability gives a better indication of the reliability of my method than using a more constrained solution. Secondly, by imposing a prior from stellar models or empirical relations based on normal stars we may fail to identify interesting examples of anomalous stars in my sample, for example, helium-rich stars. I sample the model parameter space using the Markov chain Monte Carlo method, implemented by the python package EMCEE (Foreman-Mackey et al. 2013). EMCEE uses affine-invariant ensemble sampling (parallel stretch move algorithm; Goodman 2010) to split Markov chains into sub-groups and update the position of a chain using the positions of chains in the other subgroups. The algorithm's affine-invariance can cope with skewed probability distributions and generally has shorter autocorrelation times than a classic Metropolis-Hastings algorithm.

I generate 12 Markov chains of 20,000 draws each to converge on the best atmospheric

Table 4.1: The recovery of atmospheric parameters using the wavelet method for two groups of 256 spectra: one group with no priors on $\log g$ and another with priors imposed from transit photometry. The difference between the value measured by the wavelet method and the input value used to interpolate the spectrum ($x_{out} - x_{in}$) were used to calculate the standard deviation, σ, and mean offset, μ.

	Prior on $\log g$?	σ	μ
$T_{\rm eff}$ (K)	no	46.0	-3.2
	yes	3.1	0.2
[Fe/H] (dex)	no	0.040	-0.003
	yes	0.020	-0.001
$V \sin i$ (kms^{-1})	no	0.47	0.05
	yes	0.17	-0.06
$\log g$ (dex)	no	0.060	-0.002
	yes	0.020	0.001

parameters. I found that the chains converged before the 5000^{th} draw, but as a precaution I discarded the first 10,000 draws. I take the median values of the model parameters in the remaining draws to determine the atmospheric parameters for a spectrum. An example posterior probability distribution for WASP-20 is plotted in Fig. 4.6. The parameter space is almost symmetric with small degeneracies between $T_{\rm eff}$, [Fe/H] and $\log g$. I note that the precision of the parameters determined from the standard deviation of each parameter in the Markov Chain is typically an underestimate of the true precision of these parameters because it does not account for systematic errors in the data or the models.

4.3 Self consistency

I have assessed the ability of my method to recover atmospheric parameters from synthetic spectra in order to check that my results are self consistent. I interpolated 512 spectra with random values of $T_{\rm eff}$, [Fe/H], $\log g$ and $V \sin i$ selected within the limits of my grid of models. Each spectrum was then re-sampled to have 2^{17} values in the range 450–650 nm to match

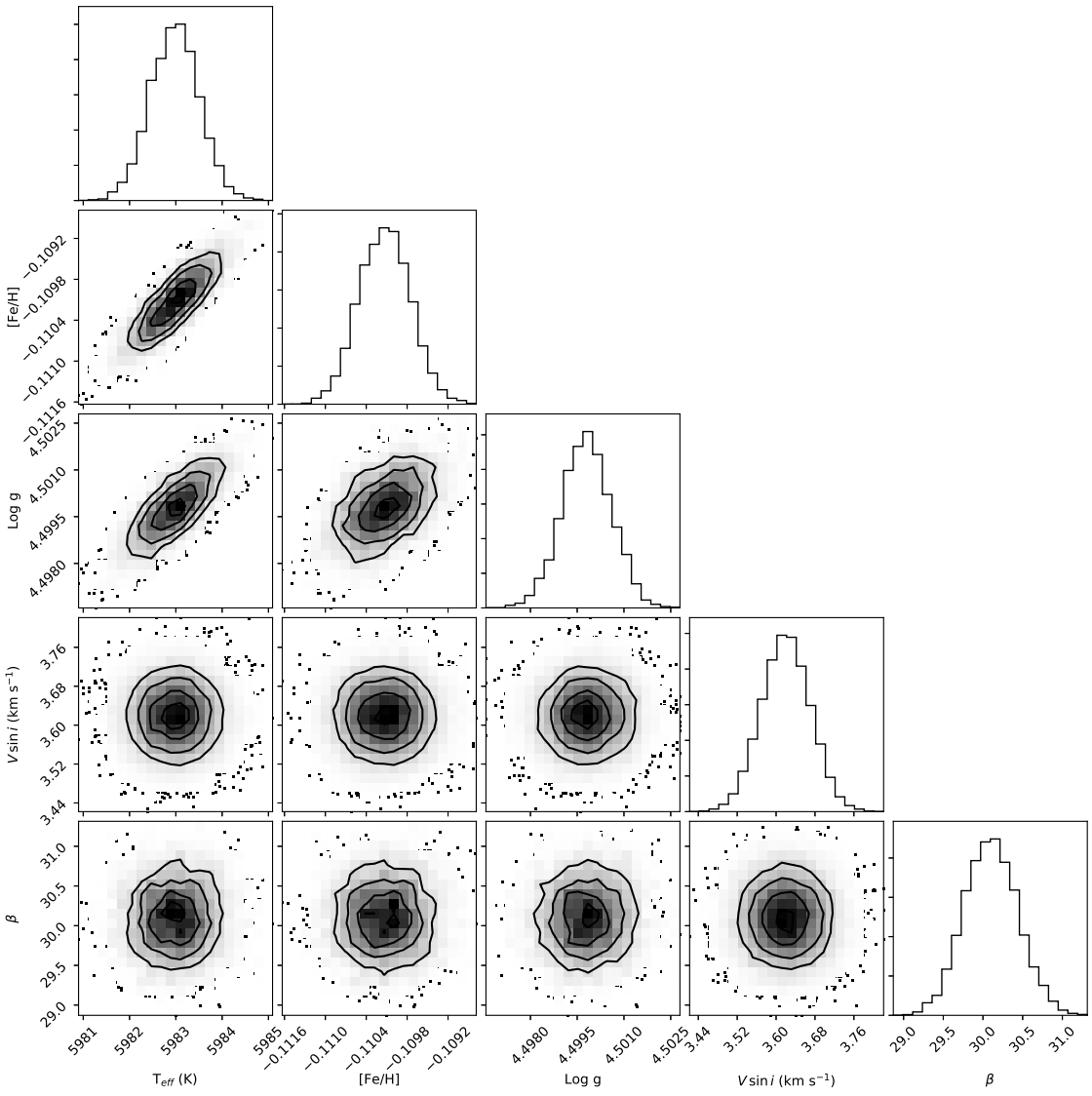

Figure 4.6: Posterior probability distributions for WASP-20.

my choice of coefficients in Sect. 4.1 and the benchmark sample in Sect. 4.4. These spectra were split into two groups and analysed with the aforementioned method. The first group had $\log g$ as a free parameter to probe for any systematics, for the second group I imposed a prior on $\log g$ to simulate the effect of well constrained surface gravity measurement from

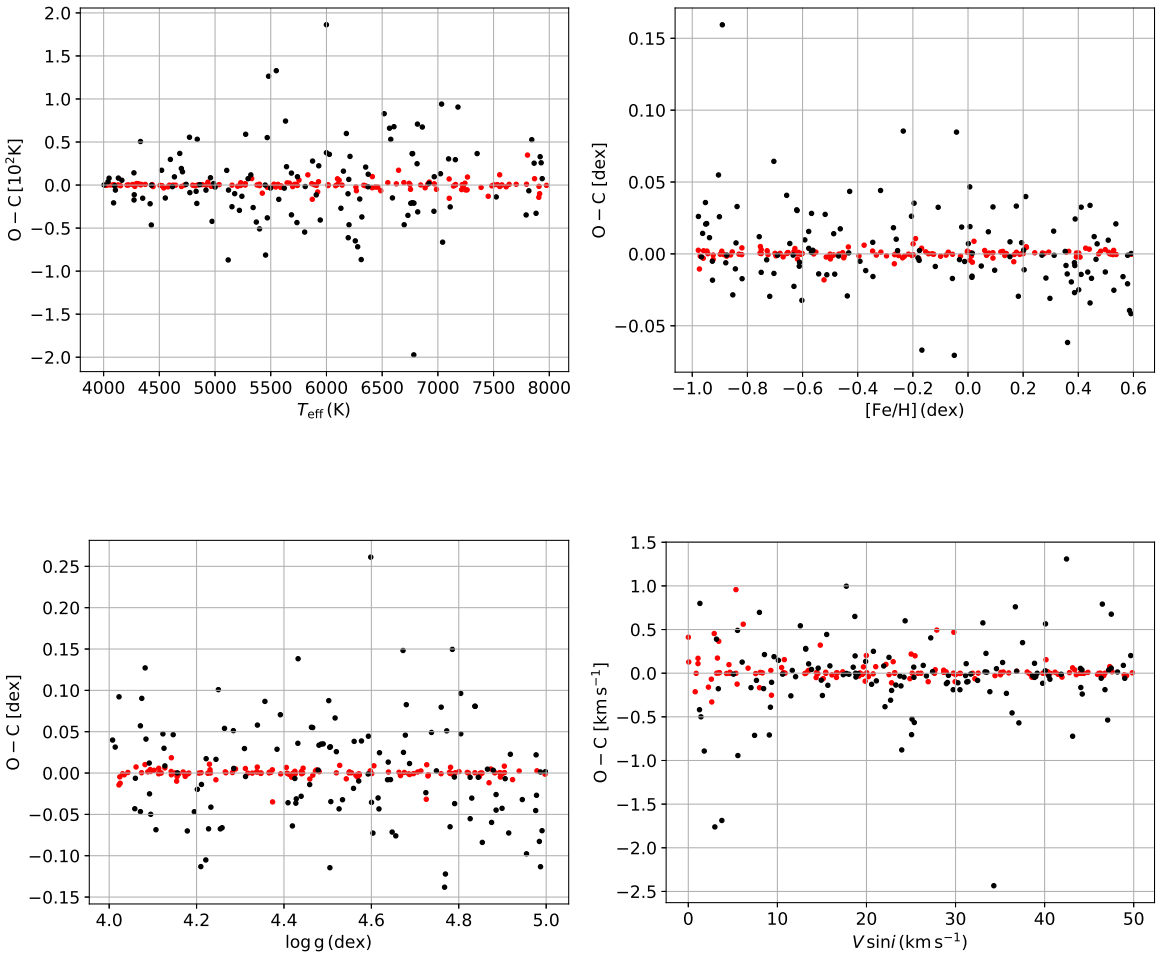

Figure 4.7: Differences between wavelet-determined atmospheric parameters and those used to synthesise spectra with all parameters free (black) and with priors on $\log g$ (red).

transit photometry. The $\log g$ prior probability distribution was assumed to be Gaussian with a mean $\log g$ value equal to the value used to interpolate the spectrum and a dispersion equal to the average uncertainty of transit $\log g$ values from Mortier et al. (2013) (hereafter referred to as M13) for 44 WASP exoplanet hosts ($\overline{\sigma_{\log g}} = 0.02$ dex). I decided not to add Gaussian noise to these spectra as noise profiles depend upon stellar parameters and instrumental conditions; this is assessed in Sect. 4.5.4. I found typical autocorrelation lengths are below 1000 steps for all parameters in the first chain and 12 chains in the second run typically produce an acceptance fraction between ~ 0.25 and 0.3.

The recovery of atmospheric parameters for both groups is shown in Fig. 4.7 and summarised in Table 4.1. I found that all parameters are recovered well across the range of my grid. With no constraints on $\log g$, there were only two measurements of $T_{\rm eff}$ that deviated from the input value by more than 150 K. A prior on $\log g$ significantly decreases the difference between measured and input atmospheric parameters and shows that my method is sensitive to $\log g$. There is a small increase in residual scatter for measurements of $V \sin i$ when the interpolated value of $V \sin i$ below $0.5\,{\rm km\,s^{-1}}$; this is seen in both groups and marginally improved with a prior on $\log g$. This is expected as the resolution of the broadening kernel in combination with the edge of parameter space makes it difficult to determine low $V \sin i$ values. The internal precision associated with the wavelet method is remarkably high; by taking 1σ values from the cumulative probability distributions I found precisions around 15 K, 0.01 dex, 0.02 dex, and $0.15\,{\rm km\,s^{-1}}$ for $T_{\rm eff}$, [Fe/H], $\log g$, and $V \sin i$ respectively. More realistic uncertainties are determined in the following sections.

I also assessed the sensitivity of my method by determining the atmospheric parameters of 9 spectra from a discrete set of grid points with different combinations of fixed parameters. I interpolate 96 spectra from the following grid points – 4800 K, 5800 K and 6500 K for $T_{\rm eff}$; -0.5, 0.0 and 0.5 dex for [Fe/H]; 3.75, 4.40 and 4.80 dex for $\log g$; 5, 10 and $15\,{\rm km\,s^{-1}}$ for $V \sin i$. In total, I determined the atmospheric parameters for each spectrum 15 times with the wavelet method using every combination of free and fixed parameters (see Fig. 4.8). I found that constraining one or more parameters increases the internal precision of the wavelet method significantly. A slight degeneracy exists between $T_{\rm eff}$ and $\log g$ resulting in a modest scatter when both parameters are left free. This also highlights the numerical

noise introduced by starting walkers at different positions, since walkers explore parameter space by random jumps which may never reach the correct solution, despite prior knowledge that an exact solution lies somewhere within the grid.

4.4 Benchmark sample

Table 4.2: My benchmark sample of FGK stars from D15. I include the V magnitude, the number of spectra and the S/N of the coadded spectra at 500 nm.

Star	V mag	# of spectra	S/N (~500 nm)
WASP-4	12.50	12	37
WASP-5	12.30	11	35
WASP-6	11.90	30	63
WASP-7	9.50	13	124
WASP-8	9.79	21	137
WASP-15	11.00	15	83
WASP-16	11.30	19	77
WASP-17	11.60	42	71
WASP-18	9.30	5	119
WASP-19	12.59	28	50
WASP-20	10.68	58	153
WASP-22	12.00	29	63
WASP-23	12.68	38	53
WASP-24	11.31	18	53
WASP-29	11.30	14	57
WASP-30	11.90	47	27
WASP-31	11.70	35	53
WASP-53	12.19	35	40
WASP-69	9.88	21	136
WASP-80	11.90	37	51

Any spectral analysis technique must be tested against stars with high-quality measurements. For this I used stars from Doyle et al. (2013) and (Doyle 2015; D15, hereafter).

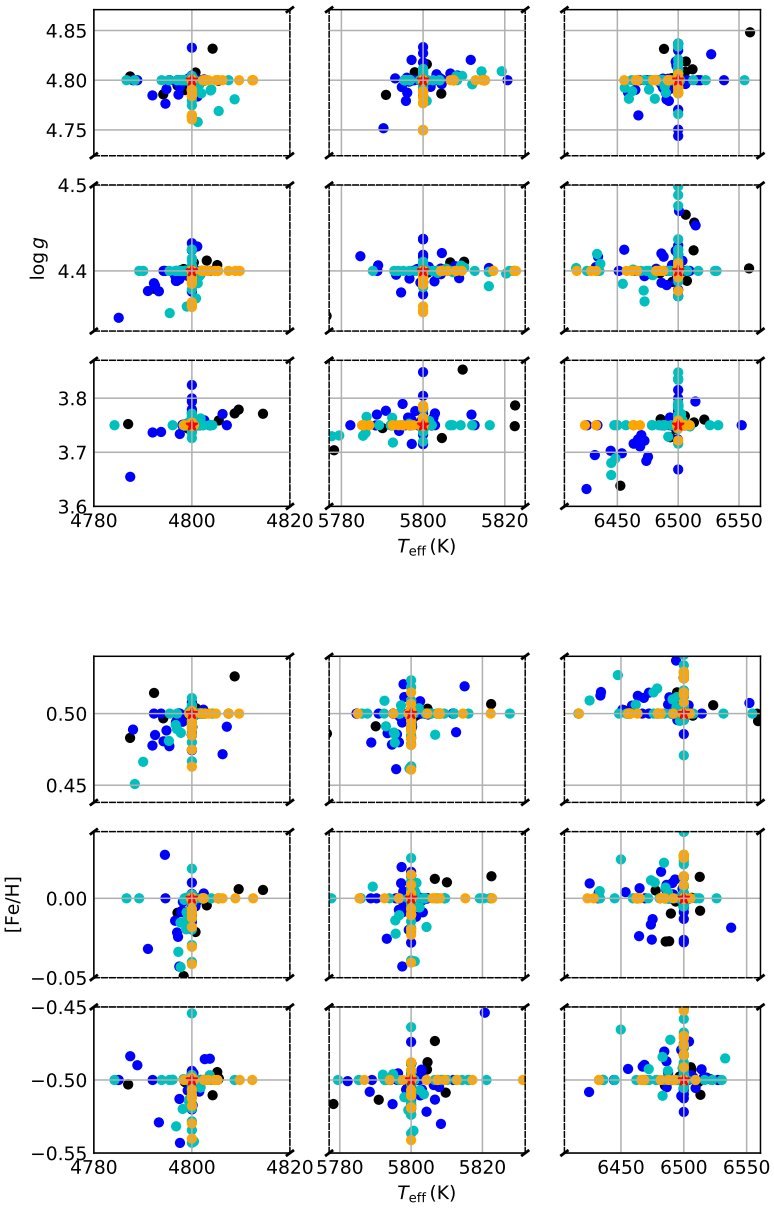

Figure 4.8: Difference between atmospheric parameters determined by the wavelet method for 9 synthetic spectra when some parameters are fixed. I plot atmospheric parameters determined with with all parameters free ($T_{\rm eff}$, [Fe/H], $\log g$, $V \sin i$) in black; with one parameter fixed in blue; with two parameters fixed in cyan; three parameters fixed in orange.

Table 4.3: Recovery of atmospheric parameters for 20 FGK stars from D15: one group with no priors on $\log g$ and another with priors from transit photometry. The difference between the value measured by the wavelet method and D15 ($x_{wavelet} - x_{D15}$) are used to calculate the mean dispersion, σ, and mean offset μ.

	Prior on $\log g$?	σ	μ
$T_{\rm eff}$ (K)	no	85.00	31.00
	yes	86.00	14.00
[Fe/H] (dex)	no	0.06	− 0.15
	yes	0.10	− 0.18
$V \sin i$ (kms^{-1})	no	1.35	− 0.79
	yes	0.62	− 1.33
$\log g$ (dex)	no	0.13	0.08
	yes	0.14	0.05

Notes. Values of σ and μ for $V \sin i$ excluded stars where macroturbulence, ξ_t, was set to $0\,{\rm km\,s^{-1}}$.

The D15 sample consists of 24 stars analysed by measurements of EW and spectral fitting of high-S/N and high-resolution (R $= 112,000$) data from the HARPS spectrograph (Queloz et al. 2001b). I used lower-quality observations from the CORALIE spectrograph to determine $T_{\rm eff}$, [Fe/H], $\log g$ and $V \sin i$ of the same stars with the wavelet method. Only 22 stars in the D15 sample have CORALIE spectra available to use and I further exclude WASP-77A and the close (3") B-component as both are un-resolved in the CORALIE fibre. This leaves a sample of 20 stars for use to calibrate my method (see Table 4.2).

4.5 Results

The wavelet method was then applied to each spectrum twice: once with no priors on $\log g$ and a second time with priors given by transit photometry. The priors on $\log g$ were set to those from M13 if quoted, or the relevant discovery papers otherwise (see Table 4.3). The results can be seen in Fig. 4.9 and are summarised in Tables 4.3 and 4.4. My method

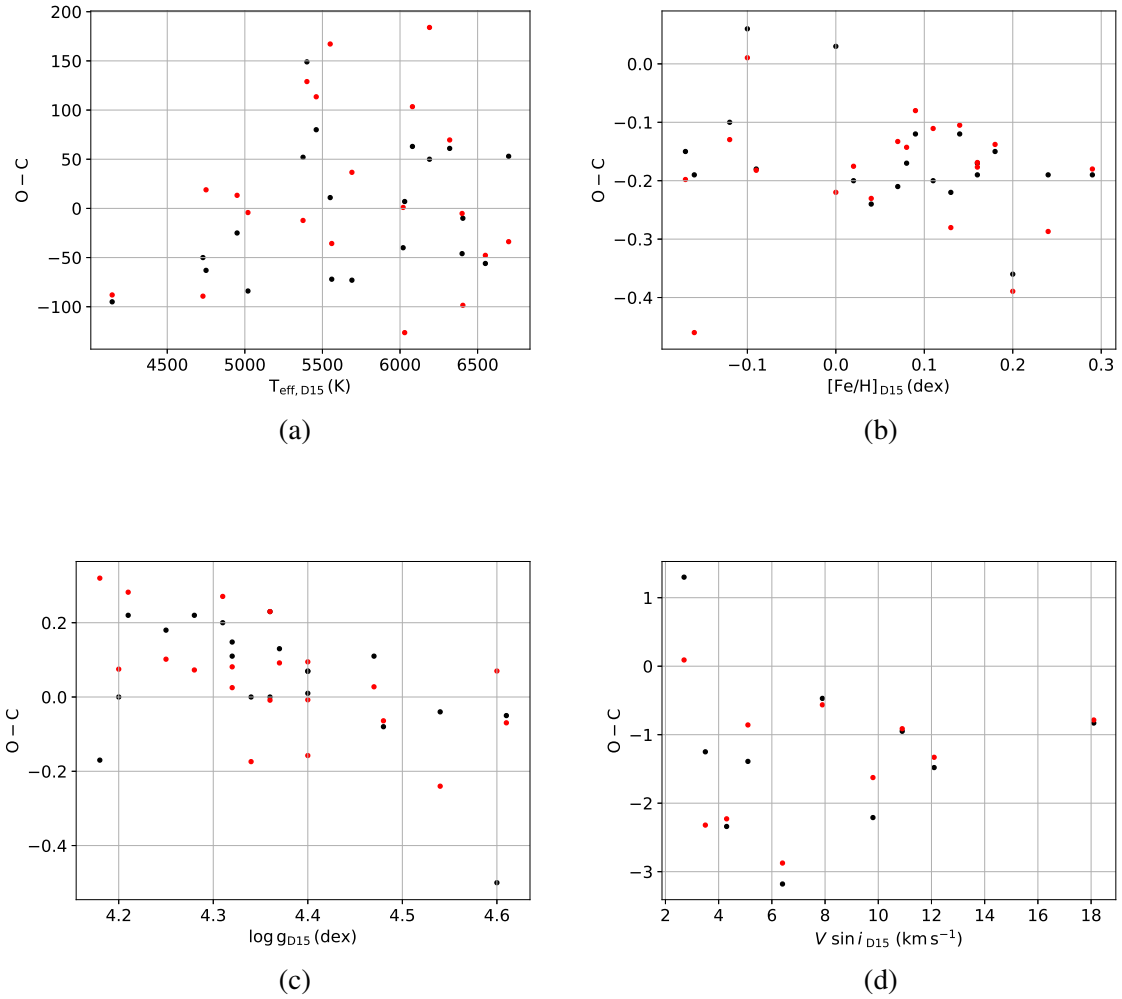

Figure 4.9: Difference between wavelet analysis and D15 (O-C) for each atmospheric parameter in the D15 sample. Each spectrum was measured twice, once with $\log g$ as a free parameter (black) and again with $\log g$ priors imposed from transit photometry (red). I exclude measurements of $V \sin i$ where macroturbulence, ξ_t, was set to 0 km s^{-1} to ensure a best model was converged upon.

determines $T_{\rm eff}$ to within 220 K of the value found by D15. My measurements of [Fe/H] are systematically offset by approximately − 0.18 dex from those of D15; this is discussed further in Sect. 4.5.1. It is difficult to constrain $\log g$ spectroscopically and my measurements often differ from those of D15 by up to 0.5 dex. My measurements of $V \sin i$ converge to $0\,{\rm km\,s^{-1}}$ for seven stars in the sample due to an over estimation of v_{mac} or instrumental resolution. To mitigate this problem I repeated the analysis with $v_{mac} = 0\,{\rm km\,s^{-1}}$. This allowed these stars to converge on best fitting models without pushing against the edge of parameter space. These stars are marked with an asterisk in Table 4.4.

I found no benefit by using priors on $\log g$. In most cases the use of $\log g$ priors increases the standard deviation in differences between atmospheric parameters from my method and published values. I investigated the level of agreement between spectroscopic values of $\log g$ from EW measurements (D15), $\log g$ from the wavelet method and those from transit photometry. Photometric surface gravity is typically measured to better precision than its spectroscopic counterpart, but relies on stellar models and correct limb-darkening parameters which in-turn rely on a constrained effective temperature, composition, and surface gravity. Recent work suggests a disagreement between spectroscopic and photometric $\log g$ which is correlated with $T_{\rm eff}$ (see Fig. 4 from Doyle et al. 2017). I compare the difference between spectroscopic and photometric $\log g$ measurements in Fig. 4.10. I found a statistically significant negative correlation (p-value $\leq 10^{-5}$) between $\Delta \log g$ ($\log g_{\rm photometry} - \log g_{\rm wavelet}$) with $T_{\rm eff}$ from my method. The origin of this is unclear, but a similar trend is seen between spectroscopic and asteroseismic measurements (Fig. 6 of Mortier et al. 2014) which suggests to us that this is a problem to spectral analysis of late-type stars using plane-parallel non-LTE model atmospheres. For a few stars, I relaxed the $\log g$ prior to have a standard deviation of 0.2 dex (instead of 0.02 dex) and found almost no difference between these solutions and those with a uniform prior on $\log g$.

In Fig. 4.11 I assessed the Hα region for the model predicted from D15 and this work for the highest-quality spectrum in my sample, WASP-20, with S/N = 150. The results from D15 were obtained using a custom line list, whereas I used version 5 of the GES atomic line list provided with ISPEC to synthesise the D15 model of WASP-20 using atmospheric parameters, $v_{\rm mac}$ and v_{mic} from D15. I found both models agree well with the data, with the

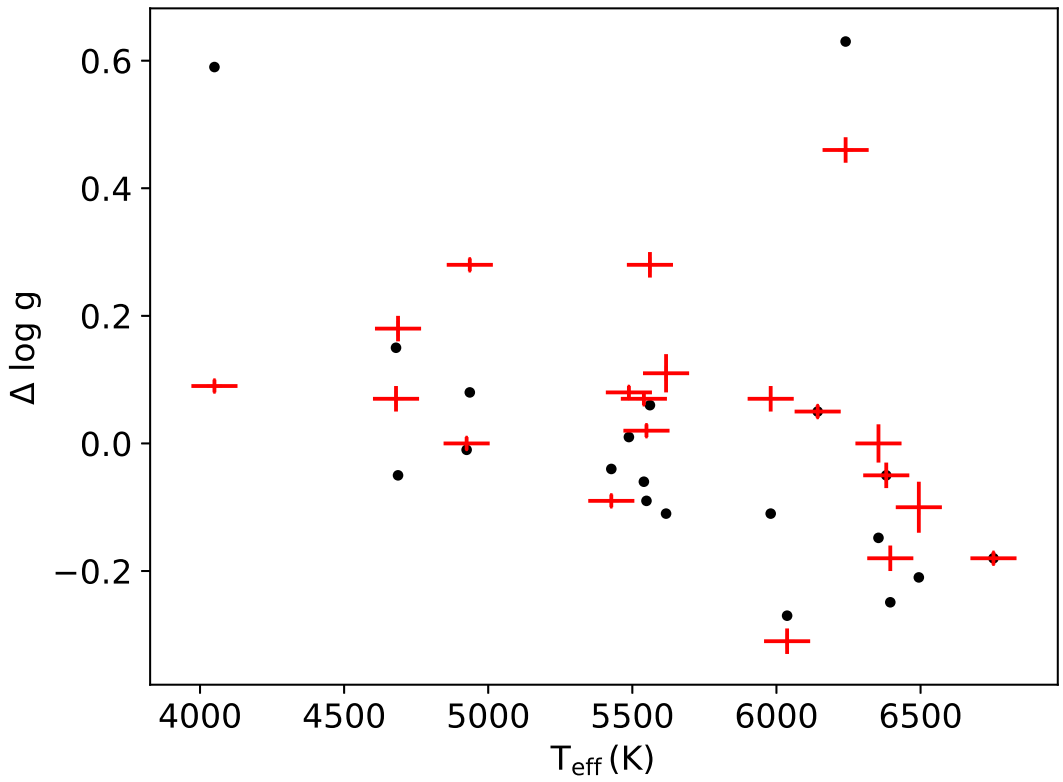

Figure 4.10: The difference between spectroscopic $\log g$ and photometric $\log g$ ($\log g_{ph}$ - $\log g_{sp}$) correlated with $T_{eff,wavelet}$ from this work (black) and from D15 (red).

left wing fitting best and a underestimation in the right wing. The discrepancies between the two wings of the Hα line seen here are the result of the difficulty in calibrating the blaze function in this region of the spectrum. I found that the majority of Fe line depths are under-predicted with the wavelet method, with the D15 model better matching individual line profiles. This test demonstrates the need to benchmark against well studied stars and visually inspect the best models against the data.

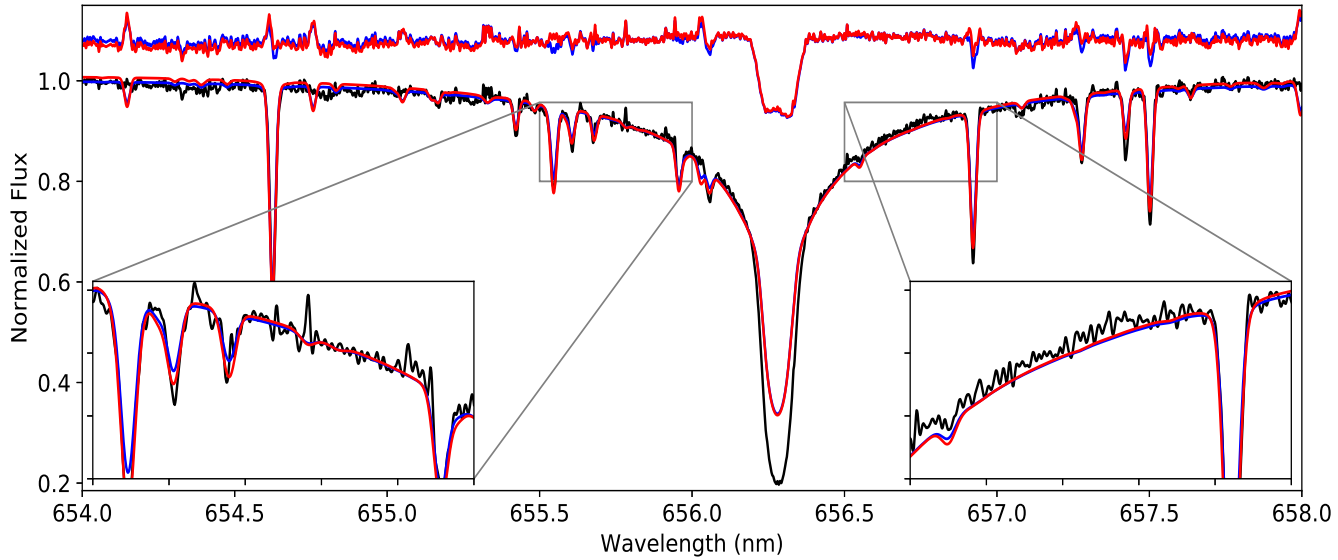

Figure 4.11: The H-α region for WASP-20 (black) fitted with the best fitted model from D15 (red) and the best model from this work (blue). The near horizontal lines at flux 1.2 are the residuals between the D15 model (red) or wavelet model (blue) and the spectrum of WASP-20.

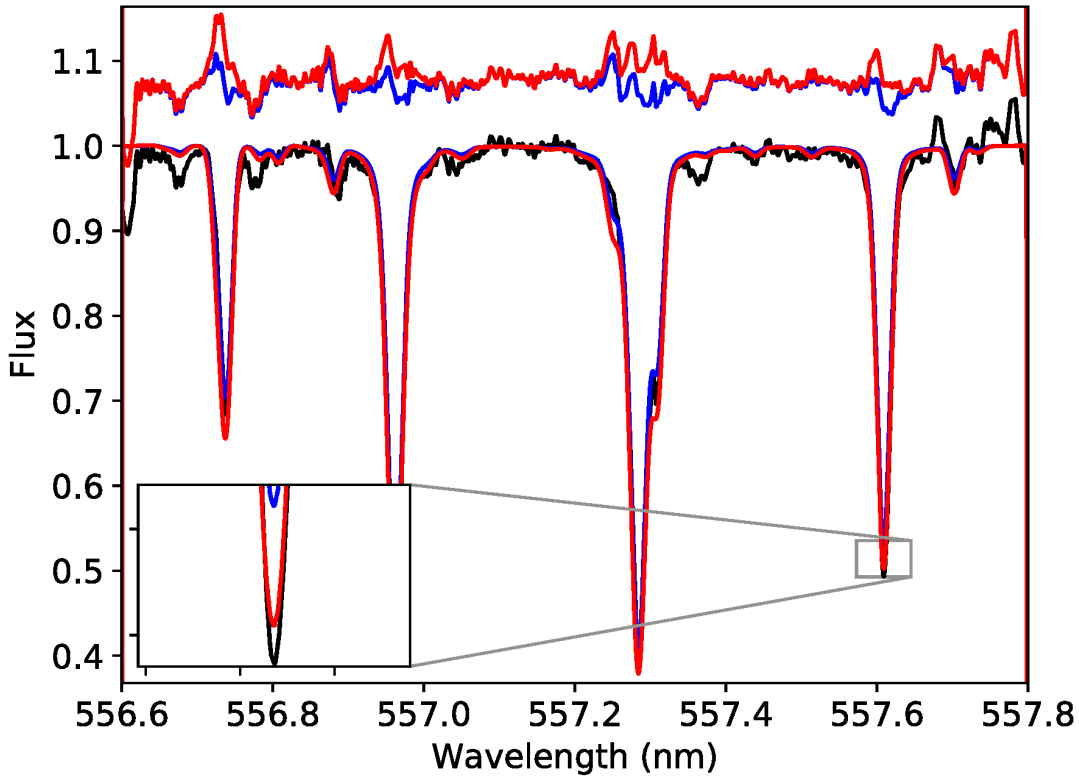

Figure 4.12: Fe lines for WASP-20 alongside the best fitting model from D15 (red) and that from this work (blue). I enlarge one of the cores of an Fe line to highlight that the D15 line-depths are a better match than those found by the wavelet method.

4.5.1 Systematic offset in [Fe/H]

There are many reasons why my method may produce composition offsets when compared with other established techniques. The interested reader should see Jofré et al. (2017) for an excellent review on how the specifics of spectroscopic analysis routines affect abundance measurements. One interesting result from Jofré et al. (2017) is the effect of continuum normalisation which increased the method-to-method scatter in abundance measurements by up to 0.3 dex (see their Fig. 5). Wavelet filtering in my method is an alternate approach to normalisation, and so an offset of around 0.18 dex is not entirely unexpected. I assessed if

there is a systematically lower continuum placement by adding an free parameter, C_0, which is a constant to add to the normalised flux of the model spectra before a discrete wavelet transform in the calculation of log-likelihood. I found values of C_0 converged to values between -0.05 and 0.05 and did not affect measurements of [Fe/H] by more than 0.05 dex; $T_{\rm eff}$ remained the same for all stars within 150 K and $\log g$ changed by as much as 0.2 dex.

I also looked at components unique to the wavelet method. For instance, the mother wavelet used (Daubechies, k=4) may not capture the true line depths when convolved with a spectrum. I again measured WASP-20 with three alternative wavelets (Daubechies k=20, Harr k=2 and bspline k=103) across the range $450-650$ nm (see Table 4.5). I found the choice of mother wavelet has little influence on the determined composition (and all other atmospheric parameters) for WASP-20 and I found similar results for the rest of the D15 sample. It is possible that the resolution of the finest wavelet convolution (2 pixels) is not sufficient to capture iron line depths. To assess this, I convolved a few iron lines with the Daubechies k=4 kernel and assessed whether line depths were under-determined. I found this not to be the case, suggesting no degradation of line depths owing to the choice in wavelets.

Finally, I consider the possibility that there may be instrumental effects at play with the CORALIE échelle spectrograph. A discrepancy in EW measurements for WASP-69 (see Fig. 3.19 in D15) suggests this instrument is prone to scattered light (Doyle 2015). This may be partly responsible for the systematic error in the iron abundance when combined with a low-quality spectrum.

The zero-point of the metalicity scale is a subject of on-going debate (e.g. Kraft & Ivans 2004). However, I can conclude that models using parameters found by D15 (as generated with line lists and atmospheres used in the above work) have better-fitting line depths for the majority of Fe lines in the D15 sample than my predicted models. For this reason, I apply the following correction for the [Fe/H] values of EBLM systems measured with the wavelet method to make them consistent with the metallicity scale of D15:

$$[\mathrm{Fe/H}]_{\rm corrected} = [\mathrm{Fe/H}]_{\rm measured} + 0.18. \tag{4.8}$$

4.5.2 Systematic trend in $\log g$

I also observe a negative correlation between residual $\log g$ measurements (wavelet - D15) and $\log g$ measured with the wavelet method (Fig. 4.9c). This trend is observed with and without Gaussian priors on $\log g$ from transit photometry. I calculate a Pearson correlation coefficient of -0.501 for measurements with no $\log g$ prior, suggesting a significant negative correlation. I fit this trend with a first-order polynomial and found a gradient of -0.692 and a y-intercept of 3.067. This correlation evaluates to zero at a wavelet $\log g$ value of 4.44. In principle, the following correction can be used to bring my $\log g$ measurements into line with those from D15,

$$\log g_{\rm corrected} = \log g_{\rm wavelet} - 3.067 + 0.692 \times \log g_{\rm wavelet}. \tag{4.9}$$

Without knowing the exact cause of this trend, and given the sensitivity of my $\log g$ estimates to the continuum placement, I am reluctant to advise applying this correction and conclude that the wavelet method cannot reliably estimate $\log g$ beyond confirming a dwarf-like surface gravity. Obtaining $\log g$ from a spectrum is typically done through ionization balance (balancing the iron abundance measured from the Fe I and Fe II lines). It is also possible to measure $\log g$ by fitting the wings of gravity sensitive lines (e.g. Mg, Na) using model spectra (the synthesis method). This is essentially how the wavelet method operates (in wavelet space rather than normalised flux space). Accurate determinations of log g from the synthesis method requires detailed element-abundance measurements for gravity-sensitive Na and Mg lines. Estimating the abundances of these elements by scaling from the solar abundance values and applying some correction for α element enhancement will lead to a systematic error in $\log g$ that is difficult to quantify in individual cases. To investigate this further requires another set of comparison stars with independent $\log g$ values (preferably from binary systems where $\log g$ can be accurately measured and not planet transiting systems).

4.5.3 Precision of atmospheric parameters

The high precision of the parameters in Table 4.4 shows that the wavelet method can reliably converge to a well-determined set of atmospheric parameters, but to make use of these parameters I also require a reliable estimate of their true precision that accounts for additional uncertainties due to systematic errors in the data and the models. To obtain a realistic estimate of true precision of the parameters from the wavelet method, $\sigma_{\rm wavelet}$, I compare the results from my method with the correction to [Fe/H] described earlier to those from D15. The standard deviation of the residuals between the measured atmospheric parameters made by D15 and from the wavelet method, $\sigma_{\rm D15-wavelet}$, is a combination of the uncertainties from methods added in quadrature:

$$\sigma^2_{\rm D15-wavelet} = \sigma^2_{\rm D15} + \sigma^2_{\rm wavelet}, \tag{4.10}$$

where $\sigma_{\rm D15}$ is the quoted error on the atmospheric parameters from D15. There are two extreme cases: the first is that the uncertainty from D15 is negligible (or at least much better than what I can achieve) giving $\sigma^2_{\rm D15-wavelet} \approx \sigma^2_{\rm wavelet}$; and the second is that the inter-method discrepancy, $\sigma^2_{\rm D15-wavelet}$, is negligible leaving uncertainties similar to those quoted by D15. In reality, the absolute uncertainty for the wavelet method is somewhere between these two extremes. I adopt a true precision of each parameter from Table 4.3 using a uniform prior on $\log g$ which is to assume that $\sigma_{D15} \langle\langle \sigma_{wavelet}$. I suggest applying a correction of +0.18 dex to [Fe/H] and not to apply a correction to $\log g$. This means precision of 85 K for $T_{\rm eff}$, 0.06 dex for [Fe/H] and 1.35 km s^{-1} for $V \sin i$. The resulting value of $\log g$ is not likely to be reliable but is good enough to confirm dwarf-like gravity around $\log g$ = 4–5 dex. I note that these values are comparable to other methods (e.g. Bruntt et al. 2010).

4.5.4 Spectrum quality

In Fig. 4.13 I plot the difference between atmospheric parameters obtained with the wavelet method (with no priors for $\log g$) to those from D15 as a function of S/N. The sample falls into two categories of quality (those with S/N $\leq$ 90 and those with S/N $\geq$ 120). There is

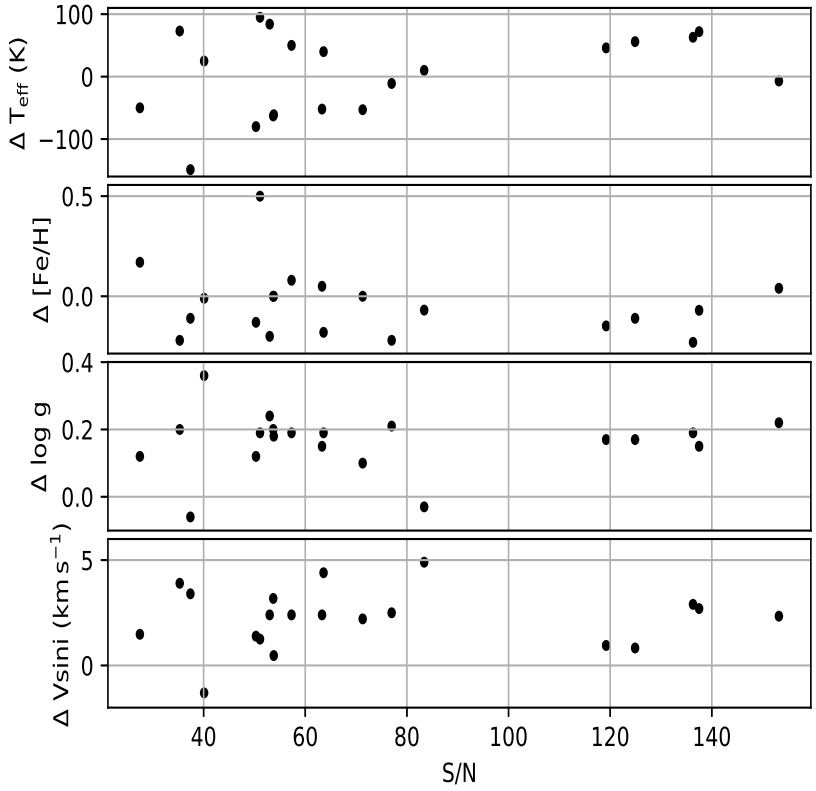

Figure 4.13: Atmospheric parameters from the wavelet method, with no prior on $\log g$, compared to those from D15 ($x_{\mathrm{D15}} - x_{\mathrm{wavelet}}$) as a function of S/N.

noticeably more scatter in the lower-quality group and suggests that the uncertainty of my atmospheric parameters decreases with a better-quality spectrum. The noise profile of a spectrum depends on observing conditions, properties of the star and the instrument used to make the observations. This is why adding Gaussian noise to a synthetic spectrum until the atmospheric parameters are no longer recoverable does not give a true reflection of a methods robustness to noise. Instead, I used 32 (out of 58) observations of the star with the highest S/N in the D15 sample - WASP-20. I dyadically split up these spectra and median combine them into different sets. The sets of splits used were 1 spectrum (1 set of 32 spectra), 2

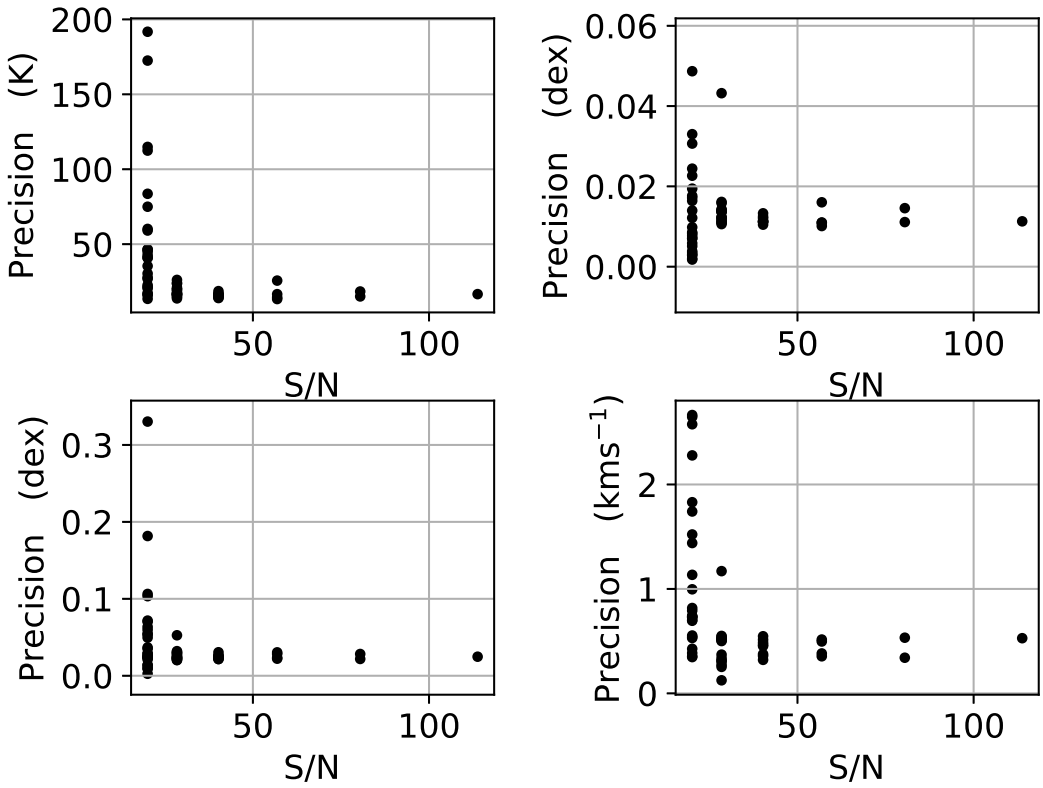

Figure 4.14: Precision of the wavelet method versus S/N for $T_{\rm eff}$ (top left), [Fe/H] (top right), $\log g$ (bottom left), and $V \sin i$ (bottom right) for WASP-20.

spectra (2 sets of 16 spectra), 4 spectra (4 sets of 8 spectra), ..., 32 spectra (32 sets each containing just 1 spectra). I scale S/N from the coaddition of all 58 spectra:

$$\mathrm{S/N} = \mathrm{S/N}_{58\,\mathrm{spectra}} \times \sqrt{\frac{N_{\rm set}}{58}}. \tag{4.11}$$

Each set was measured with the aforementioned wavelet technique with no prior probability function for $\log g$, and best fitting parameters adopted. The precision and accuracy as a function of S/N are shown in Figs. 4.14 and 4.15, respectively. I found that systematic errors dominate for a S/N below 40. A similar result is found by Smiljanic et al. (2014) who measured UVES-FLAMES spectra for FGK stars from the GAIA-ESO Survey and found a

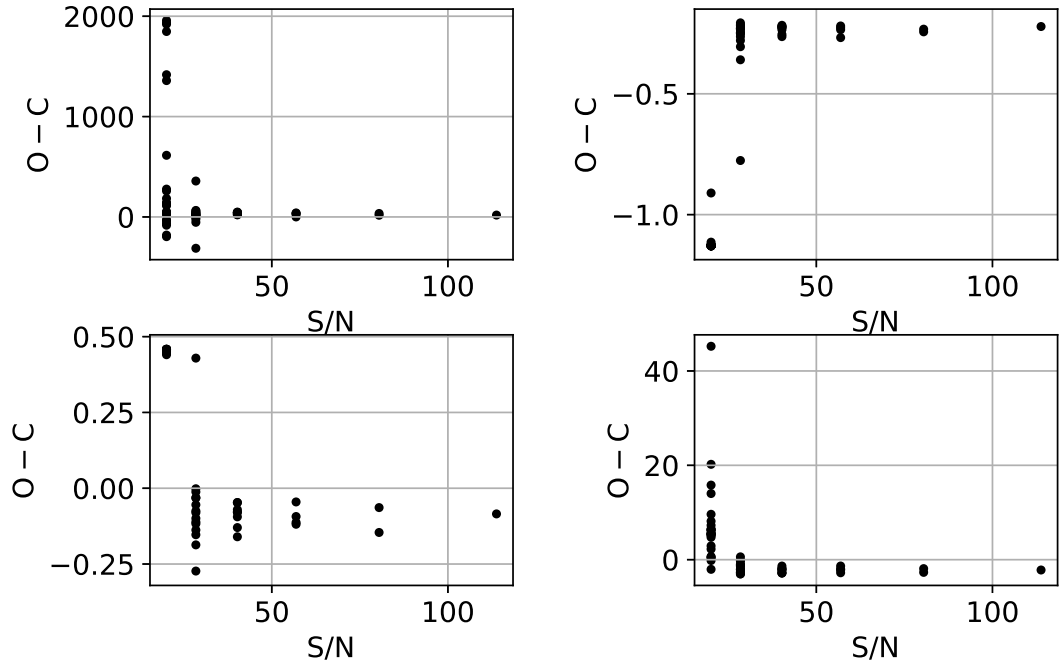

Figure 4.15: Accuracy of the wavelet method versus S/N for $T_{\rm eff}$ (top left), [Fe/H] (top right), $\log g$ (bottom left), and $V \sin i$ (bottom right) for WASP-20 using the results from D15 as a zero-point.

systematics threshold of S/N $\approx$ 50.

Table 4.4: Descriptions of 20 WASP targets used for this work.

Star	T_{eff} (K) This Work	T_{eff} (K) *logg* prior	T_{eff} (K) D15	*Log g* (c.g.s) This Work	*Log g* (c.g.s) D15	*Log g* (c.g.s) photometry	$[Fe/H]$ (dex) This Work	$[Fe/H]$ (dex) *logg* prior	$[Fe/H]$ (dex) D15	*V.sini* kms^{-1} This Work	*V.sini* kms^{-1} *logg* prior	*V.sini* kms^{-1} D15
WASP-4 *	5524 ± 11	5549 ± 10	5400 ± 90	4.5 ± 0.02	4.47 ± 0.11	4.49 ± 0.01 [1]	-0.08 ± 0.01	-0.04 ± 0.01	-0.1 ± 0.1	4.62 ± 0.11	4.92 ± 0.11	3.40 ± 0.30
WASP-5	5806 ± 17	5617 ± 16	5690 ± 80	4.58 ± 0.01	4.28 ± 0.9	4.39 ± 0.03 [1]	0.0 ± 0.01	-0.09 ± 0.01	0.11 ± 0.1	2.62 ± 0.12	≤0.5 ± 0.14	3.90 ± 0.2
WASP-6	5380 ± 15	5427 ± 19	5375 ± 65	4.57 ± 0.01	4.61 ± 0.07	4.52 ± 0.01 [1]	-0.35 ± 0.01	-0.32 ± 0.01	-0.17 ± 0.09	2.95 ± 0.21	3.01 ± 0.19	2.40 ± 0.5
WASP-7	6532 ± 10	6494 ± 9	6550 ± 70	4.41 ± 0.2	4.32 ± 0.07	4.22 ± 0.04 [1]	0.0 ± 0.01	-0.01 ± 0.01	0.16 ± 0.06	17.14 ± 0.15	17.27 ± 0.14	18.10 ± 0.02
WASP-8*	5578 ± 15	5488 ± 9	5560 ± 90	4.56 ± 0.01	4.40 ± 0.09	4.48 ± 0.01 [1]	0.09 ± 0.01	0.03 ± 0.01	0.18 ± 0.11	≤ 0.50 ± 0.17	≤ 0.50 ± 0.17	2.70 ± 0.50
WASP-15*	6428 ± 14	6395 ± 14	6405 ± 8	4.44 ± 0.01	4.40 ± 0.11	4.22 ± 0.02 [1]	-0.16 ± 0.01	0.03 ± 0.01	0.00 ± 0.10	5.47 ± 0.19	5.38 ± 0.11	4.90 ± 0.40
WASP-16*	5735 ± 14	5561 ± 13	5550 ± 60	4.48 ± 0.03	4.21 ± 0.01	4.49 ± 0.02 [1]	-0.02 ± 0.01	-0.14 ± 0.01	0.07 ± 0.10	1.30 ± 0.21	1.40 ± 0.20	2.50 ± 0.40
WASP-17	6699 ± 15	6753 ± 15	6700 ± 105	4.27 ± 0.01	4.34 ± 0.23	4.16 ± 0.02 [1]	-0.24 ± 0.01	-0.22 ± 0.01	-0.12 ± 0.10	7.86 ± 0.22	7.59 ± 0.22	9.80 ± 1.10
WASP-18	6434 ± 13	6354 ± 15	6400 ± 75	4.47 ± 0.02	4.32 ± 0.09	4.32 ± 0.03 [1]	-0.04 ± 0.01	-0.09 ± 0.01	0.08 ± 0.08	10.11 ± 0.17	9.95 ± 0.13	10.9 ± 0.7
WASP-19	5573 ± 17	5540 ± 16	5460 ± 90	4.51 ± 0.02	4.37 ± 0.14	4.44 ± 0.01 [1]	0.02 ± 0.01	0.02 ± 0.01	0.14 ± 0.11	3.75 ± 0.13	3.71 ± 0.13	5.1 ± 0.3
WASP-20	5983 ± 21	6037 ± 16	6030 ± 80	4.50 ± 0.02	4.54 ± 0.13	4.23 ± 0.02 [2]	-0.11 ± 0.01	-0.09 ± 0.01	0.13 ± 0.09	3.63 ± 0.13	1.96 ± 0.18	4.30 ± 0.40
WASP-22*	6032 ± 20	5980 ± 20	6020 ± 65	4.43 ± 0.02	4.25 ± 0.09	4.32 ± 0.02 [1]	0.00 ± 0.01	-0.03 ± 0.01	0.16 ± 0.08	4.77 ± 0.14	4.72 ± 0.19	4.40 ± 0.20
WASP-23*	4986 ± 14	4936 ± 8	5020 ± 50	4.51 ± 0.03	4.31 ± 0.12	4.59 ± 0.02 [1]	-0.17 ± 0.01	-0.20 ± 0.01	0.04 ± 0.07	1.27 ± 0.22	1.22 ± 0.22	2.40 ± 0.30
WASP-24	6295 ± 14	6143 ± 15	6080 ± 60	4.48 ± 0.01	4.20 ± 0.11	4.25 ± 0.01 [1]	-0.19 ± 0.01	-0.18 ± 0.01	0.02 ± 0.08	3.21 ± 0.21	3.22 ± 0.21	6.40 ± 0.20
WASP-29	4650 ± 20	4680 ± 23	4730 ± 50	4.40 ± 0.01	4.48 ± 0.16	4.55 ± 0.02 [1]	-0.02 ± 0.01	0.05 ± 0.01	0.24 ± 0.12	2.52 ± 0.19	2.52 ± 0.19	≤ 05 ± 0.5
WASP-30	6732 ± 14	6891 ± 13	6190 ± 50	4.74 ± 0.01	4.18 ± 0.18	4.28 ± 0.01 [3]	-0.09 ± 0.01	-0.01 ± 0.01	0.09 ± 0.07	13.40 ± 0.17	11.79 ± 0.13	12.10 ± 0.50
WASP-31	6435 ± 18	6381 ± 14	6320 ± 75	4.46 ± 0.02	4.36 ± 0.10	4.31 ± 0.02 [1]	-0.26 ± 0.01	-0.27 ± 0.01	-0.09 ± 0.10	7.51 ± 0.13	7.43 ± 0.13	7.90 ± 0.30
WASP-53	4863 ± 16	4925 ± 16	4950 ± 60	4.41 ± 0.02	4.40 ± 0.20	4.55 ± 0.02 [4]	-0.05 ± 0.01	-0.16 ± 0.01	0.11 ± 0.4	0.40 ± 0.17	4.00 ± 0.21	2.70 ± 0.30
WASP-69*	4782 ± 15	4687 ± 14	4750 ± 55	4.59 ± 0.02	4.36 ± 0.19	4.54 ± 0.02 [5]	0.10 ± 0.01	0.10 ± 0.01	0.29 ± 0.11	1.27 ± 0.22	1.32 ± 0.22	2.90 ± 0.30
WASP-80	4066 ± 22	4050 ± 23	4145 ± 100	4.60 ± 0.02	4.60 ± 0.10	4.69 ± 0.01 [6]	-0.33 ± 0.01	-0.35 ± 0.01	-0.16 ± 0.16	5.04 ± 0.19	2.25 ± 0.17	3.50 ± 0.30

Notes. References. (1) (Doyle 2015); (2) (Anderson et al. 2015); (3) (Anderson et al. 2011); (4) (Triaud et al. 2016); (3) (Anderson et al. 2011); (5) (Anderson et al. 2014); (6) (Triaud et al. 2013a)

* Macroturbulence was fixed at 0 km s^{-1}.

Uncertainities quoted here are internel and do not represent the true precision of our measurements. This is further discussed in Sect. 4.5.3.

Table 4.5: The performance of the wavelet method using different mother wavelets. Each analysis was performed on WASP-7 using the same method used in Sect. 4.4.

Wavelet	$T_{\rm eff}$ (K)	[Fe/H] (dex)	$\log g$ (dex)	$V \sin i$ (km s^{-1})
Daubechies k=4	5983	0.11	4.50	17.54
Daubechies k=20	5975	0.11	4.36	17.55
Harr k=2	5962	0.11	4.34	17.52
bspline k=20	5961	0.10	4.36	17.77

Table 4.6: The regional performance of the wavelet method on WASP-20 using a variety of wavelength ranges. No priors for $\log g$ were used.

Range	$T_{\rm eff}$ (K)	[Fe/H] (dex)	$\log g$ (dex)	$V \sin i$ (km s^{-1})
450 – 500 nm	5984	– 0.17	4.31	3.98
500 – 550 nm	6076	– 0.06	4.33	3.76
550 – 600 nm	5530	– 0.34	4.00	3.60
600 – 650 nm	6099	– 0.12	4.96	3.45
400 – 600 nm	5983	– 0.11	4.50	3.63
D15	6030	0.13	4.23	4.30

Notes. 50nm windows had 2^{15} samples and the 200nm windows had 2^{17} samples. All were subject to the same analysis in Sect. 4.4 with no priors on $\log g$.

5 Methods

5.1 SED fitting

Empirical colour–effective temperature relations were used used to estimate the effective temperature of the primary star in each system. These were used to complement our spectroscopic analysis and to provide a measurement of reddening. They were not used to interpolate stellar models and inform limb-darkening coefficients. I also assume that the flux contribution from the M-dwarf companion is negligible compared to the F-type star (see Sect. 5.6.1.3).

My model for the observed photometry has the following parameters – g'_0: the apparent g′-band magnitude corrected for extinction; $T_{\rm eff}$, the effective temperature; E(B − V), the reddening to the system; and $\sigma_{\rm ext}$, the additional systematic error added in quadrature to each measurement to account for systematic errors. For each trial combination of these parameters the empirical colour – effective temperature relations of Boyajian et al. (2013) were used to predict the apparent magnitudes of the star in each of the observed bands. The transformation between the Johnson and 2MASS photometric systems is the same as Boyajian et al. (2013). The Cousins I_C band was used as an approximation to the DENIS Gunn i′ band and the 2MASS K_s as an approximation to the DENIS K band (see Fig. 4 of Bessell 2005). Table 3 of Bessell (2000) was interpolated to transform the Johnson B, V magnitudes to Tycho-2 B_T and V_T magnitudes. This assumed that the extinction in the V band is $3.1 \times$ E(B − V). Extinction in the SDSS and 2MASS bands is calculated using $A_r = 2.770 \times$ E(B − V) from Fiorucci & Munari (2003) and extinction coefficients relative to the r′ band taken from Davenport et al. (2014).

The reddening maps by Schlafly & Finkbeiner (2011) were used to estimate the total line-of-sight extinction in the direction of each target, $E(B-V)_{\rm map}$. This value is used to impose the following (unnormalized) prior on $\Delta = E(B-V) - E(B-V)_{\rm map}$:

$$P(\Delta) = \begin{cases} 1 & \Delta \leq 0 \\ \exp(-0.5(\Delta/0.034)^2) & \Delta > 0 \end{cases} \quad (5.1)$$

The constant 0.034 is taken from Maxted et al. (2014) and is based on a comparison of $E(B-V)_{map}$ to E(B − V) determined using Strömgren photometry for 150 A-type stars. The EBLM sample observed with K2 had significantly more reddening than the ground-based sample and the priors described in Eqn. 5.1 force the sampler to unrealistically low values of E(B − V). For these four EBLMs, I used a modified prior which only included a Gaussian component:

$$P(\Delta) = \exp(-0.5(\Delta/0.034)^2). \tag{5.2}$$

I used EMCEE (Foreman-Mackey et al. 2013) to sample the posterior probability distribution (PPD) for model parameters. The empirical colour–temperature relations I have used are valid over the approximate range $T_{\rm eff}$ = 3450 K to 8600 K. Between these limits uniform priors were used on the values of $T_{\rm eff}$. I used uniform priors for g'_0. I sampled 10,000 steps from 100 walkers as a burn-in. A further 10,000 steps were drawn and the step with the median value selected as the measurement, with uncertainties equal to the largest difference between the median and the 16^{th}/ 84^{th} percentile of the cumulative PPD for each parameter. An example posterior probability distribution for J2349−32 is shown in Fig. 5.1; the PPDs for the other targets along with residuals (observed magnitudes - calculated magnitudes) are shown in Appendix A.

5.2 Spectroscopic analysis

5.2.1 CORALIE - wavelet analysis

The CORALIE spectroscopic observations and reduction were carried out using the method outlined in Chapter 4 and Gill, Maxted & Smalley (2018), which is briefly described here. I co-added the spectra and re-sample between 450-650 nm with 2^{17} values. I calculated the wavelet coefficients $W_{i=4-14,k}$ (see Fig. 4.2 for visual justification of our choice of wavelet coefficients) and fit the same coefficients with model spectra in a Bayesian framework. I initiated 12 walkers and generate 10,000 draws as a burn-in phase. I sampled a further 10,000 draws to sample the PPDs for $T_{\rm eff}$, [Fe/H], $V \sin i$ and $\log g$. Gill, Maxted & Smalley (2018)

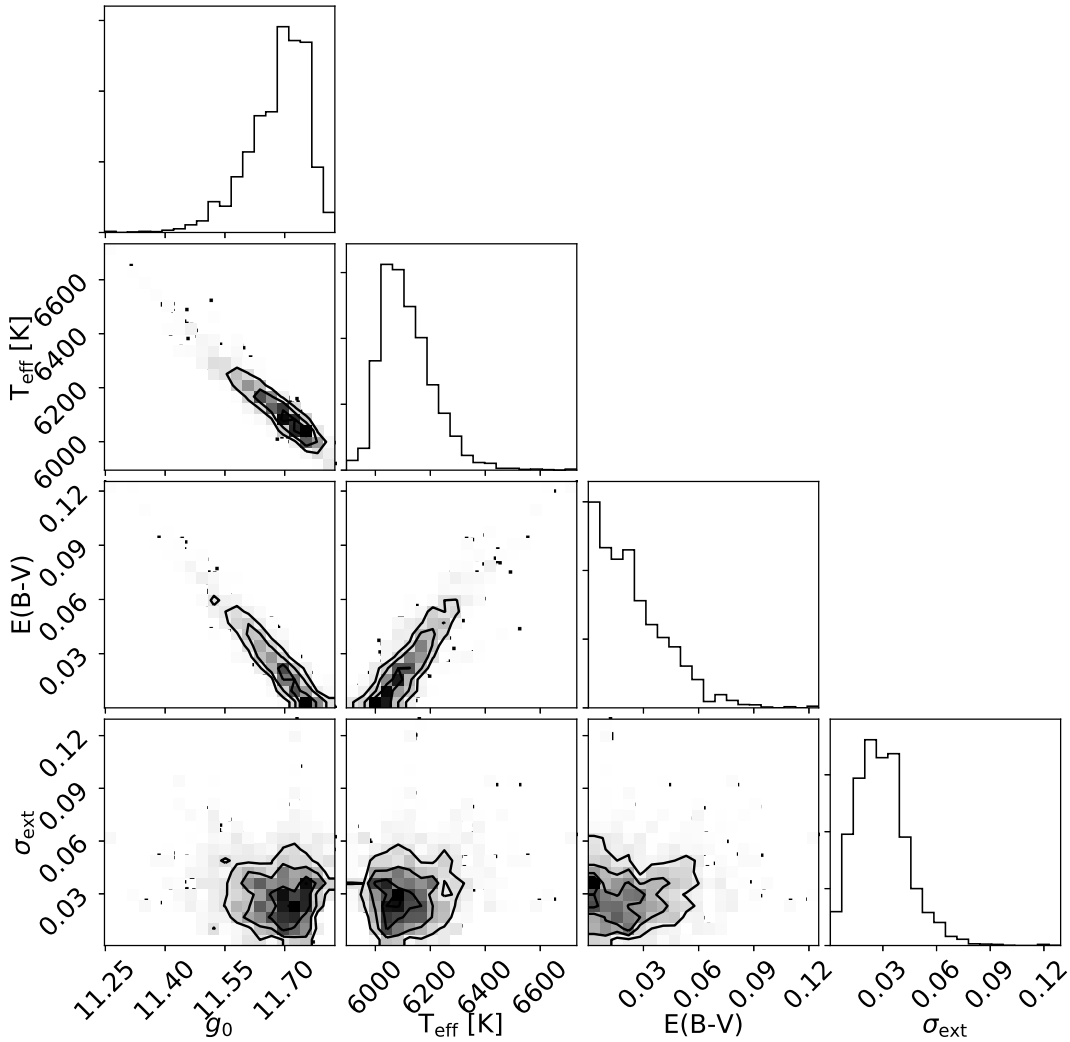

Figure 5.1: The posterior probability distribution of EBLM J2349−32 from photometric fitting. Over-plotted are the 68%, 95% and 99.7% contours.

noted an offset of -0.18 dex in [Fe/H] which I correct for using Eqn. 4.8. We also noted a significant trend in $\log g$ with $T_{\rm eff}$ which I do not correct. The wavelet method for CORALIE spectra can determine $T_{\rm eff}$ to a precision of 85 K, [Fe/H] to a precision of 0.06 dex and $V \sin i$ to a precision of $1.35\,{\rm km\,s^{-1}}$ for stars with $V \sin i \geq 5\,{\rm km\,s^{-1}}$. However, measurements of $\log g$ are not reliable beyond confirming dwarf-like gravity ($\log g \approx 4.5$). Subsequently, I fitted the wings of the magnesium triplets with spectral synthesis by fixing $T_{\rm eff}$, [Fe/H] and $V \sin i$ and changing $\log g$ until an acceptable fit was found.

5.2.2 INT - synthesis

INT observations of J1847+39 are unsuitable for wavelet analysis as only a small wavelength region around the Hα line was observable with the H1800V grating. The spectral synthesis technique was used to measure $T_{\rm eff}$ from the wings of the Hα line and mean [Fe/H] from 11 unblended Fe lines around the Hα line; I assumed an instrumental resolution of R≈10,000. I determined a goodness of fit by synthesising models which best match the spectra in shape and depth. This was assessed *by-eye*. I used the same model spectra used in Chapter 4 and Sect. 5.2.1. There are no gravity sensitive lines visible in the INT spectra and so I assume $\log g = 4.44$.

5.3 First estimates for transit parameters

Using the framework of Beatty et al. (2007), I obtained first order approximations to the ratio of semi-major axis, a, and the radius of the primary star, $R_\star$, using the width of the transit, $\Delta t_{\rm tr}$,

$$\frac{R_\star}{a} \approx \pi \frac{\Delta t_{\rm tr}}{P}, \tag{5.3}$$

Assuming a circular orbit. The ratio of the radii, k, can be estimated

$$k = \frac{R_2}{R_\star} \approx \sqrt{\Delta m}, \tag{5.4}$$

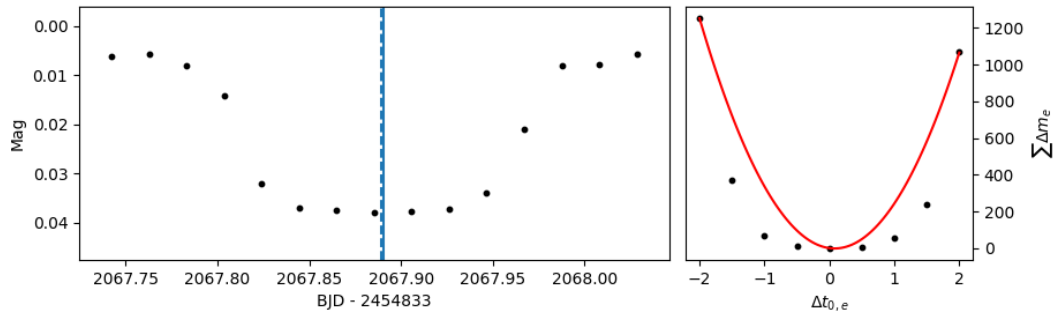

Figure 5.2: The minimum for the first transit of J1652−19 observed with K2 using the method of Kwee & van Woerden (1956). (left panel) The first transit with predicted epoch (blue-solid) and calculated epoch (blue-dashed). (right panel) The sum of the residual magnitudes as a function of time from the predicted epoch with a fitted Gaussian model (red).

where R_2 is the radius of the M-dwarf companion and Δm is the depth of the primary eclipse (in magnitudes). I used Eqns. 5.3 & 5.4 to estimate starting positions for the orbital fit (Sect. 5.6) using follow-up and K2 photometry.

5.4 Ephemerides

I used the method of Kwee & van Woerden (1956) to accurately compute the epoch of minimum of each complete eclipse in the K2 photometry; WASP photometry was of insufficient quality to accurately measure the centre of individual transits. This method re-samples the time axis around a single transit and sums up the magnitude differences ($\sum m_e$) on each side of an arbitrary time, t_e. t_e is advanced to the next time stamp where the process is repeated. The resulting values of $\sum m_e$ will form an inverted Gaussian which was fitted to determine the centre of the transit (minimum of $\sum m_e$) and the uncertainty (width of the Gaussian; Fig. 5.2).

I minimised the correlation between subsequent transits and measured epochs by fitting a straight line in the form

$$\text{epoch} = \text{P} \times \text{cycle} + \text{T}_0 \tag{5.5}$$

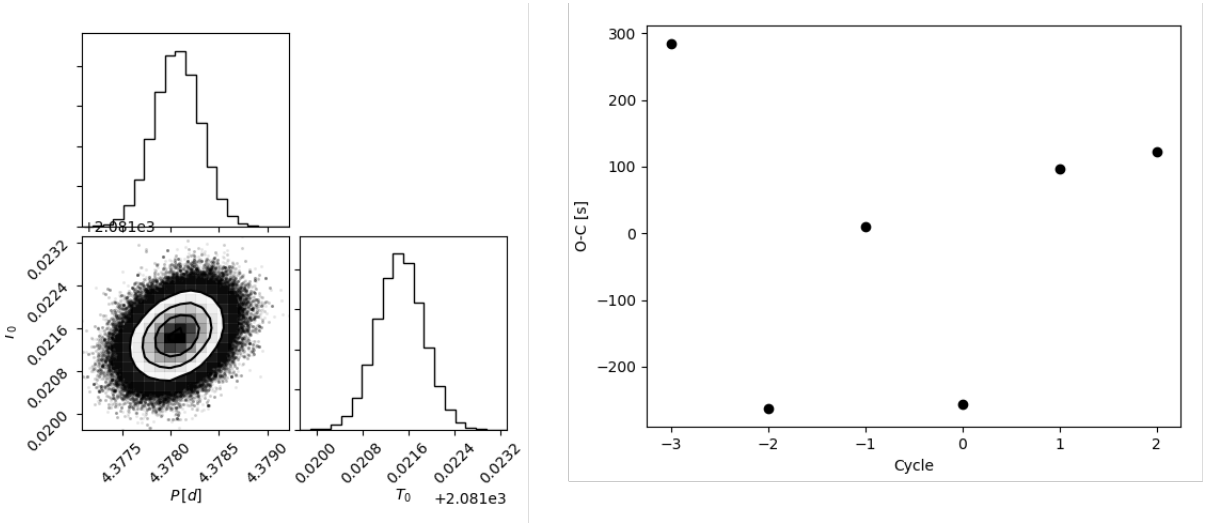

Figure 5.3: The corner plot for the period and epoch of J1652−19 (left). The residuals between predicted and observed epochs are also shown (right).

where P and T_0 are free parameters. I used EMCEE to initialise 100 walkers which were evolved for 10,000 steps. The first 5000 steps were discarded and the step with the highest log-likelihood was selected with uncertainties equal to the largest difference between the median and the 16^{th}/ 84^{th} percentile of the cumulative PPD for each parameter (Fig. 5.3). I inspected the residuals between measured and predicted epochs and found no evidence of transit-timing variations for any of the four EBLMs observed with K2.

5.5 Out-of-transit photometry

I treated the out-of-transit photometry from WASP and K2 separately to determine if variations of the star's brightness exist. In the following sections, I detail the methods used in each case.

5.5.1 WASP photometry

Each system has thousands of observations from the WASP survey which have been taken over many years. Consequently, it is possible to measure variations in the light-curve caused by spot coverage or tidal interactions. I used the method outlined in Maxted et al. (2011) to search the WASP photometry for frequencies attributed to rotational modulation. Each season of photometry is treated separately and in-transit data are excluded. I inspected the periodogram and false-alarm probabilities (FAP) for each system to assess the reliability of any detected periods. I also phase-fold the light-curve at the detected period to check for cases of ellipsoidal variation. The primary eclipses were masked in all cases along with potential secondary eclipses for J0055−00.

5.5.2 K2

The quality of K2 photometry is such that I could visually search the generalised Lomb-Scargle periodigram to identify frequencies which match spot-like variation in the lightcurve. I used the FASPER function provided within python package K2SC to calculate the Lomb-Scargle periodigram. FASPER uses a fast algorithm optimised for unevenly sampled data (Press & Rybicki 1989) and reports the false-alarm probabilities attributed to significant periods. This is the probability of a signal being real with respect to the quality of the data. I analysed the raw lightcurve along with the periodigram to determine spot-induced variation and/or ellipsoidal variation. The primary eclipses were masked in all cases along with the secondary eclipses for J0055−00. The Lomb-Scargle periodigram for J1652−19 is shown in Fig. 5.4, along with the rest of the EBLM sample in Appendix B.

5.6 Orbital solution

I determined the best-fitting orbital solution in different ways for EBLM systems with ground-based follow-up photometry (Table 3.1) and those observed with K2 (Table 3.2).

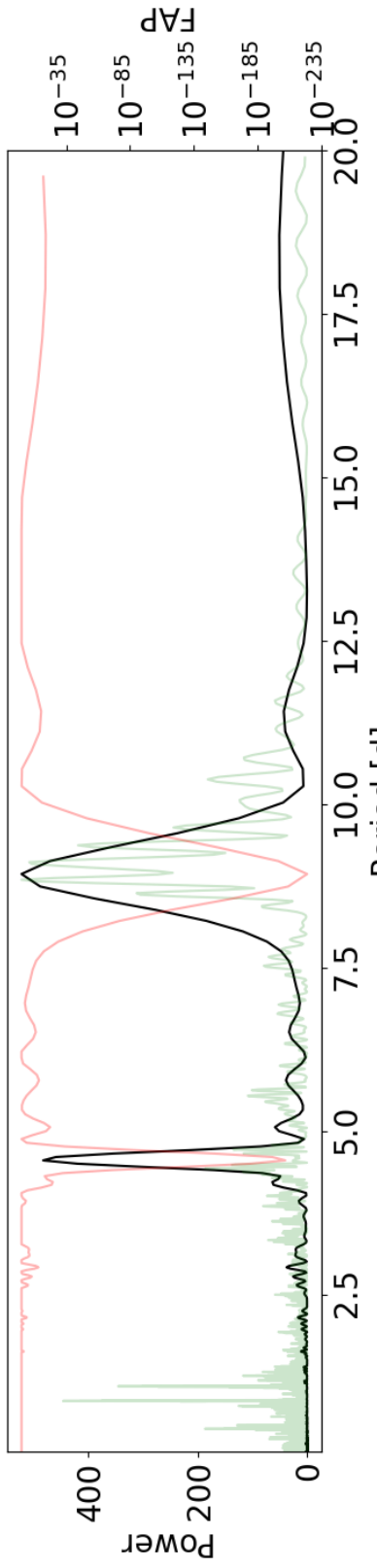

Figure 5.4: The generalised Lomb-Scargle diagram J2217−04 for K2 photometry (black) with false-alarm probabilities (FAP; red). The Lomb-Scargle diagram of WASP photometry is shown (green).

This is due to the temporal nature of this work, in which I obtained data for the EBLMs with ground-based follow-up photometry much before those with K2 photometry. Subsequently, my method evolved to meet the requirements of the larger K2 data-sets. The following sections describe the similarities and differences between the two approaches.

5.6.1 EBLMs with ground-based follow-up photometry

I fitted all follow-up photometry (from SAAO, CTIO and HAO) and radial velocity measurements simultaneously to obtain the final orbital solution for each system. I performed a χ^2 fit in a Bayesian framework to estimate the PPD of each parameter in the vector model. The vector model of parameter's includes photometric zero-points for each i^{th} light-curve – $zp_{\rm i}$, $R_\star/a$, k, the impact parameter – $b = a\cos(i)/R_\star$, T_0, P, the limb-darkening temperature – $T_{\rm eff,ld}$, the semi-amplitude of radial velocity measurements for the primary star –K_1, the systematic radial velocity – γ and the change in systematic radial velocity with time –$d(\gamma)/dt$. The first estimate of $T_{\rm eff,ld}$ comes from the spectroscopic value of $T_{\rm eff}$ from Sect. 5.2. First estimates of $R_\star/a$, k, $\rm T_0$ and P were measured as described in Sec. 5.3 & 5.4. Instead of fitting the argument of the periastron (ω) and the eccentricity (e), I chose to use the de-correlated parameter's $f_c = \sqrt{e}\cos\omega$ and $f_s = \sqrt{e}\sin\omega$ to improve the sampling efficiency at very low eccentricities, when ω is poorly constrained while maintaining a uniform prior on the value of eccentricity (see e.g. Ford 2005). I also included a "jitter" term (σ_J) to account for spot activity which can introduce noise in to the radial velocity measurements (Ford 2006). I used $T_{\rm eff,ld}$ to interpolate coefficients for the Claret limb-darkening law (provided with the python package ELLC; Maxted 2016) using fixed values of [Fe/H] and $\log g$ from Sect. 5.2. I used a Gaussian prior for $T_{\rm eff,ld}$ using the value of $T_{\rm eff}$ from Sect. 5.2 with a conservative uncertainty of 200 K. Photometric and radial velocity models are synthesised using ELLC assuming detached and spherical star-shapes.

I compare these models to data using a Bayesian framework with the likelihood func-

tion $\mathcal{L}(\mathbf{d}|\mathbf{m}) = \exp(-\chi^2/2)$, with

$$\chi^2 = \sum_{i=1}^{N_{mag}} \frac{(m_{\rm i} - m_{\rm model})^2}{\sigma^2_{m_{\rm i}}} + \sum_{i=1}^{N_{rv}} \frac{(rv_i - rv_{\rm model})^2}{\sigma^2_J + \sigma^2_{\rm rv_i}} + \frac{(T_{\rm eff,ld} - T_{\rm eff})^2}{\sigma^2_{T_{\rm eff}}}. \tag{5.6}$$

Here, $m_{\rm i}$ and $rv_{\rm i}$ represent the i^{th} measurement of magnitude and radial velocity with standard errors $\sigma_{m_{\rm i}}$ and $\sigma_{\rm rv_i}$, respectively. I initiated 50 walkers and generated 50,000 draws, after an initial burn-in phase of 50,000 draws. I initially selected the model with the highest value of $\mathcal{L}(\mathbf{d}|\mathbf{m})$ from the PPD to extract the best-fitting model parameters. For J2308−46 and J1847+39 I found these values to be up to 2-σ away from the median value of each parameters PPD, and so I chose the measurements to be the median value from each parameters PPD instead. The uncertainties were calculated from the largest difference between the median and the 16^{th}/ 84^{th} percentile of the cumulative PPD for each parameter from the second chain.

5.6.1.1 Rossiter-McLaughlin effect

Holt (1893) predicted that when one star of a binary eclipsed the other it would cover the advancing blue-shifted hemisphere and then the receding red-shifted part. This motion would create a colour anomaly perceived as a progressive red-shift of the primarys spectrum followed by a blue-shift, thus appearing as a symmetric radial-velocity anomaly on top of the main Doppler orbital motion of the eclipsed stars lines. This effect was first observed by Rossiter (1924) and McLaughlin (1924), though with some evidence of its presence noted earlier bySchlesinger (1910) (p134). The magnitude of the radial-velocity anomaly depends on $V \sin i$ of the primary star and the sky-projected angle between the orbital and stellar rotation angular momentum vectors, λ

I obtained radial velocity measurements of J0218−31 during transit that display variations caused by the Rossiter-McLaughlin effect. The orbital fit for this system required two more de-correlated parameters, $\sqrt{V \cos i} \sin \lambda$ and $\sqrt{V \sin i} \cos \lambda$.

5.6.1.2 Star shapes

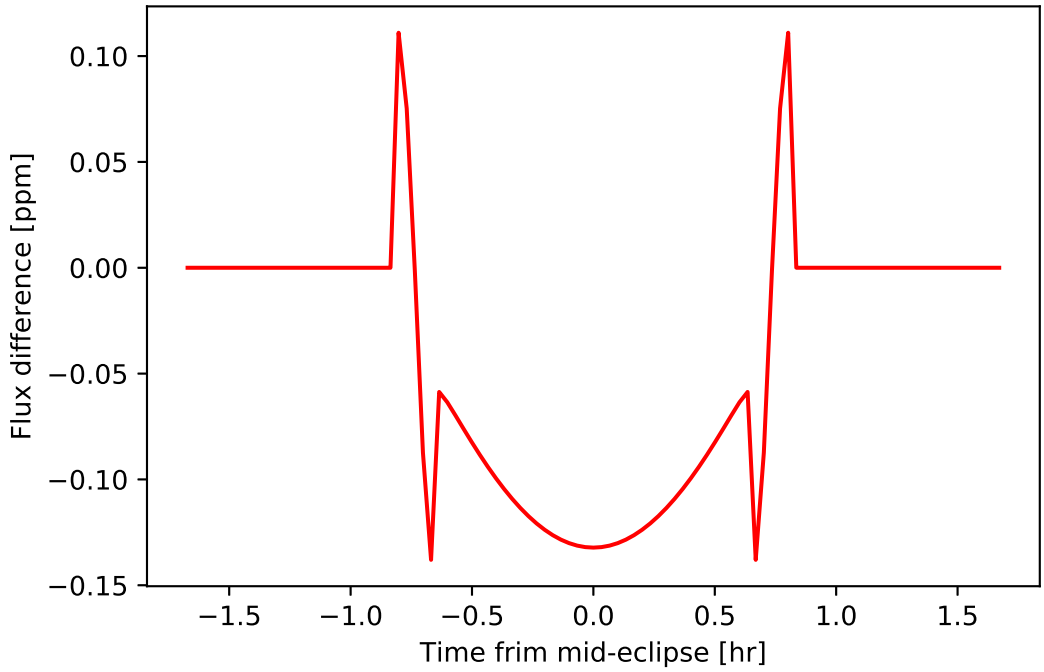

Figure 5.5: The difference between the spherical model and Roche model of J2308−46 using ELLC.

I assume stars are well separated and thus spherical. A caveat is that the spherical volume of the star will not be the same as the volume of the triaxial ellipsoid used to approximate its shape with ELLC. I assessed the magnitude of this problem by comparing the models for J2308−46 where both stars are described by spheres to those where both stars are described using Roche models (Fig. 5.5). I found a maximum difference of ≈ 0.1 ppm which is far below the white-noise level (a few thousand ppm) and so I did not attempt to correct for this.

5.6.1.3 Primary eclipses

I modelled the primary eclipses for all EBLMs (excluding J0055−00) assuming that the luminosity from the M-dwarf is negligible compared to the light from the primary star. Including light from the M-dwarf will have the effect of diluting the transit depth. Assessing whether a correction is needed for this effect requires some foreshadowing of the results (Chapter 6). For the largest M-dwarf in my sample, J1436−13 ($M_2 \approx 0.5\,M_\odot$, $k \approx 0.28$, $\log g_2 \approx 5$) I estimate a surface temperature ≈3700 K by using MESA stellar models (Choi et al. 2016; Dotter 2016). I convolved PHOENIX model spectra (Husser et al. 2013) for each companion with the K2 band-pass to estimate that the M-dwarf's flux contributes approximately 0.5% of the observed flux. By inspecting synthetic lightcurves from ELLC, I estimated a dilution of the primary transit depth by < 500 ppm; this is below the photometric precision of the ground-based light-curves and so I have not applied a transit-depth correction for these systems. The EBLMs observed with K2 have smaller values of k and so the expected flux contribution from the M-dwarf is smaller. However, the photometric precision is much higher and so the potential for introducing a bias increases. For J1652−19 ($M \approx 0.25\,M_\odot$, $k \approx 0.15$, $\log g_2 \approx 5$), the transit depth is modified by < 30 ppm when accounting for the luminosity of the M-dwarf; the rms scatter of the K2 lightcurves is between 200-1000 ppm. J1652−19 is fairly representative of the K2 EBLMs in this work and so I did not apply any corrections for the primary transit depths of these systems. For J0055−00, including a non-zero surface-brightness ratio in the model automatically modified the models primary eclipse depth. This is fortunate since J0055−00 has the best photometric precision of the K2 sample and would have been most susceptible to a bias of the transit depth from the M-dwarfs luminosity. EBLMs with early-type M-dwarfs, cooler primary stars and high-quality lightcurves will require due diligence to ensure there is no bias introduced by neglecting the flux contribution from the M-dwarf.

5.6.2 EBLMs observed with K2

The K2 data sets are more sizeable than single transits obtained from ground-based telescopes. This resulted in a significantly larger computation time to create photometric models and increased the time taken to determine the orbital solution. I decided to move away from the claret 4-parameter limb darkening law in favour of the power-2 law (Hestroffer 1997) as recommended by Morello et al. (2017) for its performance in the remit of 2-parameter limb-darkening laws for cooler stars. The power-2 law has an analytical approximation (Maxted & Gill 2018) which significantly decreases the time taken to calculate models (see Sect. 7.7 for timing tests and Appendix C). The law consists of two parameters (α & c) and has the form,

$$I(\mu) = 1 - c(1 - \mu^{-\alpha}). \tag{5.7}$$

The parameters α & c are strongly correlated. Instead, I fitted the decorrelated parameters

$$h_1 = 1 - c(1 - 2^{-\alpha}) \tag{5.8}$$

$$h_2 = c2^{-\alpha} \tag{5.9}$$

$$\tag{5.10}$$

with inverse transformations

$$c = 1 - h_1 + h_2 \tag{5.11}$$

$$\alpha = \log_2(c/h_2). \tag{5.12}$$

The parameter h_1 measures the specific intensity relative to the centre of the disk in the region on the stellar disk ($r = \sqrt{11/2} \approx 86.6\%$) and h_2 measures the drop in relative intensity from the same distance and the limb. Look-up tables are provided by Maxted (2018) using synthetic 3D LTE spectra from the Stagger-grid calculated by Magic et al. (2015). I decided against interpolating values of h_1 and h_2 for a given $T_{\rm eff,ld}$ as it was computationally expensive. I fitted h_1 and h_2 using Gaussian priors centred at the values interpolated from Maxted (2018) using atmospheric parameters from Sect. 5.2 and width of 0.011 and 0.045 respectively (Maxted 2018). In the following sections I describe the fast transit model (QPOWER2) used for K2 datasets along with the red-noise model to account for out-of-transit variations.

5.6.2.1 QPOWER2

The theory of Keplerian orbits is largely covered in Chapter 2. Determining photometric and radial velocity models hinges on the calculation of the true anomaly, ν, from the other five Keplerian elements. The QPOWER2 model uses the BATMAN transit model (Kreidberg 2015) as a template to solve Keplers equations for ν. Instead of using Newton-Raphson iteration to solve for the eccentric anomaly, E, I used the algorithm from Fukushima (1997) which avoids transcendental function evaluations. This carries a small maximum error on the order of 10^{-16}. I also used the analytical expression for the time of periastron passage prior to a given time of eclipse (t_c) which assumes an inclination of 90°. The difference in flux caused by this approximation is approximately 50 ppm in ingress and egress for an inclination of 87° (Maxted 2016). The sky-projected orbital separation in units of stellar radii, z, is then calculated using Eqn. 2.15 along with radial velocities from Eqn. 2.11.

The normalised flux in an eclipse, F, depends on the area of the primary star covered by the M-dwarf, Z, and the specific intensity, $I_\lambda(r)$,

$$F = 1 - \int_Z I_\lambda(r) dA, \tag{5.13}$$

where $I_\lambda(r) = 1 - c + c(1 - r^2)^{\alpha/2}$. Evaluating this integral requires use of hypergeometric functions which is computationally expensive. Instead, I derived an approximation to this integral by replacing $I_\lambda(r)$ by a truncated Taylor series –

$$I_\lambda(r)) \approx I_\lambda(r_0) + (r - r_0) I'_\lambda(r_0) + \frac{1}{2}(r - r_0)^2 I''_\lambda(r_0) ..., \tag{5.14}$$

where primed symbols denote derivatives with respect to r. How this Taylor expansion is evaluated depends on the projected separation between the primary star and M-dwarf companion, z. For the case where $z \leq 1 - p$ the disk of the M-dwarf lies completely within the disk of the primary star. By using $r_0 = z$ as the reference point for the Taylor series expansion and numerous approximations, the flux drop can be approximated by

$$F \approx 1 - I_0 \pi k^2 \left[c_o = \frac{1}{4} k^2 c_2 - \frac{1}{8} \alpha c k^2 s^{\alpha/2 - 1} \right], \tag{5.15}$$

where

$$c_0 = 1 - c + cs^{\alpha/2} \tag{5.16}$$

$$c_2 = \tfrac{1}{2}\alpha c s^{\alpha/2-2}\Big((\alpha - a)k^2 - a\Big), \tag{5.17}$$

and $s = 1 - z^2$.

For ingress and egress phases ($1-p < z < 1+p$) the integral is evaluated in two regions separated by the chord defined by the intersections between the two limbs. This chord is at a distance $d = (z^2 - k^2 + 1)/2z$ from the origin. Care must be taken in choosing the reference point r_0 in the Taylor expansion because $I'(r)_\lambda \to \infty$ for $r \to 1$. To avoid this problem and to ensure continuity with the light curve at other phases I choose $r_0 = r_a = (z - p + d)/2$ to evaluate the integral over the region between the chord and the limb of the planet, and $r_0 = r_b = (1 + d)/2$ for the region between the chord and the limb of the star. I then found that the lightcurve at these phases can be approximated by

$$F \approx 1 - I_0(J_1 - J_2 + K_1 - K_2), \tag{5.18}$$

where J_1, J_2, K_1 and K_2 are coefficients arising from the Taylor expansion of $I_\lambda(z)$ (Maxted & Gill, 2018. in prep). A python implementation of this algorithm is given in Appendix C.

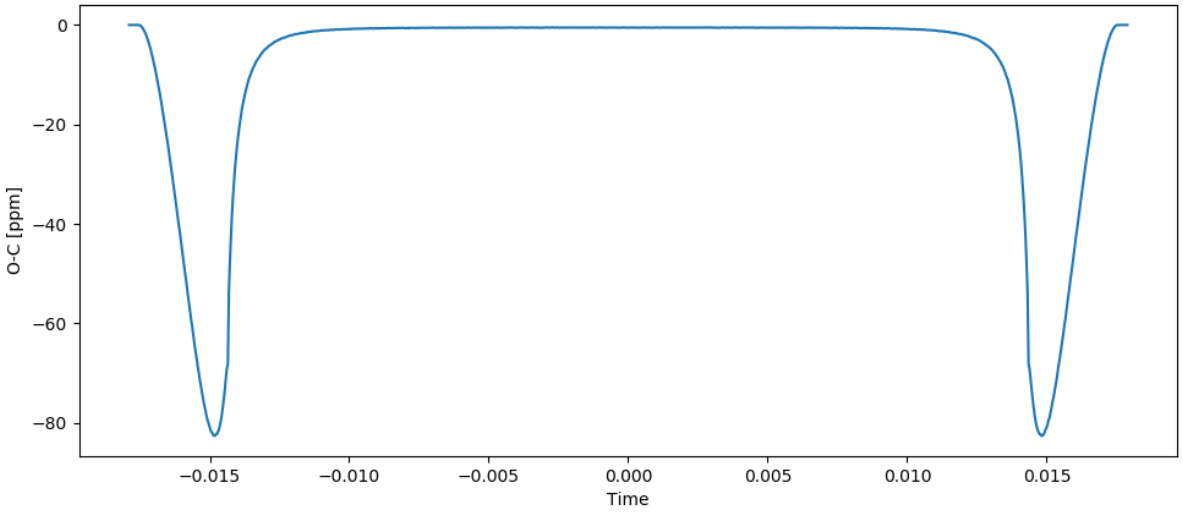

Figure 5.6: The difference between ELLC and the QPOWER2 algorithm for a circularised system with $R_\star = 0.2$ and $k = 0.2$.

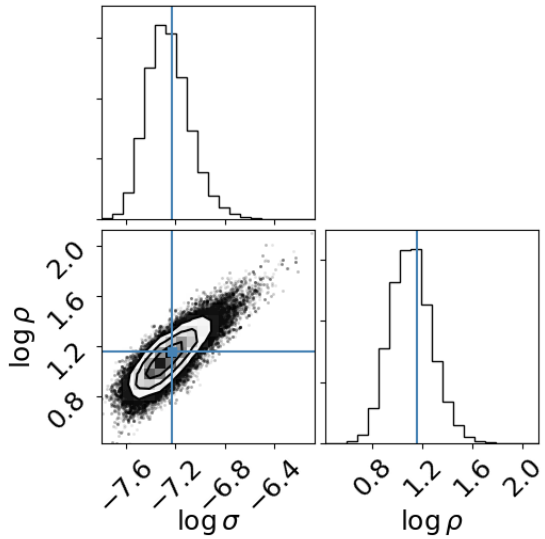

Figure 5.7: The correlation between $\log\sigma$ and $\log\rho$ for J0055−00.

I compared the accuracy of the QPOWER2 algorithm with ELLC for a system with $R_\star/a = 0.2$ and $k = 0.2$ (Fig. 5.6). From this figure it can be seen that the QPOWER2 algorithm reproduces light curves for the power-2 limb-darkening law accurate to better than 0.008% for these parameters. For J0055−00, I required an accurate prescription for the secondary eclipse. I assumed that the M-dwarf companion is uniformly illuminated which permits an analytical expression for the secondary eclipse. I used the formalism provided within the BATMAN package to calculate the secondary eclipse transit shape for a given value of z and surface brightness ratio, S. I was careful to adjust the depth of the primary eclipse appropriately for a given value of S. For J0055−00, S was added to the model vector of the orbital solution and fitted with a uniform prior between 0–0.2.

5.6.2.2 Red noise model

Photometric variations in the K2 lightcurve required a suitable red-noise model to complement QPOWER2. I used the CELERITE package (Foreman-Mackey et al. 2017) and the following

kernel with the default value of $\epsilon = 0.01$ to approximate the Matérn-3/2 covariance function:

$$k(\tau_k) = \sigma^2 \left[(1 + 1/\epsilon)\ e^{-(1-\epsilon)\sqrt{3}\,\tau_k/\rho}\,(1 - 1/\epsilon)\ e^{-(1+\epsilon)\sqrt{3}\,\tau_k/\rho}\right].$$

Here, τ_k is the time difference between two observations, ρ is a parameter that controls the time scale over which observational errors are correlated and σ controls the amplitude of such variations. This introduced two detrending parameters to the model vector: $\log\sigma$ and $\log\rho$. These two parameters are well constrained for all lightcurves (eg. see Fig. 5.7). I used uniform priors between -20 and 20 for each parameter.

5.7 Masses, radii and age

Breaking the degeneracy between the mass of the primary star – $M_\star$, the M-dwarf companion – M_2, and the age of the system – τ, is non-trivial. One approach by Hebb et al. (2009) uses Kepler's equation to estimate the density of the primary,

$$\rho_\star = \frac{3\pi}{GP^2}\left(\frac{a}{R_\star}\right)^3 - \frac{3M_2}{4\pi R_\star^3} \tag{5.19}$$

and then combine it with measurements of $T_{\rm eff}$ and [Fe/H] to interpolate between stellar models for $M_\star$ and τ. Typically, this is repeated with a better estimate of $M_\star$ until the solution converges iteratively. Another approach uses empirical mass and radius calibrations (Southworth 2011; Torres 2013) to obtain $M_\star$ and $R_\star$. These are combined with k and eqn. 5.19 to obtain M_2 and R_2. A third approach by Triaud et al. (2013b) mixes the two methods while fitting orbital parameters. The mass function (Hilditch 2001) can be expressed in terms of radial velocity parameters,

$$f(m) = \frac{(M_2 \sin i)^3}{(M_\star + M_2)^2} = (1 - e^2)^{\frac{3}{2}}\frac{PK^3}{2\pi G}, \tag{5.20}$$

where G is the gravitational constant. The middle and right part of Eqn. 5.20 can be equated and solved numerically for M_2 assuming an initial guess of $M_\star$ from empirical calibrations. Stellar models are interpolated to give a new estimate of $M_\star$. The new value of $M_\star$ can be

used to iteratively solve Eqn. 5.20 and generate better estimates of $M_\star$ and M_2 until a solution is converged upon. A final method relies on three assumptions: (1) the circularisation timescale ($\tau_{\rm circ}$) is much shorter than τ, (2) the rotation is synchronised ($\tau \gg \tau_{\rm sync}$) and (3) that rotational and orbital inclination are the same. With these assumptions it is possible to directly calculate the mass and radius of both components without dependency on stellar models (see Eqns. 14-17 of Beatty et al. 2007).

To measure the mass and age of the primary star I combined the atmospheric parameters (Sect. 5.2) and the best fitting orbital solution (Sect. 5.6) and interpolate between evolutionary models computed with the GARSTEC stellar evolution code (Weiss & Schlattl 2008). I make no assumptions regarding orbital circularisation or synchronisation. I used a modified version of the open-source code BAGEMASS (Maxted, Serenelli & Southworth 2015a) tailored exclusively for EBLM systems (EBLMMASS). EBLMMASS uses the jump parameters of τ, $M_\star$, the initial iron abundance in dex $[{\rm Fe/H}]_{\rm i}$, $\rm M_2$ and the full-width half maximum of the transit w. The vector of observed parameters is given by $\mathbf{d} = (f(m),\, T_{\rm eff},\, \log {\rm L}_\star,\, [{\rm Fe/H}]_{\rm s}, {\rm R}_\star/{\rm a}, {\rm w})$ where $\log L_\star$ is the luminosity of the primary star and $[{\rm Fe/H}]_{\rm s}$ is the surface metal abundance in dex and w is the transit width. The model parameters are $\mathbf{m} = (M_\star, M_2, \tau, [{\rm Fe/H}]_{\rm i}, {\rm w})$. $[{\rm Fe/H}]_{\rm s}$ differs from the initial abundance ($[{\rm Fe/H}]_{\rm i}$) due to diffusion and mixing processes throughout stellar evolution. The GARSTEC evolutionary models used here are the same as the ones used in BAGEMASS. GARSTEC uses the FreeEOS[1] equation of state (Cassisi, Salaris & Irwin 2003) and standard mixing length theory for convection (Kippenhahn & Weigert 1990). The mixing length parameter used to calculate the default model grid is $\alpha_{\rm MLT} = 1.78$. With this value of $\alpha_{\rm MLT}$ GARSTEC reproduces the observed properties of the present day Sun assuming that the composition is that given by Grevesse & Sauval (1998); the overall initial solar metallicity is $Z = 0.01826$, and the initial solar helium abundance is $Y = 0.26646$. These are slightly different to the value in Serenelli, Peña-Garay & Haxton (2013) because I have included additional mixing below the convective zone in order reduce the effect of gravitational settling and so to better match the properties of metal-poor stars. Due to the effects of microscopic diffusion, the initial solar composition corresponds to an initial iron

[1] http://freeeos.sourceforge.net

abundance $[\mathrm{Fe/H}]_{\mathrm{i}} = +0.06$ dex. The stellar model grid covers the mass range $0.6\,M_{\odot}$ to $2.0\,M_{\odot}$ in steps of $0.02\,M_{\odot}$. The grid of initial metallicity values covers the range $[\mathrm{Fe/H}]_i = -0.75$ dex to -0.05 dex in steps of 0.1 dex and the range $[\mathrm{Fe/H}]_i = -0.05$ dex to $+0.55$ dex in 0.05 dex steps.

To obtain M_2 from $f(m)$, $M_\star$ and P, I needed to know inclination from the transit light-curve. Degeneracies between i, $R_\star/a$ and k are such that I chose to fit the full-width half maximum of the transit,

$$w = \frac{R_\star}{a}\frac{\sqrt{1-b^2}}{\pi}, \tag{5.21}$$

instead of the inclination. I implemented a Gaussian prior on $[\mathrm{Fe/H}]_{\mathrm{s}}$ from spectroscopy and use uniform priors for age, $M_\star$ and M_2. I ran a burn-in chain of 100,000 draws before drawing 50,000 draws to sample the PPD for $M_\star$, M_2 and τ. The number of post-burn-in draws matches that of the orbital fit so I can measure the M-dwarf temperature for J0055−00 (Sect. 5.8) and assess the fractional radius and temperature residuals (Sect. 7.2 & 7.4).

I used an up-to-date constant from IAU resolution B3 (Prša et al. 2016) to calculate a from P, $M_\star$ and M_2,

$$a = 4.208278 \times P^{\frac{2}{3}}(M_\star + M_2)^{\frac{1}{3}}. \tag{5.22}$$

This can then be combined with $R_\star/a$ and k to calculate the PPD for $R_\star$ and R_2. I selected the median value of each parameters PPD as our measurements, with uncertainty equal to the largest difference between the median and the 16^{th} and 84^{th} percentile of the cumulative PPD for each parameter from the second chain.

5.8 M-dwarf temperature for J0055−00

The K2 photometry of J0055−00 has secondary eclipses from which S, and thus $T_{2,\mathrm{eff}}$, can be determined . Converting S to a PPD for $T_{2,\mathrm{eff}}$ demands a comparison of spectral energy distributions for the primary star and the M-dwarf which have been convolved with the K2 band-pass. I chose to use the PHEONIX stellar models. For each draw in the PPDs from EBLMMASS and the orbital solution, the procedure was as follows:

1. Random values of $T_{\rm eff}$, [Fe/H] and $\log g$ were generated from normal distributions using the mean as the measurements from Table.6.2 and the respective uncertainties as widths. These were used to interpolate a PHEONIX model spectra for the primary star.

2. The same value of [Fe/H] with the corresponding draw for $\log g_2$ (Eqn. 2.27) was used to continually interpolate spectra for a value of $T_{2,\rm eff}$ that matched the light ratio predicted in the K2 band-pass from the corresponding draw of S and k (until $\Delta S \leq 10^{-4}$).

The PPD for $T_{\rm eff}$ was fitted with a Gaussian from which the measurement of $T_{\rm eff}$ was taken to be the peak, with uncertainty equal to the standard deviation.

6 Results

"*The best preparation for good work tomorrow is good work today.*"

– Elbert Hubbard

In this chapter I give the key results from the measurements of nine EBLMs. Significant periods from the out-of-transit photometry of each season of WASP photometry and K2 photometry (Sect. 5.5) are shown in Table 6.1. Where applicable, I have noted if the detected period is spot-induced or from ellipsoidal variation. The results from wavelet decomposition, spectral synthesis and SED fitting are shown in Table 6.2. The spectral types reported next to the SED temperature are the closest spectral types reported in from Eric Mamajek's "A Modern Mean Dwarf Stellar Color and Effective Temperature Sequence"[1]. Values of ξ_t and $v_{\rm mac}$ come from the calibrations of Doyle (2015). I also report the Li abundances when they could be measured. The best fitting orbital solutions for all EBLMs are reported in Tables 6.3 & 6.4 along with masses, radii and ages from EBLMMASS.

[1] www.pas.rochester.edu

Table 6.1: Periods (in days) detected for each season of WASP photometry and K2 photometry. Primary transits were masked in all cases along with the secondary eclipses for J0055−00.

System	1	2	3	4	K2	Notes
J2349−32	4.42[1]	4.37[1]	5.64[1]	-	-	Spot-like variation
J2308−46	1.08[2]	1.09[2]	1.10[2]	1.09[2]	-	Ellipsoidal variation
J0218−31	2.30	2.13	2.60	-	-	
J1847+39	7.56[1]	7.14[1]	7.17[1]	-	-	Spot-like variation
J1436−13	3.99[1]	3.99[1]	4.03[1]	-	-	Spot-like variation
J0055−00	5.88	9.91	5.55	-	5.60[1]	
J0457+14	1.78[2]	1.72[2]	-	1.79[2]	1.78[2]	Ellipsoidal variation
J1652−19	4.00	4.29	3.70	-	4.43[1]	
J2217−04	9.52	9.02	-	-	8.95[1]	

Table 6.2: The atmospheric parameters of 9 EBLMs discovered by the WASP survey.

	J2349-32 TYC 7519-142-1	J2308-46 2dFGRS TGS421Z197	J0218-31 HD 14326	J1847+39 TYC 3122-289-1	J1436-13 UCAC2 26899058
From SED fitting					
$T_{\rm eff,phot}$ (K)	6090 ± 90 (F9)	6270 ± 140 (F7)	6020 ± 100 (F9)	6210 ± 220 (F7)	6080 ± 360 (F9)
E(B − V)	0.017 ± 0.017	0.032 ± 0.022	0.030 ± 0.020	0.073 ± 0.042	0.031 ± 0.024
g'_0	11.708 ± 0.067	11.565 ± 0.092	10.045 ± 0.082	11.753 ± 0.167	12.502 ± 0.121
From spectroscopy					
$T_{\rm eff}$ (K)	6130 ± 85	6185 ± 85	6100 ± 85	6200 ± 85	6310 ± 85
log g (dex)	4.42 ± 0.13	4.21 ± 0.13	4.05 ± 0.13	4.44 ± 0.13	4.25 ± 0.13
$\xi_{\rm t}$ (km s^{-1})	1.05 ± 1.50	1.07 ± 1.50	1.03 ± 1.50	1.08 ± 1.50	1.14 ± 1.50
$v_{\rm mac}$ (km s^{-1})	4.23 ± 1.50	4.95 ± 1.50	4.94 ± 1.50	4.55 ± 1.50	5.41 ± 1.50
Vsin$i$ (km s^{-1})	11.50 ± 1.35	39.83 ± 1.35	9.00 ± 1.35	10.00 ± 1.35	18.80 ± 1.35
[Fe/H] (dex)	−0.28 ± 0.06	−0.15 ± 0.06	0.15 ± 0.06	−0.25 ± 0.08	−0.10 ± 0.06
log A(Li) + 12	2.4 ± 0.1	-	3.1 ± 0.1	-	-

	J0055−00 EPIC220196587	J0457+14 EPIC246712205	J1652−19 EPIC205148699	J2217−04 EPIC206500801
From SED fitting				
$T_{\rm eff,phot}$ (K)	5880 ± 110 (G1)	7385 ± 228 (A9)	6226 ± 180 (F7)	5810 ± 120 (G2)
E(B − V)	0.031 ± 0.023	0.329 ± 0.040	0.285 ± 0.033	0.095 ± 0.024
g'_0	11.214 ± 0.091	11.076 ± 0.126	11.875 ± 0.133	12.283 ± 0.121
From spectroscopy				
$T_{\rm eff}$ (K)	5969 ± 85	7373 ± 85	6262 ± 85	5848 ± 85
log g (dex)	4.36 ± 0.13	5.04 ± 0.13	4.56 ± 0.13	4.17 ± 0.13
$\xi_{\rm t}$ (km s^{-1})	1.17 ± 1.50	1.92 ± 1.50	1.26 ± 1.50	1.15 ± 1.50
$v_{\rm mac}$ (km s^{-1})	4.67 ± 1.50	19.51 ± 1.50	6.84 ± 1.50	4.25 ± 1.50
Vsin$i$ (km s^{-1})	≤ 5	72 ± 1	11.56 ± 1.35	7.97 ± 1.35
[Fe/H]	0.39 ± 0.06	0.43 ± 0.30	0.18 ± 0.06	0.27 ± 0.30
log A(Li) + 12	2.5 ± 0.1	-	-	-

Table 6.3: The best-fitting orbital solutions and results from EBLMMASS for five EBLMs with ground-based follow-up photometry. For J2308-46 and J0218-31, I report both solutions of masses and age.

	J2349-32 TYC 7519-142-1	J2308-46 2dFGRS TGS421Z197	J0218-31 HD 14326	J1847+39 TYC 3122-289-1	J1436-13 UCAC2 26899058
From orbital fit					
$R_\star/a$	0.0980 ± 0.0003	0.1934 ± 0.0030	0.0988 ± 0.0029	0.0570 ± 0.0005	0.1084 ± 0.0005
R_2/a	0.0188 ± 0.0003	0.0239 ± 0.0001	0.0165 ± 0.0006	0.0162 ± 0.0002	0.0290 ± 0.0040
k	0.1923 ± 0.0002	0.1234 ± 0.0007	0.1685 ± 0.0033	0.2842 ± 0.0010	0.2841 ± 0.0403
b	0.33 ± 0.01	0.05 ± 0.08	0.72 ± 0.02	0.41 ± 0.02	0.87 ± 0.07
$T_{\rm eff,\,ld}$ (K)	6105 ± 260	6530 ± 320	6109 ± 400	6860 ± 260	6072 ± 360
K (km s^{-1})	21.94 ± 0.02	24.02 ± 0.18	27.80 ± 0.01	27.69 ± 0.83	46.50 ± 0.07
f_s	0.025 ± 0.023	−0.103 ± 0.050	−0.008 ± 0.051	0.070 ± 0.052	0.022 ± 0.052
f_c	−0.034 ± 0.009	0.110 ± 0.047	−0.001 ± 0.050	−0.451 ± 0.013	0.032 ± 0.027
e	0.008 ± 0.002	0.024 ± 0.015	≤ 0.001	0.209 ± 0.014	0.002 ± 0.002
ω (°)	163 ± 14	318 ± 18	-	351 ± 18	34 ± 24
γ (km s^{-1})	1.696 ±0.152	7.029 ±0.762	48.640 ±0.010	-67.431 ±0.527	6.718 ±0.257
$d(\gamma)/dt$ (m s^{-1} yr^{-1})	1.4 ±12.9	0.8 ±0.3	-69.9 ±4.1	-71.9 ±21.7	-23.5 ±86.1
$\sqrt{V \sin i}\sin\lambda$	-	-	0.131 ± 0.385	-	-
$\sqrt{V \sin i}\cos\lambda$	-	-	3.204 ± 0.331	-	-
T_0 (HJD$_{\rm TDB}$)	2454215.89918 ±0.00007	2458439.61175 ±0.00010	2455613.39969 ±0.00005	2454234.68973 ±0.00010	2454625.48447 ±0.00008
P (d)	3.5496959 ±0.0000033	2.199149 ±0.00001	8.884098 ±0.000009	7.325147 ±0.000004	3.9975236 ±0.000002
From the Torres et al. (2010) relation					
$M_\star$ ($M_\odot$)	1.12 ± 0.07	1.37 ± 0.09	1.37 ± 0.09	1.10 ± 0.07	1.23 ± 0.08
$R_\star$ ($R_\odot$)	0.58 ± 0.02	1.94 ± 0.06	1.92 ± 0.06	1.05 ± 0.03	1.37 ± 0.04
from EBLMMASS					
$M_\star$ ($M_\odot$)	1.007 ± 0.049	1.162 ± 0.054 1.062 ± 0.034	1.550 ± 0.050 1.340 ± 0.050	1.045 ± 0.039	1.177 ± 0.044
$R_\star$ ($R_\odot$)	1.018 ± 0.021	1.534 ± 0.041	2.131 ± 0.088	0.991 ± 0.014	1.347 ± 0.061
$\rho_\star$	0.963 ± 0.039	0.32 ± 0.01	0.14 ± 0.01	1.05 ± 0.03	0.50 ± 0.07
X_c	0.40 ± 0.12	0 0.10 ± 0.06	0 0.05 ± 0.06	0.55 ± 0.11	0.21 ± 0.09
M_2 ($M_\odot$)	0.176 ± 0.005	0.168 ± 0.005 0.179 ± 0.005	0.390 ± 0.009 0.428 ± 0.009	0.298 ± 0.012	0.488 ± 0.011
R_2 ($R_\odot$)	0.196 ± 0.004	0.189 ± 0.005	0.361 ± 0.020	0.281 ± 0.004	0.449 ± 0.063
Age (Gyr)	3.18 ± 1.78	3.8 ± 0.6 6.1 ± 0.9	2.3 ± 0.3 3.8 ± 0.4	1.0 ± 1.3	3.2 ± 0.8
a ($R_\star$)	10.36 ± 0.16		22.00 ± 0.24 22.70 ± 0.23	17.47 ± 0.21	12.56 ± 0.14

Table 6.4: The best-fitting orbital solution and results from EBLMMASS for four EBLMs observed with K2. For J2217−04, I report both solutions for masses and ages with the favoured solution marked with an asterisk.

	J0055−00 EPIC220196587	J0457+14 EPIC246712205	J1652−19 EPIC205148699	J2217−04 EPIC206500801
from transit timing				
T_0 (HJD_{TDB})	2457430.52105 ± 0.00032	2457861.30410 ± 0.00029	2456918.38878 ± 0.00039	2457009.81801 ± 0.00034
P (d)	11.39120 ± 0.00012	3.56140 ± 0.00004	4.37900 ± 0.00020	8.15524 ± 0.00013
from orbital fit				
$\log_\sigma$	−7.327 ± 0.183	−6.518 ± 0.082	−5.197 ± 0.121	−5.596 ± 0.204
$\log_\rho$	1.074 ± 0.172	−0.476 ± 0.081	−0.370 ± 0.118	1.019 ± 0.163
$R_\star/a$	0.063 ± 0.002	0.165 ± 0.002	0.137 ± 0.002	0.082 ± 0.002
R_2/a	0.011 ± 0.001	0.020 ± 0.002	0.020 ± 0.001	0.013 ± 0.001
k	0.176 ± 0.016	0.122 ± 0.001	0.147 ± 0.002	0.154 ± 0.004
b	0.887 ± 0.035	0.404 ± 0.020	0.409 ± 0.029	0.655 ± 0.034
S	0.042 ± 0.012	-	-	-
h_1	0.469 ± 0.011	0.546 ± 0.0102	0.510 ± 0.011	0.474 ± 0.011
h_2	0.309 ± 0.046	0.401 ± 0.0443	0.394 ± 0.042	0.305 ± 0.053
$\log g_2$	4.995 ± 0.093	5.021 ± 0.053	4.959 ± 0.025	5.047 ± 0.042
K ($km\,s^{-1}$)	21.122 ± 0.084	22.418 ± 2.503	23.450 ± 0.536	20.097 ± 0.288
f_s	−0.055 ± 0.021	0.275 ± 0.081	−0.291 ± 0.035	0.082 ± 0.090
f_c	0.233 ± 0.008	0.215 ± 0.103	0.257 ± 0.036	0.147 ± 0.046
e	0.057 ± 0.037	0.122 ± 0.063	0.151 ± 0.027	0.028 ± 0.028
w [°]	103.654 ± 7.146	73.795 ± 42.919	97.602 ± 11.892	6.095 ± 70.078
$V0$ ($km\,s^{-1}$)	−20.067 ± 0.304	17.695 ± 1.685	−56.489 ± 1.747	−38.014 ± 0.632
$d(V0)/dt$ ($m\,s^{-1-1}$)	29 ± 88	−58 ± 714	−17 ± 869	−48 ± 163
T_0 (HJD_{TDB})	2631.917936 ± 0.021928	3014.058540 ± 0.000306	2137.924409 ± 0.002572	2152.362651 ± 0.000467
P (d)	11.391868 ± 0.000226	3.561514 ± 0.000040	4.377212 ± 0.000188	8.155251 ± 0.000107
from EBLMMASS				
$M_\star$ ($M_\odot$)	1.320 ± 0.048	1.881 ± 0.063	1.432 ± 0.074	1.150 ± 0.035 1.302 ± 0.051*
$R_\star$ ($R_\odot$)	1.645 ± 0.048	2.103 ± 0.037	1.851 ± 0.044	1.624 ± 0.054
$\rho_\star$	0.334 ± 0.027	0.207 ± 0.009	0.233 ± 0.012	0.304 ± 0.025
X_c	0.203 ± 0.076	0.455 ± 0.027	0.191 ± 0.082	0.131 ± 0.075
M_2 ($M_\odot$)	0.309 ± 0.007	0.261 ± 0.048	0.251 ± 0.011	0.234 ± 0.006 0.255 ± 0.008*
R_2 ($R_\odot$)	0.316 ± 0.033	0.256 ± 0.006	0.273 ± 0.009	0.249 ± 0.013
τ (Gyr)	3.52 ± 0.66	0.69 ± 0.13	2.56 ± 0.63	6.74 ± 0.97 4.04 ± 0.66*
a ($R_\star$)	24.39 ± 0.54	12.64 ± 0.17	13.41 ± 0.16	18.96 ± 0.19 19.76 ± 0.24*

6.1 J2349−32

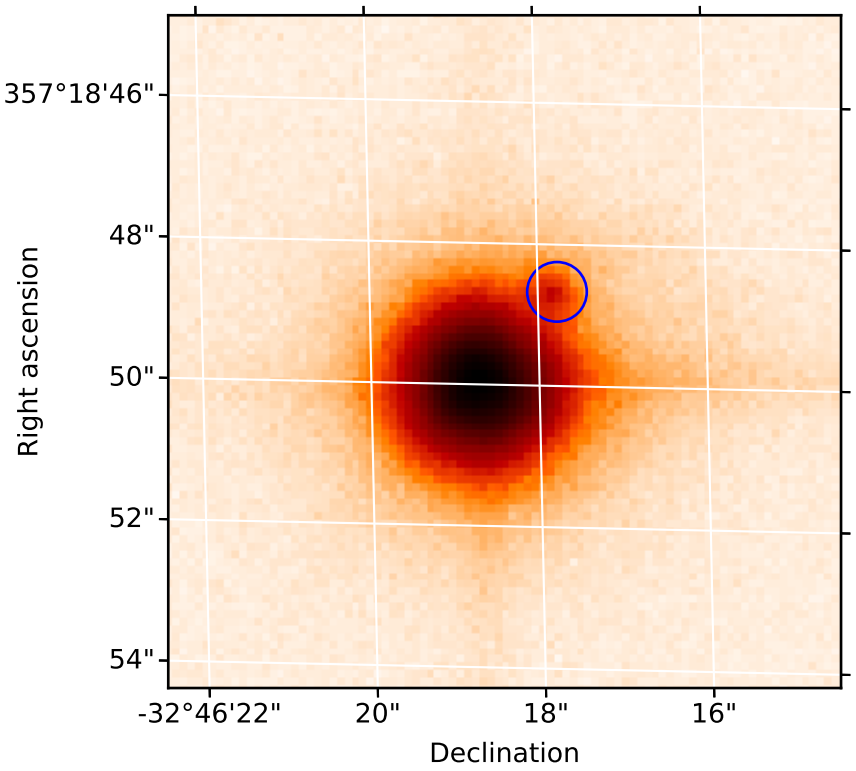

Figure 6.1: Lucky imaging of J2349−32 (red arm) revealing a close companion 1.3" (blue circle) away at a position angle of 308.6 ± 0.6° (blue circle).

J2349−32 was observed over three consecutive years by the WASP project. In each season I found quasi-periodic signals at periods of 4.42 d, 4.35 d and 4.42 d with amplitudes between 3–4 mmag. Each of these signals has a false-alarm probability $< 10^{-5}$ and so I assumed this is detection of the rotational period of the primary star ($P_{\rm rot} = 4.40 \pm 0.03$ d). From the WASP photometry, I measured $\Delta t_{\rm tr} = 0.126$ d and $\Delta m = 0.043$ mag. corresponding to $R_\star/a \approx 0.11$ and $k \approx 0.21$.

The best SED fit ($\chi^2_{\rm red}$ = 1.24) corresponds to a star with spectral type F9 with a low reddening (E(B − V) ≤ 0.034 to 1-σ). This system was included in Gaia DR2 (source ID 2314099177602409856). The G magnitude was measured to be 11.413 and the parallax is 3.43 ± 0.52 mas (260 ± 3 pc). Gaia DR2 shows a single star (G = 15.219) 48" away at a position angle of 111° (source ID 2314099173307737088). This source is not included in the sky annulus of the SAAO 1-m photometry, but falls within the WASP aperture where it will contribute around 3% of the total flux. The proper motions of this star and J2349−32 are significantly different in right ascension and declination so I concluded that they are not associated.

J2349−32 was observed with lucky imaging on 2017-07-08 where two companion stars were detected. A close companion was found at a separation of 1.402 ± 0.013" and position angle of 308.6° ± 0.6° (Fig. 6.1). I measured the companion to be 5.55 ± 0.08 magnitudes fainter in the TCI red-arm images; the companion was not sufficiently resolved in the TCI visible-arm images to obtain any reliable measurements. A second, distant companion was detected at a separation of 25.70 ± 0.07", position angle of 218.6 ± 0.3°. I find that it is 9.0 ± 0.3 magnitudes fainter with the TCI red-arm images and 8.5 ± 0.3 magnitudes fainter in the visible-arm images. This is the same source identified by Gaia DR2 (source ID 2314099173307737088). If the closest companion is blended in the CORALIE and SAAO 1-m apertures, I estimate that it only contributes 0.6 % of the light and is too faint to significantly modify the transit light-curve.

The 17 CORALIE spectra were combined to produce a spectrum with S/N= 40. The analysis of this spectrum shows that the primary is a slightly metal-deficient star with a temperature consistent with the SED fit. There is a weak Li I line at 670.7 nm from which I measured a lithium abundance $\log A_{\rm Li} + 12 = 2.4 \pm 0.08$. This value was estimated by synthesising a small region around this line in ISPEC using fixed atmospheric parameters from wavelet analysis (Table 6.2) and manually adjusting the lithium abundance to obtain the best fit by-eye.

The RVs were fitted simultaneously with a single transit in I-band from the SAAO 1-m telescope to obtain the best fitting orbital solution ($\chi^2_{\rm red}$ = 0.93; Fig. 6.2). The PPD for eccentricity is consistent with a circular orbit ($e \leq 0.05$ to 5-σ). I find a negligible drift

in systematic velocity ($\leq 15\,\mathrm{m\,s^{-1}\,yr^{-1}}$ to 1-σ). The best-fitting limb-darkening temperature agrees with effective temperatures measured with SED fitting and wavelet analysis to better than 1-σ.

EBLMMASS predicts a primary star which has a mass and radius similar to the Sun, but is approximately 350 K hotter. This is partly due to this being a metal-poor star, but also because it is approximately half the age of the Sun. The youthfulness of this star in conjunction with a convection zone which is unable to transport lithium to the core where it would be burnt may explain why lithium is detected with spectroscopy. The secondary component appears to be an M-dwarf below the fully convective limit.

6.2 J2308−46

J2308−46 has WASP photometry spanning 5 years. The last season of data had less than 400 data points so was excluded. I measured a strong $P/2$ signal in two seasons of data. Phase folding the WASP photometry at this period reveals a moderate ellipsoidal variation with an amplitude of 5 mmag (Fig. 6.4). I fixed parameters associated with ellipsoidal variation to produce a good out-of-transit fit to the WASP photometry ($q = M_2/M_\star = 0.05$, gravity darkening coefficient = 0.1) to measure $\Delta t_{\mathrm{tr}} = 0.109$ d and $\Delta m = 0.018$ magnitudes and estimate the transit parameters $R_\star/a \approx 0.20$ and $k \approx 0.13$.

SED fitting measured the effective temperature of the primary star to be consistent with a spectral type F7 ($T_{\mathrm{eff}} = 6270 \pm 140$ K; $\chi_{\mathrm{red}} = 0.77$) with a low reddening ($E(B-V) \leq 0.054$ to 1-σ). This system is included in the Gaia DR2 catalogue (Source ID 6539811294185397120; $G = 11.361$) with a parallax of 2.27 ± 0.08 mas (440.78 ± 15.19 pc). There is a close companion 22.5" from J2308−46 at a position angle of 282° ($G = 15.388$; source ID 6539811500344886016). This is clearly resolved in the follow-up 1-m R-band photometry from SAAO and does not contaminate the sky annulus. It does fall within the WASP annulus, contributing approximately 3% of the total flux. There is another source 48" away from J2308−46 at a position angle of 23°. This is also included in Gaia DR2 ($G = 14.919$; source ID 6539817204061452544) which is on the limits of the WASP aper-

ture and would contribute less flux than the source at position angle 282°. J2308−46 was observed with lucky imaging on 7 July 2017 with only a single, faint companion being found, located 21.38 ± 0.04" away at a position angle of 208.2 ± 0.4° (Fig. 6.3). I measured magnitude differences of 8.2 ± 0.3 magnitudes in the TCI red-arm images and 8.0 ± 0.2 magnitudes in the TCI visible-arm images. This object is included in the Gaia DR2 catalogue with Source ID 6539811289890737408 with $G = 19.538$. I compared the proper motion of J2308−46 with this object and conclude they are not physically associated.

I co-added 22 CORALIE spectra to produce a spectrum with S/N=20. Wavelet decomposition shows that the primary star is a rapidly-rotating ($V \sin i \approx 39\,\mathrm{km\,s^{-1}}$) and metal poor ([Fe/H] = −0.15 dex). This star appears to be close to the Kraft break (Kraft 1967) which separates stars with deep convective envelopes and efficient dynamos from those without. Magnetic fields from these dynamos maintain a transfer of angular momentum to stellar wind resulting in magnetic breaking. This high rotation rate and low S/N spectra makes it difficult to measure accurate radial velocities for this star. Initial attempts to find the best orbital solution resulted in 5 radial velocity measurements which differed by up to 2 $\mathrm{km\,s^{-1}}$; these were excluded as outliers.

Fitting the follow-up photometry jointly with radial velocity measurements was non-trivial as clear systematic errors remained in the SAAO 1-m light-curve after initial detrending. I obtained an orbital solution in the same framework as EBLM J2349−32 but found an unacceptable fit around contact point 2 and the continuum prior to contact point 1 in the SAAO 1-m light-curve (see top panel of Fig. 6.4). I attempted to further detrend the light-curve with airmass, CCD position and time but this did not successfully remove the problem. Instead, I decided to generate a red-noise model using Gaussian processes. I used the CELERITE package to model these data using a Matérn-3/2 covariance function (Sect. 5.6.2.2). The parameters $\log\rho$ and $\log\sigma$ tended to a value that over-fitted the noise in the light-curve if it remained as a free parameter in the joint fit. Instead, I adjusted these values "by-eye" until I found an acceptable red-noise model that accounted for the data around the second contact point ($\log\rho = 2$ and $\log\sigma = 2$). The parameters were then fixed at these values to find an acceptable orbital solution ($\chi^2_{\mathrm{red}} = 1.32$; Fig. 6.4) in the same way as J2349−32.

The primary star is close the the "blue-hook" phase of its post main-sequence evolution

(Fig. 6.5). This results in two peaks in the PPDs for $M_\star$, M_2 and τ. Both solutions could be valid and so it is a requirement to fit these systems to assess the likelihood and validity of each. I fitted double-Gaussian models to the PPDs of $M_\star$, M_2, τ and a which have been sorted into 100 equal bins. I used the Levenberg-Marquardt algorithm to find the optimal model vector $\mathbf{m} = (A_1, \mu_1, \sigma_1, A_2, \mu_2, \sigma_2)$ for the double Gaussian model:

$$y = A_1 e^{-\frac{(x-\mu_1)^2}{2\sigma_1^2}} + A_2 e^{-\frac{(x-\mu_2)^2}{2\sigma_2^2}}, \tag{6.1}$$

where x is the position of the bin, y is the number of models in the respective bin, μ is the measurement of the model, σ is the uncertainty associated with the model, and A represents the number of models at the peak of the of the distribution. The resulting fit for J2308−46 isn't entirely satisfactory; the fitted values of μ do not entirely match up with the peaks of the PPD for $M_\star$, M_2 and τ. This is partly due to the PPDs being poorly described by a Gaussian. Other EBLMs (e.g. J0218−31) have double-peaked PPDs which are well described by Gaussian, so I decided to add additional uncertainty rather than seeking a more complex model. To account for this, I add an additional uncertainty of 2% for $M_\star$, M_2 and τ which was estimated by measuring the offset between the fitted values of μ and the peaks of the respective PPDs. Moreover, the width of each PPD (σ) is underestimated upon visual inspection leading to an additional 1% uncertainty which was determined "by-eye". The total additional uncertainty for each σ is 3%. I assessed each solution using the ratio of likelihoods. I find that the younger solution ($\tau = 3.98 \pm 0.86$ Gyr) is preferred over the older solution ($\tau = 5.81 \pm 1.0$ Gyr) with a factor $\mathcal{L}(3.98\,\mathrm{Gyr})/\mathcal{L}(5.81\,\mathrm{Gyr}) \approx 3.18$. This is moderate evidence to favour the younger solution but far from conclusive so I report both solutions in Table 6.3.

6.3 J0218−31

J0218−31 was observed over three years by the WASP survey. I find a tentative detection of spot-induced variation across the three seasons ($P_{\mathrm{rot}} = 2.30$ d, 2.14 d and 2.60 d). Each have an amplitude around 1 mmag amongst a complex periodogram of similar (but smaller)

amplitudes making it unclear whether this is due to spot-induced variations ($P_{rot} = 2.35 \pm 0.20$ d) or poor-quality photometry. From the WASP photometry, I estimated $\Delta t_{\rm tr} = 0.241$ d and $\Delta m = 0.03$ magnitudes, corresponding to $R_1/a \approx 0.09$ and $k \approx 0.18$.

I obtained a good SED fit ($\chi^2_{\rm red} = 0.75$) with the effective surface temperature of the primary star consistent with a spectral type F9 ($T_{\rm eff} \approx 6020$ K). J0218−31 is included in the second data release of Gaia ($G = 9.734$; Source ID 4971670729566470528) with a parallax measurement of 3.84 ± 0.04 mas (260.13 ± 2.85 pc). There are 3 close and faint companions within 22" at position angles 266°, 332° and 92°. The brightest has $G = 17.140$ ($\Delta G = 7.406$) which would contribute negligible flux to the aperture of both the WASP photometry and the follow-up R-band photometry. A brighter companion ($G = 16.015$; source ID 4971670935725243904) is located 50" away at a position angle of 330°. This does not overlap the sky annulus of the 1-m SAAO photometry and will have a negligible flux contribution to the WASP photometry. The proper motions of these stars are not similar to J0218−31 and so I concluded that they are not physically associated.

I co-added fifty-three out-of-transit spectra to produce a spectrum with S/N = 30. Using wavelet decomposition, I estimated $T_{\rm eff} = 6100 \pm 85$ K confirming a spectral class of G0 from SED fitting. The effective temperature is 1-σ hotter than predicted by SED fitting suggesting there could be some additional reddening that is unaccounted for. The iron content is higher than the Sun ([Fe/H] $= 0.15 \pm 0.12$ dex). There is also a strong Li I line in the spectrum from which I measure a $\log A_{\rm Li} + 12 = 3.24 \pm 0.08$; this suggests that the convective shell of J0218−31 may be similar to that of J2349−32.

Initial attempts to determine the orbital solution resulted in a single Rossiter-McLaughlin measurement which differed from the best-fitting model by $O - C \approx 3\,{\rm km\,s^{-1}}$; I excluded this measurement as an outlier. I fitted the Rossiter-McLaughlin measurements alongside the out-of-transit radial velocity measurements with g', r', i & z' band photometry to obtain the best fitting orbital solution ($\chi^2 = 1.68$; Fig. 6.6). I initially fitted an independent value of k to the g', r', i & z' follow-up photometery. The fitted value of k for each bandpass agreed with each other to 1-σ suggesting there is no wavelength-dependent transit depths which may indicate a source of third light. However, I do find a significant drift in systematic velocity ($d(\gamma)/dt = -69.9 \pm 4.1\,{\rm m\,s^{-1}yr^{-1}}$) which suggests there may be a faint third body in the sys-

tem. With the addition of R-M measurements, I was able to calculate the sky-projected angle between the rotational and orbital axes, $\lambda = 4 \pm 7^\circ$, which is consistent with the assumption that these axes are aligned. From this I also measured $V \sin i = 10.28 \pm 2.12\,\mathrm{km\,s^{-1}}$ which is in agreement with the value inferred from wavelet decomposition.

Similarly to J2308−46, J0218−31 has entered the "blue-hook" part of it's post main-sequence evolution resulting in double-peaked PPDs of τ, $M_\star$ and M_2. I used the same approach for J2308−46 to fit a double-Gaussian to the PPDs for τ, $M_\star$ and M_2 and found that the younger solution (2.4 ± 0.25 Gyr, $M_\star = 1.55 \pm 0.05\,M_\odot$, $R_\star = 2.13 \pm 0.09\,R_\odot$) is favoured with almost twice the likelihood $\mathcal{L}(2.35\,\mathrm{Gyr})/\mathcal{L}(3.80\,\mathrm{Gyr}) \approx 3.55$ of the older solution. This is moderate evidence to suggest the younger solution is favoured but I report both solutions in Table 6.3 as a precaution.

6.4 J1847+39

J1847+39 was observed for three years with the WASP survey. From these three seasons, I find significant spot-induced variations at periods 7.55 d, 7.14 d and 7.17 d with amplitudes of 3 – 4 mmag; I assumed this is a detection of rotational spot modulation at a period of 7.29 ± 0.19 d. I find no evidence for ellipsoidal variation in the WASP lightcurve from which I estimated $\Delta t_{\mathrm{tr}} = 0.02$ d and $\Delta m = 0.10$ mag corresponding to initial estimates of $R_\star/a \approx 0.07$ and $k \approx 0.32$.

The best SED fit estimated the primary star to be of spectral type F7 with temperature of 6020 ± 100 K ($\chi^2_{\mathrm{red}} = 1.37$). This system was included in Gaia DR2 ($G = 11.677$; source ID 2098283457595740288) with a parallax of 3.6653 ± 0.0254 mas (273 ± 2 pc). The field surrounding J1847+39 is relatively more crowded compared to the other targets, with over 7 targets brighter than $G = 17$ within 1.5'. The closest companion is 12" away ($G = 17.694$; source ID 2098283457595821440) at a position angle of 196°. A magnitude difference of $\Delta G = 6.17$ results in less than 0.3% flux contribution if it was included in the apertures of the HAO photometry. There are two bright companions 1.28' and 1.07' away at position angles of 48° ($G = 11.577$) and 54° ($G = 12.135$) respectively. These are beyond the sky annulus of

WASP but may still contribute a small amount to the total flux. The proper motions of these objects are dissimilar to J1847+39 and so I conclude that they are not associated.

Ten INT spectra were co-added to produce a spectrum with S/N= 30. I used the spectral synthesis method on the wings of the Hα line to estimate $T_{\rm eff} = 6200 \pm 100$ K (spectral type F8) which is consistent with the SED fit. I was able to fit 11 un-blended Fe I lines in the region around Hα from which I measured [Fe/H] for each line. I took the mean of value of [Fe/H] as the iron abundance measurement with the standard deviation as the uncertainty ([Fe/H] $= -0.25 \pm 0.21$ dex). I was unable to determine $\log g$ due to the limited wavelength coverage of the H1800V grating so I assumed $\log g = 4.44$ for the aforementioned synthesis and interpolation of limb-darkening coefficients.

Radial velocity measurements were fitted simultaneously with single transits in *CBB*, g' and z' filters to obtain the best fitting orbital solution (reduced $\chi^2 = 1.77$; Fig. 6.8). J1847+39 has the most eccentric orbit of the sample ($e = 0.209 \pm 0.014$). I attempted to fit an independent value of k for photometry in each filter and found them all to agree within 1-σ suggesting there is no significant third-light contamination. However, I do measure $d(\gamma)/dt = -71.9 \pm 21.7\,\mathrm{km\,s^{-1}yr^{-1}}$ suggesting that there may be a faint third-body in the system. The best-fitting limb-darkening temperature, $T_{\rm eff,ld}$, is ~ 600 K hotter than spectroscopic and photometric analysis; the reason for this is unclear.

The best fitting solution from EBLMMASS describes a star similar to the Sun in mass and size, but a fifth of it's age ($\tau = 1.10 \pm 1.80$ Gyr). The systems eccentricity may be primordial in origin as there would have been insufficient time for tidal interaction to circularise the orbit. The M-dwarf's mass is in the convective transition ($\sim 0.35\,M_{\odot}$) and provides an interesting test for low-mass stellar models in a region that is highly debated.

6.5 J1436−13

J1436−13 was observed over 3 consecutive seasons with the WASP survey. I found significant variability for each season at periods of 3.99 d, 3.98 d and 4.02 d with amplitudes between 4 –5 mmag. I assumed this is due to spot modulation corresponding to a rotational

period $P_{\rm rot} = 4.00 \pm 0.02$ d. I find no evidence for ellipsoidal variation in the WASP photometry from which I measured $\Delta t_{\rm tr} = 0.188$ d and $\Delta m = 0.065$ magnitudes corresponding to initial estimates of $R_\star/a \approx 0.148$ and $k \approx 0.256$.

The SED fitting measured the primary star to have a spectral type of F9 ($T_{\rm eff} = 6080 \pm 355\,K$; $\chi_{\rm red} = 0.87$) with little reddining ($E(B-V) \leq 0.055$ to 1-σ). This system is included in Gaia DR2 ($G = 12.334$; source I.D 6323183619200685824) with a parallax of 2.1447 ± 0.0513 mas (466 ± 11 pc). There is a faint ($G = 18.994$) background star included in Gaia DR2 that is 17" away at a position angle of 302°. This is included in the WASP aperture but contributes less than 0.1% of the total flux.

Thirteen CORALIE spectra were co-added to produce a spectrum with S/N=30. Wavelet decomposition measured a value of $T_{\rm eff}$ that is around 300 K hotter than predicted by SED fitting suggesting that there may be some unaccounted reddening. The iron content is slightly less than the Sun ([Fe/H]= -0.10 ± 0.12 dex) and the magnesium lines are relatively narrow suggesting a low surface gravity. I was unable to identify any measurable lithium lines.

The best fitting orbital solution ($\chi^2_{\rm red} = 1.75$) describes a transit with a high impact parameter ($b = 0.86 \pm 0.07$; Fig. 6.9). The limb-darkening temperature agrees better with SED fitting than wavelet decomposition, but is consistent with both to 1-σ. Radial velocity measurements suggest the system is circularised ($e \leq 0.004$ to 1-σ) and there is no significant drift in systematic velocity. J1436−13 is slightly larger and more massive than the Sun. The uncertainty in $R_\star$ (5%) is the largest in the sample owing to poorly constrained values of $R_\star/a$ and k owing to a high impact parameter. The M-dwarf companion is the most massive of the sample ($M_2 = 0.49\,M_\odot$).

6.6 J0055−00

J0055−00 was observed over three seasons with the WASP survey. In two seasons I measured significant powers at 5.55 d and 5.58 d with amplitudes below 1 mmag. Both of these periods are approximately half the orbital period, however I find no convincing evidence of ellipsoidal variation in the WASP photometry. K2 photometry appears to have variations at

a similar period ($P_{\rm rot}$ = 5.6 d; 1 mmag). From the WASP photometry, I measured a primary transit transit width of 0.21 d and depth of 0.03 magnitudes corresponding to $R_\star \approx 0.06$ and $k \approx 0.17$. There is a clear secondary eclipse visible in the K2 light curve.

The SED is well fitted with $\chi^2_{\rm red} = 0.97$ and agrees with spectroscopy to 1-σ. There is a single star north of J0055−00 in Gaia DR2 that is 1.04" away at PA = 359° (G = 17.6986; source ID 2536832466426328704). The difference in magnitude $\Delta G = 7$ means that it would contribute less than 0.16% of the total flux in the WASP aperture. J2349−32 was observed with lucky imaging on 2017-07-19 where no other stars were detected (Fig. 6.10).

Twenty-four CORALIE spectra were co-added to produce a spectrum with S/N= 45. Wavelet decomposition implies a temperature consistent with a metal-rich G0-1 star. I observed a significant lithium opacity at 670.7 nm from which I measured a $\log A_{\rm Li} = 2.5 \pm 0.1$. J0055−00 has the least rotational broadening of the entire EBLM sample with a $V \sin i$ below the threshold of what can be measured with wavelet analysis ($V \sin i \leq 5\,{\rm km\,s^{-1}}$).

The orbital solution is well fitted with a $\chi^2_{\rm red} = 1.88$ (Fig. 6.11). Similar to J0218−31, I measured a high impact parameter ($i = 86.80° \pm 0.16°$) as contact points 2 and 3 are poorly undefined. This increased the uncertainty in k, $R_\star/a$ and ultimately R_1 and R_2. I measured a secondary eclipse of depth 0.27 mmag. corresponding to a surface brightness ratio $S = 0.042 \pm 0.012$. I estimate $T_{\rm eff,2} = 3464 \pm 145$ K using PHOENIX stellar models (Fig. 6.12). Similar results have been measured for J0113+31 (Gómez Maqueo Chew et al. 2014) and KIC 1571511 (Ofir et al. 2012). I discuss if this is expected in Sect. 7.4.

J0055−00 has entered the "blue-hook" part of its post main-sequence evolution. I observed a double-peaked PPD distribution for $M_\star$, M_2 and τ which was fitted in the same way as J2308−46 and J0218−31 (Fig. 6.13). The younger solution is favoured with a likelihood ratio of $\mathcal{L}_{3.5{\rm Gyr}}/\mathcal{L}_{7{\rm Gyr}} = 2$ and over 97% of the models reside within the 3.5 Gyr solution. I found that μ and σ for the older model were not well-constrained but do a good job at fitting the PPDs of M_1, M_2 and τ. I only report the $\tau = 3.5$ Gyr solution in Table 6.4 due to the high probability of the primary star residing on the youthful edge of the blue hook.

6.7 J0457+14

J0457+14 was observed over three unique seasons with WASP. There are clear peaks in the periodogram at P/2 in each season of data due to the ellipsoidal effect. Phase-folding the WASP lightcurve at these periods reveals moderate ellipsoidal variation with an amplitude ~ 2 mmag. This is observed in the K2 photometry with the same amplitude suggesting that the primary star is tidally deformed. Ellipsoidal variation was the dominant out-of-transit signal and I could not measure any spot-like variation. Assuming a mass-ratio of 0.6 and a gravity darkening coefficient of 0.15, I estimate the amplitude of ellipsoidal variation to be 1-3 mmag. For the WASP photometry, I measured a transit depth of 22 mmag and width of 0.1 d corresponding to $R_\star/a \approx 0.18$ and $k \approx 0.14$.

J0457+14 was included in Gaia DR2 ($G = 11.916 \pm 0.002$) and parallax 1.4191 ± 0.0385 mas (700 ± 20 pc). There are two sources included in Gaia DR2 which are approximately 30" west of J0457+14 at position angles of 272° ($G = 17.243$) and 255° ($G = 18.002$). The proper motions of these stars from Gaia DR2 is significantly different in right ascension and declination so I concluded that they are not associated. These stars are not included in the K2 apertures and contribute less than 1% flux in the WASP aperture. The SED fit measured the surface temperature of the primary star to be consistent with a hot, A9 star ($T_{\rm eff} \approx 7400$ K; $\chi^2_{\rm red} = 0.96$). There is also a moderate amount of reddening fitted ($E(B-V) \approx 0.33$) consistent with the reddening inferred from the maps by Schlafly & Finkbeiner (2011).

Fifteen spectra were co-added onto a common wavelength range to produce a spectrum of S/N= 30. The precision of $T_{\rm eff}$/[Fe/H] is low because there are few lines and the quality of the individual spectra is low. The co-added spectrum has strong Hα and Hβ absorption with heavily blended weak-line absorption corresponding to a $V \sin i \approx 72 \pm 1$ km s^{-1}. I measured a strong interstellar Na D line with an equivalent width ≈ 0.3 Å suggesting $E(B-V) \approx 0.11$. This is lower than measured reported by Schlafly & Finkbeiner (2011) but the measured temperature is consistent with SED fitting.

The high $V \sin i$ of J0457+14 resulted in radial velocity measurements with uncertain-

ties exceeding 5 km s^{-1} in some cases. The accuracy of such measurements is the limiting factor determining the uncertainty of $f(m)$ which sets the lower-limit of uncertainty in the masses of the system. I measured K to a precision of 11% corresponding to a 33% uncertainty in $f(m)$ ($\propto K^3$). I was able to measure a significant eccentricity in the orbital solution ($\chi^2_{\rm red}$ = 1.56) despite the quality of radial velocity measurements. The system is still young ($\tau \leq 1$ G yr to 1-σ) which suggests the eccentricity is primordial in origin and is yet to be circularised. The primary star has a thin convective shell which is less efficient at dissipating angular momentum than cooler stars with larger convective envelopes which result in longer time scales to circularise the orbit (Torres, Andersen & Giménez 2010). The M-dwarf companion may still be in the pre-main sequence part of its evolution and thus still contracting.

6.8 J1652−19

J1652−19 was observed over 3 seasons with the WASP survey. In each season I measure a strong period between 3.7-4.3 d (amplitudes between 4–6 mmag) which appears to be a marginal detection of the rotational period. The K2 photometry has a strong power peak period at 4.43 d (amplitude of 10 mmag.) consistent with spot-induced variations. I assumed this to be a detection of the rotational period of the star ($P_{\rm rot}$ = 4.1 ± 0.3). I find no evidence for ellipsoidal variation in either WASP or K2 photometry. The transit depth in the WASP photometry is measured to be 0.03 magnitudes deep with a duration of 0.19 d corresponding to $R_\star/a \approx 0.14$ and $k \approx 0.17$.

J1652−19 is included in Gaia DR2 (source ID: 4132067265306146560) with parallax measurements 2.081 ± 0.113 mas (481 ± 26 pc). There are at least 3 other stars within 1' that are detailed in Sect. 3.7.1. Lucky imaging gives a clearer picture of the field (Fig. 6.15), where the three bright stars east of J1652−19 in the K2 postage stamps are clearly visible. Lucky imaging also reveals a closer and fainter companion 4.5" south of J1652−19 (PA = 198°). This is resolved by Gaia (source I.D. 4132067265299758720) with ΔG = 6.98 and will contribute less than 0.2% flux in the K2 aperture. The proper motion of all nearby stars from Gaia DR2 is dissimilar to J1652−19 and so I conclude that they are not physically

associated. The best-fitting SED model ($\chi^2_{\rm red}$ = 0.99) is consistent with a primary star of spectral type F7 with a moderate amount of reddening.

A total of fourteen CORALIE spectra were co-added to produce a spectrum with S/N = 19. Wavelet decomposition implies a temperature consistent with an F8 star that is metal rich ([Fe/H]= 0.18 ± 0.06). I identified two separate Na absorption lines (at 589.00 nm and 589.05 nm) corresponding to pockets of interstellar Na moving at different projected velocities. I measured an EW for each Na absorption line using ISPEC and measured an independent value of reddening from the E(B-V) V. EW_{Na} of Poznanski, Prochaska & Bloom (2012): 0.14 Å ($E(B-V) = 0.04$) and 0.11 Å ($E(B-V) = 0.04$) for the 589.00 nm and 589.05 nm absorption respectively. This gives a total reddening estimate of $E(B-V) = 0.07$ and is significantly lower than the reddening estimated by Schlafly & Finkbeiner (2011) despite measurements of $T_{\rm eff}$ from SED and spectral analysis agreeing within 1-σ. I was unable to measure any lithium absorbtion.

The best-fitting orbital solution is well-fitted ($\chi^2_{\rm red}$ = 1.67; Fig. 6.16). The orbital solution describes a moderately eccentric system which has not circularised. However, the system may be pseudo-synchronised since the measured rotational period matches the orbital period. The theoretical limb-darkening coefficients from Maxted (2018) did not give a good description of the shape of the transit light-curve. I decided to relax the width of the Gaussian prior for h_1 and h_2 to 0.2 and 0.45 respectively. The best fitting value of h_1 and h_2 differ from those predicted by Maxted (2018) by +0.083 and +0.129 respectively. This difference exceeds what is observed for Kepler-17; an active star which displays variations on the order 0.8% in the Kepler short-cadence lightcurves. Like Kepler-17, the amplitude of spot-induced variations in the K2 photometry is on the order of 0.81%. The difference between expected and observed power-2 coefficients for J1652−19 and Kepler-17 is in the same direction for h_1 and opposite direction for h_2. The sign of the differences in h_1 and h_2 goes some way to suggest that part of the reason for this offset may be weak magnetic activity in solar-type stars that is not included in the stellar atmosphere models used to interpolate h_1 and h_2 (Maxted 2018).

The primary star has turned off the MS, but not into the "blue-hook" region of its post main-sequence evolution. The system is approximately half the age of the Sun but much

more massive. The primary star has likely started fusing hydrogen in a shell around the core. During this phase of stellar evolution, the effective temperature decreases and explains why I measured a $T_{\rm eff}$ similar to the primary star of J1847+39, despite being much more massive.

6.9 J2217−04

J2217−04 was observed over two seasons with the WASP survey. I measured significant power at period 9.52 d (3 mmag) and 9.02 d (5 mmag) which is similar to the orbital period. I observed spot-like variations in the K2 photometery at a similar period and so I assumed this is a detection of stellar rotation at a period of $P_{\rm rot} = 8.16 \pm 1.58$ d. From the WASP photometry, I measured a transit duration of 0.20 d with depth of 0.03 magnitudes corresponding to initial estimates $R_\star/a \approx 0.08$ and $k \approx 0.17$.

J2217−04 is included in Gaia DR2 (source ID: 2626910437568266240; $G = 12.003 \pm 0.001$) with parallax measurements 2.480 ± 0.099 mas ($403. \pm 16$ pc). The closest companion of J2217−04 is 59" away at a position angle of 85° ($G = 15.1334 \pm 0.000$; source ID 2626909720308891392). This source is on the edge of the WASP aperture and would contribute 3% of the total flux if it was included. Lucky imaging reveals no significant companions nearby (Fig. 6.18). There is a source detected 4.5" away which is around 9 magnitudes fainter than J2217−04 however it is not included in Gaia DR2. The SED fit measured a solar-like temperature consistent with a G2 spectral type ($\chi^2_{\rm red} = 0.87$).

A total of twelve CORALIE spectra were co-added to produce a spectrum with S/N= 36. I excluded one spectrum (BJD= 2456150.85392) which was incorrectly exposed. Wavelet decomposition implies the effective temperature is similar to the Sun ($T_{\rm eff} \approx 5850$ K) with an enhanced metallicity ([Fe/H]= 0.27 ± 0.06). Wavelet analysis also implies $\log g_\star \approx 4.17$ which is corroborated by characteristically narrow Mg lines. I was unable to identify any measurable lithium absorption.

The orbital solution is well-fitted ($\chi^2_{\rm red} = 1.56$; Fig. 6.18). Radial velocity measurements indicate a low eccentricity ($e \leq 0.05$ to 1-σ) resulting in a poorly constrained value of ω. The impact parameter is high but the contact points are still discernible leading to robust

measurements of $R_\star/a$, i and k. The residuals of the radial velocity measurements are less than 1.1 km s^{-1}, leading to a mass function which is constrained to 4.4%. The measured drift in systematic velocity is consistent with zero.

Like many other EBLMs in this work, J2217−04 has evolved into the "blue-hook" region of its post-main sequence evolution resulting in 2 solutions for $M_\star$, M_2 and τ (Fig. 6.19). Fortunately, the younger solution is significantly favoured; the ratio of the likelihoods between the old young and the old solution $\mathcal{L}(3.99\,\mathrm{Gyr})/\mathcal{L}(6.74\,\mathrm{Gyr}) = 6.6$ with over 85% of the models residing within the 3.99 Gyr solution. I report both solutions as a precaution in Table 6.4, marking the favoured solutions with an asterisk.

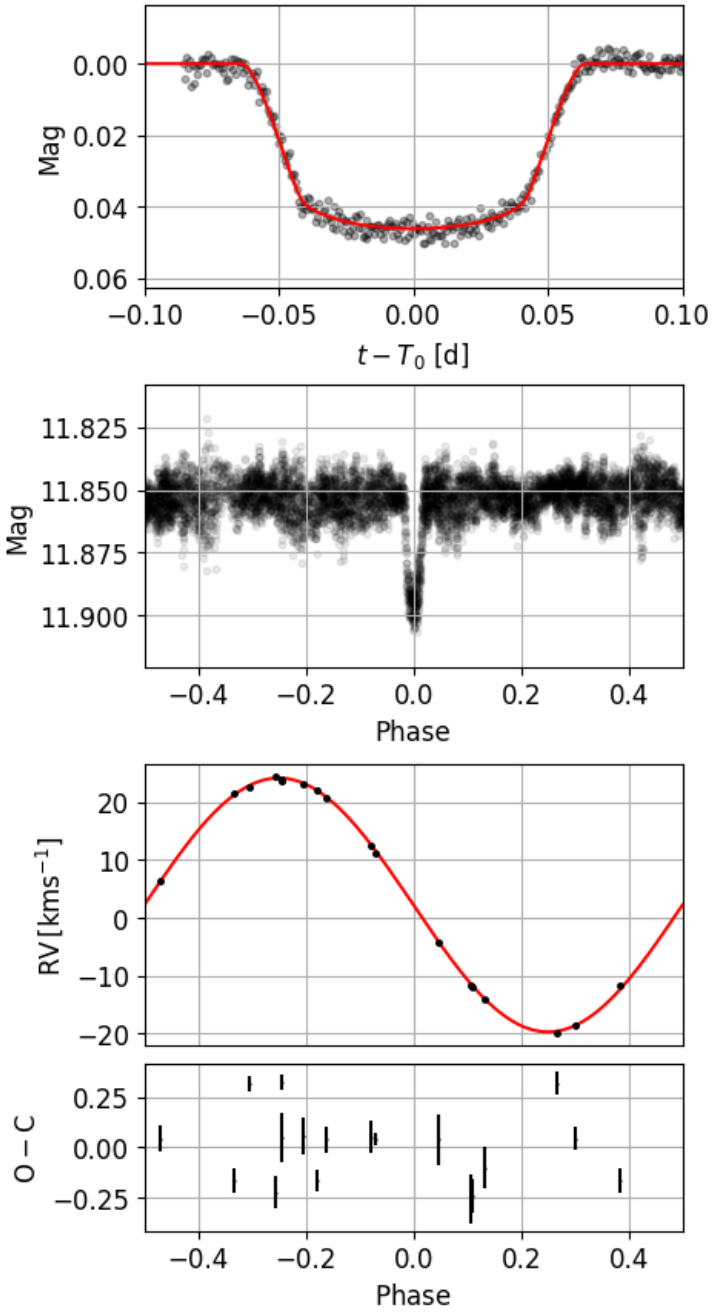

Figure 6.2: Orbital fit of EBLM J2349−32. (top panel) The detrended I-band light-curve from the SAAO 1-m telescope (black) with the best fitting transit model (red). (upper-middle panel) The phase-folded WASP lightcurve (black). (lower-middle panel) Drift-corrected radial velocity measurements (black) with the best model (red). (bottom panel) The residuals from radial velocity model measurements.

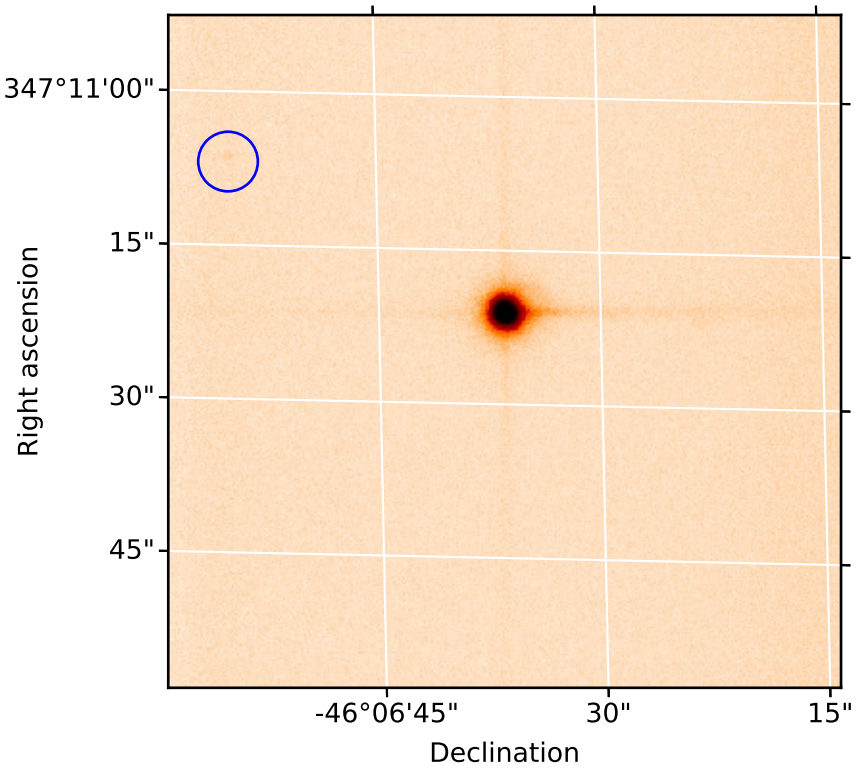

Figure 6.3: Lucky imaging of J2308−46 (red arm) revealing a companion 20” away with a position angle of 208° (blue circle).

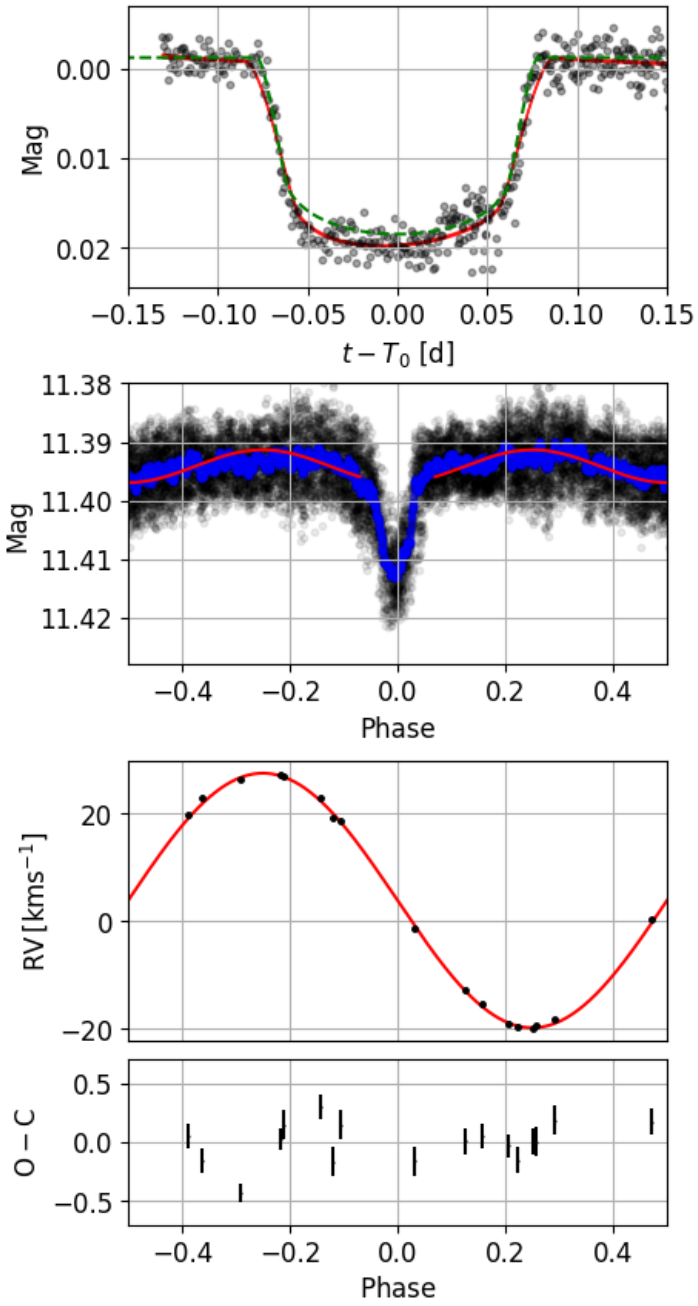

Figure 6.4: Orbital fit of EBLM J2308−46. (upper panel) R-band transit obtained from the SAAO 1-m telescope (black) with the best fitting transit model (green dashed). I also plot the best fitting transit model generated using Gaussian processes (red). (middle panel) Phase-folded WASP observations (black) and observations binned into groups of 50 (blue). I also plot the Roche model used to approximate the out-of-transit photometry used to measure transit parameters from WASP photometry (red). (lower panel) Drift-corrected radial velocity measurements (black) with the best fitting model (red) and residuals from the best fitting orbital model.

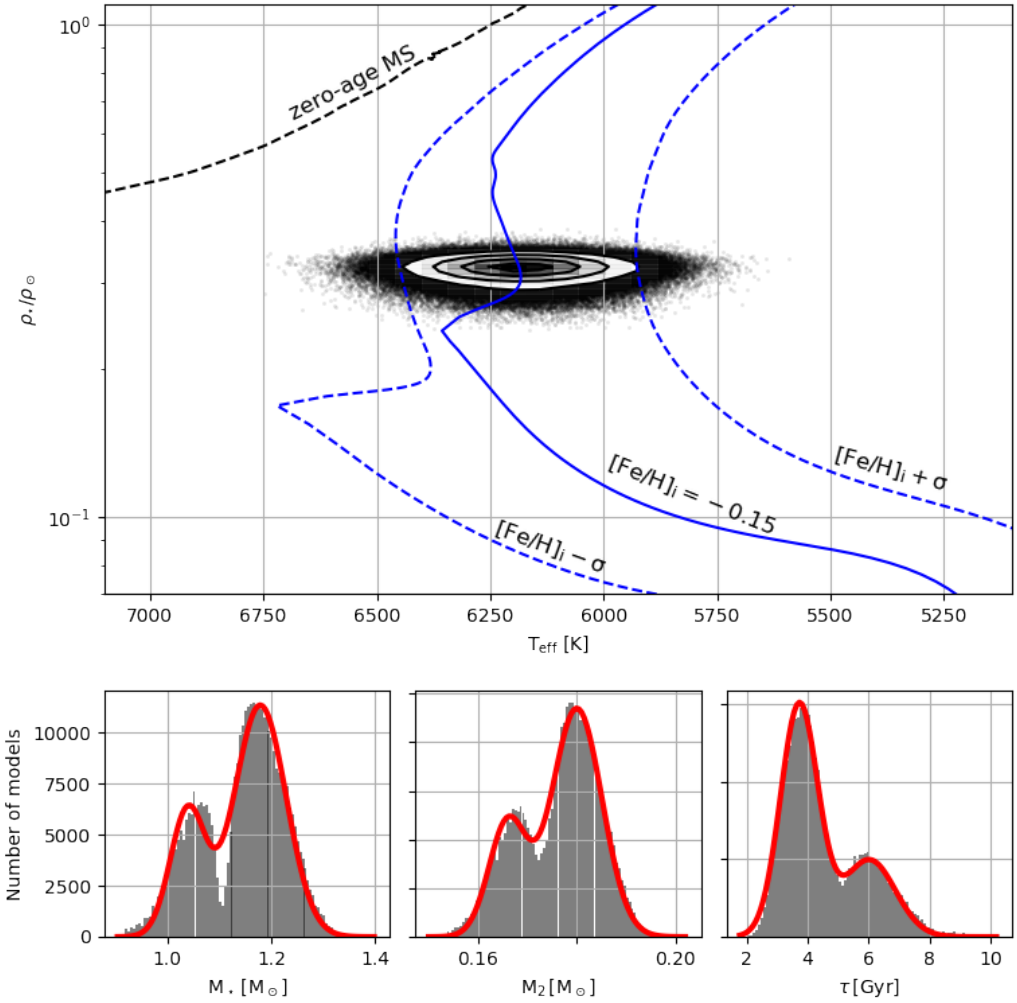

Figure 6.5: The PPD for the density and temperature of the primary star in J2308−46 is shown in the top panel. The zero-age main sequence is show(black-dashed) along with the best fitting isochrone (blue-solid) and the respective isochrones for ±1-σ in [Fe/H]. The lower panels show the PPD distributions for M_1, M_2 and τ with best-fitting double-Gaussian models in red.

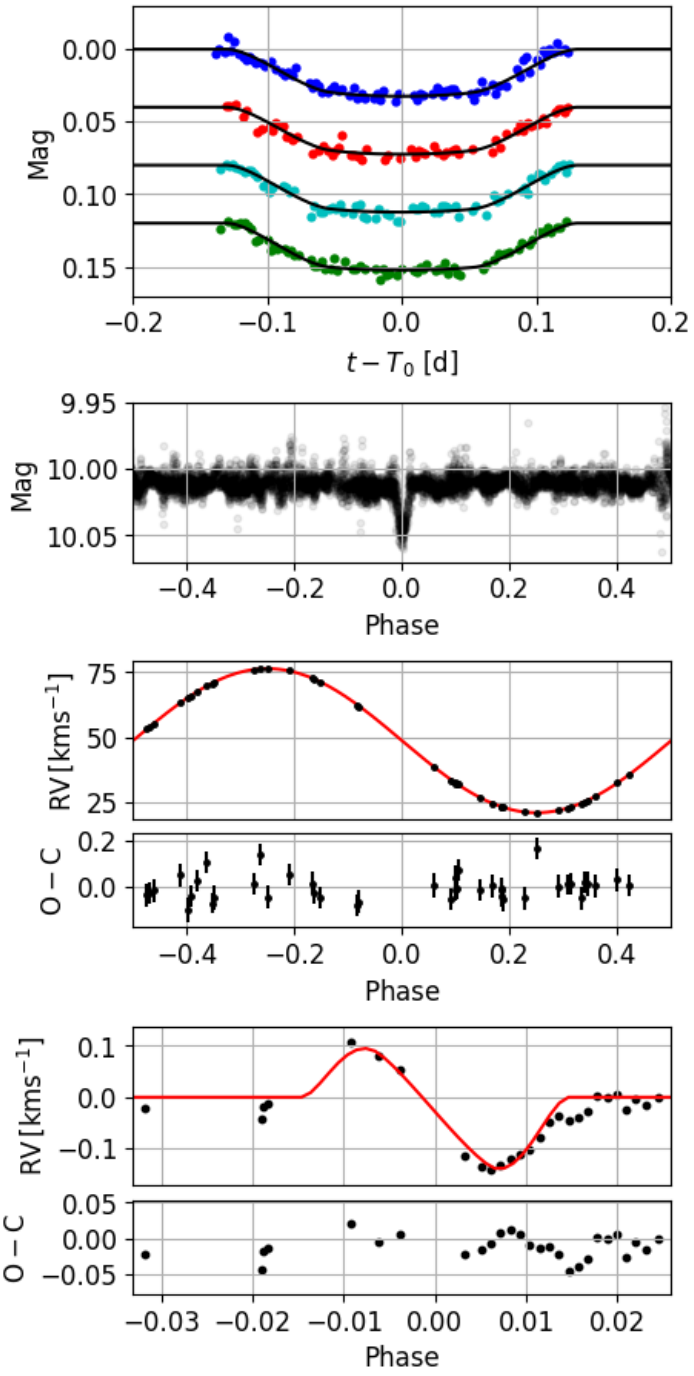

Figure 6.6: Orbital fit for EBLM J0218−31. (top panel) Transit photometry from CTIO in g' (blue), r' (red), i' (cyan) and z' (green) with best fitting models shown in black. (upper-middle panel) The phase-folded WASP lightcurve. (lower-middle panel) Drift-corrected radial velocity measurements from CORALIE with best fitting model plotted in red, along with residuals. (bottom panel) Drift-corrected radial velocity measurements during transit (the RossiterMcLaughlin effect; black) with the best fitting model (red). Error bars have been omitted for clarity.

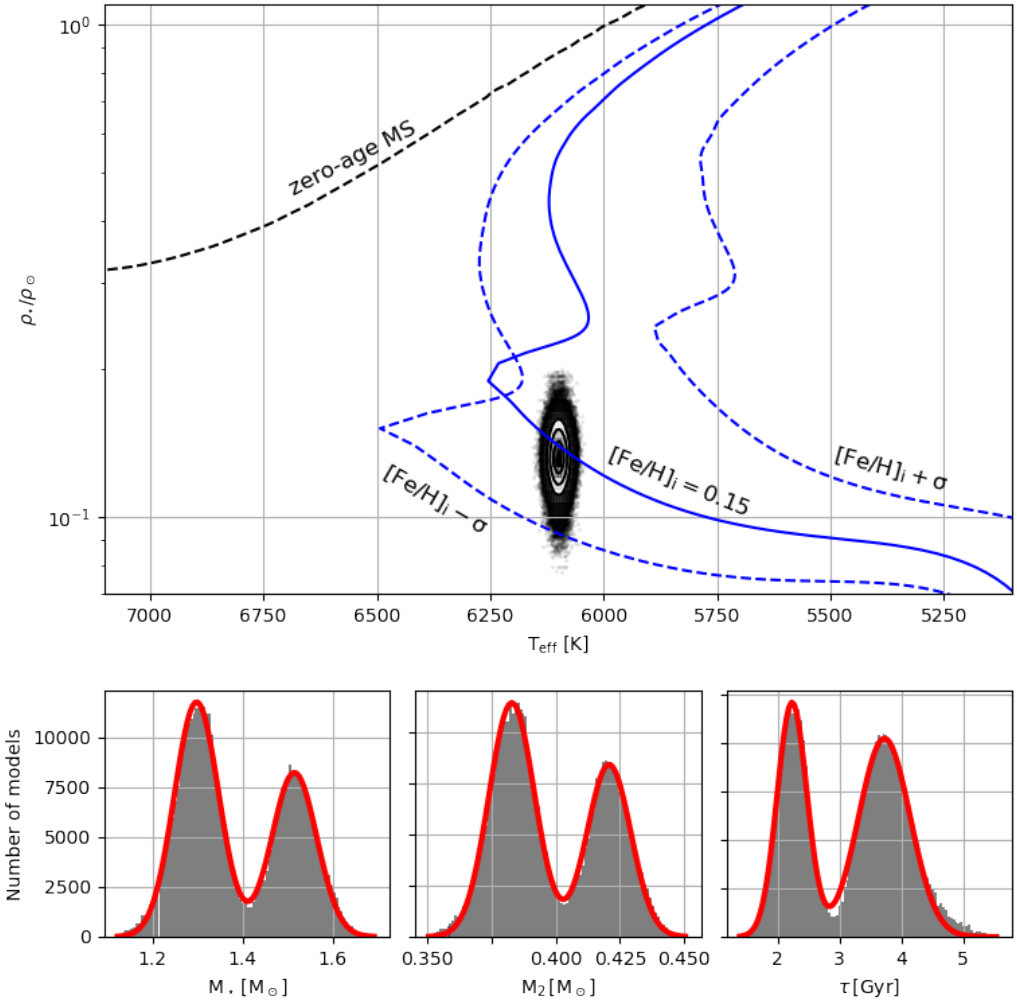

Figure 6.7: The PPD for the density and temperature of the primary star in J0218−31 is shown in the top panel. The zero-age main sequence is show(black-dashed) along with the best fitting isochrone (blue-solid) and the respective isochrones for ±1-σ in [Fe/H]. The lower panels show the PPD distributions for M_1, M_2 and τ with best-fitting double-Gaussian models in red.

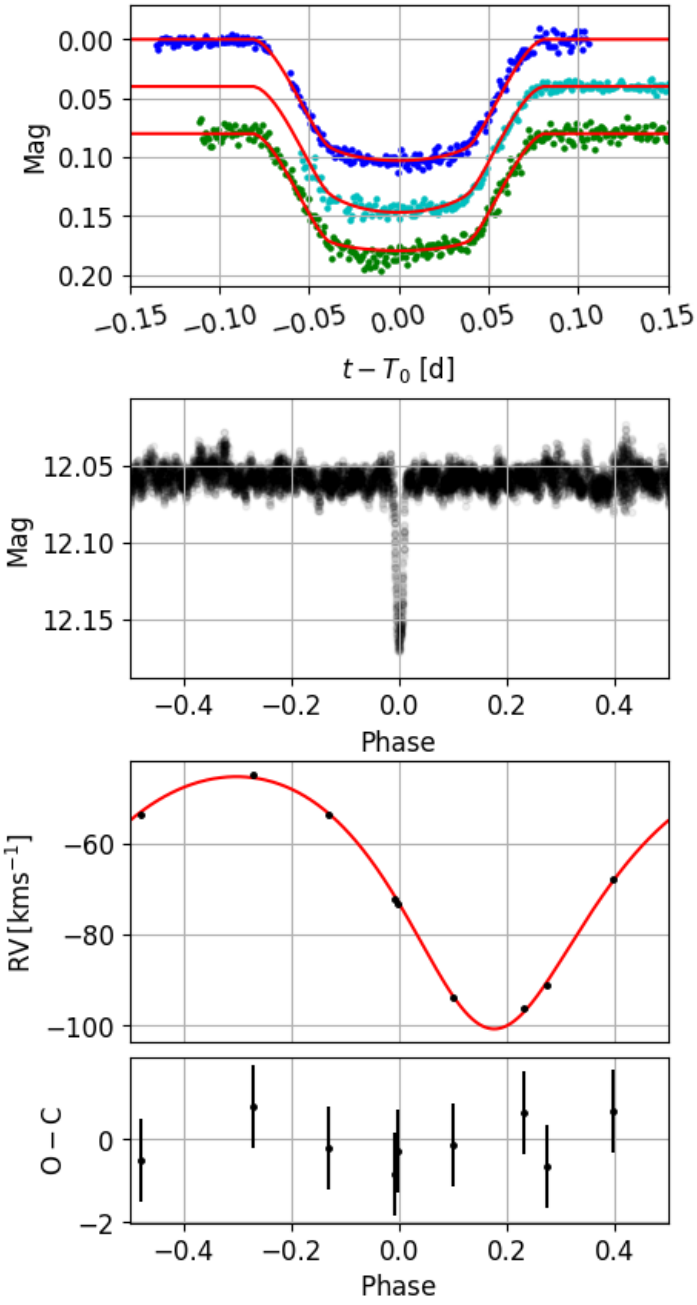

Figure 6.8: Orbital fit of EBLM J1847+39. (top panel) Single transits from the HAO in filters CBB (blue), g' (cyan) and z' (green) with best fitting models (red). (upper-middle panel) The phase-folded WASP lightcurve. (lower-middle panel) Drift-corrected radial velocity measurements (black) with the best fitting model (red) and residuals (lower panel).

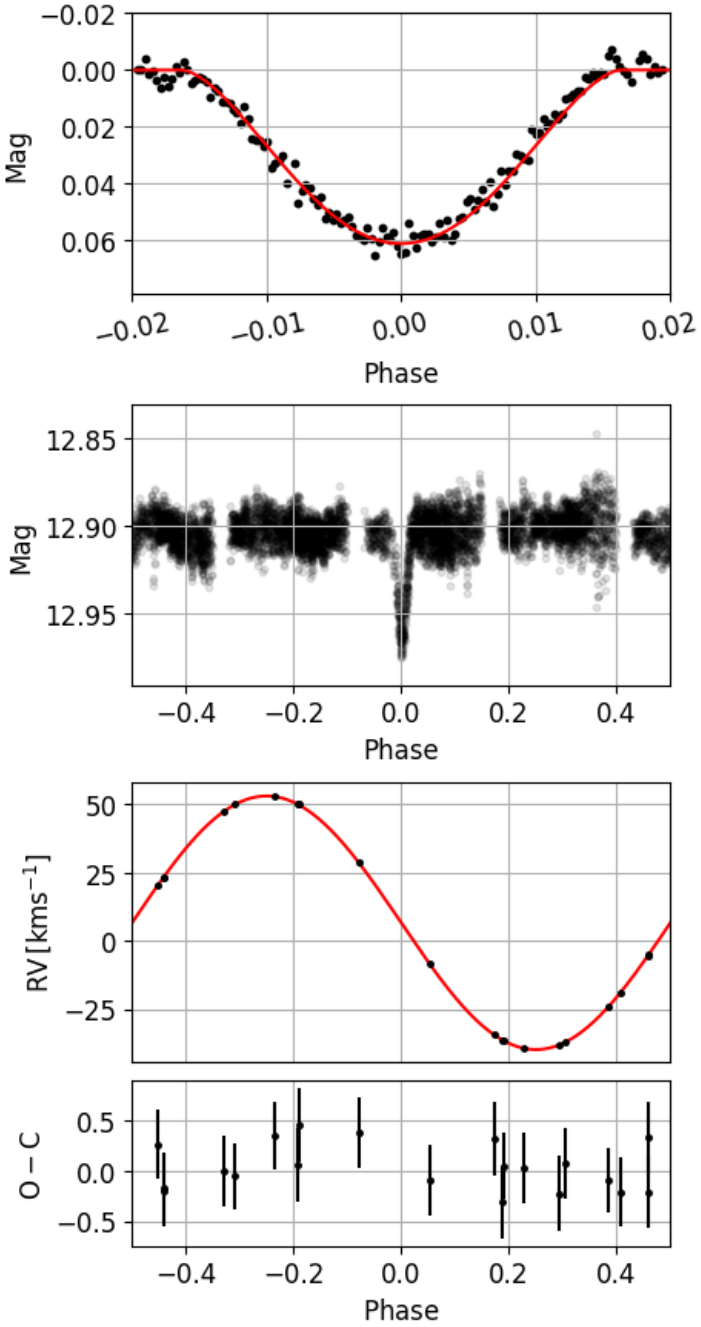

Figure 6.9: Orbital fit of EBLM J1436−13. (top panel) A single transit obtained from SAAO in R filter (black) and the best fitting transit model (red). (upper-middle panel) The phase-folded WASP lightcurve. (lower-middle panel) Drift-corrected radial velocity measurements (black) with best fitting model (red) along with residuals (lower panel).

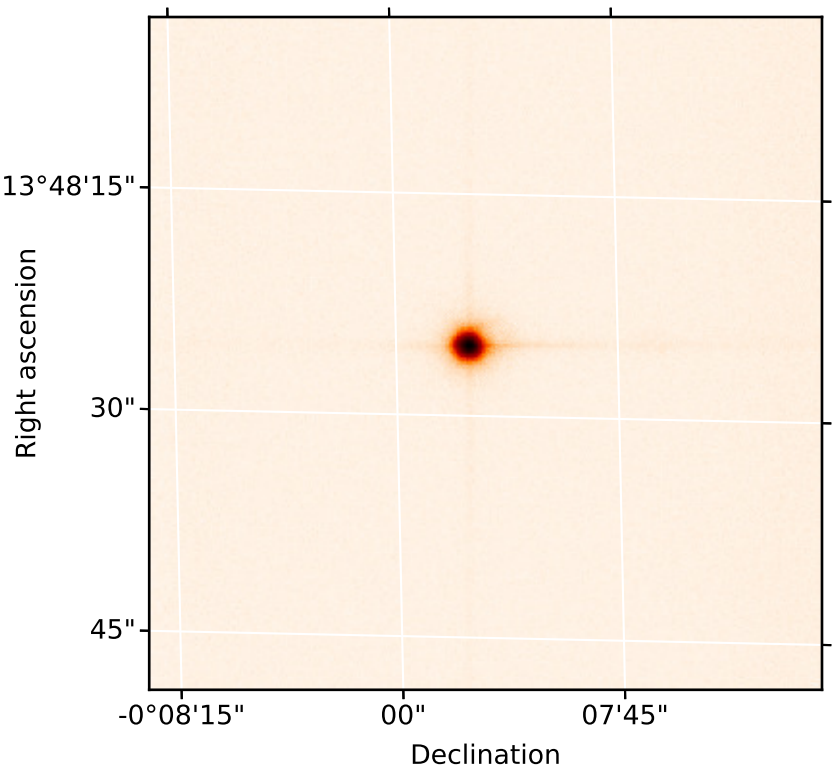

Figure 6.10: Lucky imaging of J0055−00 (red arm) where no close companions are observed.

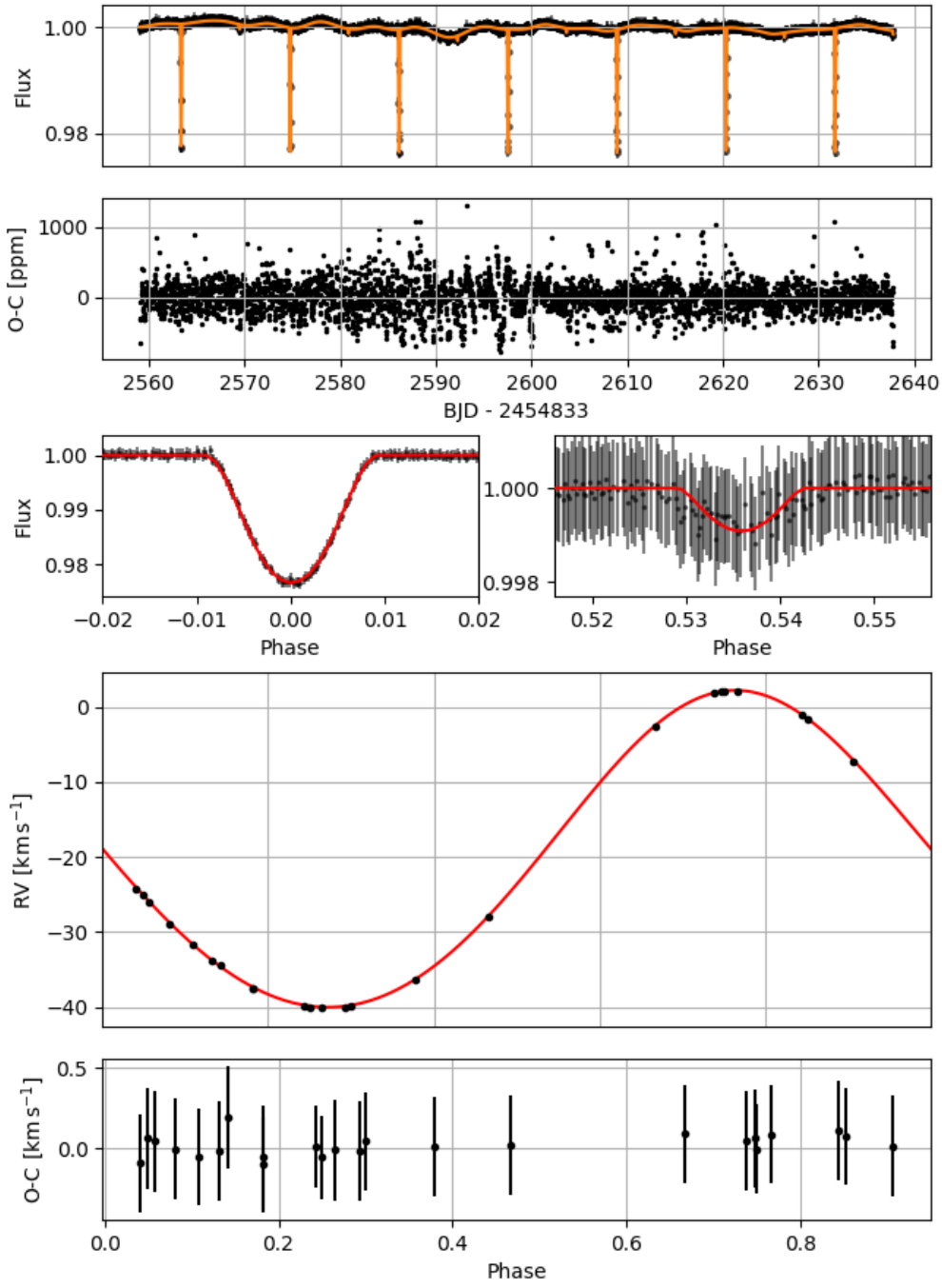

Figure 6.11: Orbital solution for J0055−00. Detrended K2 photometry (black) with model prediction using Gaussian processes (orange) is shown in the top panel with residuals in the panel below. Phase-folded K2 photometry for primary and secondary transits (black) are shown in the centre panels with best-fitting models (red). Drift-corrected radial velocity measurements are shown (black) along with the best-fitting model (red) and residuals are shown in the lower panels.

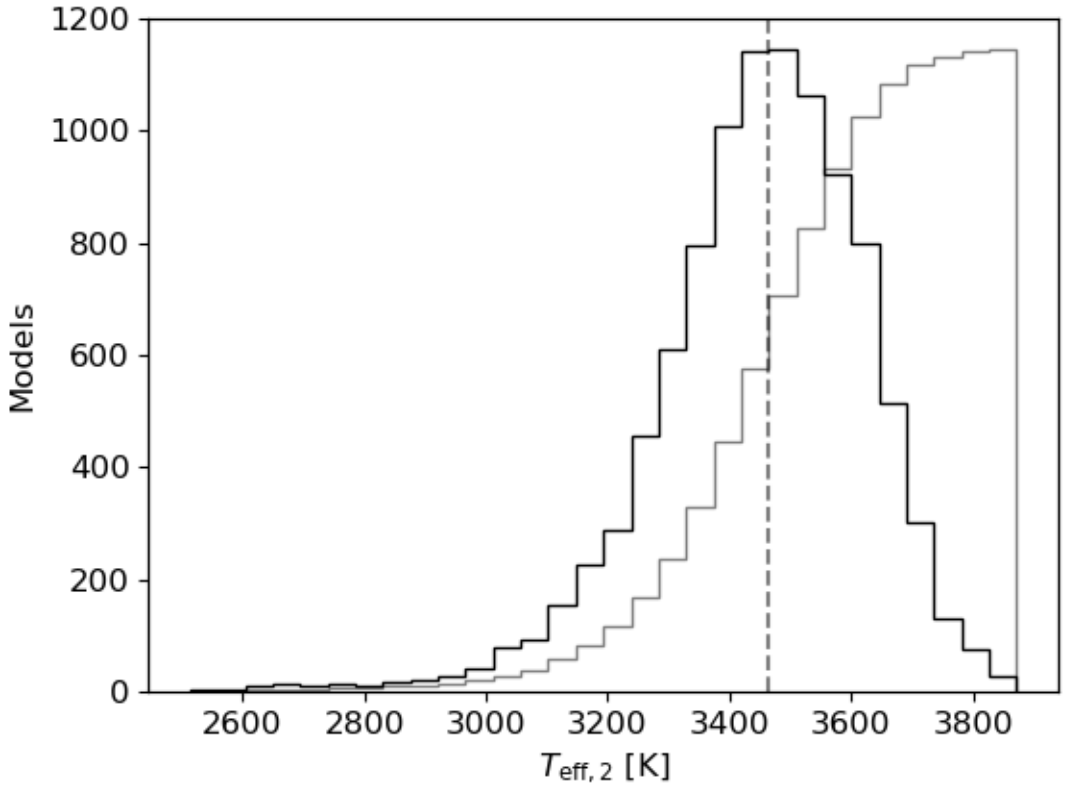

Figure 6.12: Posterior probability distribution of the M-dwarf temperature for J0055−00. I mark the median value (dashed) along with the cumulative distribution.

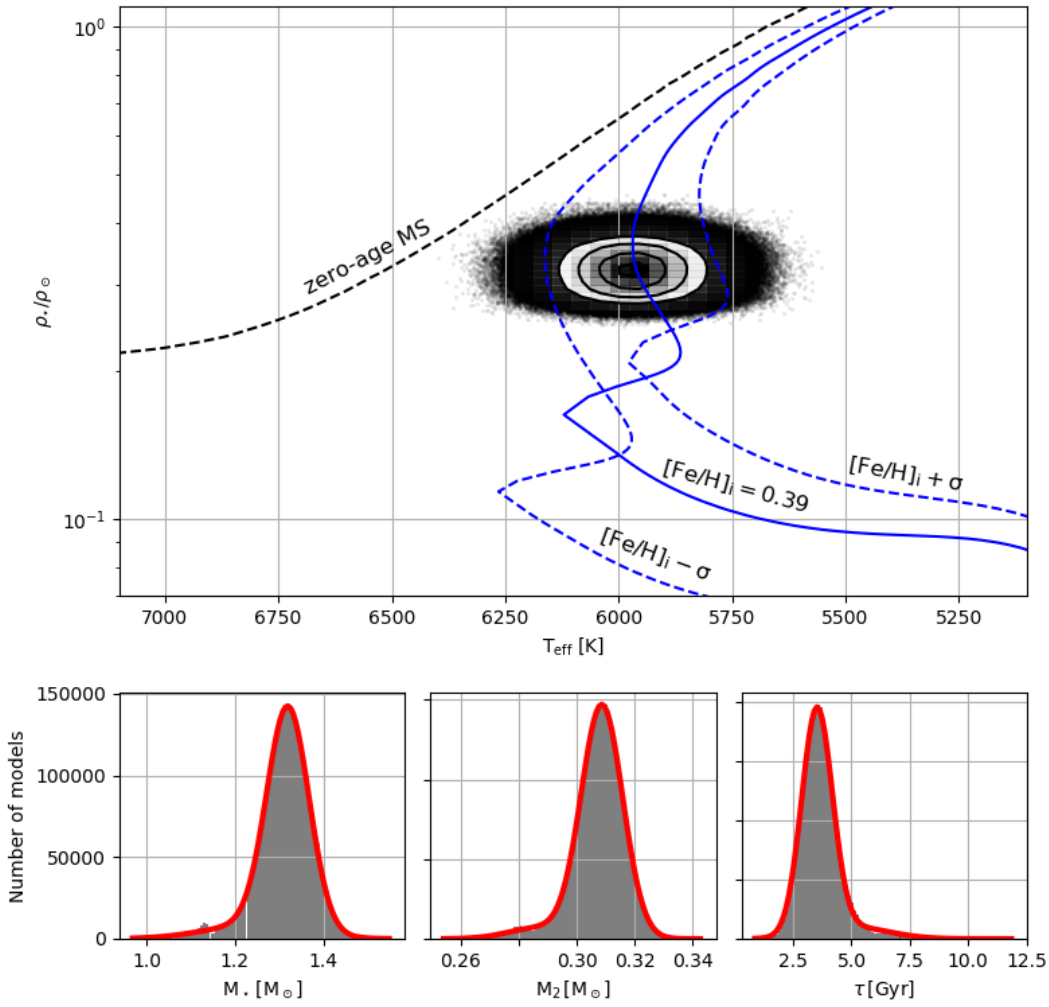

Figure 6.13: The PPD for the density and temperature of the primary star in J0055−00 is shown in the top panel. The zero-age main sequence is show(black-dashed) along with the best fitting isochrone (blue-solid) and the respective isochrones for ±1-σ in [Fe/H]. The lower panels show the PPD distributions for M_1, M_2 and τ with best-fitting double-Gaussian models in red.

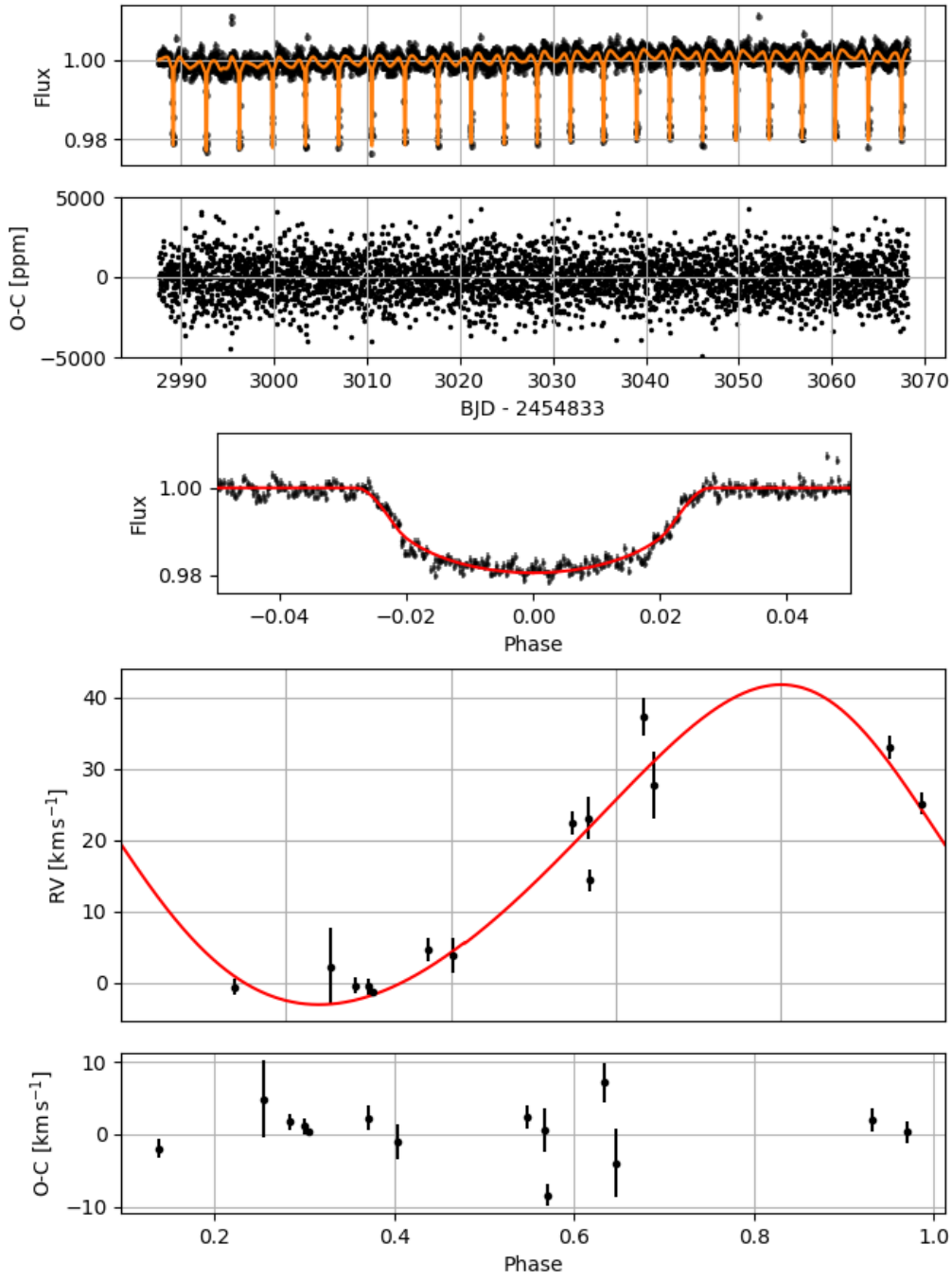

Figure 6.14: Orbital solution for J0547+14. Detrended K2 photometry (black) with model prediction using Gaussian processes (orange) is shown in the top panel with residuals in the panel below. Phase-folded K2 photometry for the primary eclipse (black) is shown in the centre panel with the best-fitting model (red). Drift-corrected radial velocity measurements (black) and the best-fitting model (red) are shown in the lower-middle panel, along with residuals in the bottom panel.

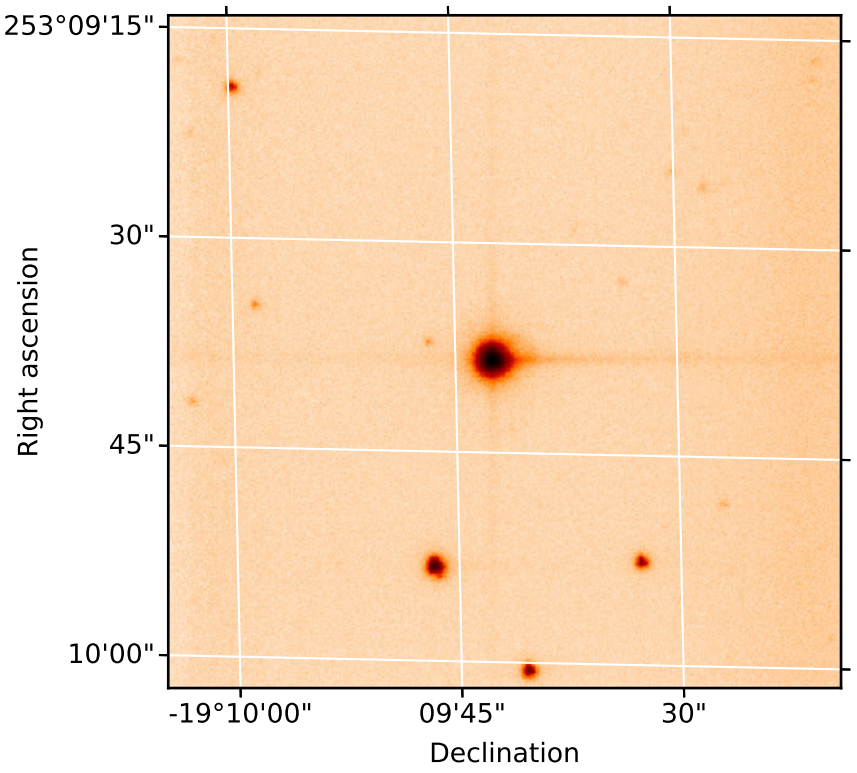

Figure 6.15: Lucky imaging of J1652−19 (red arm).

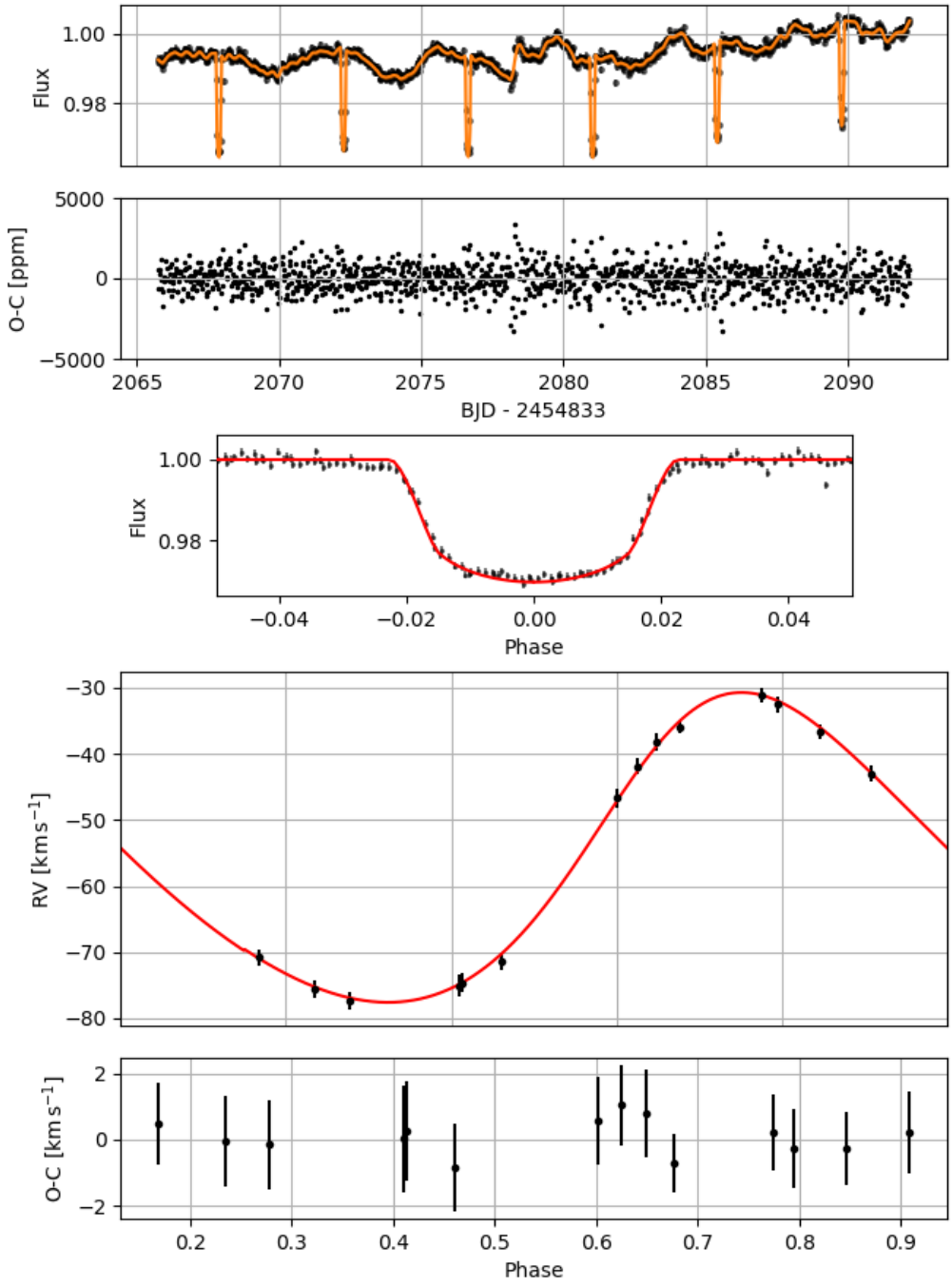

Figure 6.16: Orbital solution for J1652−19. Detrended K2 photometry (black) with model prediction using Gaussian processes (orange) is shown in the top panel with residuals in the panel below. Phase-folded K2 photometry for the primary eclipse (black) is shown in the centre panel with the best-fitting model (red). Drift-corrected radial velocity measurements (black) and best-fitting model (red) are shown in the lower-middle panel, along with residuals in the lower panel.

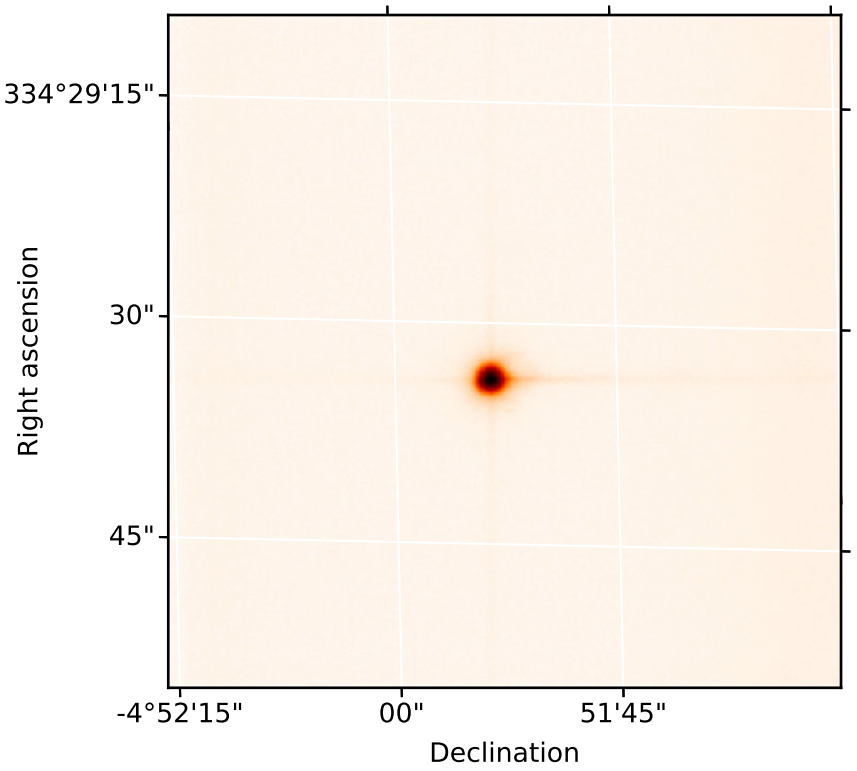

Figure 6.17: Lucky imaging of J2217−04 (red arm) showing no significant companions nearby..

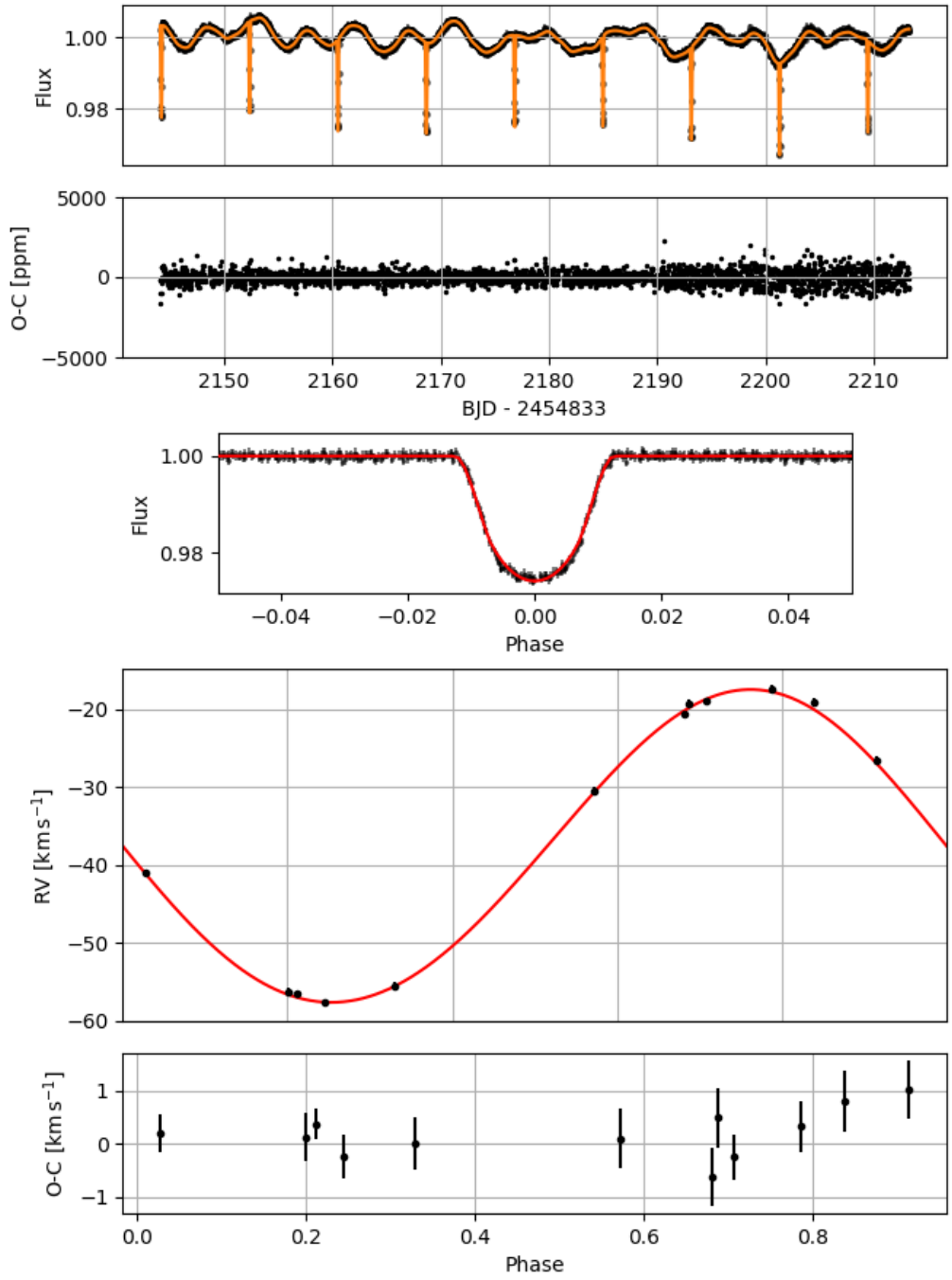

Figure 6.18: Orbital solution for J2217−04. Detrended K2 photometry (black) with model prediction using Gaussian processes (orange) is shown in the top panel with residuals in the panel below. Phase-folded K2 photometry for the primary eclipse (black) is shown in the centre panel with the best-fitting model (red). Drift-corrected radial velocity measurements (black) and best-fitting model (red) are shown in the lower-middle panel, along with residuals in the lower panel.

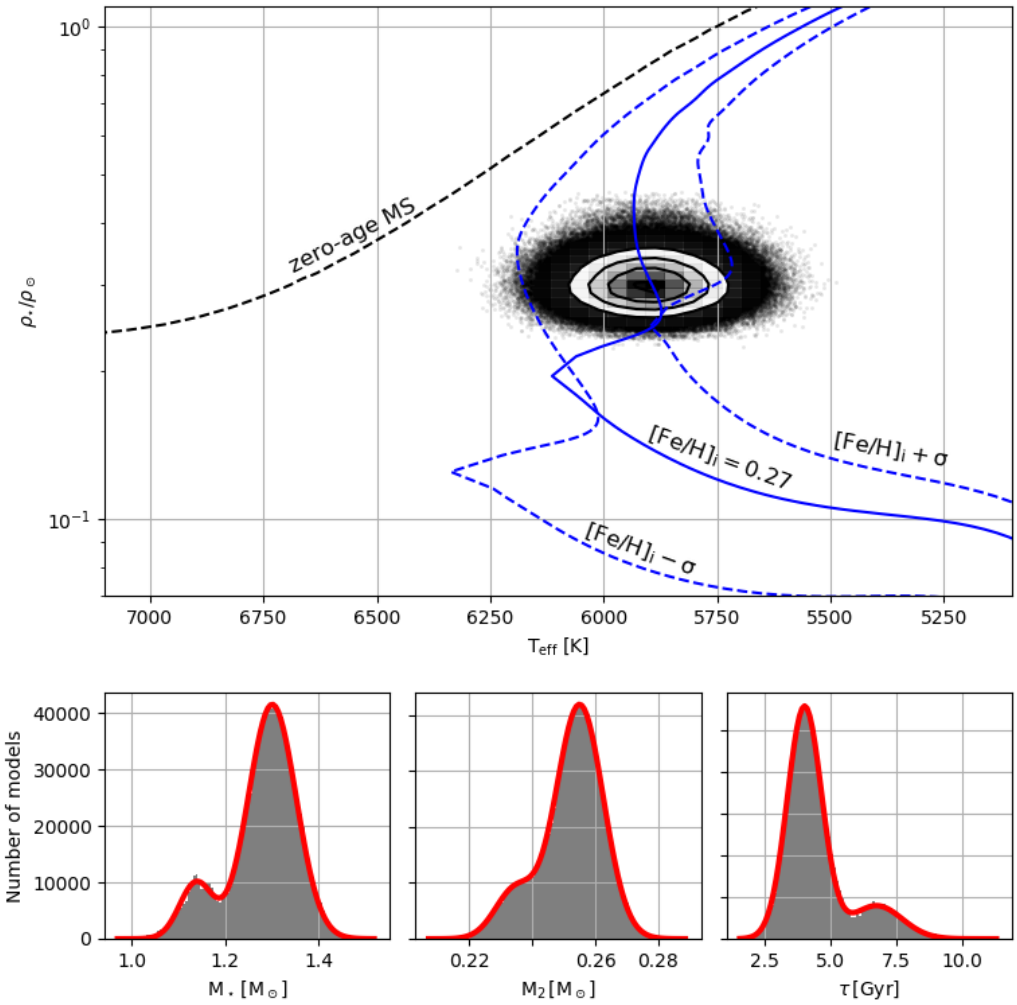

Figure 6.19: The PPD for the density and temperature of the primary star in J2217−04 is shown in the top panel. The zero-age main sequence is show(black-dashed) along with the best fitting isochrone (blue-solid) and the respective isochrones for ±1-σ in [Fe/H]. The lower panels show the PPD distributions for M_1, M_2 and τ with best-fitting double-Gaussian models in red.

7 Discussion

Fundamental properties of M-dwarfs in eclipsing binary systems is a fast progressing field in which new measurements are published frequently. I am aware that new measurements are currently being prepared and may be published during the writing of this work. Currently there are four instalments of the EBLM project; I have submitted the fifth instalment of the EBLM project to Astronomy & Astrophysics (five EBLMs observed with ground-based instruments) which is currently under review. The sixth instalment, authored by my collaborators, contains nine EBLMs which are not discussed here; this work has also been submitted and is under review. It is my intention to publish the four EBLM systems observed with K2 as the seventh instalment of the EBLM project in fore-coming months. To avoid re-writing this discussion numerous times, I will only discuss results published prior to 1st September 2018.

7.1 The mass-radius diagram

In Fig. 7.1, I plot the 5 Gyr isochrones for [Fe/H]= 0 dex (B15; Baraffe et al. 2015) and [Fe/H]= −0.5 dex (B98; Baraffe et al. 1998) and compare them to the nine EBLMs measured in this work. The B15 isochrones rectify some of the flaws in the models presented by Baraffe et al. (1998) (e.g. optical colours that are too blue). Visual inspection of the radii shows that they are broadly consistent with evolutionary models. The ground-based sample (red markers in Fig. 7.1) have a sub-solar metalicity and are expected to have radii between the B98 and B15 models. The K2 sample (cyan markers in Fig. 7.1) have supersolar metallicity and are expected to lie above the B15 isochrone.

Three EBLMs (J0218−31, J1436−13 and J0055−00) have high impact parameters leading to a larger uncertainty in $R_\star/a$, k and ultimately R_1 and R_2. The effect is most significant in J1436−13 and J0055−00 where the uncertainties in R_2 span across both B98 and B15 isochrones. The primary stars of five EBLMs (J2308−46, J0218−31, J0055−00,

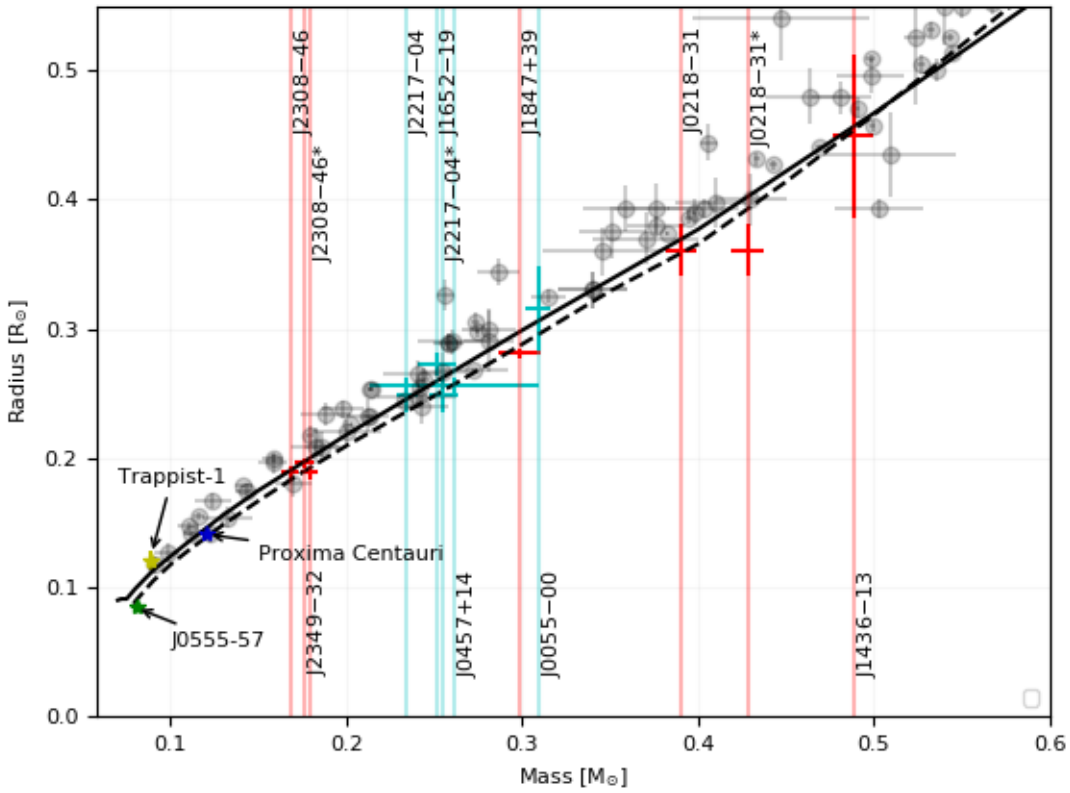

Figure 7.1: The mass and radius of 5 EBLMs from ground-based data (red) and 4 EBLMs observed with K2 (blue). Where present, an asterisk marks the younger solution for systems with two solutions of mass and age. The 5 Gyr isochrone for solar metallicity from Baraffe et al. (2015) is plotted (black-solid) along with the 5 Gyr isochrone for [M/H]= −0.5 from Baraffe et al. (1998) (black-dashed). I plot low-mass M-dwarfs with masses and radii known to better than 10% (from Table 4 of Chaturvedi et al. (2018) and references therein). For J2308−46, J0218−31 and J2217−04 I plot both solutions and label accordingly. I also plot TRAPPIST-1 (Delrez et al. 2018b), Proxima Centauri (Anglada-Escudé et al. 2016) and J0555−57 (von Boetticher et al. 2017).

J1652−19 and J2217−04) have evolved into the "blue-hook" part of their post main-sequence evolution, leading to two solutions of$M_\star$, M_2 and τ. Two of these systems (J0055−00 and J1652−19) have a single solution that is significantly favoured. The remaining three systems have solutions which are only marginally favoured and so I report both in Tables. 6.3 & 6.4 and Fig. 7.1 as a precaution.

7.2 Bayesian measurements of radius inflation

The traditional approach of interpolating between solar B98 ([Fe/H] = 0) and B15 ([Fe/H] = -0.5) isochrones of fixed age is not sufficient to assess inflation, especially for young systems below 1 Gyr which may still be contracting (e.g. J0457+14). A recent and well-sampled set of isochrones for low-mass stars are required to assess if the M-dwarf in each EBLM system is consistent with the isochrone for the respective measurement of [Fe/H] and τ. For this task, I used the MESA isochrones. The MESA isochrones are created using the protosolar abundances recommended by Asplund et al. (2009) as the reference scale for all metallicities; this is consistent with the grid of spectra from wavelet analysis (Chapter 4). MESA uses the OPAL equation of state tables from Rogers & Nayfonov (2002) along with opacity tables from Freedman, Marley & Lodders (2008), Yurchenko, Barber & Tennyson (2011) and Frommhold et al. (2010). MESA also includes complex treatments for microscopic diffusion and gravitational settling (both important for low-mass stars), radiative levitation (important for high-mass stars), rotation, convective overshooting, magnetic fields and mass-loss.

I used the web interpolater [1] to create a grid of MESA isochrones spanning the range [Fe/H]= −2 to +0.5 dex in steps of 0.5 dex and age range 0.8-9 Gyrs in steps of 0.2 Gyrs. Using this grid, I created a bi-linear interpolation routine (in dimensions of τ and [Fe/H]) to obtain an expected radius, $R_{2,\mathrm{exp}}$ for a given mass. To assess inflation, the following procedure was employed for each draw in the PPDs from EBLMMASS and the orbital solution:

1. $\log g_2$ can be calculated from the orbital solution using Eqn. 2.27.

[1] http://waps.cfa.harvard.edu/MIST/interp_isos.html

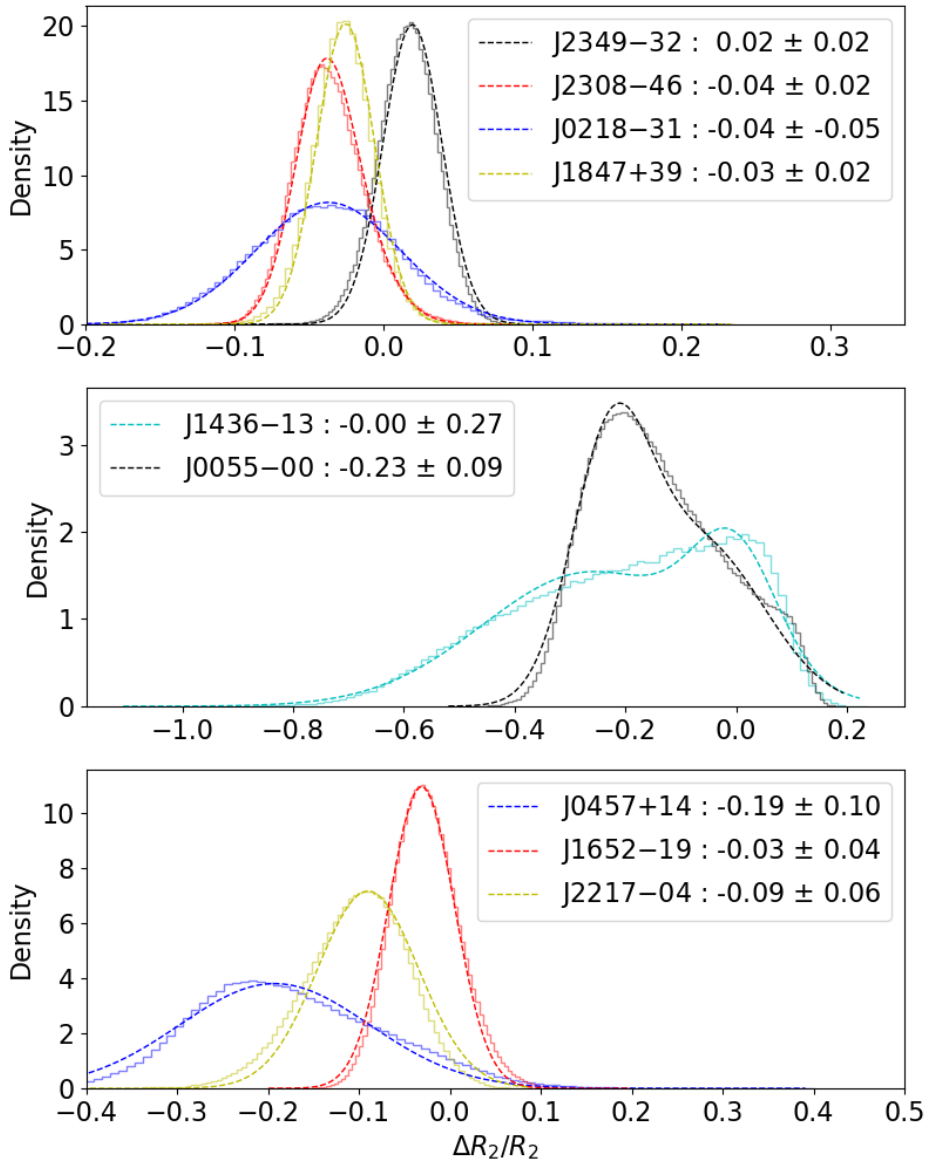

Figure 7.2: The fractional radius residual PPD for each EBLM system. The middle panel has the two EBLMs that have broader PPDs which require a double Gaussian model. Of those that are better described by a single Gaussian model, EBLMs with follow-up photomtery from the ground are shown in the top panel, and those observed with K2 in the bottom panel.

2. The corresponding draw for M_2 can be combined with $\log g_2$ to obtain the calculated value of R_2,

$$R_2 = \sqrt{\frac{GM_2}{g_2}}. \tag{7.1}$$

3. The corresponding draw for τ was used with a random value for [Fe/H] to interpolate a MESA isochrone. The random value of [Fe/H] was drawn from a Gaussian distribution of mean and width corresponding to the measurement of [Fe/H] and uncertainty of [Fe/H] reported in Table 6.2 respectively.

4. The corresponding draw of M_2 was used to interpolate an expected radius for the M-dwarf companion, $R_{2,\mathrm{exp}}$.

5. $R_{2,\mathrm{exp}}$ and R_2 can be combined to calculate the fractional radius residual,

$$\frac{\Delta R_2}{R_2} = \frac{R_2 - R_{2,exp}}{R_2}. \tag{7.2}$$

By repeating the above procedure for each step in the PPDs for EBLMASS and orbital fit, I was able to estimate the PPD for the fractional radius residual for each EBLM (Fig. 7.2). Four of the EBLMs with ground-based photometry along with three of those observed with K2 have narrow-peaked PPDs for $\Delta R_2/R_2$ (top and bottom panel of Fig. 7.2). For these, I calculated the nominal fractional radius by binning the PPD into 100 bins and fitted a Gaussian model; I took the mean of the fitted Gaussian to be the measurement of $\Delta R_2/R_2$ with uncertainty equal to the standard deviation. I found that a Gaussian shape is not a perfect fit to the PPDs of $\Delta R_2/R_2$; there are asymmetric discrepancies where one side of the Gaussian model is lower than the PPD, whilst the other is too high. On average, the under-prediction on one side and over prediction on the other are of the same magnitude and I assume the widths still accurately represent the mean uncertainty of $\Delta R_2/R_2$. The fitted models for J2308−46 and J0457+14 do not align well enough with the peak of the PPDs; the peak of the PPD was used as the measurement of $\Delta R_2/R_2$ with the same uncertainty from the fitted model.

J0055−00 and J1436−13 have significantly higher impact parameters which broadens the PPD for R_2 and thus, $\Delta R_2/R_2$ (middle panel of Fig. 7.2). I approximate this shape with

a double Gaussian, and use an identical routine used to measure the double-peaked PPDs in Sect. 5.7. The fit for J0055−00 is better than J1436−13. As a precaution, I used the peak of the PPDs for J0055−00 and J1436−13 as the measurement of $\Delta R_2/R_2$ with uncertainty equal to the standard deviations of each fitted Gaussian added in quadrature.

The majority of systems appear deflated with respect to the MESA isochrones with no obvious differences between the top and bottom panels of Fig. 7.2. J2308−46, J0218−31 and J2217−04 have double-peaked distributions for M_2 and τ and I expected the PPDs for $\Delta R_2/R_2$ to be shaped similar since M_2 is used to calculate R_2, and combined with τ to estimate $R_{2,\mathrm{exp}}$. In creating the PPD for R_2 (Eqn 7.1), the division of the PPD for M_2 with the PPD for g_2 diminishes the double-peaked nature observed in the PPD M_2, leading to a Cauchy-like PPD for R_2. The interpolated value of $R_{2,\mathrm{exp}}$ is dependent on τ and M_2 which are both double peaked. $R_{2,\mathrm{exp}}$ is not expected to have a double-peaked PPD as each combination of τ and M_2 was a trial step in EBLMMASS and will correspond to a similar expected radii (i.e. higher values of τ will correspond to lower values of M_2 and vice-versa). Thus the PPD for $\Delta R_2/R_2$ is single peaked with width controlled by the uncertainty in M_2, g_2 and [Fe/H].

7.2.1 Effect of stellar metalicity

Stellar metallicity directly affects the whole structure of a star. Most of the EBLMs have a metallicty uncertainty of 0.06 dex (excluding J0457+14 and J1847+39). The uncertainty in metallicity changes the value of $R_{2,\mathrm{exp}}$, and thus increases the uncertainty in $\Delta R_2/R_2$; this is visualised in the top panel of Fig. 7.3. Although age dependent, I found the uncertainty in $\Delta R_2/R_2$ increases between 0.005 and 0.015 depending on M_2. These uncertainties are comparable to the PPD widths of $\Delta R_2/R_2$ for J2349−32, J2308−46 and J1847+39 and suggests that uncertainty in [Fe/H] is one of the dominant sources of uncertainty in $\Delta R_2/R_2$ for EBLMs. Uncertainty in τ is typically between 0.13 - 1.78 Gyr. In the bottom panel of Fig. 7.3, an uncertainty of 0.5 Gyr can lead to an uncertainty in $\Delta R_2/R_2$ comparable with Δ[Fe/H] = 0.06 dex for stars just below the convective transition.

The metal content of M-dwarfs has been suggested to correlate with inflation (Feiden & Chaboyer 2014; Feiden 2016; Demory et al. 2009). The fractional radius residual of

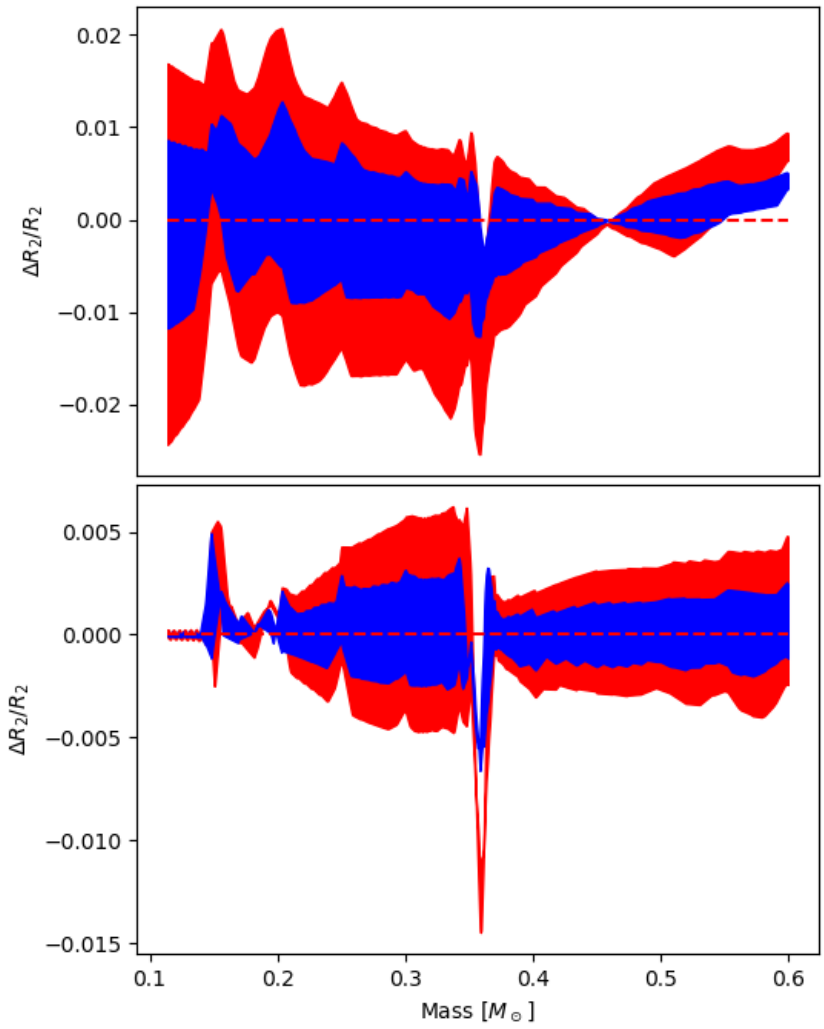

Figure 7.3: The difference in fractional radius residuals of M-dwarfs from MESA evolutionary models relative to a 5 Gyr isochrone with solar metallicity. (top panel) The difference in fractional radius residuals for an uncertainty of Δ[Fe/H]= 0.06 (blue) and Δ[Fe/H]= 0.12 (red) at a constant age of 5 Gyr. (bottom panel) The difference in fractional radius residuals for an uncertainty of $\Delta\tau$ = 0.5 Gyr (blue) and $\Delta\tau$ = 1 Gyr (red) at [Fe/H]= 0.

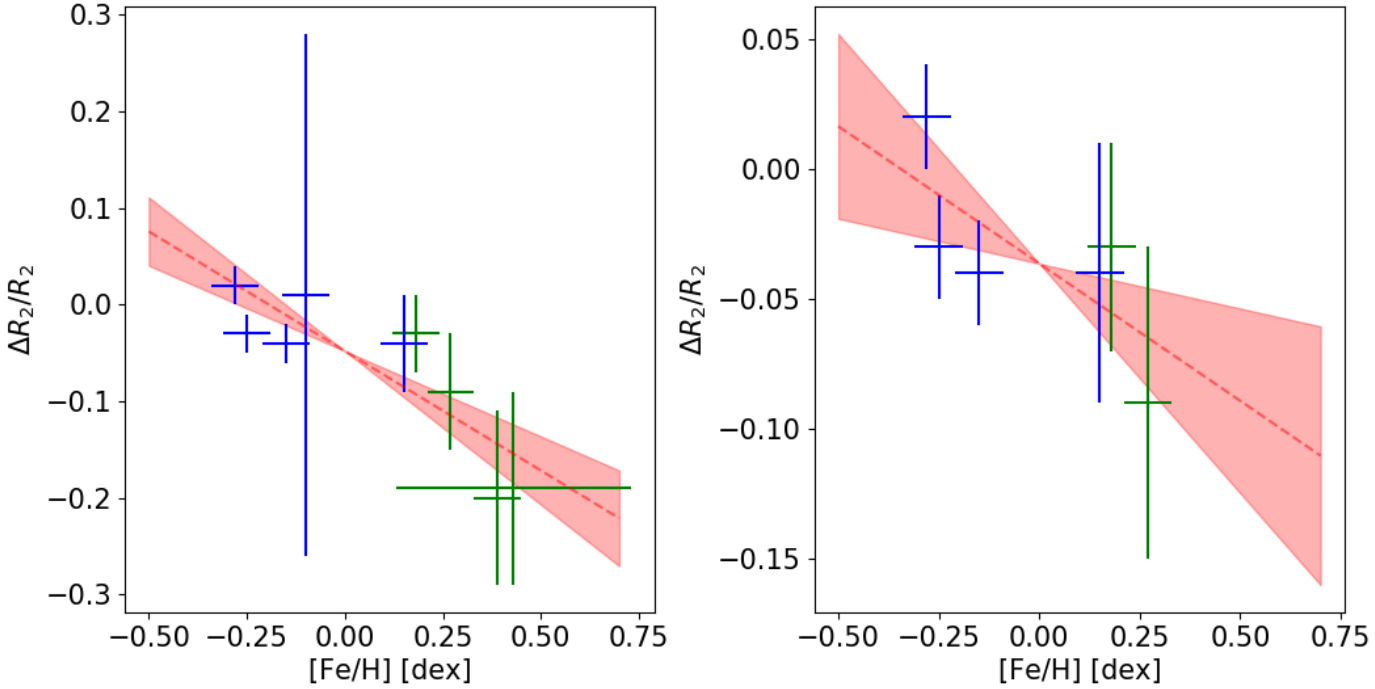

Figure 7.4: The fractional radius residual for all EBLMs measured in this work as a function of [Fe/H] (left panel). The same is also shown with J1436−13, J0055−00 and J0457+14 excluded (right panel). For each panel, I plot the best-fitting linear fit (red-dashed) with 1-σ uncertainties in the gradient (red fill).

nine EBLMs presented in this work are plotted against [Fe/H] in Fig. 7.4. There appears to be a negative correlation between [Fe/H] and $\Delta R_2/R_2$ for all EBLMs (left panel of Fig. 7.4). A Pearson correlation coefficient (Britain 1895) is measured to be -0.84, indicating a strong, negative correlation between [Fe/H] and $\Delta R_2/R_2$. A Pearson correlation coefficient may not be reliable for only nine data-points, but nevertheless aids the interpretation of any correlation. I fitted a 1st-order polynomial to determine the best linear model using linear regression,

$$\frac{\Delta R_2}{R_2} = (-0.247 \pm 0.071) \times [\mathrm{Fe/H}] - (0.048 \pm 0.019). \tag{7.3}$$

I also fitted a 1-parameter model, $\Delta R_2/R_2 = c$, where $c = -0.065 \pm 0.001$. I compared both models using the Bayesian information criterion,

$$BIC = \chi^2 + k \log_e(n), \tag{7.4}$$

where k is the number of parameters for a given model and n is the number of data points. If the standard error estimates for the data are reliable and the errors are normally distributed then the values of the BIC can be used to compare models with different numbers of free parameters. In general, the model with the lowest BIC will give the optimum balance between the number of free parameters in the model and the goodness-of-fit. Assessing models can be done by calculating the difference in BIC between the best model and the competing model. As a rule of thumb, a $\Delta BIC < 2$ means that neither model is favoured, $\Delta BIC = 2$–3 means that there is moderate evidence to suggest the model with the lowest BIC is favoured and a $\Delta BIC > 6$ means that the evidence for the best model against the weaker model is strong. The linear and 1-parameter model have $BIC s$ of 6.56 and 2.42 respectively, suggesting that the 1-parameter model is favoured. The $\Delta BIC = 4.41$ is moderate evidence to favour the 1-parameter model over the linear fit.

Some of these EBLMs are not suitable to assess inflation. For example, the high impact parameters of J1436−13 and J0055−00 broaden the PPD for $\Delta R_2/R_2$ to the extent in which they are no use for empirical calibrations or tests of evolutionary models. J0457+14 is a young, hot and fast rotating F-type star for which the M-dwarf companion's radius will still be contracting in the pre-main sequence. The uncertainty in $\Delta R_2/R_2$ for J0457+14 largely stems from an uncertain measurement of [Fe/H] as there are few measurable iron lines from

which a reliable measurement of [Fe/H] can be obtained. I repeated these fits by excluding J1436−13, J0055−00 and J0457+14 (right panel of Fig. 7.4). I found the best-fitting linear model,

$$\frac{\Delta R_2}{R_2} = (-0.105 \pm 0.071)[\mathrm{Fe/H}] - (0.036 \pm 0.016), \tag{7.5}$$

with a $BIC = 10.35$. I tested for a 1-parameter model and found $c = -0.035 \pm 0.001$ with a $BIC = -4.48$. A $\Delta BIC = 14.82$ is strong evidence to favour a 1-parameter fit. This suggests that trend with metallicity is statistically insignificant in both subsets; the absolute parameters of many more EBLMs are required to statistically assess any correlation between inflation and metallicity.

The problem is somewhat complicated by the two different sources of EBLMs: those with ground-based follow-up photometry and those observed with K2 (blue and green markers in Fig. 7.4). Both groups had different lightcurve models, treatments of limb-darkening and red-noise models which may bias measurements of $\Delta R_2/R_2$. The ground-based sample shows little evidence of any trend with [Fe/H] whilst the K2 sample appears to become increasingly deflated as metallicity increases. The validity of such conclusions is subject to interpretation as there is only a small sample size in each group.

If there are missing sources of opacity in the stellar models of low-mass stars, it may well be correlated with individual elemental abundances rather than [Fe/H] which implicitly assumes a metal scaling similar to the Sun. The grid of spectra used to measure the atmospheric parameters for these systems assumes solar abundances from Asplund et al. (2009). I am the principle investigator of a SALT proposal (2017-1-SCI-041) to investigate if this is the case. I submitted a target list of 40 EBLM systems from Triaud et al. (2017) as a priority 4 proposal. In total, 30 were observed between 19^{th} May 2017 and 7^{th} August 2017 using SALT's high-resolution spectrograph (HRS) in medium resolution mode ($R \approx 37,000$). These observations were made in long slit mode with an exposure time scaling as a function of magnitude to ensure a S/N$\geq$ 100. In future work, I will measure individual abundances for each spectra and look for correlations with inflation. At the time of writing this thesis, only 4 of the 30 EBLMs that have been observed with SALT have reliable measurements of masses and radii. In future, TESS lightcurves in combination with more 1-m class telescope

time will allow me to test this hypothesis.

7.2.2 Orbital period and stellar radii

EBLMs in tight orbits are more likely to be circularised and coerced into regimes of fast rotation. If this changes the magnetic structure of the M-dwarf leading to inflation, I would expect to see a clear link between orbital period and fractional radius residual. In Fig. 7.5, I plot the fractional radius residual as a function of orbital period. There are no obvious correlations in Fig. 7.5; Pearson correlation coefficients are -0.44 and -0.52 for the left and right panels respectively. This suggests that there is a moderate negative correlation but is far from conclusive. The BICs for the 1-parameter fits are significantly lower than the linear counterpart ($\Delta BIC = 2.84$ and 2.12 for the left and right panels of Fig. 7.5) suggesting a 1-parameter model best describes the correlation between fractional radius residual and orbital period. I conclude that there is no clear correlation between inflation and orbital period for the nine EBLMs in this work.

7.3 Systematic effects on determining mass, radius and age

The following section was written for a recently submitted paper which concerns only the EBLMs with follow-up photometry from ground-based instruments (J2349−32, J2308−46, J0218−31, J1847+39 and J1436+13). Subsequently, all discussion in this section refers only to these systems.

One major issue remains with the method employed in this work and previous publications of the EBLM project: I am attempting to test evolutionary models of low-mass stars using the models of better-understood F-/G-dwarfs. This method is acceptable when the uncertainty propagated by stellar models for F-/G-stars are much smaller than the propagated uncertainties in radial velocity measurements and transit photometry. This is not necessarily the case for the data I have used in work since it is possible to measure some orbital parameters listed in Chapter 6 to better than a 0.2%. In the following sections, I explore some

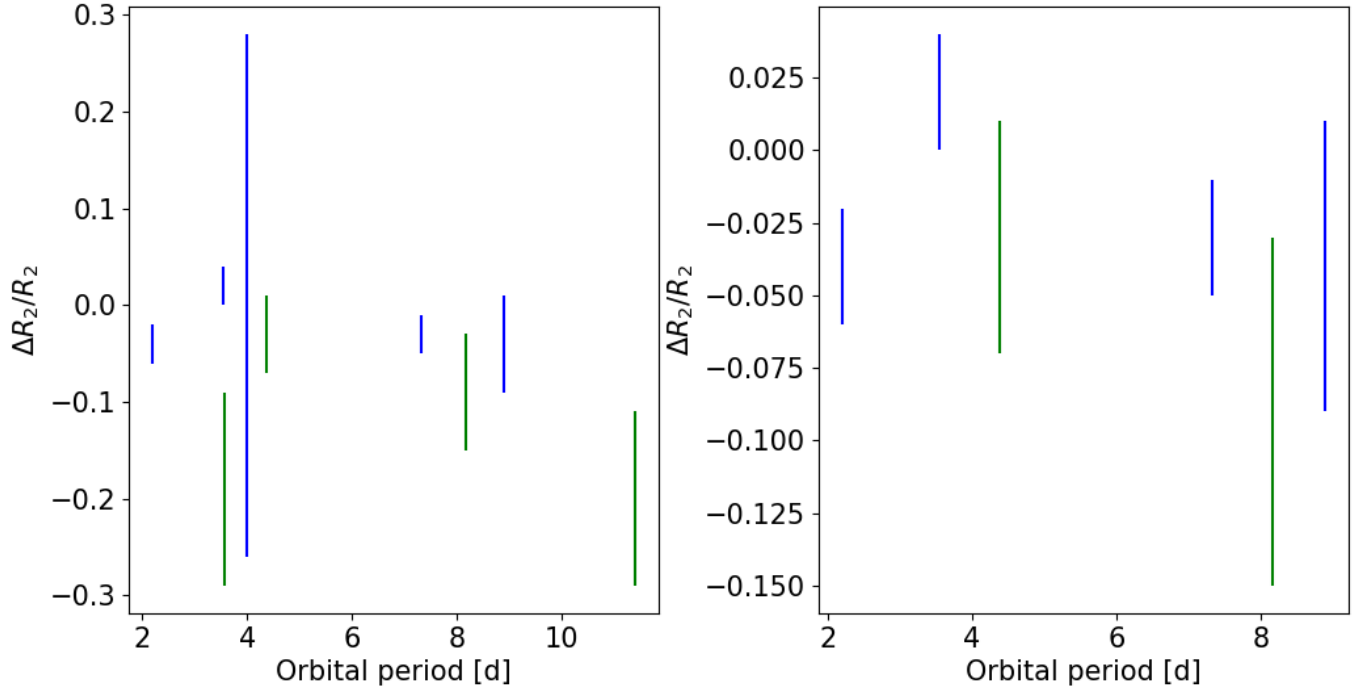

Figure 7.5: The fractional radius residual for all EBLMs measured in this work as a function of orbital period (left panel). The same is also shown with J1436−13, J0055−00 and J0457+14 excluded (right panel).

systematic sources of uncertainty arising from using evolutionary models to determine the primary star, along with the impact of unresolved blends and choice of limb-darkening.

7.3.1 Evolution ambiguity, $\alpha_{\rm MLT}$ and $Y_{\rm He}$

The default model grid used in EBLMMASS uses a mixing length parameter $\alpha_{MLT} = 1.78$ and an initial helium abundance $Y = 0.26646 + 0.984\,Z$, both of which have been calibrated on the Sun. As noted by Maxted, Serenelli & Southworth (2015a), these assumptions are subject to some level of uncertainty. Maxted, Serenelli & Southworth (2015b) estimated the uncertainty in mass, $M_\star$, and age, τ, for 28 transiting exoplanet host stars by assuming an error of 0.2 in α_{MLT} and 0.02 for initial helium enhancement, ΔY for each star. They found that systematic errors in mass and age from Y and α_{MLT} can be comparable to the random errors in these values for typical observational uncertainties in the input parameters. The sample measured by Maxted, Serenelli & Southworth (2015b) consists primarily of stars less massive than the Sun, whereas the primary stars in this work are more massive F-type stars. Three grids of models are provided with EBLMMASS: 1. $\alpha_{MLT} = 1.78$, $\Delta Y = 0.00$, 2. $\alpha_{MLT} = 1.5$, $\Delta Y = 0.00$ and 3. $\alpha_{MLT} = 1.78$, $\Delta Y = 0.02$; I used grid 1 in Tables 6.3 & 6.4. I re-measured the mass, radius and age of both components with the grids 2 and 3 to see how the uncertainties in $\alpha_{\rm MLT}$ and ΔY impact our results. I used grid 2 to assess the impact of $\Delta\alpha_{MLT} = 0.28$ and grid 3 to assess the impact of $\Delta Y = 0.02$; I used the same orbital solution and atmospheric parameters from Chapter 6.

The mass uncertainties ($\Delta M_\star$ and ΔM_2) in Table 7.1 corresponding to $\Delta\alpha_{MLT} = 0.28$ are $\approx 2-3\%$, and are similar to those found by Maxted, Serenelli & Southworth (2015b). Helium enhancement typically introduces larger mass uncertainties $\approx 4-5\%$. The opposite is seen for τ determinations, where a value of $\Delta\alpha_{MLT} = 0.28$ introduces an uncertainty of 1.07 Gyr and $\Delta Y = 0.02$ introduces an uncertainty of $\Delta\tau = 0.86$ Gyr. The typical uncertainty in τ from EBLMMASS for these EBLM systems is around 1 Gyr which can produce significant systematic offsets. The quadratic combination of uncertainty for M_2 introduced by α_{MLT} and Y is around 0.01 $M_\odot$ (3% for a $0.4-M_\odot$ M-dwarf).

Table 7.1: The difference in mass and radius of the primary star ($\star$) and the secondary (2) for a variety of different scenarios. The measured values were subtracted from those in Table. 6.3. For J2308-46 and J0218-31, I only considered the most probable solution in this work. I separately re-fitted with 10 % third light ($l3$) and using the quadratic limb-darkening law over the Claret law (ldy) from which I re-measured only the radii of the stars in the systems. I also separately recalculate the masses of the stars in each system by changing mixing length parameter from 1.50 to 1.78 (α_{mlt}) and a change in helium enhancement values from 0.00 to 0.02 (ΔY). I also show the mean of each column, $\bar{x}$, calculated with all values excluding those from J1436-13 (marked with an asterisk).

	$\Delta R_{\star,\,l3}$	$\Delta R_{2,\,l3}$	$\Delta R_{\star,\,ldy}$	$\Delta R_{2,\,ldy}$	$\Delta M_{\star,\,\alpha_{mlt}}$	$\Delta M_{2,\,\alpha_{mlt}}$	$\Delta \tau_{\alpha_{mlt}}$	$\Delta M_{\star,\,Y}$	$\Delta M_{2,\,Y}$	$\Delta \tau_{Y}$
J2349-32	−0.002	−0.016	−0.014	−0.002	−0.037	−0.004	2.208	0.048	0.005	−0.853
J2308-46	−0.003	−0.011	−0.017	−0.001	−0.045	−0.003	1.703	0.056	0.004	−1.201
J0218-31	−0.007	−0.012	−0.005	−0.002	−0.057	−0.001	0.503	0.041	0.006	−0.254
J1847+39	−0.008	−0.016	−0.015	−0.004	−0.046	−0.001	1.071	0.052	0.009	−0.820
J1436-13*	−0.162	−0.064	−0.059	−0.090	−0.024	−0.005	−0.135	0.043	0.011	−1.150
$\bar{x}$	−0.005	−0.013	−0.012	−0.003	−0.046	−0.002	1.070	0.050	0.007	0.855

Table 7.2: Distance measurements from Gaia DR2. I also report the orbital separation corresponding to a sky-projected separation of 0.3" for each EBLM system and the orbital period associated with this separation using $M_\star$ from Table 6.3.

EBLM	Parallax [mas]	d [pc]	Orbital separation at 0.3" [au]	Period [yr]
J2349-32	3.881 ± 0.108	257 ± 7	382 ± 6	18.95 ± 0.13
J2308-46	2.299 ± 0.127	435 ± 24	666 ± 27	23.80 ± 0.44
J0218-31	3.874 ± 0.108	258 ± 7	393 ± 6	15.91 ± 0.12
J1847+39	3.695 ± 0.109	271 ± 8	411 ± 5	19.88 ± 0.11
J1436-13	2.175 ± 0.112	460 ± 23	705 ± 21	24.38 ± 0.32

7.3.2 Third light effect

The fits to the transit photometry in this work assumes zero light from the M-dwarf companion. Using the PHOENIX models of stellar evolution and Bessel filters, I expect around 0.07% of the total flux in the R filter will be from the M-dwarf, with slightly more in the I filter. I re-fitted J2349−32 with 0.07% third light and measured a negligible change in k and $R_\star/a$. Spectroscopy shows no contamination > 30% (approximated from the quality of the spectrum) but is insensitive to unresolved background or nearby stars providing 5 – 30% third-light. Neglecting this will introduce addition uncertainty in radii measurements if not properly accounted for.

Lucky imaging provides constraints on nearby contaminating objects. For J2349−32 and J2308−46, I found that the close companions did not significantly contaminate follow-up photometry. For J0218−31 and J1847+39, I could put constraints on the amount of third light from the consistency between the ratio of the radii measured from transit photometry in different pass-bands. For J1436−13, I have to rely on existing surveys to identify any nearby stars which may contaminate follow-up photometry. Ground-based Lucky imaging has a upper-limit to resolve companions with a sky-projected separation of ∼0.3". The orbital separation for each EBLM corresponding to a sky-projected separation of 0.3" was calculated using parallax measurements from Gaia DR2 (Table 7.2). The period of such orbits were also calculated using measurements of $M_\star$ from Table 6.3. I found that the closest EBLM (J2349−32 at a distance of 257 ± 7 pc) would require a semi-major axis of at least 382 au

with orbital period spanning two decades. The three-body systems identified by Triaud et al. (2017) will have orbital periods on the order of decades and would be difficult or impossible to resolve through lucky imaging.

The spectrum itself can provide useful constraints on potential aperture contamination. The analysis of CORALIE spectra for 118 EBLM systems presented by Triaud et al. (2017) found that 17.8 % of these systems show significant evident for non-zero values of $d(\gamma)/dt$ (spanning $d(\gamma)/dt$ = 0.07 - 4.5 km s^{-1} yr^{-1}). J0218−31 and J1847+39 have best-fitting values of $d(\gamma)/dt$ which are at the bottom of this bracket. If these drifts are evidence of a third body, they would have separations which are challenging to resolve with lucky imaging and require decades of spectroscopic observations to characterise. The low S/N spectra from CORALIE and INT eliminates unresolved blends which contribute more than 30% of the total system luminosity of the primary star by inspection of cross-correlation functions This eliminates the presence any bright companion or back-ground star but ultimately means I cannot rule out unresolved objects which contribute $<$ 30 % of the total luminosity. The transiting M-dwarf companions would contribute between 0.1% - 15% of the total luminosity and would be lost in the noise.

Including third light as a free parameter in the orbital fit will change the shape and depth of a light-curve and lead to a degeneracy between $R_\star$, k and b. I assessed this by re-fitting the orbital solution for all stars assuming a 10% light contamination from a third body which does not interact with the EBLM system. From this fit, I combined best fitting values of $R_\star/a$, b, and k and their uncertainties with nominal values from the original fit to re-determine $R_\star$ and R_2 from EBLMMASS (first two columns in Table 7.1). On average, I found a 3-7% increase in R_2 when third light is fixed to 10 %; with the largest uncertainty for the smallest M-dwarfs. I ignore J1436−13 from this discussion since the impact parameter is too high to draw meaningful conclusions about changes in measured radi. This is comparable to the inflation in radius for low-mass stars typically quoted in the literature (e.g. 3-5%; Spada et al. 2013). However, if I were to see radius inflation in general for the M-dwarf components of EBLM systems then the third-light effect can only be a partial explanation. This is because the majority of these systems do not have detected third bodies in the system, and the third body will often contribute much less than 10% of the total flux in these triple-star systems.

Table 7.3: Theoretical (marked with an asterisk) and fitted quadratic limb-darkening coefficients for a_1 and a_2 using Eqn. 7.7.

EBLM	Filter	a_1^*	a_1	a_2^*	a_2
J2349-32	I	0.368 ± 0.050	0.400 ± 0.010	0.147 ± 0.051	0.145 ± 0.050
J2308-46	R	0.460 ± 0.050	0.444 ± 0.031	0.150 ± 0.051	0.128 ± 0.043
J0218-31	g'	0.718 ± 0.051	0.735 ± 0.022	0.050 ± 0.052	0.278 ± 0.013
	r'	0.508 ± 0.050	0.588 ± 0.012	0.136 ± 0.052	0.203 ± 0.015
	i'	0.412 ± 0.050	0.461 ± 0.011	0.143 ± 0.051	0.227 ± 0.014
	z'	0.338 ± 0.050	0.341 ± 0.009	0.146 ± 0.051	0.201 ± 0.015
J1847+39	CBB	0.468 ± 0.050	0.461 ± 0.034	0.147 ± 0.051	0.217 ± 0.015
	g'	0.659 ± 0.051	0.631 ± 0.057	0.100 ± 0.051	0.223 ± 0.015
	z'	0.303 ± 0.050	0.255 ± 0.035	0.214 ± 0.050	0.215 ± 0.022
J1436-13	R	0.453 ± 0.050	0.547 ± 0.010	0.151 ± 0.051	0.247 ± 0.015

7.3.3 Limb darkening

To determine accurate estimates for $R_\star$, k and b I required an accurate prescription for limb-darkening in our light curve model. To fit the lightcurve for five EBLM systems observed from ground-based instruments, I used the Claret 4-parameter law (Claret 2000),

$$\frac{I_\mu}{I_0} = 1 - \sum_{i=1}^{4} a_i (1 - \mu_i^{\frac{1}{2}}), \tag{7.6}$$

where a_i is the i^{th} limb-darkening coefficient and $\mu = \cos\gamma$, γ being the angle between a line normal to the stellar surface and the line of sight to the observer. The coefficient tables I used to interpolate values of a_i are described in Sect. 5.6, and are interpolated for a given $T_{\rm eff}$, [Fe/H] and $\log g$. As described in Sect. 5.6, I allowed the limb-darkening temperature, $T_{\rm eff,ld}$, to vary as a free parameter with a Gaussian prior from spectroscopy, and fix $\log g$ and [Fe/H] to values from wavelet analysis. An alternative is to use the quadratic limb-darkening law (Kopal 1950) with only 2 parameters,

$$\frac{I_u}{I_0} = 1 - \sum_{i=1}^{2} a_i (1 - \mu)^i. \tag{7.7}$$

I assessed the impact of our choice of limb-darkening law on $R_\star$ and R_2 by re-fitting the five EBLMs observed with ground-based instruments using the quadratic limb darkening law

(Eqn. 7.7). I generated coefficients a_1 and a_2 for each pass-band using the Python package LDTK (see Table 7.3; Parviainen & Aigrain 2015). LDTK uses uncertainties from $T_{\rm eff}$, [Fe/H] and $\log g$ to estimate uncertainties in the calculated values of a_1 and a_2 (σ_{a_1} and σ_{a_2}). I then used these uncertainties to apply Gaussian priors to a_1 and a_2 and stop the sampler tending to unrealistic values; the priors have a mean value and width calculated from LDTK. Errors on a_1 and a_2 from errors on $T_{\rm eff}$, etc. are very small and unlikely to reflect real uncertainty due to uncertainties in the models so I add a subjective value of 0.05 in quadrature to the uncertainties on each parameter to allow for this. A new combined orbit and light curve solution was found using the same number of draws used in Sect. 5.6. From this solution, I used $R_\star/a$, k and b with their uncertainties and combine it with the orbital solution found in Chapter 6 to measure the radii of components in each system. This ensures that only parameters relating to the radii of the stars were changed.

I found that the uncertainty introduced by choice of limb-darkening law (Table 7.3) is less than introduced by third light. The primary and secondary stars see a similar reduction in $R_\star$ and R_2 between $0.5 - 2\%$; the largest uncertainty is attributed to the smallest stars for primary or secondary stars. Csizmadia et al. (2013), from their study of exoplanet-host stars conclude that fixing the limb-darkening coefficients to theoretical values does not allow the determination of R_2 to better than 1-10%; a reason why I fitted a_1 & a_2. Intertwined in this are the effects caused by stellar activity, spots and faculae. These are time-dependent effects which change at each transit event and can modify the limb-darkening values far from what is predicted. One conclusion from Csizmadia et al. (2013) is that a star with 0.5% spot coverage can introduce a 1% uncertainty on k.

7.4 Temperature of the M-dwarf in J0055−00

The effective temperature of the M-dwarf in J0055−00 is ~ 510 K hotter than predicted by MESA isochrones. Similar results have been found for J0113+31 (Gómez Maqueo Chew et al. 2014) and KIC 1571511 (Ofir et al. 2012). The effective temperature of an M-dwarf is sensitive to metallicity and age in a similar fashion to $\Delta R_2/R_2$ (see Fig.7.6). Uncertainty in

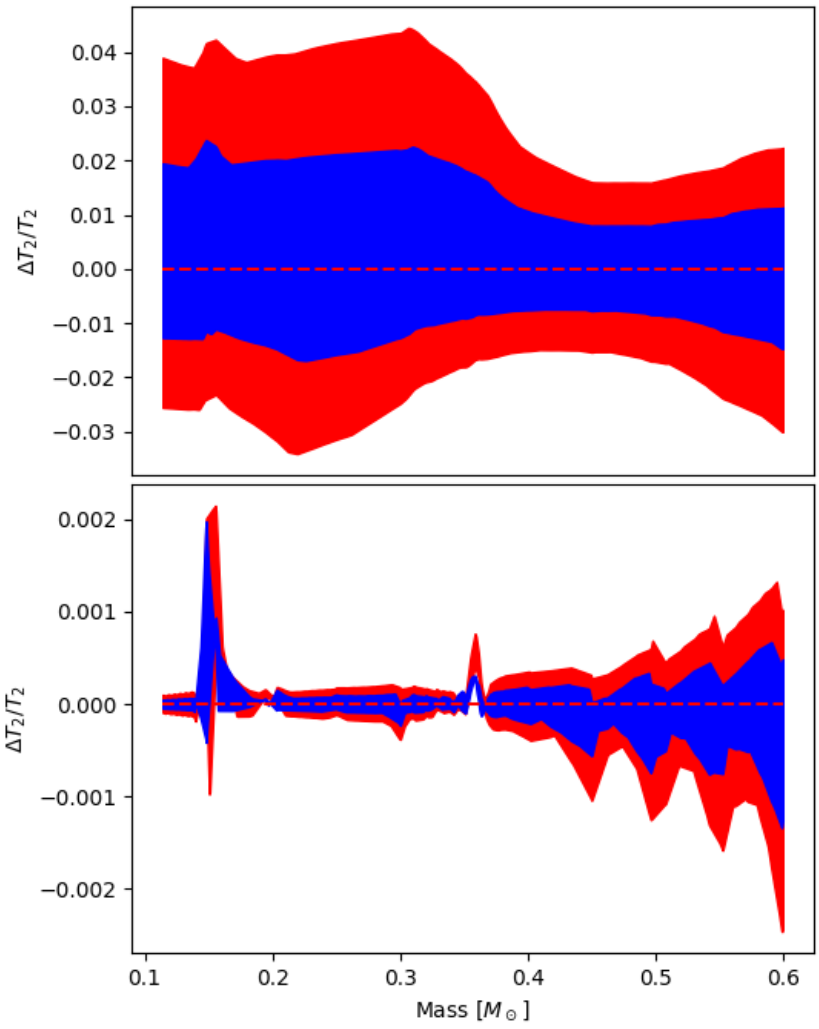

Figure 7.6: The difference in fractional residuals of M-dwarfs temperatures from MESA evolutionary models relative to a 5 Gyr isochrone with solar metallicity. (top panel) The difference in fractional radius residuals for an uncertainty of Δ[Fe/H]= 0.06 (blue) and Δ[Fe/H]= 0.12 (red) at a constant age of 5 Gyr. (bottom panel) The difference in fractional residuals of M-dwarfs temperatures for an uncertainty of $\Delta\tau = 0.5$ Gyr (blue) and $\Delta\tau = 1$ Gyr (red) at [Fe/H]= 0.

metallicity introduces additional uncertainty to the fractional temperature residual,

$$\frac{\Delta T_2}{T_2} = \frac{T_2 - T_{2,\mathrm{exp}}}{T_2}, \tag{7.8}$$

across the M spectral type, with the most influence below $0.4\,M_\odot$. The uncertainty in age affects the fractional temperature residual between 1–2 orders of magnitude less than uncertainty in metallicity depending on which mass range is considered. Age uncertainty is likely to have a negligible contribution to the uncertainty of $\Delta T_2/T_2$ ($\leq 0.2\%$) for main-sequence M-dwarfs, but may become important for younger systems below 0.5 Gyr (i.e. J0457+14) where the surface temperature drastically reduces during pre-main sequence contraction.

To assess the fractional temperature residual, I used a similar procedure to Sect. 7.2. For each draw in the PPDs from EBLMMASS and the orbital solution, the procedure was as follows:

1. Random values of T_{eff}, [Fe/H] and $\log g$ were generated from normal distributions using the mean as the measurements from Table.6.2 and the respective uncertainties as widths. These were used to interpolate a PHOENIX model spectra for the primary star.

2. The same value of [Fe/H] with the corresponding draw for $\log g_2$ was used to continually interpolate spectra for a value of T_2 that matched the light ratio predicted in the K2 band-pass from the corresponding draw of S and k (until $\Delta S \leq 10^{-4}$).

3. A MESA isochrone is interpolated using the same value of [Fe/H] with corresponding draw for τ and M_2, from which the expected temperature, $T_{2,\mathrm{exp}}$, is interpolated.

4. The value of $\Delta T_2/T_2$ is calculated using Eqn. 7.8.

The PPD for $\Delta T_2/T_2$ for the M-dwarf companion in J0055−00 is shown in Fig. 7.7, along with it's position relative to the expected M_2-T_2 isochrone. The PPD for $\Delta T_2/T_2$ is shaped similarly to PPDs for $\Delta R_2/R_2$; I fitted a Gaussian to the histogram (100 bins) and adopted the measurement of $\Delta T_2/T_2$ to be the mean of the Gaussian with uncertainty equal to the width. I find that the temperature of the M-dwarf is 3-σ (~ 510 K) hotter than

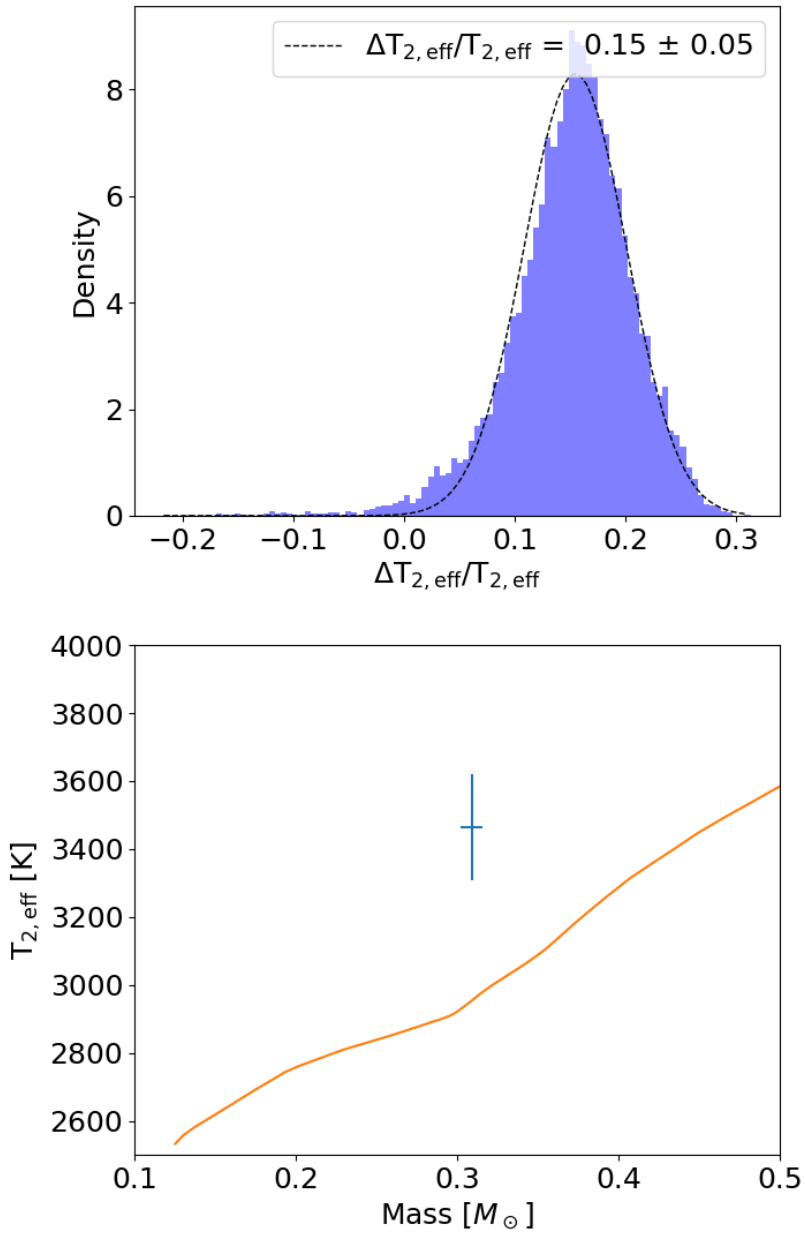

Figure 7.7: (top panel) The fractional temperature residual for the M-dwarf in J0055−00 (blue) with best-fitting Gaussian model (black-dashed). (bottom panel) The position of the M-dwarf in J0055−00 in the mass-temperature plane (blue) with best-fitting isochrone from MESA.

what is expected from MESA isochrones. The discrepancy between measured and expected temperature is similar to the temperature of the M-dwarf component for J0113+31 (600 K; Gómez Maqueo Chew et al. 2014). Gómez Maqueo Chew et al. (2014) explore a variety of scenarios which may cause a temperature which is hotter than predicted. In the following sections, I explore these scenarios in the context of J0055−00.

7.4.1 Model atmospheres

I used the PHOENIX stellar atmospheres to estimate the effective temperature of the M-dwarf companion. As a self-consistency check, I interpolated PHOENIX spectra for the primary and M-dwarf star and convolved them with the K2 band-pass (accounting for k). PHOENIX models predict a drop in flux of 0.121% for the secondary eclipse, which is consistent with observation. I interpolated the spectra of the same atmospheric parameters using Kurucz model atmospheres obtained through the STARLINK package DIPSO (Howarth et al. 2014). Kurucz spectra predict a slightly shallower secondary eclipse depth of 0.118% but this is still consistent with observations.

7.4.2 $\alpha_{\rm MLT}$, ΔY and l_3

In Sect. 7.3, I discussed the influence of $\alpha_{\rm MLT}$ and ΔY in the context of uncertainty for M_1, R_1 and τ. I found that the additional uncertainty for M_2 and τ introduced by $\Delta\alpha_{MLT} = 0.28$ and $\Delta Y = 0.02$ is 5% and 1.5 Gyr respectively. I re-determined $\Delta T_2/T_2$ for J0055−00 with errors in M_2 and τ inflated by 5% and 1.5 Gyr respectively. The PPD for $\Delta T_2/T_2$ is broadened slightly ($\Delta T_2/T_2 = 0.16 \pm 0.07$), but is not enough to be consistent with evolutionary models.

7.4.3 Metallicity offset

The MESA evolutionary models use the same solar abundances from Asplund et al. (2009) as the grid used in wavelet analysis of CORALIE spectra and synthesis of spectra for INT observations. Wavelet decomposition systematically underestimates [Fe/H] relative to Doyle

(2015) and a correction was applied using Eqn. 4.8. If I assumed the original measurement of [Fe/H] was correct, the iron content of J0055−00 would be revised to [Fe/H]= 0.21 ± 0.06. Lowering the metallicity of the M-dwarf results in a higher surface temperature. A revised calculation of $\Delta T_2/T_2$ resulted in the same PPD shape as Fig. 7.7 with a fitted Gaussian indicating $\Delta T_2/T_2 = 0.11 \pm 0.05$. This is 2-$\sigma$ too hot and so I conclude that the metallicity offset is not sufficient to account for the discrepancy in $T_{2,\mathrm{eff}}$.

7.4.4 Contamination from unresolved components

The presence of an unresolved background star or companion would affect the depth of the primary and secondary eclipses. The effect would be less for the primary eclipse than the secondary eclipse[2] due to the high luminosity ratio, except for cases with more exotic blends such as white dwarfs (Gómez Maqueo Chew et al. 2014). A physically associated tertiary component may be observable with radial velocity measurements depending on the period of the orbit, RV sensitivity, orbital inclination, and observation time-span. Indeed, Triaud et al. (2017) found an EBLM tertiary rate of 17.8% indicating that one or two systems in this sample should have a third-body in the system. For the case of J0055−00, I found that the value of $d(V_0)/dt$ is consistent with zero. However, J0055−00 was observed with CORALIE for just over one year, which may not be enough to detect an associated tertiary component that may have an orbital period of many years. I find no wavelength-dependent residuals in the SED fit which is good evidence to suggest that there is no unresolved component/background star contributing significantly different colours. There were no stars identified in Gaia DR2 other than J0055−00 within the K2 apertures. If there were, the excess flux would decrease the secondary eclipse transit depth, and thus the measured value of T_2.

[2]If the wavelength of the data for the primary and secondary eclipses are very different, as in the case of Gómez Maqueo Chew et al. (2014).

7.4.5 Star spots

Star spots on M-dwarfs have the effect of reducing the effective temperature and increasing the radius (e.g., Chabrier, Gallardo & Baraffe 2007). The presence of hotspots on M-dwarfs is highly debated (Gómez Maqueo Chew et al. 2014) and there is no evidence for M dwarf photometric variations from the ground based, WASP and K2 lightcurves. Such a hot-spot needs to be sufficient in size/coverage to increase the average surface temperature by 510 K. A second effect works in the opposite direction. Assuming that the spots on the M-dwarf companion have no bearing on R_2 or luminosity, the measured value of $T_{2,\mathrm{eff}}$ will be higher for a spotted star because the non-spotted parts of the photosphere have to be hotter to counteract the lack of flux emerging from spots. The hot parts of the photosphere dominate the flux at optical wavelengths so the flux from the spots is missed because it is emitted outside the K2 band-pass.

7.4.6 Irradiation

If both components are in a synchronous, circularised and close-in orbit then one side of the M-dwarf will be constantly irradiated by the host star. The orbital eccentricity of J0055−00 suggest a near-circularised orbit and is unlikely to be synchronised. Further to this, J0055−00 has the largest orbital period of the sample with a corresponding semi-major axis $a = 24.39 \pm 0.54\,R_\star$; only $\approx 0.001\%$ of the primary stars luminosity (1.479×10^{22} W) will be irradiated onto the surface of the M-dwarf. The required energy input to heat the M-dwarf in J0055−00 by 510 K (assuming a constant radius) is on the order of 2.336×10^{24} J meaning that even a conservative albedo of unity would not be sufficient to increase T_2 by 510 K.

7.4.7 Residual heat from formation

The surface temperature of M-dwarfs remains approximately constant over their main-sequence life. There is a possibility that the M-dwarf formed significantly after the primary star and is still contracting towards the main sequence. In the first 10 Myr, MESA models

predict that a 0.309 $M_{\odot}$ M-dwarf will cool from a surface temperature of 3400 K to 3150 K. A younger M-dwarf is unlikely for two reasons: (1) the radius of the M-dwarf would be significantly inflated and I find it consistent with the radius predicted with a 3.52 Gyr MESA isochrone and (2) it is unlikely that each component in the EBLM system formed at significantly different times (Prato, Greene & Simon 2003).

7.4.8 Mass transfer and/or accretion

Both components of J0055−00 are well-detached and inside their respective Roche lobes. They are not interacting, not transferring mass between and there is no evidence of circumbinary or circumstellar disks. Furthermore, episodic accretion is likely to end after a few Myr (Baraffe, Chabrier & Gallardo 2009) making such heating unlikely.

7.4.9 Tidal heating

The orbital separation and lack of eccentricity means that there will be little tidal deformation. In the case of J0113+31 (of similar period to J0055−00) presented by Gómez Maqueo Chew et al. (2014), they find that the smallest M-dwarf rotation period with the lowest values of dissipation created a tidal energy input $\sim 10^{21}$ W. This is 3 orders of magnitude too small to account for the measured temperature of the M-dwarf.

7.5 Tidal evolution

Eclipsing binary systems that have accurate measurements of masses, radii and rotation can be used to probe the dynamical effects of tidal friction. Probing the effects of tidal evolution requires measuring the degree of circularisation of the orbit and the level of synchronisation of the rotational velocities (Torres, Andersen & Giménez 2010). This is challenging as we are not able to follow the dynamical evolution of EBLMs from formation to the present day. It is only possible to study those which we think formed with eccentric orbits that

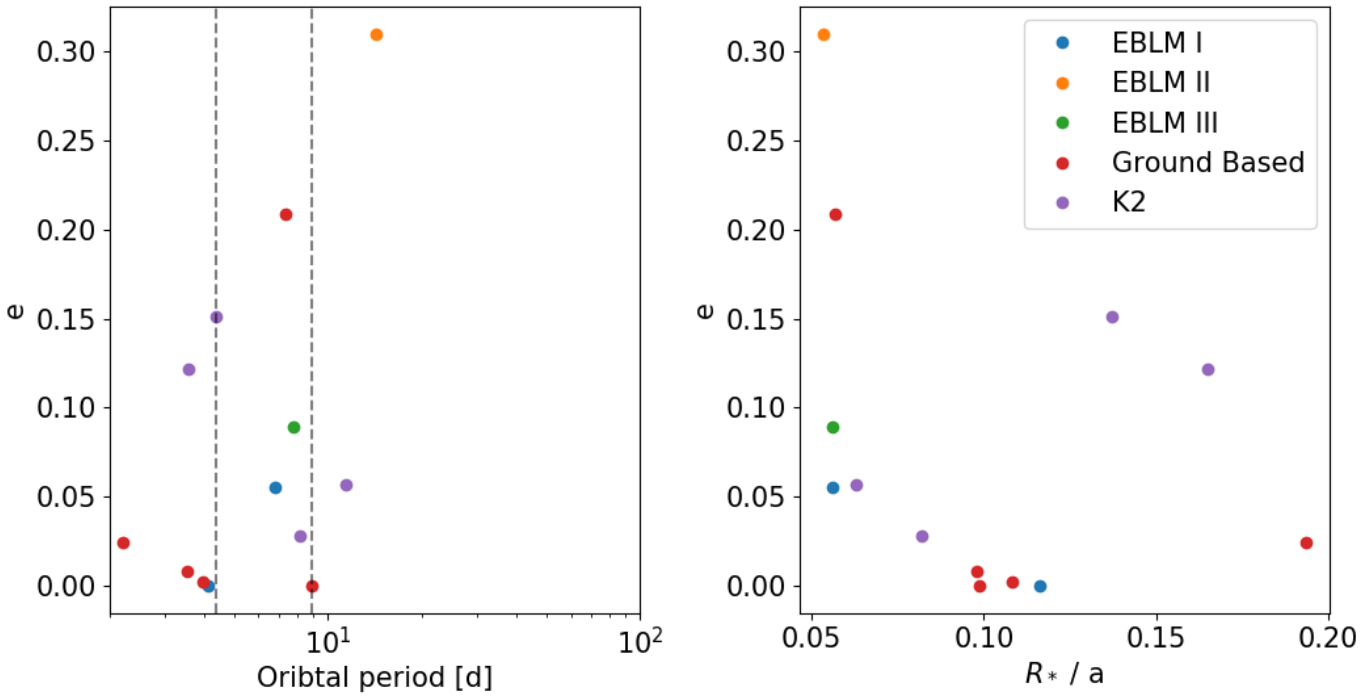

Figure 7.8: Eccentricity as a function of orbital period and scaled orbital separation. I report the EBLMs measured in the first three instalments of the EBLM project along with the nine EBLMs in this work.

are now observed to be circular, and make interpretations and conclusions which are not without questions. This is a very active field in which different prescriptions, theories and conclusions regarding tidal interactions are regularly exchanged (see Mazeh (2008) for an in-depth review). To the first approximation, tidal interactions reduce the eccentricity as a function of time such that,

$$\frac{de}{dt} = -Ce, \tag{7.9}$$

where the factor C depends on the orbital separation, the internal structure of the two stars and their rotation (Mazeh 2008). The parameter C usually varies on a timescale similar to the lifetime of the star and so is often assumed constant. In this case, the eccentricity decays exponentially,

$$\frac{d\ln e}{dt} = \frac{1}{\tau_{\rm circ}} \tag{7.10}$$

where $\tau_{\rm circ}$ is the circularisation timescale. As shown in the seminal work by Zahn (1975), $\tau_{\rm circ}$ is extremely dependent on the relative separation between stars,

$$\tau_{\rm circ} \propto \begin{cases} \left(\frac{a}{R_\star}\right)^8, & \text{for stars with } \textit{convective} \text{ envelopes} \\ \left(\frac{a}{R_\star}\right)^{6.5}, & \text{for stars with } \textit{radiative} \text{ envelopes} \end{cases} \tag{7.11}$$

assuming negligible tidal dissipation in the secondary. Therefore EBLMs which have relatively tight orbits (high values of $R_\star/a$) and short periods are expected to have the smallest circularisation timescales, and thus all if not most of them should have a low eccentricity. In Fig. 7.8 I plot eccentricity as a function period and $R_\star/a$ for all EBLMs measured within the scope of the EBLM project (including the nine reported in this work). The shorter period EBLM systems tend to have lower eccentricity although a significant number of long-period systems ($P_{\rm orb}$ = 5–10 d) also have low eccentricities. There appears to be no correlation with age. There is a clear decrease in eccentricity with scaled orbital separation indicating that EBLMs with relatively compact orbits circularise more readily. Two EBLM systems observed by K2 which deviate from this trend: (1) J0457+14 which is young and probably retained some primordial eccentricity and (2) J1652−19 which may have an active primary star akin to Kepler-17.

There is some debate about the relevant timescale on which a systems orbit changes from eccentric or circular; this is called the transition period. To quote Torres, Andersen &

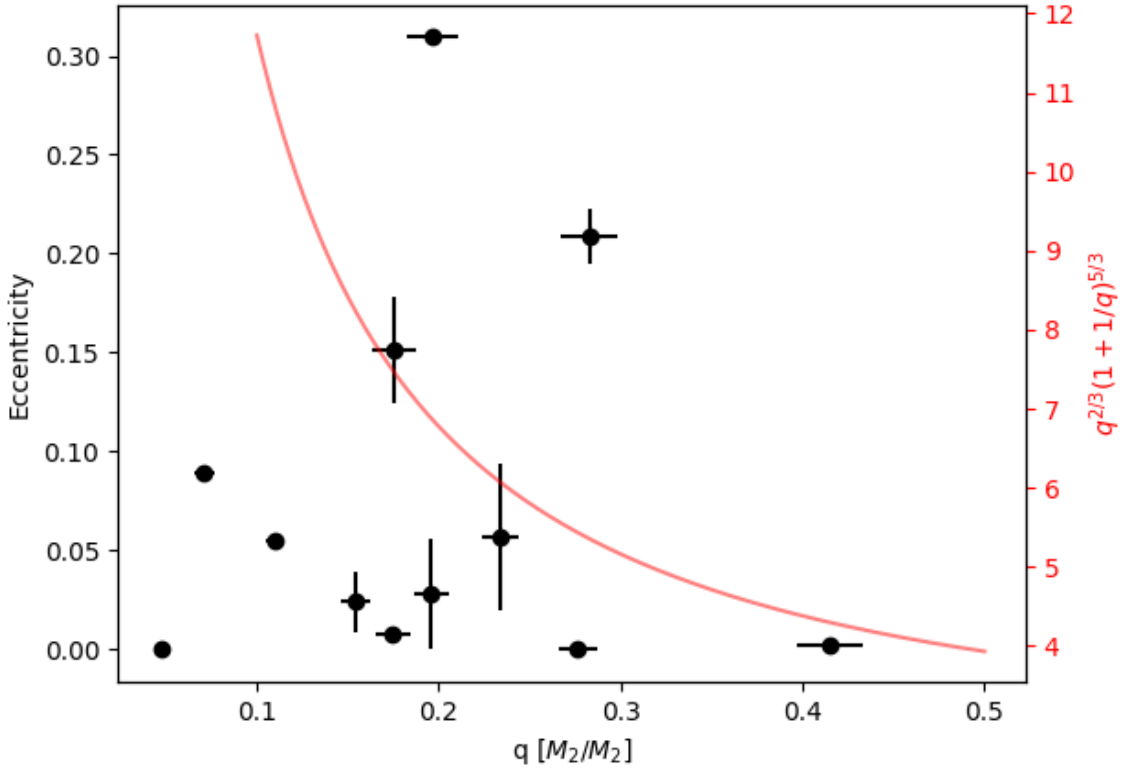

Figure 7.9: Eccentricity as a function of mass ratio, q, for all EBLMs measured within the EBLM project, and those measured in this work. I also show the predicted increase in $\tau_{\rm circ}$ found by Mathieu & Mazeh (1988).

Giménez (2010),

> "*Is the transition period the longest period for which a circular binary was found, or is it the shortest period with an eccentric orbit?*"

Assuming an eccentricity upper-limit of $e < 0.05$, there are a six EBLMs of which the longest orbital period is 8.88 d. For stars with $e > 0.05$, the shortest orbital period is 4.37 d (excluding J0457+14). These ambiguous values exist for most data-sets and I have marked in Fig. 7.8 to bound the possible range of the transition period.

The M-dwarf's mass can greatly influence the width of the transition region for EBLMs

(Mathieu & Mazeh 1988). The gravitational attraction of the M-dwarf companion is the source of the tidal force exerted on the primary star and so the circularisation timescale for the primary star is expected to be dependent on this value. The dependency of $\tau_{\rm circ}$ with $q = M_2/M_\star$ was explored by Mathieu & Mazeh (1988) who found

$$\tau_{\rm circ} \propto q^{2/3}(1 + 1/q)^{5/3}. \tag{7.12}$$

The secondary mass can extend $\tau_{\rm circ}$ by a factor of 4, when moving from $q = 1$ to $q = 0.1$. I found no evidence that eccentricity correlated with mass ratio - see Fig. 7.9.

A important factor to account for is primordial eccentricity. A binary with initial eccentricity of 0.75 needs twice the amount of time needed than a binary with initial eccentricity of 0.2 to circularise to an eccentricity of 0.05 (Torres, Andersen & Giménez 2010). The youngest EBLM of the sample, J0457+14, has approximately half the eccentricity of J1847+39 despite being only 400 Myr younger. This suggests that J1847+39 could have formed with more primordial eccentricity. However, J0457+39 has a much larger value of $R_\star/a$ and would have experienced more intense tidal interaction than J1847+39. We need a much larger sample to pick out trends that may lie within the scatter produced by a range of primordial eccentricities.

Another quantity of importance is the synchronisation of companions in binary systems. Over an eccentric orbit, the tidal forces will be strongest at periastron and so the primar star is expected to rotate with an angular velocity between what is expected for field stars (i.e. from gyro-chronology) and the orbital angular velocity at periastron. The extent in which the primary star is spun up/down depends on the strength of the tidal interaction (i.e. $R_\star/a$). In Fig. 7.10 shows the level of pseudo-synchronisation achieved by the stars as a function of $R_\star/a$ (excluding J0457+14 for its youth and J0055−00 as I was unable to measure $V \sin i < 5\,{\rm km\,s^{-1}}$). There are a distinct number of asynchronous stars with $R_\star/a < 0.08$ which is similar to the results found by Torres, Andersen & Giménez (2010). For stars with $R_\star/a > 0.08$, the majority of systems appear to be rotating slower than predicted for a synchronous orbit although this is likely an artefact of either small-number statistics or spectroscopic analysis procedure.

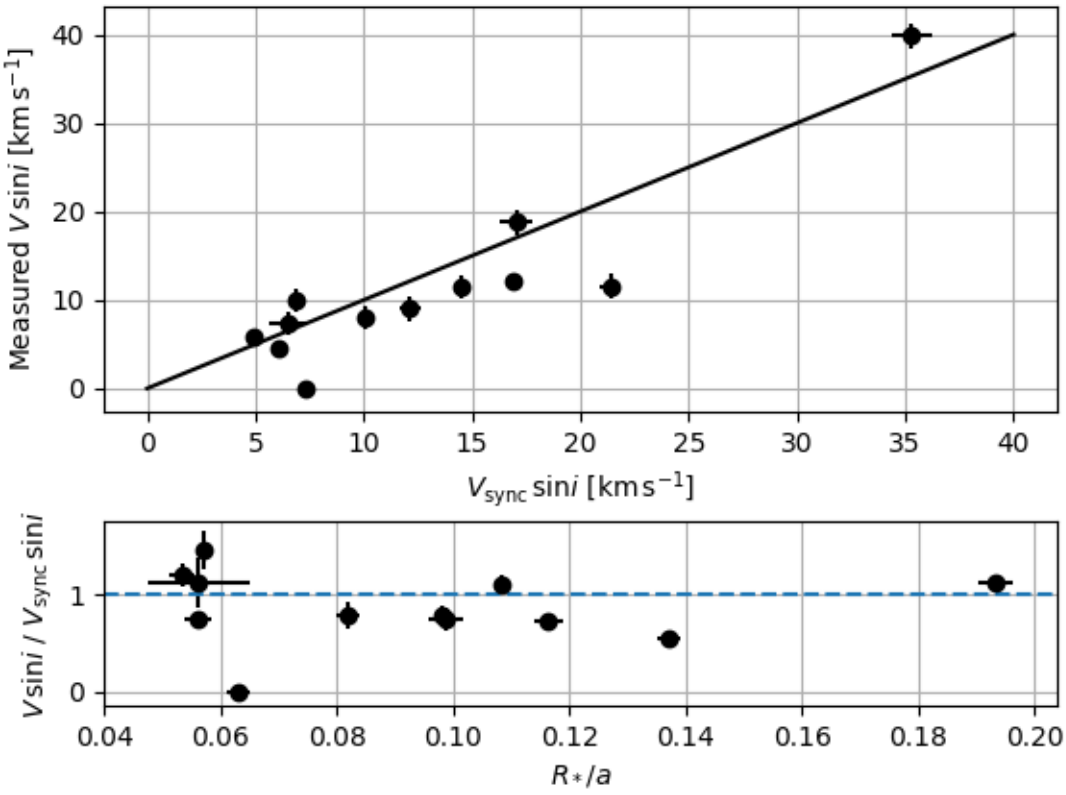

Figure 7.10: Ratio between measured and projected (pseudo-)synchronous rotational velocities for EBLMs measured in the first three instalments of the EBLM project along with the nine EBLMs in this work (top panel). The ratio is also shown as a function of $R_\star/a$ (lower panel).

7.6 Selection effects

I found that 4 out of 9 EBLM systems measured in this work have a primary star which has entered the "blue-hook" part of it's post main-sequence evolution. This occurs to stars in the mass range 1.1–1.5 $M_{\odot}$ which develop a small convective core during core hydrogen burning. Core hydrogen is depleted to the extent in which core fusion effectively stops, causing the star to contract and heat. In lower-mass stars ($\leq$ 1.1 $M_{\odot}$), the transition between core and shell hydrogen burning is gradual and so the star can remain in thermal equilibrium with an isothermal helium core. Stars which reside in or near the "blue-hook" part of it's post main-sequence evolution have some ambiguity surrounding mass and age (i.e. which side of the "blue-hook" the primary star resides on). This leads to double peaked PPDs for M_1 and τ. Ultimately, these systems are not suitable for empirical mass-radius calibrations as we cannot confidently break the mass degeneracy using the primary star.

A solution is to turn EBLMs from single-lined eclipsing binaries to double-lined eclipsing binaries, whereby the masses can be directly measured. Achieving this is no easy feat and requires separation of atomic lines from the host star with molecular lines from the M-dwarf companion. The CORALIE échelle spectrograph is unsuitable for this task for two reasons: (1) the wavelength coverage is in the optical (300–750 nm) where the contrast between the M-dwarf and the primary star is low and (2) a small telescope aperture does not permit the identification of otherwise faint molecular lines. The latter point can be addressed using the high S/N spectra obtained from SALT. I cross-correlated the red-arm spectra (560–870 nm) for the EBLMs observed with SALT which are measured in this work (J2349−32, J2308−46, J0218−31 and J2217−04) with an M5 template provided through ISPEC. I failed to measure a radial velocity for the secondary component in all cases suggesting that a high S/N in the optical is not sufficient to overcome a low contrast ratio. In future work, I intend to acquire infrared spectra from such instruments as Long-slit Intermediate Resolution Infrared Spectrograph (LIRIS) on the 4.2-m William Herschel Telescope (0.9–2.4 μm) or the Infra-Red Dual-beam Imager and Spectrograph (IRDIS) on the 8.2-m Very Large Telescope (VLT) where the contrast will be much larger than the optical. These observations will also

provide an excellent test for evolutionary models of the host star from which the mass and age of the M-dwarf companion are derived from.

To avoid spending valuable follow-up time on EBLMs which have entered the "blue-hook" part of their post-main sequence evolution, I could select follow-up targets from a volume-limited sample of candidates. Stars with masses below 1.1-$M_{\odot}$ do not exhibit a "blue-hook" phase in their evolution and so an obvious solution would be to follow-up stars with $T_{\rm eff} \lessapprox 5900$ K. Selecting cooler stars has a number of drawbacks. First, there is an inherently low probability of G/K+M binaries surviving due to predictions from tidal interactions (Sec. 1.5), and thus an inherently lower probability of finding such systems; only two out of nine systems presented here have primary star temperatures below . 5900 K. Secondly, cooler primary stars result in higher ratios of R_2/R_1 (k) and lead to a higher chance of a transit being grazing in nature ($b > 1$), or such that the radius of the two components cannot be accurately determined (e.g. J1436−13 or J0055−00). The second data release of Gaia provides some indication regarding the evolutionary status of the primary star in EBLM systems. The Gaia colours of EBLMs in Fig. 3.2 is such that those with primary stars in the "blue-hook" region of post main-sequence evolution have a smaller M_G than other EBLMs. A future vetting procedure may involve prioritising EBLMs with Gaia colours that are not consistent with the "blue-hook" EBLMs. The fraction of stars in this region is largely governed by the selection criteria of the WASP survey. This has blurred edges which have evolved with time. Querying TEPCAT (Southworth 2011)[3] reveals that there are 157 WASP exoplanet systems. Exactly half of the host stars have surface temperatures measured to be below 5900 K and have a broad metallicty peak around +0.1 dex. A query of the WASP database[4] yields 926 systems flagged as "EBLM". Of those, 455 (48%) have IRFM temperatures below 5900 K.

The field of eclipsing binaries and exoplanets is gently transitioning from an era of detection to an era of characterisation. Large quantities of data exist from numerous ground-based surveys and space observatories. Measuring the masses, radii and ages of EBLMs reliably requires a diligent screening of potential EBLM systems. Nearly a thousand sys-

[3] http://www.astro.keele.ac.uk/jkt/tepcat/, accessed 1 Oct 2018
[4] accessed 1 Oct 2018

tems have been flagged as potential EBLMs from the WASP survey. Applying strict temperature cuts ($T_{\rm eff} < 5900\,{\rm K}$) reduces the sample down to around 180 EBLMs which could be suitable to be measured withing the EBLM project. A significant portion of these will be false-positives, blended EBs, or have unfavourable transit geometries (e.g. high impact parameters). However, we only follow-up EBLMs if we detect the primary eclipse which is more likely for bigger M-dwarfs around smaller stars. This will lead to a bias in the mass-radius diagram which will need accounting for when the absolute parameters of more EBLMs are determined.

7.7 GP-GPU lightcurve model

The increase in CPU clock rates lead to an increase in execution speeds of lightcurve models. Since the early 2000s the increase in CPU clock rates has slowed as CPU manufactures struggled to dissipate the heat from faster chip-sets (Sridhar, Heald & van der Hulst 2018; Patterson & Hennessy 2014). A solution to this problem was to have multiple cores on the same chip. Graphic processing units (GPUs) extend this idea by maximising the number of cores on a chip. The GTX 1080 used in this work has 2,560 processing cores divided up onto 20 streaming micro-processors. GPUs were originally designed to be used as graphical processors to handle resolution, display rates and ray-tracing capabilities demanded by the videogame industry. The computing capability of GPUs has been exploited in general-purpose GPU (GP-GPU) programs such as projects in artificial intelligence (e.g. Baji 2017) and deep learning (e.g. Oyama et al. (2018)). A review of GPU use in scientific computing can be found in Owens et al. (2007) and Owens et al. (2008).

My implementation of the QPOWER2 model is written in *C* using CUDA®toolkit V10.0[5] provided by NVIDIA® and has a python interface. It also supports OPENMP® which permits efficient multiprocessing. When determining the orbital solution, it is more efficient to use a single processor per model and evaluate multiple models for each "step" in parallel.

[5]https://developer.nvidia.com

This is a feature offered within EMCEE and each call to QPOWER2 is thread safe.

The four EBLMs measured using QPOWER2 were called using code which executes on the CPU. A significant decrease in computational time can be achieved when this is executed on a graphics processing unit (GPU) instead. Various lightcurve models include support for GPUs; these include BATMAN, ExofastGPU (an extension of Exofast for the GPU; Eastman 2017) and PYTRANSIT (Parviainen 2015). These implementations operate in a way similar to OpenMP for CPU code; each time stamp is modelled using a single microprocessor on the GPU. The clock-speed (i.e. how fast calculations can be done) for GPU microprocessors is typically between 1-2 GHz and is not far below the speed of a typical CPU processor (2-5 GHz). A major drawback is that GPUs are separate devices which connect to a motherboard through a principle component interconnect (PCI), and thus require costly memory transfer operations between the random access memory (RAM) and videocard random access memory (VRAM). The computational gain from GPU lightcurve synthesis is often quashed by memory transfer operations of the time axis and the resulting lightcurve (Fig. 7.11). This can be demonstrated with the QPOWER2 model; calculating a lightcurve model for K2 lightcurve (4000 time stamps) takes approximately $\sim 357\,\mu s$ on the CPU and $228\,\mu s$ on the GPU ($\sim 30\%$ speed increase; see Table 7.4).

Generating a single lightcurve model is therefore inefficient due to memory transfer operations. A better approach is to generate thousands of models at once and initiate a single memory transfer back to the host (Fig. 7.12). This method offers a significant speed-up as only one memory transfer operation is called and benefits users wishing to fit lightcurves with Bayesian methods that require multiple "walkers" (such as EMCEE). In this case, I chose to calculate 10,240 models at once (2560 micro-processors $\times 4$) which corresponds to a $60\times$ speed-up than the fastest CPU implementation.

If fitting light-curves is the goal, then the only quantity of interest is the log-likelihood, $\mathcal{L}$. A further optimisation can be achieved by returning only $\mathcal{L}$ for each model, rather than the entire model itself. This implementation offers a further $\times 8$ speed-up and highlights the expense of memory transfer operations. Using the GPU to only return $\mathcal{L}$ significantly accelerates Bayesian fitting routines. The architecture of the parallel-stretch move algorithm is such that convergence benefits from a large number of walkers, resulting in faster conver-

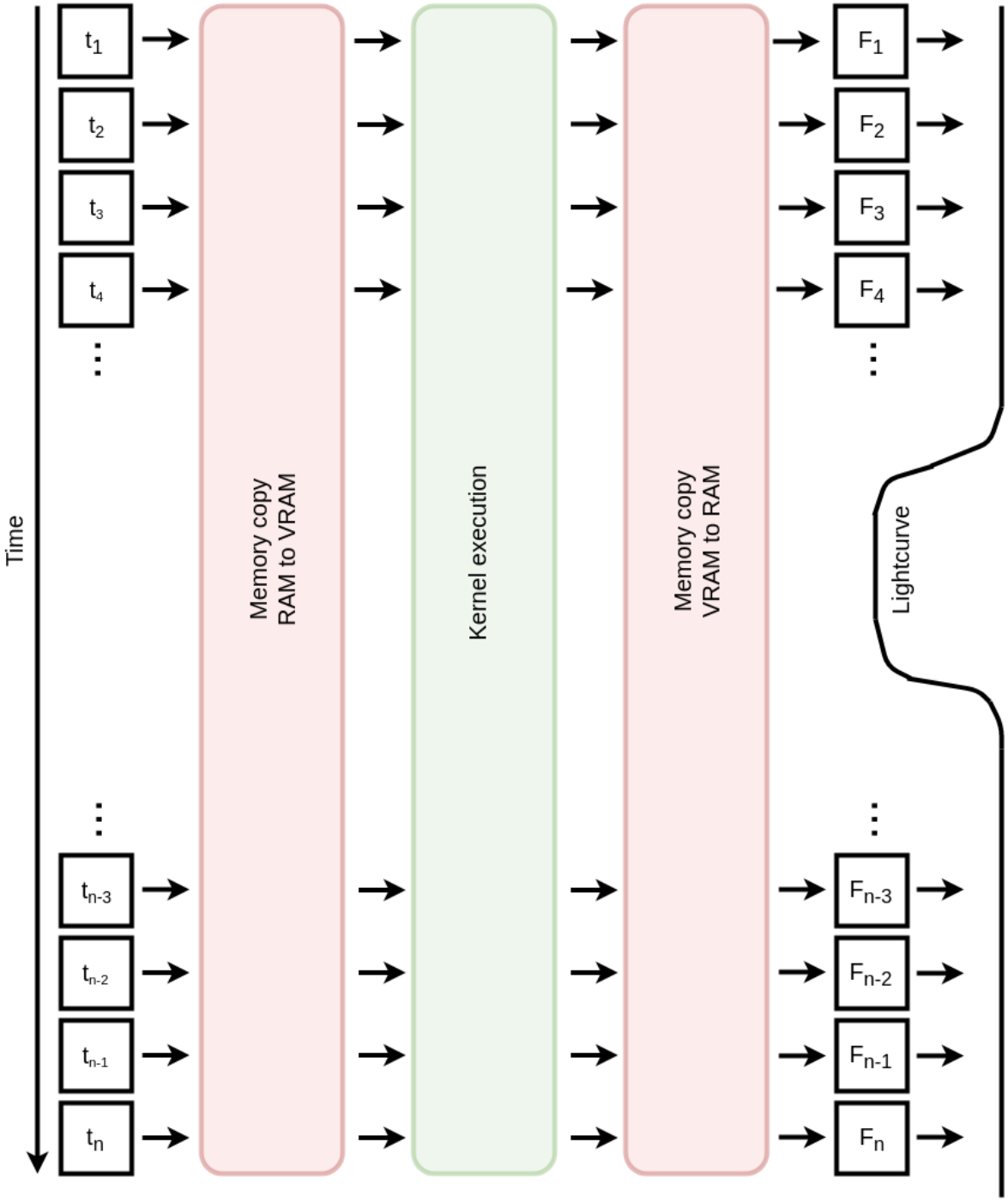

Figure 7.11: The sequence of execution when calculating a lightcurve model on the GPU. The time sequence is represented by time stamps, t_i, and the respective flux, F_i.

Table 7.4: Execution times for the analytical QPOWER2 model for a typical Kepler/K2 lightcurve and ground-based lightcurve. I assumed a planet with $k = 0.1$.

Algorithm	Processor	Single model	Models /s	Notes
Hardware				
Intel®Core™ i7-7700K CPU 4.20 GHz	8 (overclocked to 4.8 GHz)			
GeForce GTX™ 1080 (/PCIe/SSE2)				
Ubuntu 17.10				
Kepler lightcurve (3840 time stamps)				
QPOWER2 (CPU)	4.8 GHz CPU	357 μs	2801	
QPOWER2 (CPU)	4.8 GHz CPU×8	112 μs	8928	Using OpenMP®
QPOWER2 (GPU)	GTX 1080	228 μs	4385	
QPOWER2 (GPU)	GTX 1080	13 μs	75,851	Computing 10,240 lightcurves
QPOWER2 (GPU)	GTX 1080	2 μs	390,839	Computing 10,240 lightcurves, returning only $\mathcal{L}$
SAAO light curve (345 time stamps)				
QPOWER2 (CPU)	4.8 GHz CPU	50 μs	20,80	
QPOWER2 (CPU)	4.8 GHz CPU×8	21 μs	48,780	Using OpenMP®
QPOWER2 (GPU)	GTX 1080	12 μs	83,334	
QPOWER2 (GPU)	GTX 1080	1.3 μs	753,012	Computing 10,240 lightcurves
QPOWER2 (GPU)	GTX 1080	4.52 ns	2,211,900	Computing 10,240 lightcurves, returning only $\mathcal{L}$

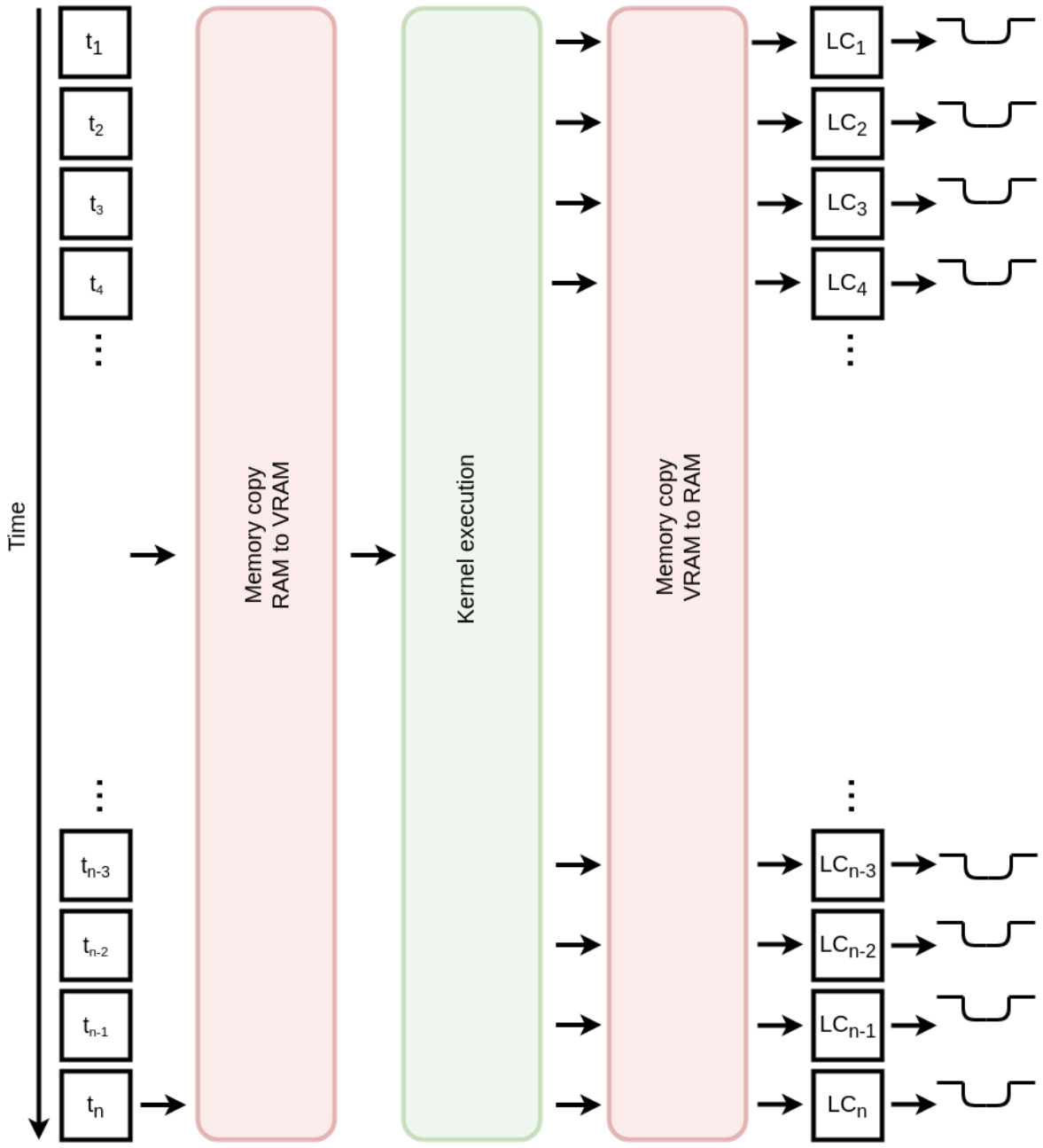

Figure 7.12: The sequence of execution when calculating many lightcurve models on the GPU. The time sequence is represented by time stamps, t_i, and the respective lightcurve model, LC_i.

gence and more reasonable acceptance fractions. To implement this, I modified the source code for EMCEE to accept an array of $\mathcal{L}$ for each "step" in Bayesian analysis. For a typical K2 lightcurve, I was able to sample 2 million draws in less than 10 seconds (using 10,240 walkers) which converged after only a few hundred steps. Further optimisations could be made to increase the performance of a GPU lightcurve model in the context of Bayesian fitting. For example, the bounds checking for 10,240 models is costly on the CPU and could easily be offloaded onto the GPU. The matrix operations with EMCEE which decide new trial steps could also be offloaded to the GPU. The only downfall from using a GPU accelerated lightcurve model and fitting routine is the amount of data it produces. A small fit ($\sim$ 1000 steps) with a length-20 model vector can produce over 10 Gb of data. Consequently, chain-thinning is required unless a different approach is used which does not require the data to be stored during convergence.

In Sect. 5.6, I used Gaussian processes to account for red noise in the K2 lightcurves. Conventional Gaussian processes requires an n^2 covariance matrix for a lightcurve with length n. Memory quickly becomes an issue when 10,240 $n \times n$ matrices are required to batch-compute red-noise models on the GPU. The package CELERITE used in Sect. 5.6.2.2 cleverly reduces this dependency to an array of length n from which to calculate a red-noise model. However, the dependencies of CELERITE are not GPU compatible and I am actively seeking a solution. The capability to generate thousands of lightcurve models on the GPU with a red-noise model will be an incredible powerful tool to analyse data from a variety of upcoming space-based missions.

8 Conclusion

"*Astronomy compels the soul to look upwards and leads us from this world to another.*"
– Plato

During the course of this work I developed an automated spectral analysis routine to measure the atmospheric parameters of FGK stars. I used this technique to measure the absolute parameters of 9 M-dwarfs in eclipsing binary systems. At the beginning of this work I asked two questions which set the context of this research. In the following paragraphs I address these questions with respect to the work accomplished here.

How well can I measure the atmospheric parameters of FGK stars using wavelet decomposition? I have shown that my method accurately recovers the atmospheric parameters of synthetic spectra from a grid of models using subsets of wavelet coefficients in a Bayesian framework. The same method was applied to the CORALIE spectra of 20 FGK stars which have been analysed independently by measurements of EWs from higher-quality HARPS spectra. From this I determine a precision for the parameters derived from the wavelet method of 85 K for $T_{\rm eff}$, 0.06 dex for [Fe/H] and 1.35 kms^{-1} for $V \sin i$. Surface gravity, $\log g$, can also be estimated using my method but it is difficult to assess the precision of this parameter in individual cases. Consequently, I recommend that $\log g$ estimates from my method are only used to decide whether or not a star is a dwarf ($\log g \approx 4.5$). I found an offset in my metallicity scale compared to the results of Doyle et al. (2013) and Doyle (2015) in the sense that my values of [Fe/H] are lower by 0.18 dex, despite using a consistent solar abundance, and recommend that this offset be applied as a correction to the [Fe/H] values from my method. I found my method is robust for échelle spectra with a S/N above 40. Below this value the uncertainty in the measured atmospheric parameters increases to unusable levels.

My method has already been used to determine the atmospheric parameters of the EBLM J0555−57 (von Boetticher et al. 2017), which hosts one of the densest main sequence stars currently known. For both exoplanet systems and EBLM binaries, the contribution of

the companion star to the optical flux is negligible (they are SB1 binaries) and so my method using models of single stars is appropriate, but it would not be suitable for cases where the companion is detectable in the spectrum (SB2 binaries).

Wavelet coefficients were weighted using a Mote Carlo approach which marginalised over parts of the spectrum that are noisy and of poor quality. A more sophisticated weighting system might help the systematic offset in [Fe/H] and correlation between $\log g$ and $T_{\rm eff}$. This would focus on key spectral features such as iron, sodium and magnesium lines. It would also have to be "triangular-shaped" in a power-hövmoller diagram to match the power of spectral lines in wavelet space (Fig. 4.1). It is unclear if this would be a worthwhile pursuit; such a weighting system would be complicated to develop and may not significantly improve the accuracy/reliability of the method.

The wavelet method could be applied to other large spectroscopic surveys such as 4most (de Jong et al. 2012), HARPS or SALT HRS. However, there may be problems since the wavelet method was fine-tuned to work with the systematics and noise profiles of the CORALIE spectragraph. I attempted to apply my method to the HARPS spectra with a moderate level of success – the atmospheric parameters were very sensitive to how I treated the data discontinuity at 532 nm. I also applied my method to the red and blue arms of the SALT spectra for J2349−32 and J02308−46. Measurements of $T_{\rm eff}$ and [Fe/H] were spurious and generally not consistent with D15, CORALIE spectra or SED fitting. This is probably due to the restricted usable wavelength range in each arm, different systematics and smaller noise profile (S/N > 100). The wavelet method could be "tuned" to work with SALT spectra but there is a question of whether it is a worthwhile pursuit since synthetic/equivalent width fitting will be far more reliable given the quality of the spectra.

To what extent can EBLM systems contribute to empirical mass-radius relationships at the bottom of the main sequence? EBLMs can be used to measure the absolute parameters of M-dwarfs to a precision of a few percent. I have measured the absolute parameters of 5 EBLMs with data from ground-based instruments and 4 EBLMs which have been observed with K2. I found that the precision of absolute parameters between each subset of EBLMs is similar.

The sample of EBLMs with absolute parameters is currently too small for an empirical relation of low-mass stars to be derived. A good place to start will be the sample of 118 EBLMs presented by Triaud et al. (2017). There are three benefits to this sample: (1) they already have spectroscopic orbits which can be difficult to obtain, (2) some already have SALT spectra which will allow us to determine individual elemental abundances and (3) the atmospheric parameters can be measured in a homogeneous way using wavelet decomposition. This work highlights that some EBLMs are more useful to empirical calibrations than others due to the precision of which absolute parameters can be measured. An example is that the primary stars of 3/9 EBLMs measured in this work have evolved into the "blue-hook" part of their main-sequence evolution such that I cannot confidently select the best-model for the primary star. This is a disappointing result as a significant amount of time had been invested to measure these systems. In Sec. 7.6, I discussed how EBLMs could be "prioritised" based on primary star photometric colours and effective temperatures. The down-side to selecting smaller primary stars is the increased probability of transit geometries with high impact parameters. Systems like J1436−13 and J0055−00 have sufficiently high impact parameters that the radii are poorly constrained. These too cannot contribute to empirical calibrations.

An important conclusion from this work is that the way EBLM systems are analysed significantly effects the absolute stellar parameters. More community-driven data challenges (*hare-and-hounds experiments*) are required to characterise and determine the extent of non-astrophysical scatter in empirical calibrations. Such a test would use a carefully selected sample of EBLMs which are suitable for empirical calibrations (e.g. J2349−32 and J1652−19).

Further study of the 118 EBLMs presented by Triaud et al. (2017) will produce a substantial amount of calibratable points from which empirical relations can be created. Achieving this goal requires follow-up transit photometery for each system to measure the radii to a precision of a few percent. The primary transit width of an EBLM (≈2-6 hours) is a significant fraction of an observable night and therefore the chance of of observing a full EBLM transit is small; I observed only 2 full transits (J2349−32 and J2308−46) across 4 weeks of 1-m telescope time. TESS will produce light-curves for most of the sky, but ground-based instruments will be more competitive for the fainter EBLMs ($T \geq 12$). TESS is also significantly redder than K2 and will provide more measurements of secondary eclipses, and thus

M-dwarf temperatures. The CHEOPs mission (CHaracterising ExOPlanets Satellite; Broeg et al. 2013) will observe EBLMs as part of the guaranteed time observing programme. In the more distant future, the PLAnetary Transits and Oscillations of stars (PLATO) mission will provide lightcurves capable of determining the mass and age of stars to better than 10%. The constraint on mass and age from asteroseismology is an alternative way to break the mass degeneracy and it would be of interest to compare these results from those of EBLMMASS.

Generally, the M-dwarfs measured in this work agree with stellar models. There is an emerging trend that M-dwarfs in EBLM systems are significantly hotter than predicted by evolutionary models. The dearth of EBLMs with measured secondary eclipses provides little insight into the origin this phenomena. Understanding this requires more measurements of secondary eclipse depths which are most observable in the infrared. The eventual release of the James Webb Space Telescope (JWST; Mollière et al. 2017) will provide a healthy sample of light-curves, however recent delays in the mission mean that this data may not come for some time. Ground-based infrared observatories such as the InfRared Survey Facility (IRSF; Nagayama et al. 2003) could provide a suitable alternative in the meantime.

The method to study EBLM systems is now well established and I expect that the number of M-dwarfs with absolute parameters from these systems to grow substantially in coming years. This will be of particular interest to those who study exoplanets around M-dwarfs. TESS and JWST will find these systems in abundance and reliable empirical mass-radius-luminosity calibration will provide valuable constraints on host-star parameters.

A SED

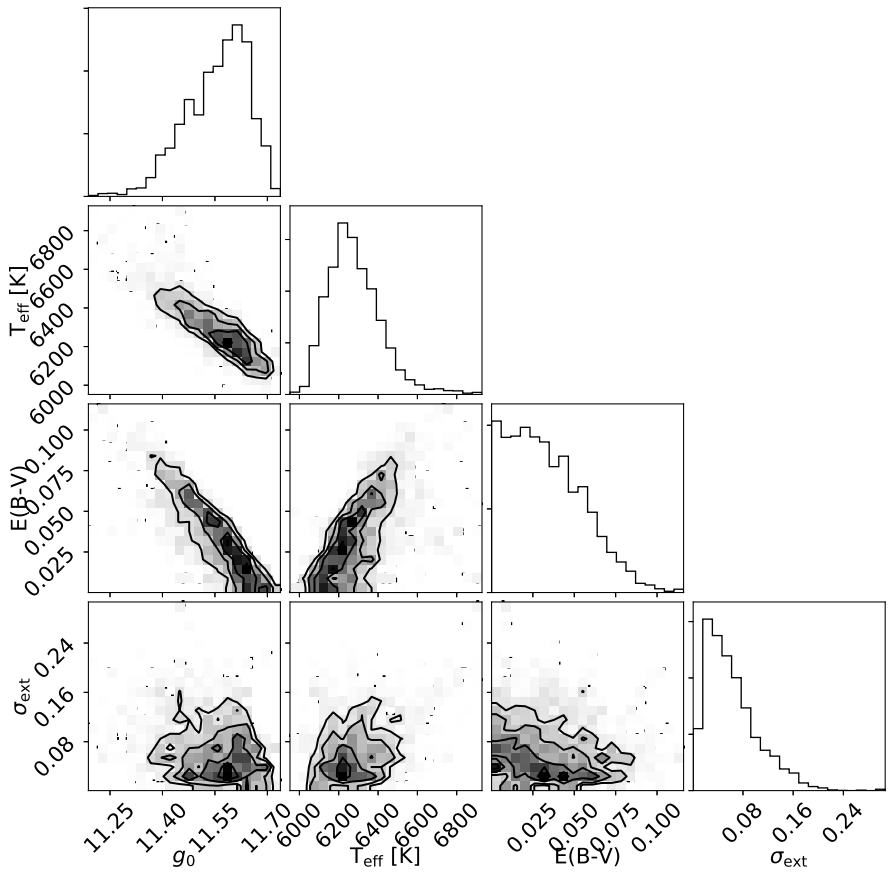

Figure A.1: The posterior probability distribution of EBLM J2308−46 from photometric fitting. Over-plotted are the 68%, 95% and 99.7% contours.

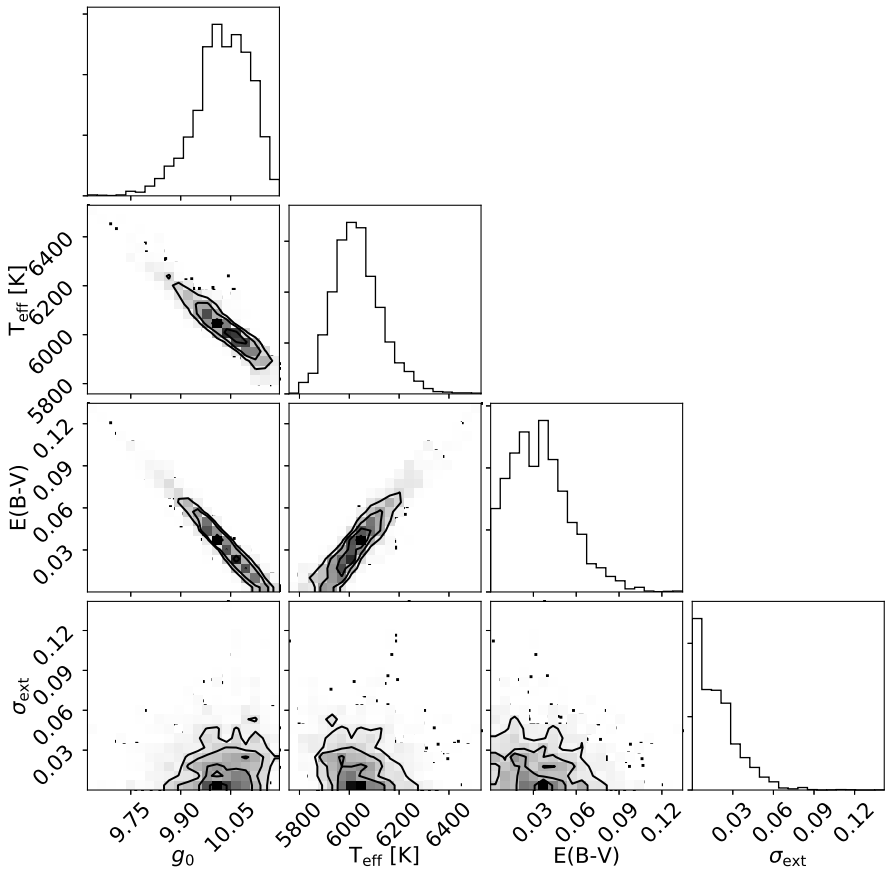

Figure A.2: The posterior probability distribution of EBLM J0218−31 from photometric fitting. Over-plotted are the 68%, 95% and 99.7% contours.

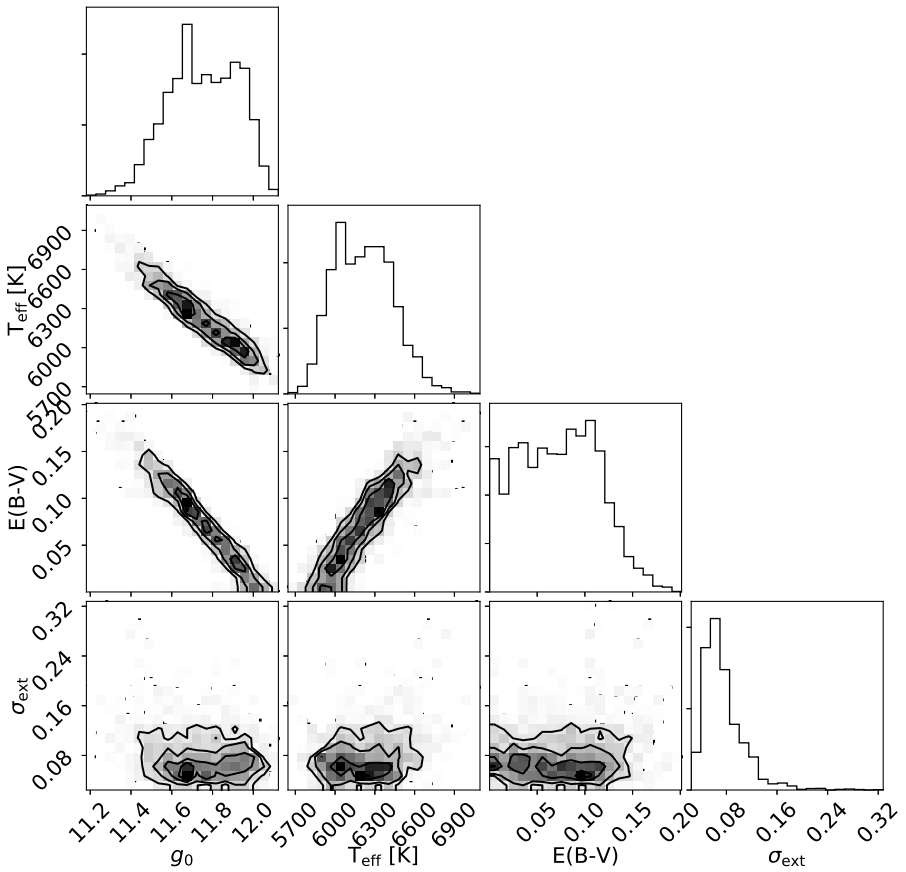

Figure A.3: The posterior probability distribution of EBLM J1847+39 from photometric fitting. Over-plotted are the 68%, 95% and 99.7% contours.

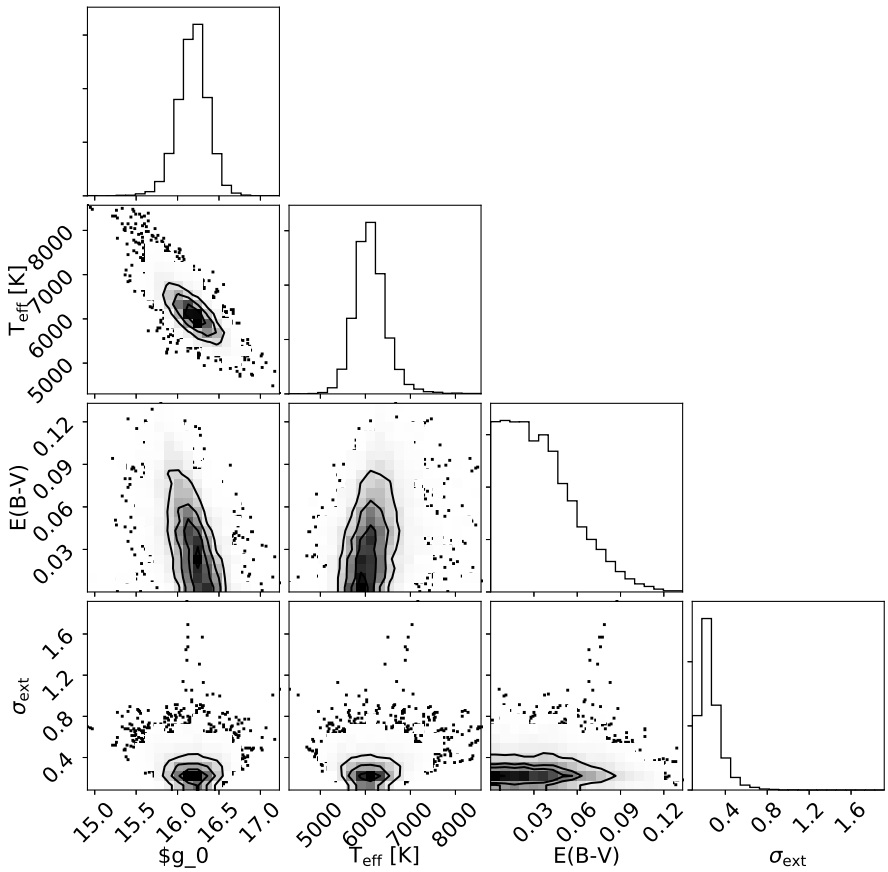

Figure A.4: The posterior probability distribution of EBLM J1436−13 from photometric fitting. Over-plotted are the 68%, 95% and 99.7% contours.

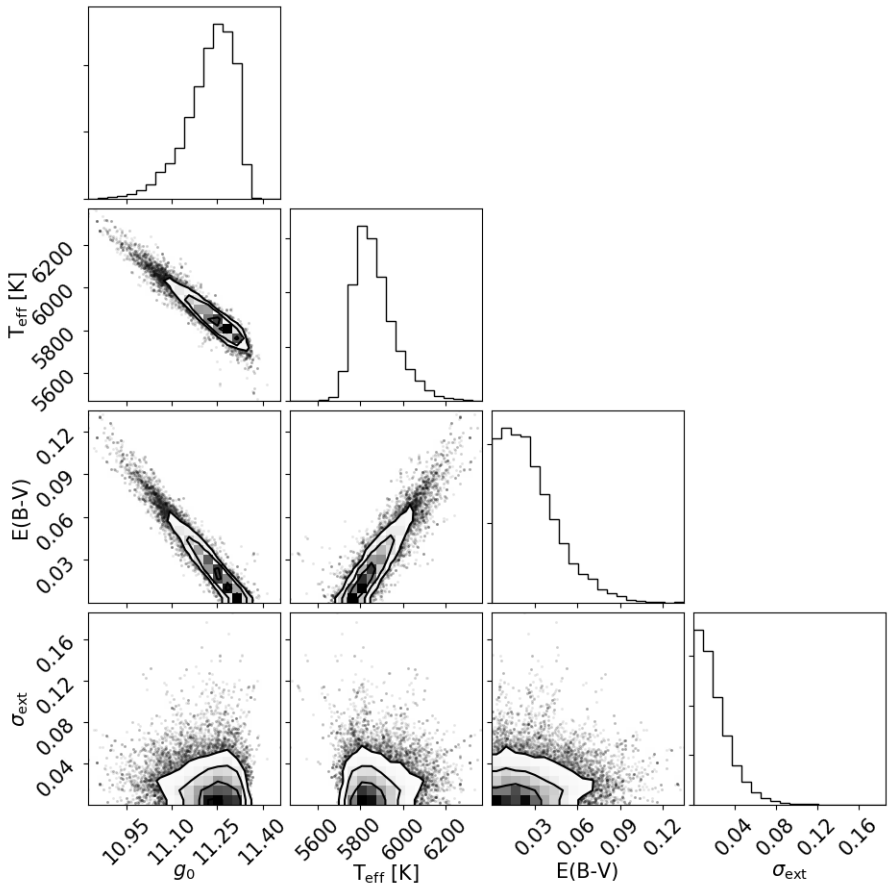

Figure A.5: The posterior probability distribution of EBLM J0055−00 from photometric fitting. Over-plotted are the 68%, 95% and 99.7% contours.

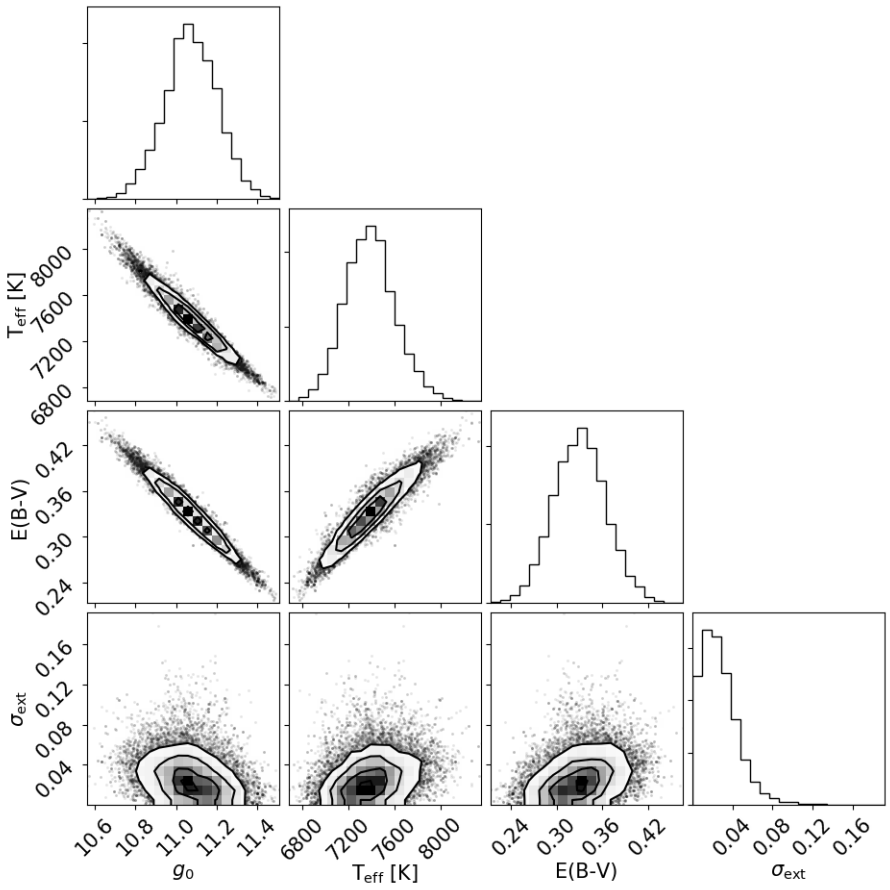

Figure A.6: The posterior probability distribution of EBLM J0457+14 from photometric fitting. Over-plotted are the 68%, 95% and 99.7% contours.

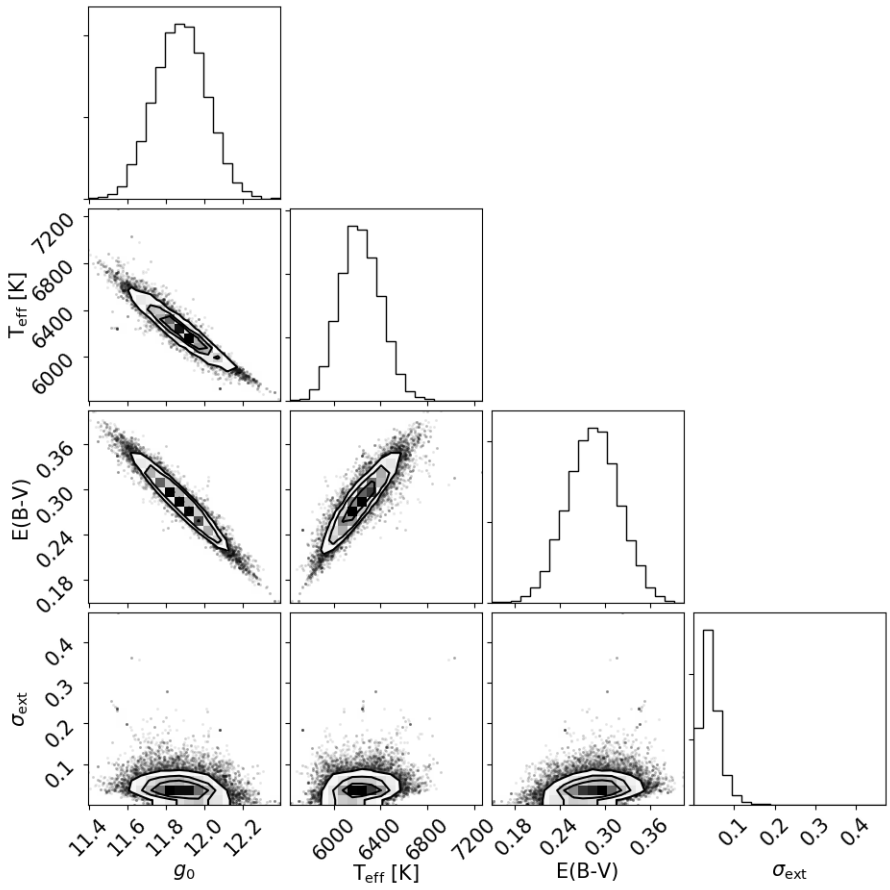

Figure A.7: The posterior probability distribution of EBLM J1652−19 from photometric fitting. Over-plotted are the 68%, 95% and 99.7% contours.

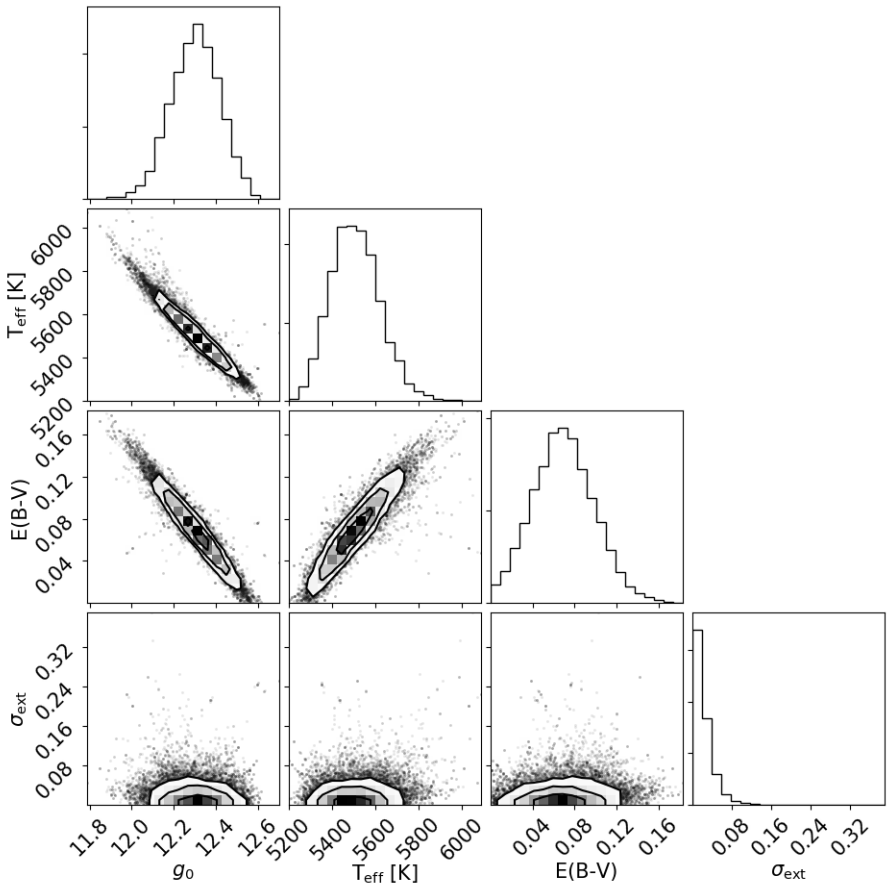

Figure A.8: The posterior probability distribution of EBLM J2217−04 from photometric fitting. Over-plotted are the 68%, 95% and 99.7% contours.

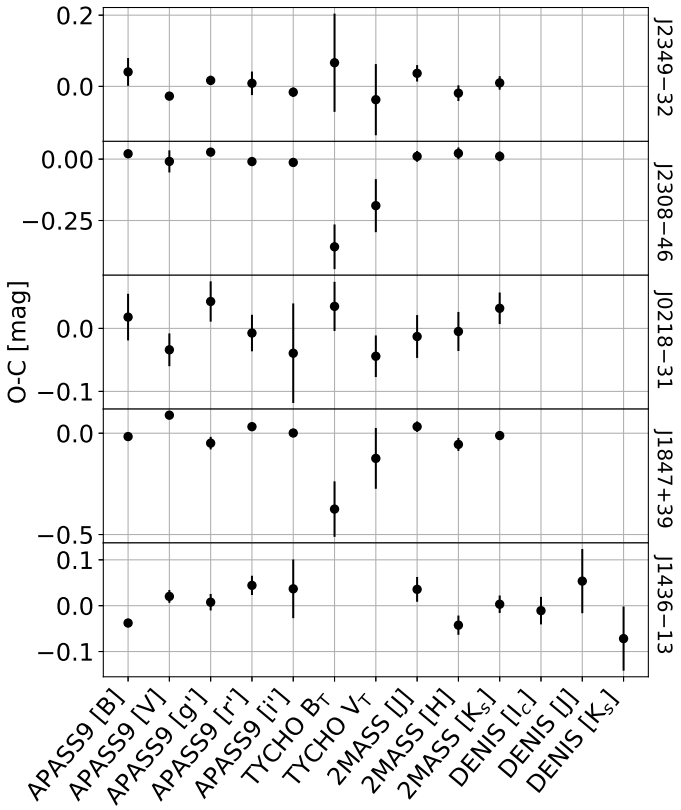

Figure A.9: Difference between observed and fitted magnitudes for EBLMs observed with ground-based follow-up photometry.

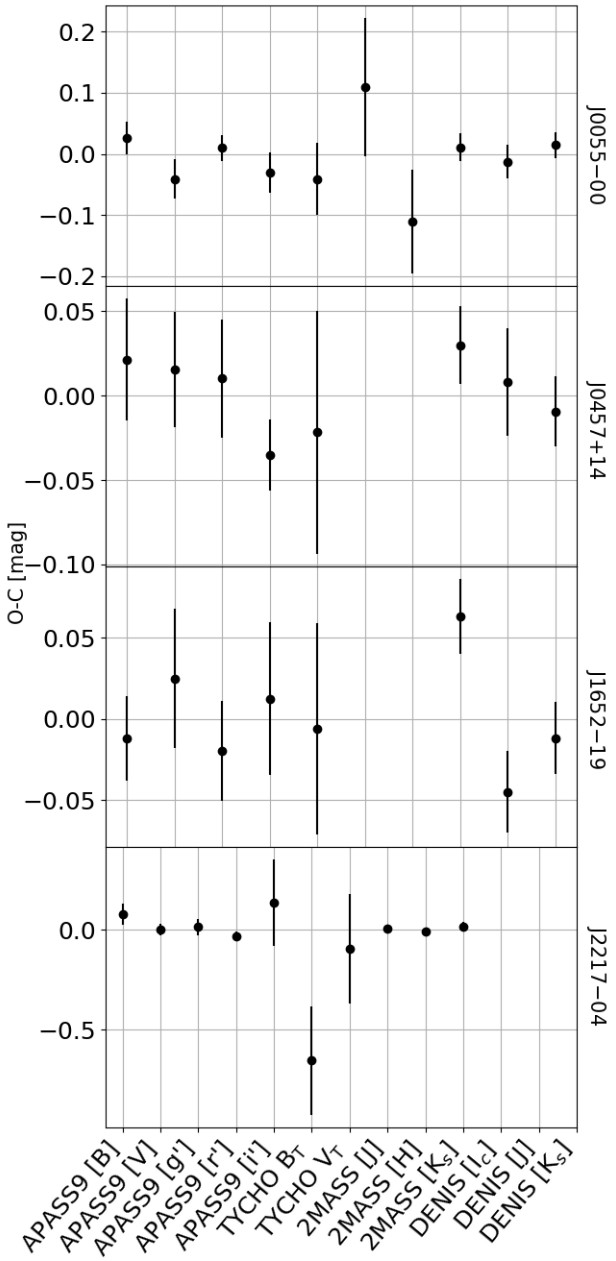

Figure A.10: Difference between observed and fitted magnitudes for EBLMs observed with K2 photometry.

B Lomb-Scargle diagrams

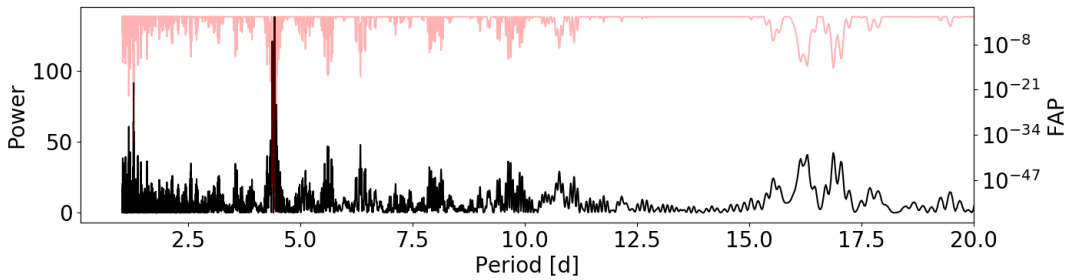

Figure B.1: The generalised Lomb-Scargle diagram J2349−32 for WASP photometry (black) with false-alarm probabilities (FAP; red).

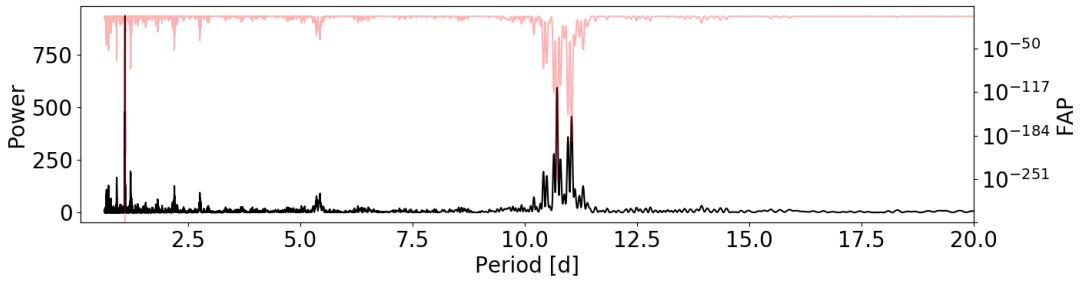

Figure B.2: The generalised Lomb-Scargle diagram J2308−46 for WASP photometry (black) with false-alarm probabilities (FAP; red).

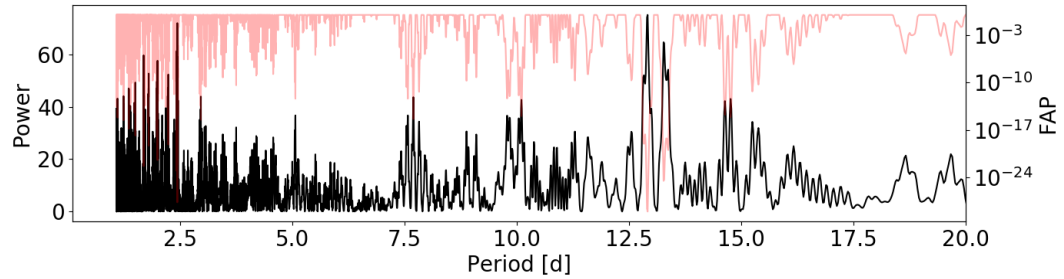

Figure B.3: The generalised Lomb-Scargle diagram J0218−31 for WASP photometry (black) with false-alarm probabilities (FAP; red).

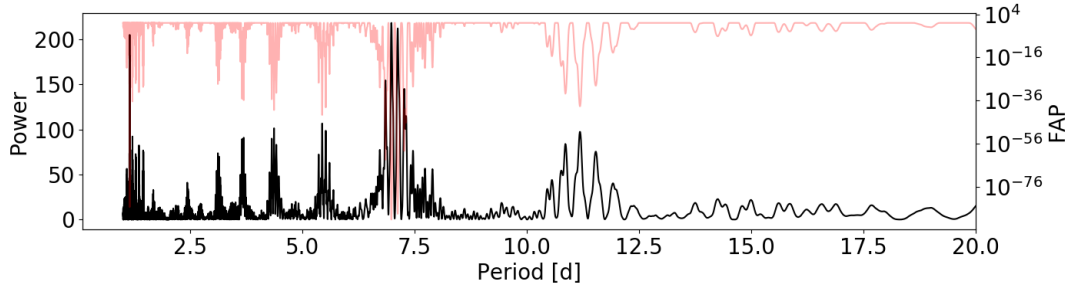

Figure B.4: The generalised Lomb-Scargle diagram J1847−39 for WASP photometry (black) with false-alarm probabilities (FAP; red).

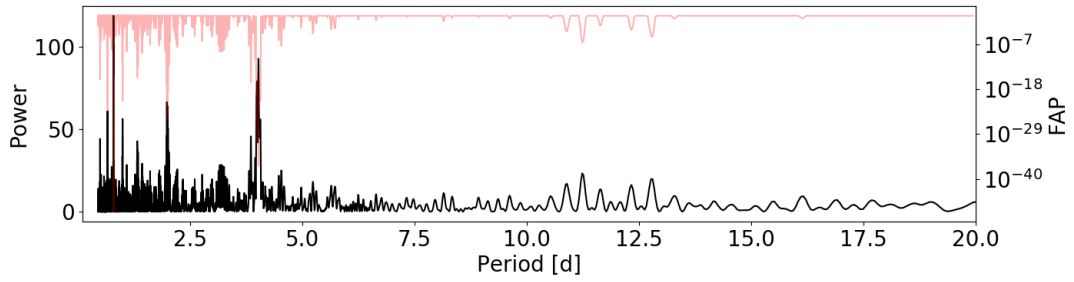

Figure B.5: The generalised Lomb-Scargle diagram J1436−13 for WASP photometry (black) with false-alarm probabilities (FAP; red).

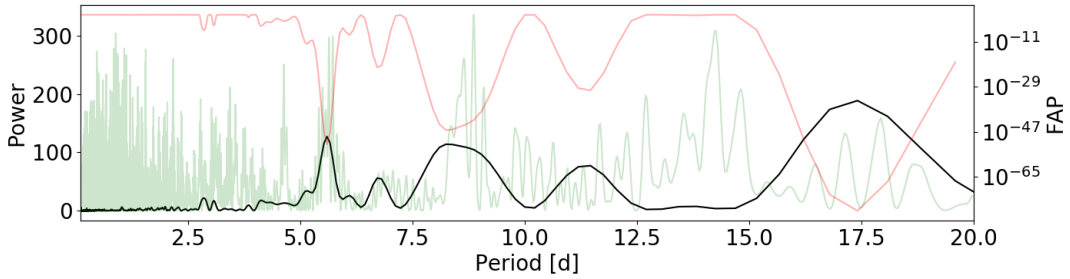

Figure B.6: The generalised Lomb-Scargle diagram J0055−00 for K2 photometry (black) with false-alarm probabilities (FAP; red). The Lomb-Scargle diagram of WASP photometry is also shown (green).

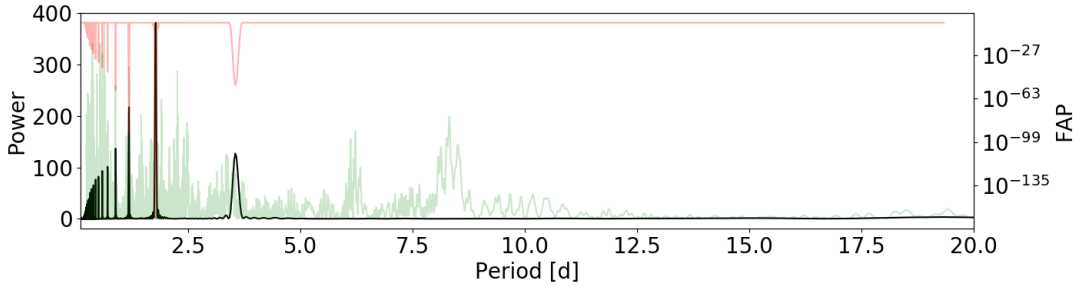

Figure B.7: The generalised Lomb-Scargle diagram J0457+14 for K2 photometry (black) with false-alarm probabilities (FAP; red). The Lomb-Scargle diagram of WASP photometry is also shown (green).

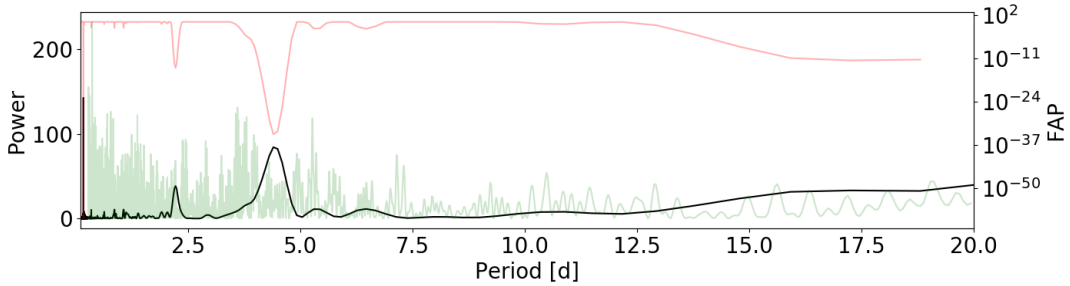

Figure B.8: The generalised Lomb-Scargle diagram J1652−19 for K2 photometry (black) with false-alarm probabilities (FAP; red). The Lomb-Scargle diagram of WASP photometry is also shown (green).

C QPOWER2

```
1  import math
2
3  def q1(z, p, c, a, g, I_0):
4    zt = clip(abs(z), 0,1-p)
5    s = 1-zt*zt
6    c0 = (1-c+c*math.pow(s,g))
7    c2 = 0.5*a*c*math.pow(s,(g-2))*((a-1)*zt*zt-1)
8    return 1-I_0*math.pi*p*p*(c0 + 0.25*p*p*c2 - 0.125*a*c*p*p*math.pow(s,(g-1)))
9
10
11
12
13 def q2(z, p, c, a, g, I_0, eps):
14   zt = clip(abs(z), 1-p,1+p)
15   d = clip((zt*zt - p*p + 1)/(2*zt),0,1)
16   ra = 0.5*(zt-p+d)
17   rb = 0.5*(1+d)
18   sa = clip(1-ra*ra,eps,1)
19   sb = clip(1-rb*rb,eps,1)
20   q = clip((zt-d)/p,-1,1)
21   w2 = p*p-(d-zt)*(d-zt)
22   w = math.sqrt(clip(w2,eps,1))
23   c0 = 1 - c + c*math.pow(sa,g)
24   c1 = -a*c*ra*math.pow(sa,(g-1))
25   c2 = 0.5*a*c*math.pow(sa,(g-2))*((a-1)*ra*ra-1)
26   a0 = c0 + c1*(zt-ra) + c2*(zt-ra)*(zt-ra)
27   a1 = c1+2*c2*(zt-ra)
28   aq = math.acos(q)
29   J1 =  (a0*(d-zt) -(2./3.)*a1*w2 + 0.25*c2*(d-zt)*(2.0*(d-zt)*(d-zt)-p*p))*w + (a0*p*p + 0.25*c2*math.pow(p,4))*aq
30   J2 = a*c*math.pow(sa,(g-1))*math.pow(p,4)*(0.125*aq + (1./12.)*q*(q*q-2.5)*math.sqrt(clip(1-q*q,0.0,1.0)) )
31   d0 = 1 - c + c*math.pow(sb,g)
32   d1 = -a*c*rb*math.pow(sb,(g-1))
33   K1 = (d0-rb*d1)*math.acos(d) + ((rb*d+(2./3.)*(1-d*d))*d1 - d*d0)*math.sqrt(clip(1-d*d,0.0,1.0))
34   K2 = (1/3)*c*a*math.pow(sb,(g+0.5))*(1-d)
35   return 1 - I_0*(J1 - J2 + K1 - K2)
36
37
38
39 def Flux_drop_analytical_power_2(z, k, c, a, f, eps):
40     '''
41     Calculate the analytical flux drop por the power-2 law.
42     Parameters
43     z : double
44         Projected seperation of centers in units of stellar radii.
45     k : double
46         Ratio of the radii.
47     c : double
48         The first power-2 coefficient.
49     a : double
50         The second power-2 coefficient.
51     f : double
52         The flux from which to drop light from.
53     eps : double
54         Factor (1e-9)
55     '''
56     I_0 = (a+2)/(math.pi*(a-c*a+2))
57     g = 0.5*a
58
59     if (z < 1-k) : return q1(z, k, c, a, g, I_0)
60     elif (abs(z-1) < k) : return q2(z, k, c, a, g, I_0, eps)
61     else: return 1.0
```

Appendix/qpower2/qpower2.py

Bibliography

Adams F. C., Graves G. J. M., Laughlin G., 2004, in Garcia-Segura G., Tenorio-Tagle G., Franco J., Yorke H. W., eds, Revista Mexicana de Astronomia y Astrofisica Conference Series, Revista Mexicana de Astronomia y Astrofisica, vol. 27 Vol. 22, p. 46

Aigrain S., Parviainen H., Pope B. J. S., 2016, MNRAS, 459, 2408

Allard F., 1998, in Rebolo R., Martin E. L., Zapatero Osorio M. R., eds, Brown Dwarfs and Extrasolar Planets, Astronomical Society of the Pacific Conference Series Vol. 134, p. 370

Ambikasaran S., Foreman-Mackey D., Greengard L., Hogg D. W., O'Neil M., 2014

Andersen J., 1991, A&A Rv, 3, 91

Anderson D. R., Collier Cameron A., Hellier C., Lendl M., Maxted P. F. L., Pollacco D., Queloz D., Smalley B., Smith A. M. S., Todd I., Triaud A. H. M. J., West R. G., Barros S. C. C., Enoch B., Gillon M., Lister T. A., Pepe F., Ségransan D., Street R. A., Udry S., 2011, ApJL, 726, L19

Anderson D. R., Collier Cameron A., Delrez L., Doyle A. P., Faedi F., Fumel A., Gillon M., Gómez Maqueo Chew Y., Hellier C., Jehin E., Lendl M., Maxted P. F. L., Pepe F., Pollacco D., Queloz D., Ségransan D., Skillen I., Smalley B., Smith A. M. S., Southworth J., Triaud A. H. M. J., Turner O. D., Udry S., West R. G., 2014, MNRAS, 445, 1114

Anderson D. R., Collier Cameron A., Hellier C., Lendl M., Lister T. A., Maxted P. F. L., Queloz D., Smalley B., Smith A. M. S., Triaud A. H. M. J., Brown D. J. A., Gillon M., Neveu-VanMalle M., Pepe F., Pollacco D., Ségransan D., Udry S., West R. G., Wheatley P. J., 2015, A&A, 575, A61

Anglada-Escudé G., Rojas-Ayala B., Boss A. P., Weinberger A. J., Lloyd J. P., 2013, A&A, 551, A48

Anglada-Escudé G., Amado P. J., Barnes J., Berdiñas Z. M., Butler R. P., Coleman G. A. L., de La Cueva I., Dreizler S., Endl M., Giesers B., Jeffers S. V., Jenkins J. S., Jones H. R. A., Kiraga M., Kürster M., López-González M. J., Marvin C. J., Morales N., Morin J., Nelson R. P., Ortiz J. L., Ofir A., Paardekooper S.-J., Reiners A., Rodríguez E., Rodríguez-López C., Sarmiento L. F., Strachan J. P., Tsapras Y., Tuomi M., Zechmeister M., 2016, Nature, 536, 437

Aoki K., 2010, PASJ, 62, 1333

Arenou F., Luri X., Babusiaux C., Fabricius C., Helmi A., Muraveva T., Robin A. C., Spoto F., Vallenari A., Antoja T., Cantat-Gaudin T., Jordi C., Leclerc N., Reylé C., Romero-Gómez M., Shih I.-C., Soria S., Barache C., Bossini D., Bragaglia A., Breddels M. A., Fabrizio M., Lambert S., Marrese P. M., Massari D., Moitinho A., Robichon N., Ruiz-Dern L., Sordo R., Veljanoski J., Eyer L., Jasniewicz G., Pancino E., Soubiran C., Spagna A., Tanga P., Turon C., Zurbach C., 2018, A&A, 616, A17

Asplund M., Grevesse N., Sauval A. J., Scott P., 2009, ARA&A, 47, 481

Baji T., 2017, Society of Photo-Optical Instrumentation Engineers (SPIE) Conference Series, Society of Photo-Optical Instrumentation Engineers (SPIE) Conference Series Vol. 10454, p. 1045406

Baker J., Bizzarro M., Wittig N., Connelly J., Haack H., 2005, Nature, 436, 1127

Baraffe I., Chabrier G., Gallardo J., 2009, ApJL, 702, L27

Baraffe I., Chabrier G., Allard F., Hauschildt P. H., 1998, A&A, 337, 403

Baraffe I., Chabrier G., Allard F., Hauschildt P., 2003, in Martín E., ed., Brown Dwarfs, IAU Symposium Vol. 211, p. 41

Baraffe I., Homeier D., Allard F., Chabrier G., 2015, A&A, 577, A42

Baranne A., Queloz D., Mayor M., Adrianzyk G., Knispel G., Kohler D., Lacroix D., Meunier J.-P., Rimbaud G., Vin A., 1996, A&AS, 119, 373

Barclay T., Quintana E. V., Adams F. C., Ciardi D. R., Huber D., Foreman-Mackey D., Montet B. T., Caldwell D., 2015, ApJ, 809, 7

Barnes S. A., 2003, ApJ, 586, 464

Bastian N., Covey K. R., Meyer M. R., 2010, ARA&A, 48, 339

Bate M. R., Bonnell I. A., 2005, MNRAS, 356, 1201

Beatty T. G., Fernández J. M., Latham D. W., Bakos G. Á., Kovács G., Noyes R. W., Stefanik R. P., Torres G., Everett M. E., Hergenrother C. W., 2007, ApJ, 663, 573

Beatty T. G., Morley C. V., Curtis J. L., Burrows A., Davenport J. R. A., Montet B. T., 2018, AJ, 156, 168

in Bedding T. R., Booth A. J., Davis J., eds, Fundamental stellar properties: the interaction between observation and theory. Proceedings. 189th Symposium of the International Astronomical Union, Sydney (Australia), 13 - 17 Jan 1997., 1997

Belmon L., Benoit-Cattin H., Baskurt A., Bougeret J.-L., 2002, A&A, 386, 1143

Benedict G. F., Henry T. J., Franz O. G., McArthur B. E., Wasserman L. H., Jao W.-C., Cargile P. A., Dieterich S. B., Bradley A. J., Nelan E. P., Whipple A. L., 2016, AJ, 152, 141

Berger D. H., Gies D. R., McAlister H. A., ten Brummelaar T. A., Henry T. J., Sturmann J., Sturmann L., Turner N. H., Ridgway S. T., Aufdenberg J. P., Mérand A., 2006, ApJ, 644, 475

Bernstein R. A., McCarthy P. J., Raybould K., Bigelow B. C., Bouchez A. H., Filgueira J. M., Jacoby G., Johns M., Sawyer D., Shectman S., Sheehan M., 2014, Ground-based and Airborne Telescopes V, Proc. SPIEVol. 9145, p. 91451C

Bertin E., Arnouts S., 1996, A&AS, 117, 393

Bessell M. S., 1991, AJ, 101, 662

Bessell M. S., 2000, PASP, 112, 961

Bessell M. S., 2005, ARA&A, 43, 293

Blanco-Cuaresma S., Nordlander T., Heiter U., Jofré P., Masseron T., Casamiquela L., Tabernero H. M., Bhat S. S., Casey A. R., Meléndez J., Ramírez I., 2016, 19th Cambridge Workshop on Cool Stars, Stellar Systems, and the Sun (CS19), p. 22

Blanco-Cuaresma S., Anderson R. I., Eyer L., Mowlavi N., 2017, in Arribas S., Alonso-Herrero A., Figueras F., Hernández-Monteagudo C., Sánchez-Lavega A., Pérez-Hoyos S., eds, Highlights on Spanish Astrophysics IX, p. 495

Bochanski J. J., West A. A., Hawley S. L., Covey K. R., 2007, AJ, 133, 531

Bouchy F., Bonomo A. S., Santerne A., Moutou C., Deleuil M., Díaz R. F., Eggenberger A., Ehrenreich D., Gry C., Guillot T., Havel M., Hébrard G., Udry S., 2011a, A&A, 533, A83

Bouchy F., Deleuil M., Guillot T., Aigrain S., Carone L., Cochran W. D., Almenara J. M., Alonso R., Auvergne M., Baglin A., Barge P., Bonomo A. S., Bordé P., Csizmadia S., de Bondt K., Deeg H. J., Díaz R. F., Dvorak R., Endl M., Erikson A., Ferraz-Mello S., Fridlund M., Gandolfi D., Gazzano J. C., Gibson N., Gillon M., Guenther E., Hatzes A., Havel M., Hébrard G., Jorda L., Léger A., Lovis C., Llebaria A., Lammer H., MacQueen P. J., Mazeh T., Moutou C., Ofir A., Ollivier M., Parviainen H., Pätzold M., Queloz D., Rauer H., Rouan D., Santerne A., Schneider J., Tingley B., Wuchterl G., 2011b, A&A, 525, A68

Boyajian T. S., McAlister H. A., Baines E. K., Gies D. R., Henry T., Jao W.-C., O'Brien D., Raghavan D., Touhami Y., ten Brummelaar T. A., Farrington C., Goldfinger P. J., Sturmann L., Sturmann J., Turner N. H., Ridgway S., 2008, ApJ, 683, 424

Boyajian T. S., von Braun K., van Belle G., McAlister H. A., ten Brummelaar T. A., Kane S. R., Muirhead P. S., Jones J., White R., Schaefer G., Ciardi D., Henry T., López-Morales M., Ridgway S., Gies D., Jao W.-C., Rojas-Ayala B., Parks J. R., Sturmann L., Sturmann J., Turner N. H., Farrington C., Goldfinger P. J., Berger D. H., 2012, ApJ, 757, 112

Boyajian T. S., von Braun K., van Belle G., Farrington C., Schaefer G., Jones J., White R., McAlister H. A., ten Brummelaar T. A., Ridgway S., Gies D., Sturmann L., Sturmann J., Turner N. H., Goldfinger P. J., Vargas N., 2013, ApJ, 771, 40

Britain R. S. G., 1895, Proceedings of the Royal Society of London, Taylor & Francis

Broeg C., Fortier A., Ehrenreich D., Alibert Y., Baumjohann W., Benz W., Deleuil M., Gillon M., Ivanov A., Liseau R., Meyer M., Oloffson G., Pagano I., Piotto G., Pollacco D., Queloz D., Ragazzoni R., Renotte E., Steller M., Thomas N., 2013, European Physical Journal Web of Conferences, European Physical Journal Web of Conferences Vol. 47, p. 03005

Browning M. K., 2008, ApJ, 676, 1262

Bruntt H., Bedding T. R., Quirion P.-O., Lo Curto G., Carrier F., Smalley B., Dall T. H., Arentoft T., Bazot M., Butler R. P., 2010, MNRAS, 405, 1907

Çakırlı Ö., İbanoğlu C., Sipahi E., 2013, MNRAS, 429, 85

Caffau E., Ludwig H.-G., Steffen M., Freytag B., Bonifacio P., 2011, SoPh, 268, 255

Cantat-Gaudin T., Donati P., Pancino E., Bragaglia A., Vallenari A., Friel E. D., Sordo R., Jacobson H. R., Magrini L., 2014, A&A, 562, A10

Carter J. A., Fabrycky D. C., Ragozzine D., Holman M. J., Quinn S. N., Latham D. W., Buchhave L. A., Van Cleve J., Cochran W. D., Cote M. T., Endl M., Ford E. B., Haas M. R., Jenkins J. M., Koch D. G., Li J., Lissauer J. J., MacQueen P. J., Middour C. K., Orosz J. A., Rowe J. F., Steffen J. H., Welsh W. F., 2011, Science, 331, 562

Cassisi S., Salaris M., Irwin A. W., 2003, ApJ, 588, 862

Chabrier G., Baraffe I., 1997, A&A, 327, 1039

Chabrier G., 2003, PASP, 115, 763

Chabrier G., Baraffe I., Allard F., Hauschildt P., 2000, ApJ, 542, 464

Chabrier G., Gallardo J., Baraffe I., 2007, A&A, 472, L17

Charbonneau P., 2013, Solar and Stellar Dynamos, Saas-Fee Advanced Courses, Volume 39. ISBN 978-3-642-32092-7. Springer-Verlag Berlin Heidelberg, 2013, p. 187, 39, 187

Chaturvedi P., Sharma R., Chakraborty A., Anandarao B. G., Prasad N. J. S. S. V., 2018, AJ, 156, 27

Choi J., Dotter A., Conroy C., Cantiello M., Paxton B., Johnson B. D., 2016, ApJ, 823, 102

Claret A., Hauschildt P. H., 2003, A&A, 412, 241

Claret A., 2000, A&A, 363, 1081

Collier Cameron A., Bouchy F., Hébrard G., Maxted P., Pollacco D., Pont F., Skillen I., Smalley B., Street R. A., West R. G., Wilson D. M., Aigrain S., Christian D. J., Clarkson W. I., Enoch B., Evans A., Fitzsimmons A., Fleenor M., Gillon M., Haswell C. A., Hebb L., Hellier C., Hodgkin S. T., Horne K., Irwin J., Kane S. R., Keenan F. P., Loeillet B., Lister T. A., Mayor M., Moutou C., Norton A. J., Osborne J., Parley N., Queloz D., Ryans R., Triaud A. H. M. J., Udry S., Wheatley P. J., 2007, MNRAS, 375, 951

Covey K. R., Ivezić Ž., Schlegel D., Finkbeiner D., Padmanabhan N., Lupton R. H., Agüeros M. A., Bochanski J. J., Hawley S. L., West A. A., Seth A., Kimball A., Gogarten S. M., Claire M., Haggard D., Kaib N., Schneider D. P., Sesar B., 2007, AJ, 134, 2398

Crossfield I. J. M., Petigura E., Schlieder J. E., Howard A. W., Fulton B. J., Aller K. M., Ciardi D. R., Lépine S., Barclay T., de Pater I., de Kleer K., Quintana E. V., Christiansen J. L., Schlafly E., Kaltenegger L., Crepp J. R., Henning T., Obermeier C., Deacon N., Weiss L. M., Isaacson H. T., Hansen B. M. S., Liu M. C., Greene T., Howell S. B., Barman T., Mordasini C., 2015, ApJ, 804, 10

Csizmadia S., Pasternacki T., Dreyer C., Cabrera J., Erikson A., Rauer H., 2013, A&A, 549, A9

Cuby J. G., Saracco P., Moorwood A. F. M., D'Odorico S., Lidman C., Comerón F., Spyromilio J., 1999, A&A, 349, L41

Dafonte C., Fustes D., Manteiga M., Garabato D., Álvarez M. A., Ulla A., Allende Prieto C., 2016, A&A, 594, A68

Davenport J. R. A., Ivezić Ž., Becker A. C., Ruan J. J., Hunt-Walker N. M., Covey K. R., Lewis A. R., AlSayyad Y., Anderson L. M., 2014, MNRAS, 440, 3430

David T. J., Hillenbrand L. A., Cody A. M., Carpenter J. M., Howard A. W., 2016, ApJ, 816, 21

de Jong R. S., Bellido-Tirado O., Chiappini C., Depagne É., Haynes R., Johl D., Schnurr O., Schwope A., Walcher J., Dionies F., Haynes D., Kelz A., Kitaura F. S., Lamer G., Minchev I., Müller V., Nuza S. E., Olaya J.-C., Piffl T., Popow E., Steinmetz M., Ural U., Williams M., Winkler R., Wisotzki L., Ansorge W. R., Banerji M., Gonzalez Solares E., Irwin M., Kennicutt R. C., King D., McMahon R. G., Koposov S., Parry I. R., Sun D., Walton N. A., Finger G., Iwert O., Krumpe M., Lizon J.-L., Vincenzo M., Amans J.-P., Bonifacio P., Cohen M., Francois P., Jagourel P., Mignot S. B., Royer F., Sartoretti P., Bender R., Grupp F., Hess H.-J., Lang-Bardl F., Muschielok B., Böhringer H., Boller T., Bongiorno A., Brusa M., Dwelly T., Merloni A., Nandra K., Salvato M., Pragt J. H., Navarro R., Gerlofsma G., Roelfsema R., Dalton G. B., Middleton K. F., Tosh I. A., Boeche C., Caffau E., Christlieb N., Grebel E. K., Hansen C., Koch A., Ludwig H.-G., Quirrenbach A., Sbordone L., Seifert W., Thimm G., Trifonov T., Helmi A., Trager S. C., Feltzing S., Korn A., Boland W., 2012, Ground-based and Airborne Instrumentation for Astronomy IV, Proc. SPIEVol. 8446, p. 84460T

de Wit J., Seager S., 2013, Science, 342, 1473

Delfosse X., Forveille T., Ségransan D., Beuzit J.-L., Udry S., Perrier C., Mayor M., 2000, A&A, 364, 217

Delrez L., Gillon M., Queloz D., Demory B.-O., Almleaky Y., de Wit J., Jehin E., Triaud A. H. M. J., Barkaoui K., Burdanov A., Burgasser A. J., Ducrot E., McCormac J., Murray C., Silva Fernandes C., Sohy S., Thompson S. J., Van Grootel V., Alonso R., Benkhaldoun Z., Rebolo R., 2018a, Society of Photo-Optical Instrumentation Engineers (SPIE) Conference Series, Society of Photo-Optical Instrumentation Engineers (SPIE) Conference Series Vol. 10700, p. 107001I

Delrez L., Gillon M., Triaud A. H. M. J., Demory B.-O., de Wit J., Ingalls J. G., Agol E., Bolmont E., Burdanov A., Burgasser A. J., Carey S. J., Jehin E., Leconte J., Lederer S., Queloz D., Selsis F., Van Grootel V., 2018b, MNRAS, 475, 3577

Demory B.-O., Ségransan D., Forveille T., Queloz D., Beuzit J.-L., Delfosse X., di Folco E., Kervella P., Le Bouquin J.-B., Perrier C., Benisty M., Duvert G., Hofmann K.-H., Lopez B., Petrov R., 2009, A&A, 505, 205

di Folco E., Absil O., Augereau J.-C., Mérand A., Coudé du Foresto V., Thévenin F., Defrère D., Kervella P., ten Brummelaar T. A., McAlister H. A., Ridgway S. T., Sturmann J., Sturmann L., Turner N. H., 2007, A&A, 475, 243

Diaz-Cordoves J., Gimenez A., 1992, A&A, 259, 227

Dieterich S. B., Henry T. J., Jao W.-C., Winters J. G., Hosey A. D., Riedel A. R., Subasavage J. P., 2014, AJ, 147, 94

Dobler W., Stix M., Brandenburg A., 2006, ApJ, 638, 336

Dotter A., 2016, ApJS, 222, 8

Doyle A. P., 2015, PhD thesis, Keele University

Doyle L. R., Carter J. A., Fabrycky D. C., Slawson R. W., Howell S. B., Winn J. N., Orosz J. A., Přsa A., Welsh W. F., Quinn S. N., Latham D., Torres G., Buchhave L. A., Marcy G. W., Fortney J. J., Shporer A., Ford E. B., Lissauer J. J., Ragozzine D., Rucker M., Batalha N., Jenkins J. M., Borucki W. J., Koch D., Middour C. K., Hall J. R., McCauliff S., Fanelli M. N., Quintana E. V., Holman M. J., Caldwell D. A., Still M., Stefanik R. P., Brown W. R., Esquerdo G. A., Tang S., Furesz G., Geary J. C., Berlind P., Calkins M. L., Short D. R., Steffen J. H., Sasselov D., Dunham E. W., Cochran W. D., Boss A., Haas M. R., Buzasi D., Fischer D., 2011, Science, 333, 1602

Doyle A. P., Smalley B., Maxted P. F. L., Anderson D. R., Cameron A. C., Gillon M., Hellier C., Pollacco D., Queloz D., Triaud A. H. M. J., West R. G., 2013, MNRAS, 428, 3164

Doyle A. P., Davies G. R., Smalley B., Chaplin W. J., Elsworth Y., 2014, MNRAS, 444, 3592

Doyle A. P., Smalley B., Faedi F., Pollacco D., Gómez Maqueo Chew Y., 2017, MNRAS, 469, 4850

Eastman J., 2017, *EXOFASTv2: Generalized publication-quality exoplanet modeling code*, Astrophysics Source Code Library

Epchtein N., de Batz B., Capoani L., Chevallier L., Copet E., Fouqué P., Lacombe P., Le Bertre T., Pau S., Rouan D., Ruphy S., Simon G., Tiphène D., Burton W. B., Bertin E., Deul E., Habing H., Borsenberger J., Dennefeld M., Guglielmo F., Loup C., Mamon G., Ng Y., Omont A., Provost L., Renault J.-C., Tanguy F., Kimeswenger S., Kienel C., Garzon F., Persi P., Ferrari-Toniolo M., Robin A., Paturel G., Vauglin I., Forveille T., Delfosse X., Hron J., Schultheis M., Appenzeller I., Wagner S., Balazs L., Holl A., Lépine J., Boscolo P., Picazzio E., Duc P.-A., Mennessier M.-O., 1997, The Messenger, 87, 27

Essaouabi A., Regragui F., Ibnelhaj E., 2009, ArXiv e-prints

Evans D. F., Southworth J., Smalley B., Jørgensen U. G., Dominik M., Andersen M. I., Bozza V., Bramich D. M., Burgdorf M. J., Ciceri S., D'Ago G., Figuera Jaimes R., Gu S.-H., Hinse T. C., Henning T., Hundertmark M., Kains N., Kerins E., Korhonen H., Kokotanekova R., Kuffmeier M., Longa-Peña P., Mancini L., MacKenzie J., Popovas

A., Rabus M., Rahvar S., Sajadian S., Snodgrass C., Skottfelt J., Surdej J., Tronsgaard R., Unda-Sanzana E., von Essen C., Wang Y.-B., Wertz O., 2018, A&A, 610, A20

Feiden G. A., Chaboyer B., 2013, ApJ, 779, 183

Feiden G. A., Chaboyer B., 2014, ApJ, 789, 53

Feiden G. A., 2016, A&A, 593, A99

Fiorucci M., Munari U., 2003, A&A, 401, 781

Fischer D. A., Marcy G. W., 1992, ApJ, 396, 178

Ford E. B., 2005, AJ, 129, 1706

Ford E. B., 2006, ApJ, 642, 505

Foreman-Mackey D., Hogg D. W., Lang D., Goodman J., 2013, PASP, 125, 306

Foreman-Mackey D., Agol E., Ambikasaran S., Angus R., 2017, AJ, 154, 220

Freedman R. S., Marley M. S., Lodders K., 2008, ApJS, 174, 504

Frommhold L., Abel M., Wang F., Gustafsson M., Li X., Hunt K. L. C., 2010, Molecular Physics, 108, 2265

Fukushima T., 1997, Celestial Mechanics and Dynamical Astronomy, 66, 309

Gaia Collaboration, Babusiaux C., van Leeuwen F., Barstow M. A., Jordi C., Vallenari A., Bossini D., Bressan A., Cantat-Gaudin T., van Leeuwen M., et al., 2018, A&A, 616, A10

Gardner J. P., Mather J. C., Clampin M., Doyon R., Greenhouse M. A., Hammel H. B., Hutchings J. B., Jakobsen P., Lilly S. J., Long K. S., Lunine J. I., McCaughrean M. J., Mountain M., Nella J., Rieke G. H., Rieke M. J., Rix H.-W., Smith E. P., Sonneborn G., Stiavelli M., Stockman H. S., Windhorst R. A., Wright G. S., 2006, SSRv, 123, 485

Gill S., Maxted P. F. L., Smalley B., 2018, A&A, 612, A111

Gillen E., Hillenbrand L. A., David T. J., Aigrain S., Rebull L., Stauffer J., Cody A. M., Queloz D., 2017, ApJ, 849, 11

Gillon M., Smalley B., Hebb L., Anderson D. R., Triaud A. H. M. J., Hellier C., Maxted P. F. L., Queloz D., Wilson D. M., 2009, A&A, 496, 259

Gillon M., Triaud A. H. M. J., Demory B.-O., Jehin E., Agol E., Deck K. M., Lederer S. M., de Wit J., Burdanov A., Ingalls J. G., Bolmont E., Leconte J., Raymond S. N., Selsis F., Turbet M., Barkaoui K., Burgasser A., Burleigh M. R., Carey S. J., Chaushev A., Copperwheat C. M., Delrez L., Fernandes C. S., Holdsworth D. L., Kotze E. J., Van Grootel V., Almleaky Y., Benkhaldoun Z., Magain P., Queloz D., 2017, Nature, 542, 456

Goldsmith H., 2001, Biophysical Journal, 81, 2020

Gómez Maqueo Chew Y., Morales J. C., Faedi F., García-Melendo E., Hebb L., Rodler F., Deshpande R., Mahadevan S., McCormac J., Barnes R., Triaud A. H. M. J., Lopez-Morales M., Skillen I., Collier Cameron A., Joner M. D., Laney C. D., Stephens D. C., Stassun K. G., Cargile P. A., Montañés-Rodríguez P., 2014, A&A, 572, A50

Goodman, J. . W. J., 2010, Commun. Appl. Math. Comput. Sci., 5(65), p. 68-75

Gray R. O., Corbally C. J., 1994, AJ, 107, 742

Gray D. F., 2008, The Observation and Analysis of Stellar Photospheres

Grevesse N., Sauval A. J., 1998, SSRv, 85, 161

Gustafsson B., Edvardsson B., Eriksson K., Jørgensen U. G., Nordlund Å., Plez B., 2008, A&A, 486, 951

Han E., Muirhead P. S., Swift J. J., Baranec C., Law N. M., Riddle R., Atkinson D., Mace G. N., DeFelippis D., 2017, AJ, 154, 100

Harpsøe K. B. W., Jørgensen U. G., Andersen M. I., Grundahl F., 2012, A&A, 542, A23

Hartman J. D., Quinn S. N., Bakos G. Á., Torres G., Kovács G., Latham D. W., Noyes R. W., Shporer A., Fulton B. J., Esquerdo G. A., Everett M. E., Penev K., Bhatti W., Csubry Z., 2018, AJ, 155, 114

Hayes D. S., Latham D. W., 1975, ApJ, 197, 593

Hebb L., Collier-Cameron A., Loeillet B., Pollacco D., Hébrard G., Street R. A., Bouchy F., Stempels H. C., Moutou C., Simpson E., Udry S., Joshi Y. C., West R. G., Skillen I., Wilson D. M., McDonald I., Gibson N. P., Aigrain S., Anderson D. R., Benn C. R., Christian D. J., Enoch B., Haswell C. A., Hellier C., Horne K., Irwin J., Lister T. A., Maxted P., Mayor M., Norton A. J., Parley N., Pont F., Queloz D., Smalley B., Wheatley P. J., 2009, ApJ, 693, 1920

Henden A. A., Templeton M., Terrell D., Smith T. C., Levine S., Welch D., 2016, VizieR Online Data Catalog, 2336

Henry T. J., McCarthy, Jr. D. W., 1993, AJ, 106, 773

Henry T. J., Jao W.-C., Subasavage J. P., Beaulieu T. D., Ianna P. A., Costa E., Mndez R. A., 2006, The Astronomical Journal, 132(6), 2360

Hestroffer D., 1997, A&A, 327, 199

Hilditch R. W., 2001, An Introduction to Close Binary Stars

Hjellming M. S., Taam R. E., 1991, ApJ, 370, 709

Høg E., Fabricius C., Makarov V. V., Urban S., Corbin T., Wycoff G., Bastian U., Schwekendiek P., Wicenec A., 2000, A&A, 355, L27

Holt J. R., 1893, Astro-Physics, 11, 646

Howarth I. D., Murray J., Mills D., Berry D. S., 2014, *DIPSO: Spectrum analysis code*, Astrophysics Source Code Library

Howell S. B., Sobeck C., Haas M., Still M., Barclay T., Mullally F., Troeltzsch J., Aigrain S., Bryson S. T., Caldwell D., Chaplin W. J., Cochran W. D., Huber D., Marcy G. W., Miglio A., Najita J. R., Smith M., Twicken J. D., Fortney J. J., 2014, PASP, 126, 398

Husser T.-O., Wende-von Berg S., Dreizler S., Homeier D., Reiners A., Barman T., Hauschildt P. H., 2013, A&A, 553, A6

Iglesias-Marzoa R., López-Morales M., Arévalo M. J., Coughlin J. L., Lázaro C., 2017, A&A, 600, A55

Ingalls J. G., Krick J. E., Carey S. J., Stauffer J. R., Lowrance P. J., Grillmair C. J., Buzasi D., Deming D., Diamond-Lowe H., Evans T. M., Morello G., Stevenson K. B., Wong I., Capak P., Glaccum W., Laine S., Surace J., Storrie-Lombardi L., 2016, AJ, 152, 44

Irwin M., Lewis J., 2001, NewAR, 45, 105

Irwin J., Buchhave L., Berta Z. K., Charbonneau D., Latham D. W., Burke C. J., Esquerdo G. A., Everett M. E., Holman M. J., Nutzman P., Berlind P., Calkins M. L., Falco E. E., Winn J. N., Johnson J. A., Gazak J. Z., 2010, ApJ, 718, 1353

Irwin J., Berta Z. K., Burke C. J., Charbonneau D., Nutzman P., West A. A., Falco E. E., 2011a, ApJ, 727, 56

Irwin J. M., Quinn S. N., Berta Z. K., Latham D. W., Torres G., Burke C. J., Charbonneau D., Dittmann J., Esquerdo G. A., Stefanik R. P., Oksanen A., Buchhave L. A., Nutzman P., Berlind P., Calkins M. L., Falco E. E., 2011b, ApJ, 742, 123

Jeffries R. D., 2012, in Reylé C., Charbonnel C., Schultheis M., eds, EAS Publications Series, EAS Publications Series Vol. 57, p. 45

Jofré P., Heiter U., Worley C. C., Blanco-Cuaresma S., Soubiran C., Masseron T., Hawkins K., Adibekyan V., Buder S., Casamiquela L., Gilmore G., Hourihane A., Tabernero H., 2017, A&A, 601, A38

Kervella P., Mérand A., Pichon B., Thévenin F., Heiter U., Bigot L., ten Brummelaar T. A., McAlister H. A., Ridgway S. T., Turner N., Sturmann J., Sturmann L., Goldfinger P. J., Farrington C., 2008, A&A, 488, 667

Kippenhahn R., Weigert A., 1990, Stellar Structure and Evolution

Kirkpatrick J. D., Henry T. J., McCarthy, Jr. D. W., 1991, ApJS, 77, 417

Klinglesmith D. A., Sobieski S., 1970, AJ, 75, 175

Kopal Z., 1950, Harvard College Observatory Circular, 454, 1

Kraft R. P., Ivans I. I., 2004, Origin and Evolution of the Elements

Kraft R. P., 1967, ApJ, 150, 551

Kraus A. L., Tucker R. A., Thompson M. I., Craine E. R., Hillenbrand L. A., 2011, ApJ, 728, 48

Kraus A. L., Douglas S. T., Mann A. W., Agüeros M. A., Law N. M., Covey K. R., Feiden G. A., Rizzuto A. C., Howard A. W., Isaacson H., Gaidos E., Torres G., Bakos G., 2017, ApJ, 845, 72

Kreidberg L., 2015, PASP, 127, 1161

Kroupa P., Weidner C., Pflamm-Altenburg J., Thies I., Dabringhausen J., Marks M., Maschberger T., The Stellar and Sub-Stellar Initial Mass Function of Simple and Composite Populations, 115, 2013

Kwee K. K., van Woerden H., 1956, BAN, 12, 327

Lada C. J., 2006, ApJL, 640, L63

Lane B. F., Boden A. F., Kulkarni S. R., 2001, ApJL, 551, L81

Larson R. B., 1992, MNRAS, 256, 641

Law N. M., Mackay C. D., Baldwin J. E., 2006, A&A, 446, 739

Leggett S. K., Allard F., Dahn C., Hauschildt P. H., Kerr T. H., Rayner J., 2000, ApJ, 535, 965

Leinert C., Henry T., Glindemann A., McCarthy, Jr. D. W., 1997, A&A, 325, 159

Levecque K., Anseel F., Beuckelaer A. D., der Heyden J. V., Gisle L., 2017, Research Policy, 46(4), 868

Li X., Lu Y., Comte G., Luo A., Zhao Y., Wang Y., 2015, ApJS, 218, 3

Lindegren L., Hernández J., Bombrun A., Klioner S., Bastian U., Ramos-Lerate M., de Torres A., Steidelmüller H., Stephenson C., Hobbs D., Lammers U., Biermann M., Geyer R., Hilger T., Michalik D., Stampa U., McMillan P. J., Castañeda J., Clotet M., Comoretto G., Davidson M., Fabricius C., Gracia G., Hambly N. C., Hutton A., Mora A., Portell J., van Leeuwen F., Abbas U., Abreu A., Altmann M., Andrei A., Anglada E., Balaguer-Núñez L., Barache C., Becciani U., Bertone S., Bianchi L., Bouquillon S., Bourda G., Brüsemeister T., Bucciarelli B., Busonero D., Buzzi R., Cancelliere R., Carlucci T., Charlot P., Cheek N., Crosta M., Crowley C., de Bruijne J., de Felice F., Drimmel R., Esquej P., Fienga A., Fraile E., Gai M., Garralda N., González-Vidal J. J., Guerra R., Hauser M., Hofmann W., Holl B., Jordan S., Lattanzi M. G., Lenhardt H., Liao S., Licata E., Lister T., Löffler W., Marchant J., Martin-Fleitas J.-M., Messineo R., Mignard F., Morbidelli R., Poggio E., Riva A., Rowell N., Salguero E., Sarasso M., Sciacca E., Siddiqui H., Smart R. L., Spagna A., Steele I., Taris F., Torra J., van Elteren A., van Reeven W., Vecchiato A., 2018, A&A, 616, A2

López-Morales M., Ribas I., 2005, ApJ, 631, 1120

López-Morales M., 2007, ApJ, 660, 732

Lubin J. B., Rodriguez J. E., Zhou G., Conroy K. E., Stassun K. G., Collins K., Stevens D. J., Labadie-Bartz J., Stockdale C., Myers G., Colón K. D., Bento J., Kehusmaa P., Petrucci R., Jofré E., Quinn S. N., Lund M. B., Kuhn R. B., Siverd R. J., Beatty T. G., Harlingten C., Pepper J., Gaudi B. S., James D., Jensen E. L. N., Reichart D., Kedziora-Chudczer L., Bailey J., Melville G., 2017, ApJ, 844, 134

Luhman K. L., 2000, ApJ, 544, 1044

Luhman K. L., Rieke G. H., Young E. T., Cotera A. S., Chen H., Rieke M. J., Schneider G., Thompson R. I., 2000, ApJ, 540, 1016

Mackey J., Mohamed S., Gvaramadze V. V., Kotak R., Langer N., Meyer D. M.-A., Moriya T. J., Neilson H. R., 2014, Nature, 512, 282

Magain P., 1984, A&A, 134, 189

Magic Z., Chiavassa A., Collet R., Asplund M., 2015, A&A, 573, A90

Maldonado J., Affer L., Micela G., Scandariato G., Damasso M., Stelzer B., Barbieri M., Bedin L. R., Biazzo K., Bignamini A., Borsa F., Claudi R. U., Covino E., Desidera S., Esposito M., Gratton R., González Hernández J. I., Lanza A. F., Maggio A., Molinari E., Pagano I., Perger M., Pillitteri I., Piotto G., Poretti E., Prisinzano L., Rebolo R., Ribas I., Shkolnik E., Southworth J., Sozzetti A., Suárez Mascareño A., 2015, A&A, 577, A132

Mamajek E. E., Hillenbrand L. A., 2008, ApJ, 687, 1264

Mann A. W., Brewer J. M., Gaidos E., Lépine S., Hilton E. J., 2013, AJ, 145, 52

Mann A. W., Feiden G. A., Gaidos E., Boyajian T., von Braun K., 2015, ApJ, 804, 64

Manteiga M., Ordóñez D., Dafonte C., Arcay B., 2010, PASP, 122, 608

Masseron T., Merle T., Hawkins K., 2016, *BACCHUS: Brussels Automatic Code for Characterizing High accUracy Spectra*, Astrophysics Source Code Library

Mathieu R. D., Mazeh T., 1988, ApJ, 326, 256

Matt S., Pudritz R. E., 2005, ApJL, 632, L135

Maxted P. F. L., Gill S., 2018, arXiv e-prints

Maxted P. F. L., 2016, A&A, 591, A111

Maxted P. F. L., 2018, A&A, 616, A39

Maxted P. F. L., Anderson D. R., Collier Cameron A., Hellier C., Queloz D., Smalley B., Street R. A., Triaud A. H. M. J., West R. G., Gillon M., Lister T. A., Pepe F., Pollacco D., Ségransan D., Smith A. M. S., Udry S., 2011, PASP, 123, 547

Maxted P. F. L., Bloemen S., Heber U., Geier S., Wheatley P. J., Marsh T. R., Breedt E., Sebastian D., Faillace G., Owen C., Pulley D., Smith D., Kolb U., Haswell C. A., Southworth J., Anderson D. R., Smalley B., Collier Cameron A., Hebb L., Simpson E. K., West R. G., Bochinski J., Busuttil R., Hadigal S., 2014, MNRAS, 437, 1681

Maxted P. F. L., Serenelli A. M., Southworth J., 2015a, A&A, 575, A36

Maxted P. F. L., Serenelli A. M., Southworth J., 2015b, A&A, 577, A90

Mazeh T., 2008, in Goupil M.-J., Zahn J.-P., eds, EAS Publications Series, EAS Publications Series Vol. 29, p. 1

McKee C. F., Krumholz M. R., 2010, ApJ, 709, 308

McLaughlin D. B., 1924, 60, 22

Mollière P., van Boekel R., Bouwman J., Henning T., Lagage P.-O., Min M., 2017, A&A, 600, A10

Monnier J. D., Zhao M., Pedretti E., Thureau N., Ireland M., Muirhead P., Berger J.-P., Millan-Gabet R., Van Belle G., ten Brummelaar T., McAlister H., Ridgway S., Turner N., Sturmann L., Sturmann J., Berger D., 2007, Science, 317, 342

Morello G., Tsiaras A., Howarth I. D., Homeier D., 2017, AJ, 154, 111

Morgan W. D., 1943, SoPh, 275

Mortier A., Santos N. C., Sousa S. G., Fernandes J. M., Adibekyan V. Z., Delgado Mena E., Montalto M., Israelian G., 2013, A&A, 558, A106

Mortier A., Sousa S. G., Adibekyan V. Z., Brandão I. M., Santos N. C., 2014, A&A, 572, A95

Muirhead P. S., Johnson J. A., Apps K., Carter J. A., Morton T. D., Fabrycky D. C., Pineda J. S., Bottom M., Rojas-Ayala B., Schlawin E., Hamren K., Covey K. R., Crepp J. R., Stassun K. G., Pepper J., Hebb L., Kirby E. N., Howard A. W., Isaacson H. T., Marcy G. W., Levitan D., Diaz-Santos T., Armus L., Lloyd J. P., 2012, ApJ, 747, 144

Mullan D. J., MacDonald J., 2001, ApJ, 559, 353

Nagayama T., Nagashima C., Nakajima Y., Nagata T., Sato S., Nakaya H., Yamamuro T., Sugitani K., Tamura M., 2003, in Iye M., Moorwood A. F. M., eds, Instrument Design and Performance for Optical/Infrared Ground-based Telescopes, Proc. SPIEVol. 4841, p. 459

Narayanan D., Davé R., 2012, MNRAS, 423, 3601

Nelan E. P., Makidon R., Benedict G. F., McArthur Q. B., 2001, American Astronomical Society Meeting Abstracts #198, Bulletin of the American Astronomical Society Vol. 33, p. 861

Nesvorný D., Kipping D., Terrell D., Hartman J., Bakos G. Á., Buchhave L. A., 2013, ApJ, 777, 3

Newton E. R., Irwin J., Charbonneau D., Berta-Thompson Z. K., Dittmann J. A., West A. A., 2016, ApJ, 821, 93

Nordlund Å., Stein R. F., Asplund M., 2009, Living Reviews in Solar Physics, 6, 2

Nutzman P., Charbonneau D., 2008, PASP, 120, 317

Offner S. S. R., Clark P. C., Hennebelle P., Bastian N., Bate M. R., Hopkins P. F., Moraux E., Whitworth A. P., 2014, Protostars and Planets VI, , 53

Ofir A., Gandolfi D., Buchhave L., Lacy C. H. S., Hatzes A. P., Fridlund M., 2012, MNRAS, 423, L1

Ohnaka K., Weigelt G., Hofmann K.-H., 2017, Nature, 548, 310

Olkkonen J. T., 2011, Discrete Wavelet Transforms, InTech

Omukai K., 2007, PASJ, 59, 589

Owens J., Luebke D., Govindaraju N., Harris M., Krger J., Lefohn A., Purcell T., 2007, 26, 80

Owens J. D., Houston M., Luebke D., Green S., Stone J. E., Phillips J. C., 2008, Proceedings of the IEEE, 96(5), 879

Oyama Y., Ben-Nun T., Hoefler T., Matsuoka S., 2018, ArXiv e-prints

Paladini C., Baron F., Jorissen A., Le Bouquin J.-B., Freytag B., van Eck S., Wittkowski M., Hron J., Chiavassa A., Berger J.-P., Siopis C., Mayer A., Sadowski G., Kravchenko K., Shetye S., Kerschbaum F., Kluska J., Ramstedt S., 2018, Nature, 553, 310

Parsons S. G., Marsh T. R., Copperwheat C. M., Dhillon V. S., Littlefair S. P., Gänsicke B. T., Hickman R., 2010, MNRAS, 402, 2591

Parsons S. G., Gänsicke B. T., Marsh T. R., Ashley R. P., Breedt E., Burleigh M. R., Copperwheat C. M., Dhillon V. S., Green M. J., Hermes J. J., Irawati P., Kerry P., Littlefair S. P., Rebassa-Mansergas A., Sahman D. I., Schreiber M. R., Zorotovic M., 2018, MNRAS, 481, 1083

Parviainen H., Aigrain S., 2015, MNRAS, 453, 3821

Parviainen H., 2015, MNRAS, 450, 3233

Patterson D., Hennessy J., 2014, *The Morgan Kaufmann Series in Computer Architecture and Design*, Computer Organization and Design, Enhanced: The Hardware/Software Interface, Elsevier Science

Phillips K. J. H., 1995, Guide to the Sun

Piskunov N., Valenti J. A., 2017, A&A, 597, A16

Plez B., 2012, *Turbospectrum: Code for spectral synthesis*, Astrophysics Source Code Library

Pollacco D. L., Skillen I., Collier Cameron A., Christian D. J., Hellier C., Irwin J., Lister T. A., Street R. A., West R. G., Anderson D. R., Clarkson W. I., Deeg H., Enoch B., Evans A., Fitzsimmons A., Haswell C. A., Hodgkin S., Horne K., Kane S. R., Keenan F. P., Maxted P. F. L., Norton A. J., Osborne J., Parley N. R., Ryans R. S. I., Smalley B., Wheatley P. J., Wilson D. M., 2006a, PASP, 118, 1407

Pollacco D. L., Skillen I., Collier Cameron A., Christian D. J., Hellier C., Irwin J., Lister T. A., Street R. A., West R. G., Anderson D. R., Clarkson W. I., Deeg H., Enoch B., Evans A., Fitzsimmons A., Haswell C. A., Hodgkin S., Horne K., Kane S. R., Keenan F. P., Maxted P. F. L., Norton A. J., Osborne J., Parley N. R., Ryans R. S. I., Smalley B., Wheatley P. J., Wilson D. M., 2006b, PASP, 118, 1407

Poppenhaeger K., 2017, in Nandy D., Valio A., Petit P., eds, Living Around Active Stars, IAU Symposium Vol. 328, p. 308

Poznanski D., Prochaska J. X., Bloom J. S., 2012, MNRAS, 426, 1465

Prato L., Greene T. P., Simon M., 2003, ApJ, 584, 853

Press W. H., Rybicki G. B., 1989, ApJ, 338, 277

Prialnik D., 2009, An Introduction to the Theory of Stellar Structure and Evolution

Prša A., Harmanec P., Torres G., Mamajek E., Asplund M., Capitaine N., Christensen-Dalsgaard J., Depagne É., Haberreiter M., Hekker S., Hilton J., Kopp G., Kostov V., Kurtz D. W., Laskar J., Mason B. D., Milone E. F., Montgomery M., Richards M., Schmutz W., Schou J., Stewart S. G., 2016, AJ, 152, 41

Queloz D., Henry G. W., Sivan J. P., Baliunas S. L., Beuzit J. L., Donahue R. A., Mayor M., Naef D., Perrier C., Udry S., 2001a, A&A, 379, 279

Queloz D., Mayor M., Udry S., Burnet M., Carrier F., Eggenberger A., Naef D., Santos N., Pepe F., Rupprecht G., Avila G., Baeza F., Benz W., Bertaux J.-L., Bouchy F., Cavadore C., Delabre B., Eckert W., Fischer J., Fleury M., Gilliotte A., Goyak D., Guzman J. C., Kohler D., Lacroix D., Lizon J.-L., Megevand D., Sivan J.-P., Sosnowska D., Weilenmann U., 2001b, The Messenger, 105, 1

Quintana E. V., Barclay T., Raymond S. N., Rowe J. F., Bolmont E., Caldwell D. A., Howell S. B., Kane S. R., Huber D., Crepp J. R., Lissauer J. J., Ciardi D. R., Coughlin J. L., Everett M. E., Henze C. E., Horch E., Isaacson H., Ford E. B., Adams F. C., Still M., Hunter R. C., Quarles B., Selsis F., 2014, Science, 344, 277

Raghavan D., McAlister H. A., Henry T. J., Latham D. W., Marcy G. W., Mason B. D., Gies D. R., White R. J., ten Brummelaar T. A., 2010, ApJS, 190, 1

Reiners A., 2012, Living Reviews in Solar Physics, 9, 1

Ribas I., 2003, A&A, 398, 239

Ribas I., Morales J. C., Jordi C., Baraffe I., Chabrier G., Gallardo J., 2008, MmSAI, 79, 562

Rogers F. J., Nayfonov A., 2002, ApJ, 576, 1064

Rossiter R. A., 1924, 60, 15

Rowe J. F., Bryson S. T., Marcy G. W., Lissauer J. J., Jontof-Hutter D., Mullally F., Gilliland R. L., Issacson H., Ford E., Howell S. B., Borucki W. J., Haas M., Huber D., Steffen J. H., Thompson S. E., Quintana E., Barclay T., Still M., Fortney J., Gautier, III T. N., Hunter R., Caldwell D. A., Ciardi D. R., Devore E., Cochran W., Jenkins J., Agol E., Carter J. A., Geary J., 2014, ApJ, 784, 45

Salaris M., Althaus L. G., García-Berro E., 2013, A&A, 555, A96

Salaris M., Domínguez I., García-Berro E., Hernanz M., Isern J., Mochkovitch R., 1997, ApJ, 486, 413

Santos N. C., Sousa S. G., Mortier A., Neves V., Adibekyan V., Tsantaki M., Delgado Mena E., Bonfils X., Israelian G., Mayor M., Udry S., 2013, A&A, 556, A150

Schlafly E. F., Finkbeiner D. P., 2011, ApJ, 737, 103

Schlesinger F., 1910, Publications of the Allegheny Observatory of the University of Pittsburgh, 1, 123

Schlieder J. E., Crossfield I. J. M., Petigura E. A., Howard A. W., Aller K. M., Sinukoff E., Isaacson H. T., Fulton B. J., Ciardi D. R., Bonnefoy M., Ziegler C., Morton T. D., Lépine S., Obermeier C., Liu M. C., Bailey V. P., Baranec C., Beichman C. A., Defrère D., Henning T., Hinz P., Law N., Riddle R., Skemer A., 2016, ApJ, 818, 87

Schwarzschild K., 1906, Astronomische Mitteilungen der Universitaets-Sternwarte zu Goettingen, 13

Seager S., Mallen-Ornelas G., 2002, ArXiv Astrophysics e-prints

Ségransan D., Delfosse X., Forveille T., Beuzit J. L., Perrier C., Udry S., Mayor M., 2003a, in Martín E., ed., Brown Dwarfs, IAU Symposium Vol. 211, p. 413

Ségransan D., Kervella P., Forveille T., Queloz D., 2003b, A&A, 397, L5

Serenelli A., Peña-Garay C., Haxton W. C., 2013, PhRvD, 87(4), 043001

Shields A. L., Ballard S., Johnson J. A., 2016, PhR, 663, 1

Sing D. K., Désert J.-M., Lecavelier Des Etangs A., Ballester G. E., Vidal-Madjar A., Parmentier V., Hebrard G., Henry G. W., 2009, A&A, 505, 891

Skottfelt J., Bramich D. M., Hundertmark M., Jørgensen U. G., Michaelsen N., Kjærgaard P., Southworth J., Sørensen A. N., Andersen M. F., Andersen M. I., Christensen-Dalsgaard J., Frandsen S., Grundahl F., Harpsøe K. B. W., Kjeldsen H., Pallé P. L., 2015, A&A, 574, A54

Skrutskie M. F., Cutri R. M., Stiening R., Weinberg M. D., Schneider S., Carpenter J. M., Beichman C., Capps R., Chester T., Elias J., Huchra J., Liebert J., Lonsdale C., Monet D. G., Price S., Seitzer P., Jarrett T., Kirkpatrick J. D., Gizis J. E., Howard E., Evans T., Fowler J., Fullmer L., Hurt R., Light R., Kopan E. L., Marsh K. A., McCallon H. L., Tam R., Van Dyk S., Wheelock S., 2006, AJ, 131, 1163

Smalley B., 2005, Memorie della Societa Astronomica Italiana Supplementi, 8, 130

Smiljanic R., Korn A. J., Bergemann M., Frasca A., Magrini L., Masseron T., Pancino E., Ruchti G., San Roman I., Sbordone L., Sousa S. G., Tabernero H., Tautvaišienė G., Valentini M., Weber M., Worley C. C., Adibekyan V. Z., Allende Prieto C., Barisevičius G., Biazzo K., Blanco-Cuaresma S., Bonifacio P., Bragaglia A., Caffau E., Cantat-Gaudin T., Chorniy Y., de Laverny P., Delgado-Mena E., Donati P., Duffau S., Franciosini E., Friel E., Geisler D., González Hernández J. I., Gruyters P., Guiglion G., Hansen C. J., Heiter U., Hill V., Jacobson H. R., Jofre P., Jönsson H., Lanzafame A. C., Lardo C., Ludwig H.-G., Maiorca E., Mikolaitis Š., Montes D., Morel T., Mucciarelli A., Muñoz C., Nordlander T., Pasquini L., Puzeras E., Recio-Blanco A., Ryde N., Sacco G., Santos N. C., Serenelli A. M., Sordo R., Soubiran C., Spina L., Steffen M., Vallenari A., Van Eck S., Villanova S., Gilmore G., Randich S., Asplund M., Binney J., Drew J., Feltzing S., Ferguson A., Jeffries R., Micela G., Negueruela I., Prusti T., Rix H.-W., Alfaro E., Babusiaux C., Bensby T., Blomme R., Flaccomio E., François P., Irwin M., Koposov S., Walton N., Bayo A., Carraro G., Costado M. T., Damiani F., Edvardsson B., Hourihane A., Jackson R., Lewis J., Lind K., Marconi G., Martayan C., Monaco L., Morbidelli L., Prisinzano L., Zaggia S., 2014, A&A, 570, A122

Smith A. M. S., WASP Consortium, 2014, Contributions of the Astronomical Observatory Skalnate Pleso, 43, 500

Sousa S. G., Santos N. C., Adibekyan V., Delgado-Mena E., Israelian G., 2015, A&A, 577, A67

Southworth J., 2009, MNRAS, 394, 272

Southworth J., 2011, MNRAS, 417, 2166

Southworth J., 2015, in Rucinski S. M., Torres G., Zejda M., eds, Living Together: Planets, Host Stars and Binaries, Astronomical Society of the Pacific Conference Series Vol. 496, p. 164

Southworth J., Hinse T. C., Jørgensen U. G., Dominik M., Ricci D., Burgdorf M. J., Hornstrup A., Wheatley P. J., Anguita T., Bozza V., Novati S. C., Harpsøe K., Kjærgaard P., Liebig C., Mancini L., Masi G., Mathiasen M., Rahvar S., Scarpetta G., Snodgrass C., Surdej J., Thöne C. C., Zub M., 2009, MNRAS, 396, 1023

Spada F., Demarque P., Kim Y.-C., Sills A., 2013, ApJ, 776, 87

Sridhar S. S., Heald G., van der Hulst J. M., 2018, ArXiv e-prints

Stassun K. G., Torres G., 2018, ApJ, 862, 61

Stempels H. C., Collier Cameron A., Hebb L., Smalley B., Frandsen S., 2007, MNRAS, 379, 773

Stumpe M. C., Smith J. C., Van Cleve J., Jenkins J. M., Barclay T. S., Fanelli M. N., Girouard F., Kolodziejczak J., McCauliff S., Morris R. L., Twicken J. D., 2012, American Astronomical Society Meeting Abstracts #220, American Astronomical Society Meeting Abstracts Vol. 220, p. 330.04

Szabó G. M., Szabó R., Benkő J. M., Lehmann H., Mező G., Simon A. E., Kővári Z., Hodosán G., Regály Z., Kiss L. L., 2011, ApJL, 736, L4

Tamuz O., Mazeh T., Zucker S., 2005, MNRAS, 356, 1466

Torres G., Ribas I., 2002, ApJ, 567, 1140

Torres G., 2013, Astronomische Nachrichten, 334, 4

Torres G., Andersen J., Giménez A., 2010, A&A Rv, 18, 67

Torres G., Sandberg Lacy C. H., Pavlovski K., Feiden G. A., Sabby J. A., Bruntt H., Viggo Clausen J., 2014, ApJ, 797, 31

Torres G., Kipping D. M., Fressin F., Caldwell D. A., Twicken J. D., Ballard S., Batalha N. M., Bryson S. T., Ciardi D. R., Henze C. E., Howell S. B., Isaacson H. T., Jenkins J. M., Muirhead P. S., Newton E. R., Petigura E. A., Barclay T., Borucki W. J., Crepp J. R., Everett M. E., Horch E. P., Howard A. W., Kolbl R., Marcy G. W., McCauliff S., Quintana E. V., 2015, ApJ, 800, 99

Triaud A. H. M. J., Anderson D. R., Collier Cameron A., Doyle A. P., Fumel A., Gillon M., Hellier C., Jehin E., Lendl M., Lovis C., Maxted P. F. L., Pepe F., Pollacco D., Queloz D., Ségransan D., Smalley B., Smith A. M. S., Udry S., West R. G., Wheatley P. J., 2013a, A&A, 551, A80

Triaud A. H. M. J., Hebb L., Anderson D. R., Cargile P., Collier Cameron A., Doyle A. P., Faedi F., Gillon M., Gomez Maqueo Chew Y., Hellier C., Jehin E., Maxted P., Naef D., Pepe F., Pollacco D., Queloz D., Ségransan D., Smalley B., Stassun K., Udry S., West R. G., 2013b, A&A, 549, A18

Triaud A. H. M. J., Neveu-VanMalle M., Lendl M., Anderson D. R., Collier Cameron A., Delrez L., Doyle A., Gillon M., Hellier C., Jehin E., Maxted P. F. L., Ségransan D., Smalley B., Queloz D., Pollacco D., Southworth J., Tregloan-Reed J., Udry S., West R., 2016, ArXiv e-prints

Triaud A. H. M. J., Martin D. V., Ségransan D., Smalley B., Maxted P. F. L., Anderson D. R., Bouchy F., Collier Cameron A., Faedi F., Gómez Maqueo Chew Y., Hebb L., Hellier C., Marmier M., Pepe F., Pollacco D., Queloz D., Udry S., West R., 2017, A&A, 608, A129

Uitenbroek H., Dupree A. K., Gilliland R. L., 1998, AJ, 116, 2501

Valyavin G., Shulyak D., Wade G. A., Antonyuk K., Zharikov S. V., Galazutdinov G. A., Plachinda S., Bagnulo S., Fox Machado L., Alvarez M., Clark D. M., Lopez J. M., Hiriart D., Han I., Jeon Y.-B., Zurita C., Mujica R., Burlakova T., Szeifert T., Burenkov A., 2014, Nature, 515, 88

van Dokkum P., Conroy C., Villaume A., Brodie J., Romanowsky A. J., 2017, ApJ, 841, 68

van Loon J. T., 2013, in Kervella P., Le Bertre T., Perrin G., eds, EAS Publications Series, EAS Publications Series Vol. 60, p. 307

Vaytet N., Chabrier G., Audit E., Commerçon B., Masson J., Ferguson J., Delahaye F., 2013, A&A, 557, A90

Vincius Z., Barentsen G., Gully-Santiago M., Cody A. M., Hedges C., Still M., Barclay T., 2017, *KeplerGO/PyKE*

von Boetticher A., Triaud A. H. M. J., Queloz D., Gill S., Lendl M., Delrez L., Anderson D. R., Collier Cameron A., Faedi F., Gillon M., Gómez Maqueo Chew Y., Hebb L., Hellier C., Jehin E., Maxted P. F. L., Martin D. V., Pepe F., Pollacco D., Ségransan D., Smalley B., Udry S., West R., 2017, A&A, 604, L6

von Braun K., Boyajian T. S., van Belle G. T., Mann A., Kane S. R., 2015, in van Belle G. T., Harris H. C., eds, 18th Cambridge Workshop on Cool Stars, Stellar Systems, and the Sun, Cambridge Workshop on Cool Stars, Stellar Systems, and the Sun Vol. 18, p. 839

Weiss A., Schlattl H., 2008, Ap&SS, 316, 99

Weiss L. M., Marcy G. W., Rowe J. F., Howard A. W., Isaacson H., Fortney J. J., Miller N., Demory B.-O., Fischer D. A., Adams E. R., Dupree A. K., Howell S. B., Kolbl R., Johnson J. A., Horch E. P., Everett M. E., Fabrycky D. C., Seager S., 2013, ApJ, 768, 14

Welsh W. F., Orosz J. A., Aerts C., Brown T. M., Brugamyer E., Cochran W. D., Gilliland R. L., Guzik J. A., Kurtz D. W., Latham D. W., Marcy G. W., Quinn S. N., Zima W., Allen C., Batalha N. M., Bryson S., Buchhave L. A., Caldwell D. A., Gautier, III T. N., Howell S. B., Kinemuchi K., Ibrahim K. A., Isaacson H., Jenkins J. M., Prsa A., Still M., Street R., Wohler B., Koch D. G., Borucki W. J., 2011, ApJS, 197, 4

West A. A., Bochanski J. J., Hawley S. L., Cruz K. L., Covey K. R., Silvestri N. M., Reid I. N., Liebert J., 2006, AJ, 132, 2507

West A. A., Hawley S. L., Bochanski J. J., Covey K. R., Reid I. N., Dhital S., Hilton E. J., Masuda M., 2008, AJ, 135, 785

Wilson D. M., Gillon M., Hellier C., Maxted P. F. L., Pepe F., Queloz D., Anderson D. R., Collier Cameron A., Smalley B., Lister T. A., Bentley S. J., Blecha A., Christian D. J., Enoch B., Haswell C. A., Hebb L., Horne K., Irwin J., Joshi Y. C., Kane S. R., Marmier M., Mayor M., Parley N., Pollacco D., Pont F., Ryans R., Segransan D., Skillen I., Street R. A., Udry S., West R. G., Wheatley P. J., 2008, ApJL, 675, L113

Windmiller G., Orosz J. A., Etzel P. B., 2010, ApJ, 712, 1003

Winn J. N., 2009, in Pont F., Sasselov D., Holman M. J., eds, Transiting Planets, IAU Symposium Vol. 253, p. 99

Winn J. N., Matthews J. M., Dawson R. I., Fabrycky D., Holman M. J., Kallinger T., Kuschnig R., Sasselov D., Dragomir D., Guenther D. B., Moffat A. F. J., Rowe J. F., Rucinski S., Weiss W. W., 2011, ApJL, 737, L18

Yurchenko S. N., Barber R. J., Tennyson J., 2011, MNRAS, 413, 1828

Zahn J.-P., 1975, A&A, 41, 329